University of Technology, Sydney

A study of the dynamic response of wind turbine gearboxes

This thesis is submitted for the degree of

Doctor of Philosophy

Mingming Zhao

July 2016

This page intentionally left blank

Certificate of original authorship

I certify that the work in this thesis has not previously been submitted for a degree nor has it been submitted as part of requirements for a degree except as fully acknowledged within the text.

I also certify that the thesis has been written by me. Any help that I have received in my research work and the preparation of the thesis itself has been acknowledged. In addition, I certify that all information sources and literature used are indicated in the thesis.

Signature of Student: ……..

Date: ……

Acknowledgment

I would like to thank my supervisor A/Prof Dr. Jinchen Ji for guiding me throughout this research. Dr. Jinchen Ji has been very generous, his profession and enthusiasm always encourage me through the good and bad phases during my research.

I would also like to thank Dr. Jinchen Ji for giving me the opportunity to participate in lecturing and tutoring during the period of my research, which has been a great experience to me, and I believe such experience would help my early academic career in many ways.

Nomenclature

Symbols	Definitions
α	pressure angle
α_{pL}	pressure angle of the planet gear at the first planetary gear stage
α_{sL}	pressure angle of the sun pinion at the first planetary gear stage
α_{pH}	pressure angle of the planet gear at the second planetary stage
α_{sH}	pressure angle of the sun pinion at the second planetary stage
α_{GL}	pressure angle of the low-speed gear at the parallel gear stage
α_{GH}	pressure angle of the high-speed pinion at the parallel gear stage
a_g	addendum of the gear
a_p	addendum of the pinion
β	helix angle
β_s	helix angle of sun pinion
b	dedendum
b_i	gear backlash
C	damping matrix
c	radial clearance
$_c$	the subscript representing the planet carrier arm
Cd	center distance of gear pairs
CR	contact ratio
C_p	wind power utilization
c_{rp_L}	damping coefficient of the ring-planet gear pair at the first planetary gear stage

c_{sp_L}	damping coefficient of the sun-planet gear pair at the first planetary gear stage
c_{rp_H}	damping coefficient of the ring-planet gear pair at the second planetary gear stage
c_{sp_H}	damping coefficient of the sun-planet gear pair at the second planetary gear stage
c_{GHGL}	damping coefficient of the parallel gears at the parallel gear stage
c_{cH_sL}	damping coefficients of the shaft that links the sun pinion in the first planetary gear stage and the planet carrier arm of the second planetary gear stage
c_{GL_sH}	damping coefficient of the shaft that links the sun pinion in the second planetary gear stage and the low-speed gear of the parallel gear stage
E	modulus of elasticity
e_i	static transmission error
e_{ai}	alternating term of the static transmission error
F_{ai}	fluctuating meshing force caused by the static transmission error e_i
F_{me}	constant external loading
$f(X_i)$	non-linear gear mesh displacement function
$f(q_i)$	nonlinear gear mesh displacement function, with the consideration of gear backlash
F_L	load on rolling bearings
F_a	axial load
F_r	radial load
F_{r_max}	maximum load on rolling element

GH	subscript representing the gear at the parallel gear stage
GL	subscript representing the pinion at the parallel gear stage
Gr	gearbox gear ratio
h	tooth thickness
I	area moment of inertia
i	the number of the rows of rollers
K	gear mesh stiffness matrix
k_r	radial stiffness
k_{rp_L}	gear mesh stiffness of the ring-planet gear pair at the first planetary gear stage
k_{sp_L}	gear mesh stiffness of the sun-planet gear pair at the first planetary gear stage
k_{GHGL}	gear mesh stiffness of the gears in the parallel gear stage
K_{cH_sL}	torsional stiffness of the shaft that connects the sun pinion in the first planetary gear stage and the planet carrier arm of the second planetary stage
K_{GL_sH}	torsional stiffness of the shaft that links the sun pinion in the second planetary gear stage and the low-speed gear of the parallel gear stage
$k_{ij}(t)$	time-varying mesh stiffness function
k_{mij}	mean term of the time-varying mesh stiffness function
k_{aij}	alternating term of the time-varying mesh stiffness function
L	depth of gear tooth
LA	distance along the line of action between meshing points
L_{we}	effective contact length of roller bearings

m_{gear}	mass of the gear
m_{pinion}	mass of the pinion
M_{cL}	equivalent mass of the planet carrier arm at the first planetary gear stage
M_{pL_n}	equivalent mass of the planet gear at the first planetary gear stage
M_{sL}	equivalent mass of the sun pinion arm at the first planetary gear stage
M_{cH}	equivalent mass of the planet carrier arm at the second planetary gear stage
M_{pH_n}	equivalent mass of the planet gear at the second planetary gear stage
M_{sH}	equivalent mass of the sun pinion arm at the second planetary gear stage
M_{GL}	equivalent mass of the gear at the parallel gear stage
M_{GH}	equivalent mass of the pinion at the parallel gear stage
M	equivalent mass matrix
M_y	aerodynamic bending moment
N_g	gear teeth number, or the teeth number of the ring gear for the planetary gear stage
P	applied load at the tooth tip
P_b	base pitch
P_d	diameteral pitch
$_p$	subscript representing the planet gear
$p_i(t)$	excitation term
ρ_{air}	air density
r_{blade}	radius of blades
$_r$	subscript representing the ring gear
r_{bp_L}	base radius of the planet gear at the first planetary gear stage

r_{bs_L}	base radius of the sun pinion at the first planetary gear stage
r_{br_L}	base radius of the ring gear at the first planetary gear stage
r_{bp_H}	base radius of the planet gear at the second planetary gear stage
r_{bs_H}	base radius of the sun pinion at the second planetary gear stage
r_{br_H}	base radius of the ring gear at the second planetary gear stage
r_{bG_L}	base radius of the low-speed gears at the parallel gear stage
r_{bG_H}	base radius of the high-speed gears at the parallel gear stage
r_{pL}	pitch radius of the planet gear at the first planetary gear stage
r_{sL}	pitch radius of the sun pinion at the first planetary gear stage
r_p	pitch radius of planet gears
r_{pH}	pitch radius of the planet gear at the second planetary gear stage
r_{sH}	pitch radius of the sun pinion at the second planetary gear stage
r_{GL}	pitch radius of the low-speed gears at the parallel gear stage
r_{GH}	pitch radius of the high-speed gears at the parallel gear stage
s	subscript representing the sun pinion
T_{in}	driving torque
T_{out}	output torque
V_{wind}	average wind speed
ω_g	rotational speed of the gear, or the rotational speed of the planet carrier arm for the planetary gear stage
ω_i	meshing frequency
ω_e	external excitation frequency
ω_{blade}	rotational speed of blades

x_{cL}	equivalent transverse displacements of the planet carrier arm at the first planetary gear stage
x_{pL_n}	equivalent transverse displacements of the planet gear at the first planetary gear stage
x_{sL}	equivalent transverse displacements of the sun pinion at the first planetary gear stage
x_{cH}	equivalent transverse displacements of the planet carrier arm at the second planetary gear stage
x_{pH_n}	equivalent transverse displacements of the planet gear at the second planetary gear stage
x_{sH}	equivalent transverse displacements of the sun pinion at the second planetary gear stage
x_{GL}	equivalent transverse displacements of the low-speed gear at the parallel gear stage
x_{GH}	equivalent transverse displacements of the high-speed pinion at the parallel gear stage
X_i	relative meshing displacements on the direction of action
X_k	translational displacements
$y_{\max\_gear}$	maximum deflection of the gear tooth
$y_{\max\_pinion}$	maximum deflection of the pinion tooth
Z	number of rollers per bearing row
θ	rotational displacements
θ_{xj}	rotational displacements of gearbox components on x-axis
θ_{yj}	rotational displacements of gearbox components on y-axis

θ_{zj}	rotational displacements of gearbox components on z-axis
δ_a	axial deformation of the cylindrical roller bearing
δ_r	elastic displacement of the cylindrical roller bearing
ξ	damping ratio
γ	contact angle

Table of contents

Certificate of original authorship i

Acknowledgment ii

Nomenclature iii

Table of contents x

List of figures xiv

List of tables xxiii

Abstract xxiv

Chapter 1 Introduction 1

1.1 Background of wind energy 1

1.1.1 Sustainability 1

1.1.2 Economic benefits 2

1.1.3 Noise 4

1.1.4 Health issues 4

1.2 Current challenges 5

1.2.1 Turbine size 5

1.2.2 Gearbox reliability 6

1.2.3 Communication and data sharing 7

1.3 Research objectives 8

1.4 Thesis outline 9

Chapter 2 Literature review 11

2.1 Wind turbine drivetrain 11

2.1.1 Finite element model 11

2.2.2 Mathematical model 24
2.2 Gear dynamics 26
2.2.1 Spur gears 26
2.2.2 Helical gears 29
2.2.3 Planetary gears 31

Chapter 3 Wind turbine drivetrain structures 37
3.1 Drivetrain configurations 37
3.1.1 Modular drivetrain 39
3.1.2 Integrated drivetrain 40
3.1.3 Partially integrated drivetrain 40
3.2 Gearbox suspension layouts 41
3.2.1 Three-point mounting configuration 41
3.2.2 Two-bearing configuration 42
3.2.3 Hydraulic suspension 42
3.3 Parallel-shaft and planetary gearboxes 43
3.4 Spur and helical gears 46
3.5 Bearings 48

Chapter 4 Torsional vibrations of wind turbine gearboxes 51
4.1 Mathematical modelling 51
4.2 Derivation of equations 56
4.3 Specifications 65
4.3.1 General information 65
4.3.2 Excitation conditions 67

4.3.3 Time-varying mesh stiffness 69
4.3.4 Damping 72
4.4 Results 72
4.4.1 Effect of the static transmission error E 74
4.4.2 Effect of the mesh stiffness K 80
4.4.3 Mean-to-alternating force ratio Fm/Fa 87
4.5 Discussions 92

Chapter 5 Dynamic response of a 4DOF wind turbine gearbox 95
5.1 Modelling 95
5.2 Derivation of equations 97
5.3 Specifications 105
5.4 Results 107
5.4.1 External excitation only 107
5.4.2 Constant external excitation 110
5.4.3 Mean-to-alternating force ratio Fm/Fa 113
5.5 Discussions 118

Chapter 6 Effect of bending moment on a 6DOF wind turbine planetary gearbox 121
6.1 Modelling 121
6.2 Derivation of equations 122
6.3 Simulation and results 132
6.3.1 Constant external excitations 132
6.3.2 Wind fluctuation and bending moment with $My/Tin = 0.5$ 136
6.3.3 Wind fluctuation and bending moment with $My/Tin = 1$ 140

6.3.4 Wind fluctuation and bending moment with $My/Tin = 5$ 144

6.3.5 Increased driving torque and bending moment with $My/Tin = 1$ 148

6.3.6 Effects of the bearing clearances 152

6.4 Discussions 153

Chapter 7 Conclusions and future research 157

Chapter 8 Appendices 161

8.1 Gear 161

8.2 Wind fluctuation and bending moment with $My/Tin = 0.5$ 163

8.2.1 Mean-to-alternating force ratio $Fm/Fa = 10$ 163

8.2.2 Mean-to-alternating force ratio $Fm/Fa = 2$ 166

8.3 Wind fluctuation and bending moment with $My/Tin = 1$ 168

8.3.1 Mean-to-alternating force ratio $Fm/Fa = 10$ 168

8.3.2 Mean-to-alternating force ratio $Fm/Fa = 2$ 171

8.4 Wind fluctuation and bending moment with $My/Tin = 5$ 173

8.4.1 Mean-to-alternating force ratio $Fm/Fa = 10$ 173

8.4.2 Mean-to-alternating force ratio $Fm/Fa = 2$ 176

8.5 Increased wind fluctuation and bending moment with $My/Tin = 1$ 178

8.5.1 Mean-to-alternating force ratio $Fm/Fa = 10$ 178

8.5.2 Mean-to-alternating force ratio $Fm/Fa = 2$ 181

References 183

Publications 204

List of figures

Figure 1.1. Australia's wind resources 2

Figure 3.1. Horizontal-axis wind turbines 38

Figure 3.2. Wind turbine drivetrain with gearbox 38

Figure 3.3. Drivetrain of a 750 kW wind turbine 39

Figure 3.4. Three point mounting configuration 41

Figure 3.5. Two-point mounting configuration 42

Figure 3.6. Hydraulic suspension system 43

Figure 3.7. Hydraulic suspension system 43

Figure 3.8. Wind turbine gearboxes with (a) one-planetary-two-parallel gear stages (b) two-planetary-one-parallel gear stages 44

Figure 3.9. Involute tooth nomenclature 46

Figure 3.10. Nomenclature of a gear tooth 47

Figure 3.11. Geometry of a helical gear 47

Figure 3.12. Bearing nomenclature and locations 49

Figure 4.1. Torsional model of a wind turbine gearbox 52

Figure 4.2: Side view of the proposed gearbox 54

Figure 4.3: A gear pair in planetary gear stage 55

Figure 4.4. Simplified model of a gear tooth 71

Figure 4.5. The vibrational responses of Qrp_H caused by $e = 10\,\mu m$ (a) Time histories (b) FFT spectrum (c) Phase Portrait (d) Poincare map 75

Figure 4.6. The vibrational responses of $QGHGL$ caused by $e = 10\,\mu m$ (a) Time histories (b) FFT spectrum (c) Phase Portrait (d) Poincare map 75

Figure 4.7. The vibrational responses of Qrp_H caused by $e = 100\,\mu m$ (a) Time histories (b) FFT spectrum (c) Phase Portrait (d) Poincare map 77

Figure 4.8. The vibrational responses of $QGHGL$ caused by $e = 100\,\mu m$ (a) Time histories (b) FFT spectrum (c) Phase Portrait (d) Poincare map 77

Figure 4.9. The vibrational responses of Qrp_H caused by $e = 300\,\mu m$ (a) Time histories (b) FFT spectrum (c) Phase Portrait (d) Poincare map 79

Figure 4.10. The vibrational responses of $QGHGL$ caused by $e = 300\,\mu m$ (a) Time histories (b) FFT spectrum (c) Phase Portrait (d) Poincare map 79

Figure 4.11. The vibrational responses of Qrp_H caused by $KmKa = 10$ (a) Time histories (b) FFT spectrum (c) Phase Portrait (d) Poincare map 81

Figure 4.12. The vibrational responses of $QGHGL$ caused by $KmKa = 10$ (a) Time histories (b) FFT spectrum (c) Phase Portrait (d) Poincare map 82

Figure 4.13. The vibrational responses of Qrp_H caused by $KmKa = 3.33$ (a) Time histories (b) FFT spectrum (c) Phase Portrait (d) Poincare map 83

Figure 4.14. The vibrational responses of $QGHGL$ caused by $KmKa = 3.33$ (a) Time histories (b) FFT spectrum (c) Phase Portrait (d) Poincare map 84

Figure 4.15. The vibrational responses of Qrp_H caused by $KmKa = 2$ (a) Time histories (b) FFT spectrum (c) Phase Portrait (d) Poincare map 86

Figure 4.16. The vibrational responses of $QGHGL$ caused by $KmKa = 2$ (a) Time histories (b) FFT spectrum (c) Phase Portrait (d) Poincare map 86

Figure 4.17. The vibrational responses of Qrp_H caused by $FmFa = 100$ (a) Time histories (b) FFT spectrum (c) Phase Portrait (d) Poincare map 88

Figure 4.18. The vibrational responses of $QGHGL$ caused by $FmFa = 100$ (a) Time histories (b) FFT spectrum (c) Phase Portrait (d) Poincare map 88

Figure 4.19. The vibrational responses of Qrp_H caused by $FmFa = 10$ (a) Time histories (b) FFT spectrum (c) Phase Portrait (d) Poincare map 89

Figure 4.20. The vibrational responses of $QGHGL$ caused by $FmFa = 10$ (a) Time histories (b) FFT spectrum (c) Phase Portrait (d) Poincare map 90

Figure 4.21. The vibrational responses of Qrp_H caused by $FmFa = 1.67$ (a) Time histories (b) FFT spectrum (c) Phase Portrait (d) Poincare map 91

Figure 4.22. The vibrational responses of $QGHGL$ caused by $FmFa = 1.67$ (a) Time histories (b) FFT spectrum (c) Phase Portrait (d) Poincare map 92

Figure 5.1. Sketch of the proposed wind turbine gearbox 96

Figure 5.2. The vibrational responses of $Qrp1$ (a) Time histories (b) FFT spectrum .. 108

Figure 5.3. The vibrational responses of $Qsp1$ (a) Time histories (b) FFT spectrum .. 109

Figure 5.4. The vibrational responses of $Qg1g2$ (a) Time histories (b) FFT spectrum109

Figure 5.5. The axial vibrational responses $Xg1a$ (a) Time histories (b) FFT spectrum 109

Figure 5.6. The axial vibrational responses $Xg4a$ (a) Time histories (b) FFT spectrum 110

Figure 5.7. The vibrational responses of $Qrp1$ (a) Time histories (b) FFT spectrum .. 111

Figure 5.8. The vibrational responses of $Qsp1$(a) Time histories (b) FFT spectrum ... 111

Figure 5.9. The vibrational responses of $Qg1g2$ (a) Time histories (b) FFT spectrum112

Figure 5.10. The axial vibrational responses $Xg1a$ (a) Time histories (b) FFT spectrum 112

Figure 5.11. The vibrational responses $Xg4a$ (a) Time histories (b) FFT spectrum 112

Figure 5.12. The vibrational responses of $Qrp1$ with the mean-to-fluctuating external force ratio Fm/Fa of 5 (a) Time histories (b) FFT spectrum 114

Figure 5.13. The vibrational responses of $Qsp1$ with the mean-to-fluctuating external force ratio Fm/Fa of 5 (a) Time histories (b) FFT spectrum 114

Figure 5.14. The vibrational responses of $Qg1g2$ with the mean-to-fluctuating external force ratio Fm/Fa of 5 (a) Time histories (b) FFT spectrum 115

Figure 5.15. The axial vibrational responses $Xg1a$ with the mean-to-fluctuating external force ratio Fm/Fa of 5 (a) Time histories (b) FFT spectrum 115

Figure 5.16. The vibrational responses of $Xg4a$ with the mean-to-fluctuating external force ratio Fm/Fa of 5 (a) Time histories (b) FFT spectrum 115

Figure 5.17. The vibrational responses of $Qrp1$ with the mean-to-fluctuating external force ratio Fm/Fa of 2 (a) Time histories (b) FFT spectrum 117

Figure 5.18. The vibrational responses of $Qsp1$ with the mean-to-fluctuating external force ratio Fm/Fa of 2 (a) Time histories (b) FFT spectrum 117

Figure 5.19. The vibrational responses of $Qg1g2$ with the mean-to-fluctuating external force ratio Fm/Fa of 2 (a) Time histories (b) FFT spectrum 117

Figure 5.20. The axial vibrational responses $Xg1a$ with the mean-to-fluctuating external force ratio Fm/Fa of 2 (a) Time histories (b) FFT spectrum 118

Figure 5.21. The axial vibrational responses $Xg4a$ with the mean-to-fluctuating external force ratio Fm/Fa of 2 (a) Time histories (b) FFT spectrum 118

Figure 6.1. A wind turbine planetary gearbox 122

Figure 6.2. A sun-planet gear pair..... 123

Figure 6.3. A sun-planet gear pair (a) with $\phi 1 = 0°$ (b) with $\phi 2 = 120°$ (c) with $\phi 3 = 240°$ 124

Figure 6.4. Bearing stiffness function with clearance [55] 128

Figure 6.5. The vibrational responses of $Qrp1$ (a) Time histories (b) FFT spectrum (c) Phase Portrait (d) Poincare map 133
Figure 6.6. The vibrational responses of $Qsp1$ (a) Time histories (b) FFT spectrum (c) Phase Portrait (d) Poincare map 134
Figure 6.7. Load share ratio (LSR) 135
Figure 6.8. The radial vibrational responses of planet gear Xp (a) Time histories (b) FFT spectrum 136
Figure 6.9. The axial vibrational responses of planet gear Xpa (a) Time histories (b) FFT spectrum 136
Figure 6.10. The vibrational responses of $Qrp1$ (a) Time histories (b) FFT spectrum (c) Phase Portrait (d) Poincare map 137
Figure 6.11. The vibrational responses of $Qsp1$ (a) Time histories (b) FFT spectrum (c) Phase Portrait (d) Poincare map 138
Figure 6.12. Load share ratio (LSR) 139
Figure 6.13. The radial vibrational responses of planet gears Xp (a) Time histories (b) FFT spectrum 139
Figure 6.14. The axial vibrational responses of planet gears Xpa (a) Time histories (b) FFT spectrum 140
Figure 6.15. The vibrational responses of $Qrp1$ (a) Time histories (b) FFT spectrum (c) Phase Portrait (d) Poincare map 141
Figure 6.16. The vibrational responses of $Qsp1$ (a) Time histories (b) FFT spectrum (c) Phase Portrait (d) Poincare map 142
Figure 6.17. Load share ratio (LSR) 143
Figure 6.18. The radial vibrational responses Xp (a) Time histories (b) FFT spectrum 143

Figure 6.19. The axial vibrational responses Xpa (a) Time histories (b) FFT spectrum 144

Figure 6.20. The vibrational responses of $Qrp1$ (a) Time histories (b) FFT spectrum (c) Phase Portrait (d) Poincare map 145

Figure 6.21. The vibrational responses of $Qsp1$ (a) Time histories (b) FFT spectrum (c) Phase Portrait (d) Poincare map 146

Figure 6.22. Load share ratio (LSR) 147

Figure 6.23. The radial vibrational responses Xp (a) Time histories (b) FFT spectrum 147

Figure 6.24. The axial vibrational responses Xpa (a) Time histories (b) FFT spectrum 148

Figure 6.25. The vibrational responses of $Qrp1$ (a) Time histories (b) FFT spectrum (c) Phase Portrait (d) Poincare map 149

Figure 6.26. The vibrational responses of $Qsp1$ (a) Time histories (b) FFT spectrum (c) Phase Portrait (d) Poincare map 150

Figure 6.27. Load share ratio (LSR) 151

Figure 6.28. The radial vibrational responses Xp (a) Time histories (b) FFT spectrum 151

Figure 6.29. The axial vibrational responses Xpa (a) Time histories (b) FFT spectrum 152

Figure 6.30. Comparison between the vibrational responses $Qrp1$ with and without bearing clearances. (a) Driving torque only; (b) $MyTin = 0.5$; (c) $MyTin = 1$; (d) with increased Tin at $MyTin = 0.5$ 153

Figure 8.1. Nomenclature of a gear tooth [182] 161

Figure 8.2. Gear tooth nomenclature 161

Figure 8.3. The vibrational responses of Qrp (a) Time histories (b) FFT spectrum (c) Phase Portrait (d) Poincare map 163

Figure 8.4. The vibrational responses of Qsp (a) Time histories (b) FFT spectrum (c) Phase Portrait (d) Poincare map 164

Figure 8.5. Load share ratio (LSR) 164

Figure 8.6. The radial vibrational responses of planet gears Xp (a) Time histories (b) FFT spectrum 165

Figure 8.7. The axial vibrational responses of planet gears Xpa (a) Time histories (b) FFT spectrum 165

Figure 8.8. The vibrational responses of Qrp (a) Time histories (b) FFT spectrum (c) Phase Portrait (d) Poincare map 166

Figure 8.9. The vibrational responses of Qsp (a) Time histories (b) FFT spectrum (c) Phase Portrait (d) Poincare map 166

Figure 8.10. Load share ratio (LSR) 167

Figure 8.11. The radial vibrational responses of Xp (a) Time histories (b) FFT spectrum 167

Figure 8.12. The axial vibrational responses of Xpa (a) Time histories (b) FFT spectrum 167

Figure 8.13. The vibrational responses of Qrp (a) Time histories (b) FFT spectrum (c) Phase Portrait (d) Poincare map 168

Figure 8.14. The vibrational responses of Qsp (a) Time histories (b) FFT spectrum (c) Phase Portrait (d) Poincare map 169

Figure 8.15. Load share ratio (LSR) 169

Figure 8.16. The radial vibrational responses Xp (a) Time histories (b) FFT spectrum 170

Figure 8.17. The axial vibrational responses (a) Time histories (b) FFT spectrum 170

Figure 8.18. The vibrational responses of Qrp (a) Time histories (b) FFT spectrum (c) Phase Portrait (d) Poincare map 171

Figure 8.19. The vibrational responses of Qsp (a) Time histories (b) FFT spectrum (c) Phase Portrait (d) Poincare map 171

Figure 8.20. Load share ratio (LSR) 172

Figure 8.21. The radial vibrational responses Xp (a) Time histories (b) FFT spectrum 172

Figure 8.22. The axial vibrational responses Xpa (a) Time histories (b) FFT spectrum 172

Figure 8.23. The vibrational responses of Qrp (a) Time histories (b) FFT spectrum (c) Phase Portrait (d) Poincare map 173

Figure 8.24. The vibrational responses of Qsp (a) Time histories (b) FFT spectrum (c) Phase Portrait (d) Poincare map 174

Figure 8.25. Load share ratio (LSR) 174

Figure 8.26. The radial vibrational responses Xp (a) Time histories (b) FFT spectrum 175

Figure 8.27. The axial vibrational responses Xpa (a) Time histories (b) FFT spectrum 175

Figure 8.28. The vibrational responses of Qrp (a) Time histories (b) FFT spectrum (c) Phase Portrait (d) Poincare map 176

Figure 8.29. The vibrational responses of Qsp (a) Time histories (b) FFT spectrum (c) Phase Portrait (d) Poincare map 176

Figure 8.30. Load share ratio (LSR) 177

Figure 8.31. The radial vibrational responses Xp (a) Time histories (b) FFT spectrum 177

Figure 8.32. The axial vibrational responses Xpa (a) Time histories (b) FFT spectrum 177

Figure 8.33. The vibrational responses of Qrp (a) Time histories (b) FFT spectrum (c) Phase Portrait (d) Poincare map 178

Figure 8.34. The vibrational responses of Qsp (a) Time histories (b) FFT spectrum (c) Phase Portrait (d) Poincare map 179

Figure 8.35. Load share ratio (LSR) 179

Figure 8.36. The radial vibrational responses Xp (a) Time histories (b) FFT spectrum 180

Figure 8.37. The axial vibrational responses Xpa (a) Time histories (b) FFT spectrum 180

Figure 8.38. The vibrational responses of Qrp (a) Time histories (b) FFT spectrum (c) Phase Portrait (d) Poincare map 181

Figure 8.39. The vibrational responses of Qsp (a) Time histories (b) FFT spectrum (c) Phase Portrait (d) Poincare map 181

Figure 8.40. Load share ratio (LSR) 182

Figure 8.41. The radial vibrational responses Xp (a) Time histories (b) FFT spectrum 182

Figure 8.42. The axial vibrational responses Xpa (a) Time histories (b) FFT spectrum 182

List of tables

Table 1. Mass moment of inertia, radius and pressure angle of each gear of gearbox ... 66

Table 2. AGMA full-depth gear tooth specifications ... 71

Table 3. List of gears and specifications ... 106

Abstract

Gearbox is an important component for large modern wind turbines incorporated either by a squirrel cage induction generator or a doubly fed induction generator. Wind turbine gearboxes have distinct features from standard gearboxes. They are used to increase the rotor speed to a speed suitable for the electricity generation and operate under varying load conditions, while standard gearboxes are designed to step down from high speed to low speed and operate under full load conditions. The modern wind energy industry has been experiencing high gearbox failure rates since its inception. However, the fundamental mechanisms of gearbox failures have not been fully understood yet. Thus, this thesis studies the dynamic response of wind turbine gearbox components in order to provide useful information to the wind energy industry to reduce the possibility of the gearbox failures at an early stage.

The torsional vibrations of wind turbine gearbox are firstly investigated in this thesis. The nonlinear dynamic model developed considers the factors such as time-varying mesh stiffness, damping, static transmission error and gear backlash. Both the external excitation due to wind gust and the internal excitation due to static transmission error are included. With the help of time history, FFT spectrum, phase portrait, Poincare map and the effects of the static transmission error, mean-to-alternating force ratio and time-varying mesh stiffness on the dynamic behaviour of wind turbine gearbox components are investigated by using the numerical integration method. It is found that the external excitation has the most influence on the torsional vibrations of the wind turbine gearbox components. The gear mesh stiffness has more influence than the static transmission error, and the static transmission error has the least influence.

Secondly, the dynamic response of a proposed four-degree-of-freedom (4DOF) wind turbine gearbox dynamic model is studied. The effects of different excitation conditions are discussed. The results show that the external excitation fluctuation has large influence on the dynamic responses of both the gears and bearings, and explain under which conditions the fretting corrosion, as one of the wind turbine gearbox failure modes, may occur.

Thirdly, the effects of bending moments on the dynamic responses of a wind turbine planetary gearbox are analysed. The proposed six-degree-of-freedom (6DOF) dynamic model takes into account the key factors such as the time-varying mesh stiffness, bearing stiffness, damping, static transmission error, gear backlash and bearing clearances. It is found that the bending moments can affect the gear meshes. What is more, the driving torque may have the effect on the bending moments. Furthermore, the bearing clearance has negligible effect in the planetary gear stage.

This page intentionally left blank

Chapter 1 Introduction

Wind is a vast potential source of renewable energy, generated by the complex natural mechanisms such as the rotation of earth, the heat capacity of sun, and the cooling effect of the oceans, etc. Wind energy is generated by converting the natural wind kenetic energy into electrical energy. It was used for grinding grain and rural battery charging in early 1970s, and along with the development of the modern wind turbines since late 1970s, the wind energy industry has improved dramatically up to present [1, 2].

In this chapter, the background of wind energy is introduced in Section 1.1, the current challenges are listed in Section 1.2, the research objectives are presented in Section 1.3, and the thesis outline is provided in Section 1.4.

1.1 Background of wind energy

This section presents the general background of wind energy. In particular, it describes the aspects such as sustainability, economic benefits, noise and health issues.

1.1.1 Sustainability

Compared with the traditional energy sources such as coal and gas, the electricity generated by wind energy industry is estimated to be one million gigawatts (GW) for the total global land coverage. A standard-sized wind farm (e.g. 150MW) can provide the electricity for 60,000-65,000 homes, and can save up to 360,000 tonnes of carbon emissions annually. Large wind farms (e.g. 500MW) can produce electricity to power 200,000 homes, and save 1.3 million tonnes of carbon emissions [3, 4]. The wind energy has been a fast growing renewable energy source since 1970s, and it is still

expected to grow with an increasing annual rate of 30% up to 2030. The wind energy is largely used in Europe and United States, and has been a rapid growth in China and India.

In Australia, the wind farms are mainly located in South Australia, Victoria and Western Australia, as shown in Figure 1.1. The Australian wind energy industry has increased with an average annual growth of 69.5% since 1999, and have the total electricity generated by wind energy increased from 1.5% in 2008 to the predicted 12.1% in 2030 [1].

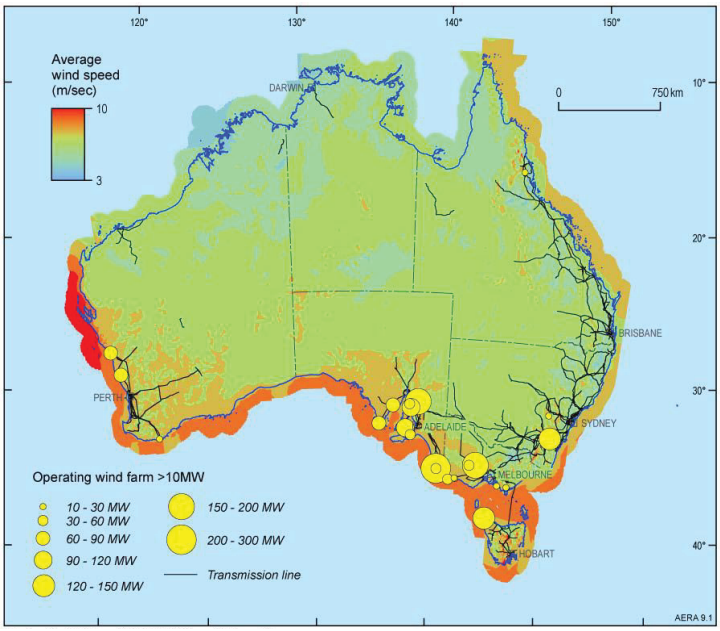

Figure 1.1. Australia's wind resources [1]

1.1.2 Economic benefits

The best estimates of the equivalent cost of wind energy is $60 to $80 per megawatt hour (MWh), compared with $31 to $40 per megawatt hour (MWh) for coal and $37 to $44 per megawatt hour (MWh) for gas. It can be seen that the electricity produced from

wind energy is currently more expensive than fuel and gas. However, wind energy is the only pollution free option, and these cost estimates do not include the cost of pollution. As the world is paying more attention to reduce the carbon emissions to respond to the threat of climate change, the traditional energy sources, such as coal and gas, would cost more than wind energy in the future. In addition, the efficiency is another important aspect for wind energy, as modern wind turbines convert around 45% of the passing wind into electricity. However, the coal-fired power stations convert 29% to 37% of the coal into electricity, and the gas plants convert 32% to 50% of gas into electricity [3].

What is more, the job opportunities created by wind energy industries would be another important benefit. According to the United Nations Energy Program (UNEP)[1], wind energy creates more jobs for each dollar invested than the traditional power generations such as coal and gas [5]. Under the Australian Government's Renewable Energy Target (RET) scheme[2], it is estimated that wind energy projects could lead to the creation of more than 6000 jobs in New South Wales (NSW), Australia [6]. A large proportion of them is in the construction and operation of wind farms in regional areas, and the increased employment could also provide benefits to the local businesses in the areas where the wind farms locate. For example, AGL energy provides $15,000 per year to a community fund for each of the four wind farms it has built in South Australia over their operational lifetime [3].

[1] The United Nations Environment Programme (UNEP), established in 1972, provides leadership and encourage partnership in caring for the environment by inspiring, informing and enabling nations and peoples to improve their quality of life without compromising that of future generations.

[2] The Renewable Energy Target (RET) is an Australian Government scheme designed to reduce emissions of greenhouse gases in the electricity sector, and encourage the additional generation of electricity from sustainable and renewable sources.

1.1.3 Noise

Wind turbines are currently one of the quietest forms of energy generation. Although a low frequency noise is generated due to some factors, such as turbine height and the impact of wind, the modern wind turbines have significantly reduced the noises compared with those built 20 years ago. Furthermore, NSW currently uses the South Australian Wind Farms Environmental Noise Guidelines for the assessment process for approving wind farms [7]. A wind farm is required to demonstrate that the noise levels at neighbouring residences would strictly meet noise limits before operation, and planning the approvals requires that the noise monitoring is routinely carried out on wind farms, with the results provided to planning authorities. Independent monitoring would also ensures the compliance with noise standards [3, 8].

1.1.4 Health issues

In Australia, the anti-wind activists have claimed that the non-audible infrasound, generated by wind turbines, can make people sick. However, the National Health and Medical Research Council (NHMRC) have currently conducted a review of scientific literatures, and stated that there is no scientific evidence to link the wind turbines with adverse health effects. For the residents with the symptoms such as sleeplessness, headaches or racing heartbeat, it was suggested by the National Health and Medical Research Council (NHMRC) that such health effects may be caused by the misinformation about wind turbines, but not the turbine itself. In fact, the low frequency infrasound is everywhere in the environment, such as wind, rivers and traffics, and the modern wind turbines have already reduced the level of infrasound significantly. On the other hand, there are many health benefits when using the wind energy over traditional

energy forms such as coal and gas. As wind energy is a sustainable energy, it improves air quality by reducing the amount of pollution [3].

1.2 Current challenges

With the dramatic increasing of energy consumption and the improvement of the environment pollution, the global installed capacity of wind energy has increased 20 times over the last decade. Wind energy has aroused extensive attention and received a rapid development as a renewable energy source. However, the wind energy industry is currently facing many challenges. This section introduces the challenges of wind energy, and mainly focus on three aspects: the challenges regarding the turbine size, gearbox reliabilities, and the difficulties of the communication and data sharing.

1.2.1 Turbine size

Wind turbine industry has been continuously improving the turbine designs since its inception, and the size optimization has become a challenge for the wind energy industry. Although to increase the turbine capacity is the major task for the industry, there are still economic and logistical constraints to the continued growth to larger turbine sizes. The primary argument for limiting the size of wind turbines is based on the square-cube law, which states that as a wind turbine rotor grows in size, its energy output increases, while the cost of material increases with the blade diameter. This suggests that the cost of a larger turbine grows faster than the resulting energy output. Thus, optimized turbine size is still expected to be one of the topics for academics and engineers in the future [2, 8].

1.2.2 Gearbox reliability

Being one of the most expensive components of a wind turbine, the gearbox has experienced higher-than-expected failure rates since the inception of wind energy. In 2006, The German Allianz received 1000 wind turbine damage claims. One of the common maintenance requirements of the wind turbine damage claims is to replace the gearbox every 5 years over the 20-year design lifetime, and the studies have also shown that the wind turbine gearboxes could fail in their early life of operation within 3-7 years. The long downtime and high maintenance cost of wind turbine gearboxes have been the challenges for the modern wind energy industry [9].

Wind turbine gearbox is a complex dynamic system that is subjected to highly complex loadings. Unlike other industrial gearbox applications, most problems in wind turbine gearboxes are considered to be generic in nature, meaning that the problems are not specific to a single turbine model or manufacturer [10, 11]. During turbine operation, the internal load varies with the fluctuating driving torque, gravitational loads, corresponding bending moments and reverse torques during emergency stops, etc. [12, 13]. The wind gust could result in unbalanced aerodynamic loads of the rotor, which may lead to the non-torque bending moments feed into the gearbox. Large driving torques may lead to contact loss of the missing gear teeth. The bending moments applied on the main shaft could cause the loads on gear teeth to change dramatically. Vibrations inherently exist within the entire gearbox [8].

Although the presence of problems is evident, and the wind turbine manufactures, gear designers and bearing manufacturers have improved the load prediction, design, and operation of gearboxes over the past two decades, the root causes of the failure

mechanisms have not been fully understood yet. Thus, there is a need for the fundamental studies to support the reliability analyses, and to improve the reliability of wind turbines [14-17].

1.2.3 Communication and data sharing

The design process for wind turbine gearboxes is characterized by the integration of multiple disciplines, which work independently toward the final integration of many turbine components. Each component is affected by other surrounding components, as described in Section 1.2.2. Thus, to follow the design process appropriately, all parties involved in the design process must have a complete knowledge of the behaviour of all components. For example, the wind turbine manufacturers should understand the behaviour of gearbox, the gearbox manufacturers should understand the loading conditions, and the bearing manufacturers should know the interaction of the internal components of wind turbine gearbox. An absolute transparency and data sharing is required for the design process [18].

Unfortunately, data sharing has become one of the challenges between the wind turbine designers and the component providers. For example, the gearbox supplier may work with multiple wind turbine manufacturers. A single wind turbine company may have more than one gearbox suppliers. Such intense competition has made the transparency and information sharing virtually impossible, and the information accessibility produced by the fierce competition and inherent proprietary data have become a barrier to prevent the iterative nature of the design process [18, 19].

1.3 Research objectives

Wind turbine gearboxes experience complicated loadings during operation, as introduced in Section 1.2.2. The studies have found that the wind turbines with different sizes or configurations have similar gearbox failures. Thus, to study the dynamic model of a wind turbine gearbox could provide useful information to understand its fundamental mechanism, and reduce the possibility of gearbox failures [10, 18, 20]. The objectives of the current research are presented as follows:

(1). To propose a torsional model of a wind turbine gearbox, which consists of two planetary and one parallel gear stages for large capacity wind turbines. Both the driving torque and the internal excitation due to static transmission error are included, with the consideration of some key factors such as time-varying mesh stiffness, damping, static transmission error and gear backlash.

(2). To study the dynamic response of a 4DOF wind turbine gearbox model under different excitation conditions. The dynamic responses of the gearbox components, such as gears and bearings, would be investigated.

(3). To study the effects of the bending moments on a 6DOF wind turbine gearbox model. The effects of the driving torque and the bending moment would be analysed and compared.

This research would provide a deeper understanding of wind turbine gearboxes. The proposed dynamic models can then be used to study the fundamental mechanism of wind turbine gearbox components including gears and bearings. It is likely that the

lessons learned in solving the problems on a smaller scale gearbox can be applied directly to the future wind turbines with a larger scale, which could provide useful information to reduce the possibility of the gearbox failures at an early stage.

1.4 Thesis outline

Chapter 1 introduces the background and challenges of wind energy industry, and presents the objectives of the current PhD research.

Chapter 2 provides the literature review regarding the wind turbine gearboxes and gear dynamics.

Chapter 3 provides the general information of wind turbines, including the drivetrain configurations, gearbox suspension layouts, gearbox types and components.

Chapter 4 presents the study of the torsional vibrations of wind turbine gearboxes. The proposed nonlinear dynamic model considers the key factors such as time-varying mesh stiffness, damping, static transmission error and gear backlash, and takes into account both the external excitation due to wind and the internal excitation due to static transmission error.

Chapter 5 extends the torsional wind turbine gearbox model, and investigates the dynamic response of gearbox components under different excitation conditions.

Chapter 6 focuses on the effects of bending moments on the dynamic responses of a 6DOF wind turbine planetary gearbox, and explores the effects of planet bearing clearance.

Chapter 7 gives the conclusion, and Chapter 8 presents the appendices.

Chapter 2 Literature review

Gearbox has been the major cause of many reliability problems for the modern wind energy industry, and most problems are currently considered to be generic in nature, meaning that they are not specific to a single gear manufacturer or turbine model, but to all wind turbine gearboxes [17]. Due to the complexity and distinct nature, the fundamental failure mechanisms of wind turbine gearboxes have not been fully understood yet, to the author's best knowledge. Consequently, the study of wind turbine gearboxes has been receiving significant attention from both the industry and researchers as an understanding of failure modes and failure sources could provide useful information to the wind energy industry to reduce the possibility of gearbox failures at an early stage.

In this chapter, a literature review is provided regarding the researches on wind turbine drivetrains and gearboxes. In addition, gears are used to transmit the power in wind turbine gearboxes. The ability to incorporate them into wind turbine gearbox models has become an essential topic. Thus, a general understanding of gear dynamics has also been provided.

2.1 Wind turbine drivetrain

2.1.1 Finite element model

Peeters et al. [21, 22] studied the torsional behaviours of a wind turbine drivetrain using the finite element method, and then extended their multibody models with the inclusion of gears and bearings for both the planetary and parallel gear stages. Later, Peeters et al. [23, 24] verified their wind turbine drivetrain model, and presented the calculations for

the gear meshing force, and a Campbell analysis for the possible resonance behaviour and transient load cases. Heege et al. [25] studied the nonlinear dynamic behaviours of a wind turbine planetary gearbox using the finite element method. They found that the dynamic radial and axial bearing load oscillations of the individual drivetrain bearings are not necessarily proportional to the driving torque. Helsen et al. [26] studied a flexible multibody model of a wind turbine gearbox, and compared the results with the rigid model.

Oyague, Gorman and Sheng [19] established a dynamic model for a wind turbine drivetrain, and validated the results by experiments. They also discussed the differences between the fully integrated design process and the coupled design process. Oyague [18] studied the loading conditions of a wind turbine gearbox, and found that the level of complexity does not greatly affect torsional behaviour, but the models of higher complexity can be used to study the loading conditions for the gearbox bearings. Later, Oyague, Butterfield and Sheng [27] presented a brief review of the gearbox design developed by the National Renewable Energy Laboratory (NREL), and described the design procedures and manufacturing standards. Oyague, Gorman and Sheng [28] also gave a review of the experimental data and analysis of the Gearbox Reliability Collaborative (GRC) project[3] for the study of the planet carrier deformation. Oyague [29] studied the load cases of a wind turbine design process. He provided a broad understanding of the 750kW wind turbine drivetrain established by the Gearbox

[3] National Renewable Energy Laboratory (NREL) initiated the Gearbox Reliability Collaborative (GRC) in 2007. This project combines field testing, dynamometer testing, analysis, modelling, condition monitoring, development of a failure database, and operations.

Reliability Collaborative (GRC). In addition, they also presented the fatigue and ultimate strength drivetrain loads resulting from simulations.

Coultate et al. [13] proposed a method to calculate the damages of wind turbine components, and the obtained lateral and axial loads could be used for the component life predictions. After that, Coultate et al. [30] presented four models of wind turbine gearboxes with various levels of flexibilities, including the nonlinear bearings, flexible planet carrier arm and flexible housing. They found that the flexing of the structure affects the misalignment at the contacting tooth and roller surfaces, depending on the design and location of particular gears and bearings. Later, Zhang et al. [20] studied the gear and bearing stress of a wind turbine gearbox by using the combination of multi-body dynamic and quasi-static models. Crowther, Ramakrishnan, Zaidi and Halse [31] also addressed the design issues of wind turbine planetary gearboxes. They showed how the misalignment of the planet pins varies with the rotation of the planetary gears, and how subsequently time-varying contact stresses and load distributions occur in the planet gears and bearings, which influence the fatigue life of the gearbox components. Spinato et al. [32] investigated the reliability of more than 6000 modern onshore wind turbines in Denmark and Germany over 11 years, and they also observed the particularly changes of the generators, gearboxes and converters in a subset of 650 turbines in Schleswig Holstein, Germany. The average failure rate of turbine populations and wind turbine subassemblies were studied.

Todorov, Dobrev and Massouh [16] proposed a dynamic multibody model of a wind turbine drivetrain with consideration of the gear mesh stiffness, and concluded that the transient loads in the gearbox are very high and may need special attention. Todorov

and Vukov [33] continued their study on the dynamic multibody model, and took into account the time-varying mesh stiffness. The results showed that the transient loads in the gearbox have complex characteristics, and the proposed model can be used for fault and wear gear monitoring. De Coninck et al. [34] conducted a test on a wind turbine gearbox under realistic conditions, and studied the load cases. Abboudi et al. [35] studied the dynamic behaviour of a two-stage wind turbine gearbox by using the numerical integration algorithm. The dynamic response of bearings, shafts and gear teeth were obtained. Allen et al. [36] simulated a 5MW wind turbine model, with the consideration of both the structural and aerodynamic effects. Haastrup, Hansen and Ebbesen [37] investigated the gearbox bushings of wind turbine drivetrains, and compared three different models: linear, nonlinear and hydro-dynamic bushing. The results showed that all three models are capable of displaying the main dynamic characteristics of gearbox bushings, and the linear and nonlinear models are better on accuracy compared with the hydro-dynamic model. Helsen et al. [38] studied the dynamic response of a wind turbine drivetrain. They investigated both the planetary and parallel gear stages, and concluded that the optimization method should be used for the accurate bearing representation. Moreover, they also observed the time-varying gear mesh stiffness excitations within the modal participation factors, which indicates that the time-varying gear mesh stiffness should be used for accurately modelling. Furthermore, a test of 13.2MW dynamic testing facility was conducted, and the experimental results showed that the test rig can show the dynamics responses of gearboxes. Later, Helsen et al. [39] continued their research and focussed on the gearbox component behaviour using three modelling techniques with varying complexity: the torsional model, the rigid model with discrete flexibility and the flexible multibody model. Both simulation and experimental results were discussed.

Furthermore, the interaction between the structural modes of the planet carrier arm and planetary ring flexibility with the overall gearbox modes was investigated. Jain and Hunt [40] compared the experimental results of the NREL gearbox on the field testing. The results showed that the non-torque loads would influence the ring gear face width load distribution.

Keller et al. [41] investigated the effects of the non-torque load on load sharing and the influence of the thrust. They found that the bending moment could affect dynamic response of gearbox components and play an important role in gearbox reliability, such as tooth contact patterns and tooth edge loads in the low-speed gear stage. What is more, when the gear clearance is included, they observed the ideal tooth load distribution, and found that the contact pattern varies periodically. Guo, Keller and LaCava [42] also developed a multibody dynamic model of a wind turbine gearbox for the study of the planetary gear load sharing. The proposed model is validated against the experimental results, and it is found that the planet load sharing is a combined effect of gravity, bending moment, bearing clearance and input torque. In addition, they found that the bending moments and gravity could increase the gearbox internal loads and disturb the load sharing. Later, Guo, Keller and Parker [43] studied the dynamics of wind turbine planetary gears with gravitational effects using an extended harmonic balance method. Floquet theory was applied to the dynamic model, and they found that gravity causes tooth wedging and bearing contact at resonances, which may lead to stiffening effects in the dynamic response. Moreover, tooth wedging is a combined effect of bearing clearance, backlash, and sun support stiffness, and can occur at a lower speed than the planetary stage resonant frequency.

Villa et al. [44] presented an angular resampling algorithm for wind turbines. The results proved the accuracy improvement compared with other resampling algorithms, and they have shown that the angular resampling algorithm is suitable for wind turbines. Dong, Xing and Moan [45] studied the gear contact fatigue under three dynamic conditions: the torque reversal problem under the low wind speed conditions, statistical uncertainty effects due to time domain simulations and the simplified long-term contact fatigue of the gear tooth under dynamic conditions. Haastrup et al. [46] focused on the planetary gear stage of a wind turbine drivetrain, and compared the results with experimental results. They found that the misalignment between the main shaft and the planet carrier is the dominant excitation source, and may affect the expected life of the planet gears. Hall and Chen [47, 48] studied a wind turbine drivetrain with a variable ratio gearbox. They demonstrated how the wind capture capability of a fixed-speed wind turbine can be improved through the implementation of a variable ratio gearbox, and the findings suggested that the variable ratio gearbox can benefit wind turbines.

Helsen et al. [8] presented a review of different trends in gearbox loadings for wind turbine upscaling conditions, and discussed the influence of the gearbox flexibility. In addition, they studied the influence of gear meshes on the gearbox mounting structures. After that, Helsen et al. [49] conducted the experimental investigation of the wind turbine gearbox components. The obtained results proved that the accurate gear mesh representation are useful for wind turbine gearbox simulations. Later, they [50] investigated the effectiveness of three wind turbine drivetrains: the three-point mounting configuration, two-bearing configuration and the hydraulic suspension configuration. They validated the multibody model to characterize the ability of these three configurations to minimize the effects of the non-torque loads in the gearbox.

Vanhollebeke et al. [51] also validated the dynamic model of a wind turbine planetary gearbox by experiments, and they used a multi-level validation campaign to identify the uncertainties in the model.

LaCava, Keller and McNiff [52] studied the sun gear's orbit of a wind turbine planetary gearbox, and they discussed the relationship between the measured motions of the planet carrier arm, planet tilt, main shaft bending, gear mesh alignment, pin load distribution, planet position error, and sun gear orbit. LaCava, Xing, Guo and Moan [53] continued their research on the dynamometer tests, and studied the planet-bearing life calculations. Their results suggested that the planet-bearing life calculations should be made separately for each bearing due to the unequal load distribution, and they concluded that fully flexible models were needed to predict planet-bearing loading, although less complex models were able to achieve good correlation in the field-loading case. Austin [54] proposed a dynamic model of a wind turbine planetary gearbox using the finite element method, and evaluated the effect of manufacturing errors on gear load distributions. The results showed that the planet load share is affected by the misalignment of the carrier, and the floating sun cannot fully mitigate this error.

Dong, Xing, Moan and Gao [55] predicted the contact fatigue life of the gears in a wind turbine drivetrain, and presented a dynamic model validated by comparisons with the published experimental results. Greco, Sheng, Keller and Erdemir [56] examined contact failures of gearbox bearings, and used scanning electron microscopy to observe the subsurface material microstructure. Guo, Keller, Errichello and Halse [57] investigated the spline coupling design of a wind turbine gearbox. They derived the formulation and compared to the existing higher fidelity spline coupling modelling tools,

and studied the effect of spline design parameters on the spline behaviour. The results showed that a freely floating sun minimizes the negative effect of the gear meshes on the planet gears, sun pinion and the ring gear. Guo, Keller, Moan and Xing [58] also presented a combined modelling and experimental approach for wind turbine gearboxes, considering the condition of emergency stops. They found that the flexibility of the main shaft and planet carrier arm is important to simulate emergency stops. Later, Link, Keller and Guo [59] conducted a dynamometer test for the analysis of wind turbine gearbox components, including the force reactions, load distributions, displacements and stresses. The results showed that the pitch and yaw moments affect gear meshes in the planetary gear stage, and the driving torque would change the effect of the non-torque loads on the bearing loads and tooth-contact patterns.

Lutschinger and Howard [60] discussed the failure modes of wind turbines gearboxes. They conducted a small-scale wind turbine test rig to observe the displacement of the main shaft. The experiments took into account the wind fluctuations, and analysed the conditions of shaft bending and fatigue theories. Nejad, Gao and Moan [61] presented a long-term load analysis of a wind turbine gearbox. They also presented three statistical methods for the main shaft torque in offshore wind turbines, and studied the extreme value of the gear transmitted load. Park, Lee, Song and Nam [62] investigated the external loads of wind turbine gearbox caused by wind fluctuation. Two models for different design loads are employed, one model considered only the torque for the design load, the other model considered non-torque loads. The results obtained for the gear mesh misalignment, contact pattern, load distribution, and load sharing are different, which suggested that it is appropriate to consider the non-torque loads for a wind turbine gearbox.

Xing and Moan [63] examined the modelling and analysis of a wind turbine planet carrier arm, with the consideration of planet pins, bearings and the main shaft. Furthermore, they studied the flexible body modelling of the planet carrier arm by using the finite element method, and performed both eigenvalue analyses and time-domain simulations. Abouel-Seoud and Mohamed [64] diagnosed the level of defects of the wind turbine gearbox using gear mesh stiffness. The optimization approach used a dynamic model of both time-varying and frequency-varying mesh stiffness that corresponds to the given vibrational data. They have also conducted experiments and obtained the optimum mesh stiffness. Alemayehu and Ekwaro-Osire [9] performed a multibody dynamic analysis of a wind turbine gearbox, they considered the uncertainties of main shaft speed, the generator-side torque and design parameter uncertainties. Girsang et al. [65] established a wind turbine drivetrain model, and studied the transient loads and their couplings across the drivetrain components, and Jorgensen, Pedersen, Sorensen and Paulsen [66] simulated a 500kW wind turbine drivetrain, and verified the results by experiments. Luo et al. [67] studied the dynamic responses of a wind turbine planetary gearbox using the amplitude modulation and trigonometric function manipulations. They found that the modulation function does not die out before the next planet gear, which is important for when the number of planets increases. What is more, for a sequential mesh planetary gear, in comparison with the fundamental gear mesh frequency, the modulation structure is not only different in amplitude but also different in frequency composition.

Nejad, Gao and Moan [68] presented a fatigue damage analysis for the gear tooth root bending in wind turbine drivetrains. They used load duration distribution method to

obtain the short-term stress cycles, and provided the long-term fatigue damage analysis based on the ISO gear design codes. The load effects were obtained by using two dynamic models: a simplified approach and a multibody model. Good agreement between these two methods was observed. What is more, they found that the sun pinion in planetary gear stage and the pinion in the parallel gear stage are those with the highest damages. Nejad et al. [69] continued the work completed by Nejad, Gao and Moan [68], and addressed the effect of gear geometrical errors in wind turbine planetary gearboxes. Numerical simulations and experiments are employed for the study. Various load cases involving errors in the floating and non-floating sun pinion designs were simulated, and the planet bearing reactions, gear mesh loads and bearing fatigue lives were calculated. They found that the non-floating sun pinion design performs better for gear load variation, whereas the upwind planet bearing has more damage.

Sawalhi, Randall and Forrester [70] discussed the methods to analyse the gear and bearing faults in a wind turbine drivetrain. Whittle, Trevelyan, Shin and Tavner [15] modelled a 2MW wind turbine to find the misalignment between gearbox and the generator, and predicted the impact of the misalignment. They observed the misalignment of 8500 μm at rated torque, and found that the $L10$ fatigue lives of the bearings of the high-speed gear stage were not significantly affected by this misalignment, but that of the generator bearings could be significantly reduced. They suggested to apply a nominal offset to the generator to reduce the misalignment under operation, thereby reducing the loading on the gearbox. Xing, Karimirad and Moan [71] studied a spar-type floating wind turbine drivetrain, and obtained the results for the main shaft loads, including the axial forces, shear forces and bending moments. The results showed that there are increases in the standard deviations of the main shaft loads

and internal drivetrain responses. In addition, these increases are a result of the increased main shaft loads in the wind turbine. Zappala, Tavner, Crabtree and Sheng [72] presented an automatic gear fault detection and diagnosis method, and evaluated the gear damage during non-stationary load and speed operating conditions. They also conducted a test on a wind turbine gearbox with sustained gear damages, and showed that the proposed method was efficient for detecting the gear damages.

Zhu et al. [73] proposed a dynamic model of a wind turbine drivetrain, and then conducted a remote experimental system to monitor the vibration performance of the drivetrain. They found that the most vibration energy occurs at the gearbox, followed by the generator, and then the main shaft. Zhu et al. [74] developed a dynamic model for a wind turbine gearbox with flexible pins. They studied the dynamic behaviours using the finite element method. The results showed that the flexible pins can improve the load sharing ability for planet gears, and the number of planet gears can be increased to improve the power density of the gearbox. Bielecki, Barszcz and Wojcik [75] presented a wind turbine gearbox model under varying operational conditions, and discussed the characteristics of the wind and the chaotically varying loads on the gear teeth and bearings. Cho, Jeong and Park [12] presented a dynamic model of a 5MW wind turbine gearbox using finite element method. The obtained results of the proposed dynamic model were verified by experiments.

Guo et al. [76] compared two wind turbine drivetrain designs to minimize the impact of non-torque loads on the gearbox. The redesigned the National Renewable Energy Laboratory's gearbox intends to solve the reliability issues associated with the non-torque loads inside the gearbox, and the Alstom's pure-torque drivetrain solves the

reliability issues outside the gearbox by altering the non-torque load transfer path. Guo, Keller and LaCava [77] developed an analytical formulation to estimate the load share and planetary gear loads of a three-point mounting wind turbine drivetrain, with the consideration of non-torque loads, gravity and bearing clearance. This model includes the mesh stiffness variation, tooth modifications and gearbox housing flexibility. Guo, Keller, Wallen and Errichello [78] also presented an analytical model for the analysis of the articulated spline coupling designs for a wind turbine gearbox. They found that when the spline is in perfect alignment, the load is shared equally across all spline teeth and the tooth load distribution has a parabolic shape. When the spline is misaligned, the number of teeth in contact decreases and the maximum tooth load increases sharply. Furthermore, the driving torque could affect the spline load share, maximum tooth load and safety factors, which is important to evaluate the spline design within the torque spectrum. Jiang et al. [79] performed a fatigue analysis for the rolling element bearings in wind turbine gearboxes. They found that the planetary bearings, together with intermediate shaft-locating bearings and high-speed locating bearings, exhibited a high percentage of failures. Such a high failure rate indicated that the accepted design practices for other industrial bearings are deficient when applied to wind turbine gearboxes.

Park, Kim, Lee and Shim [80] investigated how the optimal helix modification influence both the load distribution over gear tooth flank and planet load sharing. The results showed that if the optimal helix modification is applied, the edge loading of the gear tooth ends would disappear and the contact pattern would improve. Moreover, the helix modification is not directly related to the mesh load factor. Perisic, Kirkegaard and Pederson [81] presented an approach for the low-cost, indirect monitoring of the shaft

torque from the standard wind turbine measurements. Struggl, Berbyuk and Johansson [82] presented a review on the latest researches regarding the modelling and load analysis of wind turbine drivetrains. The common methods of modelling and simulation have also been addressed. Wei, Zhao, Han and Chu [83] developed a torsional model of a wind turbine gearbox using the Chebyshev interval method, and considered the uncertain parameters such as gear mesh stiffness, damping, transmission error and the moment of inertia of blades. They found that the small parameter uncertainties are propagated in the gearbox, and may lead to relatively large uncertainties of the dynamic responses. Xu, Dong and Luo [84] developed a dynamic model to study the flexible pin-type wind turbine planetary gearbox, which takes into account the effects of nonlinearity caused by the gear contact loss, bearing clearance and flexible pins. They found that reducing the flexible pin stiffness can significantly reduce the nonlinear effects. Gear contact loss and bearing clearance can cause parameter instability, which causes larger dynamic loads and lead to gear teeth and bearing failures. Moreover, the fluctuating gear mesh stiffness is an important vibrational source that cause parametric instability in wind turbine planetary gearboxes.

Zhu et al. [85] analysed the dynamic behaviour of a wind turbine drivetrain. They observed that the resonances are not within the normal operating speed range, and the main vibration modes are the torsional and bending vibrations. What is more, the results of the Campbell diagram suggested that the curve of the first-order natural frequency merely interacts with that of the second-harmonic rotating frequency for the intermediate shaft, thus the main model energy point does not coincide with the frequency intersection point. The results indicated that the risk frequencies are mainly observed around the harmonics of the mesh frequencies at the intermediate stage and

high-speed stage. Wei, Han, Peng and Chu [86] presented a non-probabilistic analysis method for solving the dynamic responses of parametrically excited wind turbine gearbox under uncertainties and multi-frequency excitations. By using the multi-dimensional harmonic balance method and the Chebyshev inclusion function, an interval multi-dimensional harmonic balance method was obtained. The results showed that the proposed method is effective, and the uncertain bearing stiffnesses of the intermediate and high-speed gear stages may lead to relatively large uncertainties in the dynamic responses around resonant regions. Jin et al. [87] presented a flexible multibody dynamic model of a wind turbine gearbox, using the artificial neural network method. The results indicated that the combination of the multibody method and the artificial neural network can improve the simulation runtime and accuracy. Lastly, Guo, Lambert, Wallen, Errichello and Keller [88] addressed an analytic model to study the tooth contact and the loads of gear couplings, taking into account the misalignment, torque and friction. They found that the load amplitude depends on the misalignment, torque and friction. At low torque, coupling motion was induced by the eccentricity between the hub and sleeve even with nearly perfect alignment, and when the torque was larger than a threshold, the motion amplitude can be greatly reduced.

2.2.2 Mathematical model

Park, Lee, Song and Nam [89] developed a dynamic model of a wind turbine gearbox, including the nonlinear gear mesh stiffness and bearing stiffness, and they studied the influence of the wind fluctuation on gear teeth and planet load sharing. The results indicated that the gear mesh misalignment, contact pattern, load distribution and load sharing are different when comparing different dynamic models. These concluded that the gear safety factor could be varied due to the difference of the design load. Wang and

Wu [90] established a nonlinear dynamic model of a wind turbine gearbox using the numerical integration method, and takes into account the nonlinear factors, such as time-varying mesh stiffness, gear backlash and transmission error. They observed period-one response, sub-harmonic response, quasi-periodic response and chaotic response on gearbox components. Sun, Chen and Wei [91] focused on the dynamic reliability of wind turbine gearbox components, with the consideration of the wind fluctuations. They found that the dynamic reliability of the ring gear depends on the stress-strength interference model and Monte Carlo sampling, and wind fluctuation could influence the probability distribution of gear stress.

Shi, Kim, Chung and Park [92] developed a torsional multibody dynamic model for a wind turbine drivetrain using the Lagrange's equation, and solved them numerically with the direct numerical integration. Shi et al. [93] extended their model to a three-dimensional dynamic model, which takes into account the kinetic energy of each component and potential energies from the shaft, bearing, and gear meshes. Wei et al. [14] modelled a nonlinear wind turbine planetary gearbox, with the consideration of time-varying mesh stiffness and dynamic transmission error. They provided an optimum design approach, and showed that the reliability of original parameters is higher than that of the optimized parameters, while the volume of planetary gearbox can greatly be decreased with the overall system reliability requirements.

Zhao and Ji [94] studied the torsional vibrations of wind turbine gearbox with two planetary and one parallel gear stages. The proposed nonlinear dynamic model considers the factors such as time-varying mesh stiffness, damping, static transmission error and gear backlash. Both the external excitation due to wind gust and the internal

excitation due to static transmission error are included. With the help of time history, FFT spectrum, phase portrait, Poincare map and Lyapunov exponent, the effects of the static transmission error, mean-to-alternating force ratio and time-varying mesh stiffness on the dynamic behaviour of wind turbine gearbox components were investigated by using the numerical integration method. They found that the external excitation has the most influence on the torsional vibrations of the wind turbine gearbox components. The mesh stiffness, being another significant factor, has more influence than the other internal excitation source, the static transmission error. The static transmission error has the least influence. Zhao and Ji [95] also studied the dynamic responses of a wind turbine gearbox under different excitation conditions. They explained under which conditions the fretting corrosion, as one of the wind turbine gearbox failure modes, may occur. Furthermore, they observed that the external excitation fluctuation has large influence on the dynamic responses on both the gears and bearings.

2.2 Gear dynamics

2.2.1 Spur gears

Ozguven and Houser [96] presented a few mathematical models for gear dynamics, and summarized some of the important existing researches of gear dynamics. They [97] also studied a nonlinear model for the dynamic analysis of a gear pair, which included the effects of time-varying mesh stiffness and mesh damping, gear error, runout errors, profile modifications and gear backlash. The accuracy of the method was demonstrated by numerical simulations. In addition, they concluded that the displacement excitation resulting from variable gear mesh stiffnesses is more important than the change of natural frequency. Later, Ozguven [98] developed a 6DOF nonlinear semi-definite model for the dynamic analysis of spur gears. The model includes a spur gear pair, two

shafts, two inertias representing load and bearings, and takes into account the shaft and bearing dynamics and the effect of lateral-torsional vibration coupling. In the proposed model, several factors such as time-varying mesh stiffness and damping, separation of teeth, backlash, single and double-sided impacts, various gear errors and profile modifications were considered. The dynamic response was calculated for the meshing forces, dynamic factors for the gears, dynamic transmission error, bearing forces and torsions of shafts. Kahraman and Blankenship [99] studied the influence of involute contact ratio on the torsional vibration behaviour of a spur gear pair. The dynamic transmission error was used for study. Al-shyyab and Kahraman [100] studied a nonlinear time-varying dynamic model for a multi-mesh drivetrain, with the consideration of gear backlash in the form of clearance-type displacement functions. The dimensionless equations of motion were solved for the steady-state period-one response by using a Multi-term Harmonic Balance Method and Floquet theory. They found that neglecting gear backlash non-linearity by forcing the teeth to stay in contact would result in inaccurate predictions near these resonance frequencies. Furthermore, the period-n sub-harmonic motions is expected to play a significant role in the areas of parametric resonance frequencies, especially when the system is lightly damped and the mesh stiffness amplitudes are significant. Al-shyyab and Kahraman [101, 102] studied a torsional model of a multi-mesh drivetrain for the investigation of sub-harmonic and chaotic behaviours. Both gear backlash clearances and parametric gear mesh stiffness fluctuations were taken into account, and the steady-state period-one motions were studied by using the harmonic balance method in conjunction with discrete Fourier transforms. They found that stable sub-harmonic motions mostly in the form of softening type resonances dictate the frequency ranges in which the period-one motions are unstable due to parametric excitations. In addition, the torsional stiffness of the shaft

influences not only modal characteristics of the system but also the nonlinear response, and the gear mesh stiffness amplitude, gear mesh damping ratio, the torque transmitted and the ratio of the gear mesh frequencies all influenced the forced response significantly. Blankenship and Kahraman [103] studied a mathematical model of rotating machines, including parametric excitation and clearances. The resulting non-linear algebraic equations were solved using Harmonic Balance Method and Direct Newton-raphson technique, in which a closed form Jacobian matrix was computed using frequency domain methods. They validated the results by the comparison with numerical integration results and experimental measurements obtained from a test rig. After that, they [104] conducted experiments with clearances combined with parametric and external forcing excitations, and observed the jump discontinuities in forced response curves and subharmonic resonances.

Amabili and Rivola [105] studied the steady-state response and stability of a single degree-of-freedom (DOF) model of spur gears. In the proposed model, the time-varying stiffness of the meshing tooth pairs and a viscous damping proportional to the mesh stiffness were considered. Liu and Parker [106] developed a translational-rotational dynamic model to study the influences of tooth friction on the dynamic response of a gear pair. The impacts of friction coefficient, bending effect, contact ratio and modal damping on the stability boundaries were revealed. Later, Parker, Vijayakar and Imajo [107] studied the dynamic response of a spur gear pair across a range of operating speeds and torques using the finite element model. The results showed the sensitivity of such models to the Fourier spectrum of the changing gear mesh stiffness. Shen, Yang and Liu [108] studied the nonlinear dynamics of a spur gear pair using the Incremental Harmonic Balance Method, where the gear backlash, time-varying mesh stiffness and

static transmission error are included. They investigated the effects of the multi-order harmonic on the periodic solutions. Kim, Yoo and Chung [109] studied the dynamic responses of the translation motions of spur gear pairs. They found that the gear mesh damping has little effect on the dynamic responses for gears' radial displacements, and the torsional bearing damping has stronger effect on gears than radial bearing damping does. Furthermore, the bearing stiffness has a significant effect on radial vibration and has little effect on mesh deformation. Chen, Tang, Luo and Wang [110] studied the effects of the friction and gear backlash on a nonlinear gearbox. They found that the friction force may enlarge the displacement magnitude and affect the high frequency gears at low speeds, and the gear system may have chaotic responses due to gear backlash. Fernandez et al. [111] developed a model for the analysis of contact forces and deformations in spur gear transmissions, based on a Litvin's vector approach. They found that when the coupling is considered the deformation is greater than that estimated purely kinetic approaches.

2.2.2 Helical gears

Kahraman [112] developed a linear dynamic model of a helical gear pair. The model takes into account the shaft and bearing flexibilities, and the coupling dynamics among the transverse, torsional, axial and rotational motions due to gear meshes. He predicted the natural frequencies and the mode shapes, and performed a parametric study to investigate the effect of the helix angle on the vibrational characteristics of the gear pair. It showed that the effect of the helix angle can be neglected in predicting the natural frequencies and the dynamic mesh forces. He [113] also studied the dynamic behaviour of a multi-mesh helical drivetrain, which consists of three helical gears. A three-dimensional dynamic model which includes transverse, torsional, axial and rotational

motions of the flexibility mounted gears was developed, and the natural modes were predicted. The forced response, which includes dynamic mesh and bearing forces, due to the static transmission error excitation were obtained. Later, Kang and Kahraman [114] developed a dynamic model of double-helical gear pair including the shafts and bearings. The results were compared with the experimental results, and it was found that the double-helical gear pair behaves linearly. Cai [115] studied a dynamic model of helical gear pairs, including the effect of tooth numbers and addendum modification coefficients, and verified the results by experiments. They found that the resulted time waveforms and their frequency characteristics agreed precisely with Umezawa's findings. Cooley, Parker and Vijayakar [116] proposed a finite element model for the dynamic response of gear pairs, which provided an accurate calculation for the static solution.

Howard, Jia and Wang [117] proposed a 16DOF gear dynamic model with the effect of friction and gear tooth torsional mesh stiffness. The comparison between the results with friction and without friction was investigated. Kubur, Kahraman, Zini and Kienzle [118] proposed a dynamic model of a multi-shaft helical gearbox with flexible shafts. They found that a large amount of design parameters can influence the dynamic behaviour of the system. Ebrahimi and Eberhard [119] studied the elastic elements between the gear teeth, and they gave a brief overview of different approaches on contact modelling of multi-meshed geared systems. Spitas. C and Spitas. V [120] provided a non-linear dynamic model of tooth meshing, with the consideration of the effect of pitch errors, tooth separation, coupling and profile corrections. The results showed that the optimal corrections can reduce the overload by a factor of 35%. They [121] also derived a modified form for the fundamental gear meshing equations, which

improved the solving speed and the stability. Later they developed a new form for the equations of the non-conjugate meshing, the solution was fast implemented and stable [122]. Spitas C., Spitas V. and Amani [123, 124] recently studied the effect of the dedendum coefficient and the tip radius coefficient of spur gears, and generated a new generalized model for calculating the corner penetration at tooth root.

Iglesias, Fernandez, De-Juan, Sancibrian and Garcia [125] studied the influence of planet pin-hole position errors on the behaviour of the gearbox transmission. Tangential and radial planet pin hole position errors were considered independently. Han and Chu [126] studied the dynamic behaviours of a geared rotor system under time-periodic motions. The lateral and torsional responses of the geared system under transmission error and unbalanced mass excitations were investigated. They found that the rolling-base motion has the greatest impact on the dynamic behaviours of the geared system. When the pitching or yawing base motion was considered, the amplitudes of other lateral and torsional responses were affected, and the transient response of the geared rotor system was greatly enhanced, which is independent on the type of base angular motions.

2.2.3 Planetary gears

Kahraman [127] developed a nonlinear dynamic model of a planetary gearbox, which includes the manufacturing errors, tooth separation and time-varying gear mesh stiffness. The dynamic load sharing factor was predicted. Yuksel and Kahraman [128] provided a mathematical model of a planetary gearbox to study the surface wear, which defines the contacting gear tooth surfaces. A quasi-static gear contact model was employed to compute contact pressures and the wear depth distributions. The results indicated that

the dynamic behaviour is nonlinear due to tooth separations in its resonance regions, and it was found that the surface wear has a significant influence in off-resonance speed ranges while its influence diminishes near resonance peaks primarily due to tooth separations. Boguski, Kahraman and Nishino [129] studied the planet load sharing under quasi-static conditions. They found that the planet mesh phasing has negligible effects on planet load sharing, and the planet load sharing factor is proportional to an effective error parameter. Moreover, the floating sun configuration could help to better distribute the loads equally among the planets. Sondkar and Kahraman [130] presented a model of a double-helical planetary gear to study the torsional, transverse, axial and rotational motions of gears. They found that the staggering of gear teeth influences the dynamic behaviour of the gear system substantially. Velex and Flamand [131] developed an extended three-dimensional model for the analysis of the tooth loads on a planetary gear. They showed that the external gear meshes are more loaded than the internal gear meshes, and the gear mesh stiffness has much larger effects on the tooth loads compared to the effects of the floating sun and ring gears.

Lin and Parker [132, 133] developed an analytical model of planetary gears to investigate the natural frequencies and vibration modes, which included some key factors such as gyroscopic effects and time-varying stiffness. The natural frequency sensitivity to operating speed was calculated to estimate the impact of gyroscopic effects. They [134] also studied the free vibration of systems with unequally spaced planets. Then Lin and Parker [135] studied the parametric instabilities of a multi-mesh gearbox, and discussed the effects of mesh stiffness parameters, including stiffness variation amplitudes, mesh frequencies, contact ratios and mesh phasing. For the mesh stiffness fluctuation, formulas were derived to control the instability regions by

adjusting the contact ratios and mesh phasing. Lin and Parker [136] also studied the parametric instabilities caused by the mesh stiffness fluctuations in planetary gears. The time-varying mesh stiffnesses of the sun-planet and ring-planet meshes were modelled as rectangular waveforms with different contact ratios and mesh phasing. Tooth separation from parametric instability was also simulated to show the impact of this non-linearity on the dynamic response. After that, Parker and Lin [137] provided an analytical description for the mesh phase relationships, and indicated that the mesh phasing has a dramatic impact on the static and dynamic behaviour of planetary.

Parker, Agashe and Vijayakar [138] studied the dynamic response of a helicopter planetary gearbox. They observed the resonances when a harmonic of meshing frequency coincides with the natural frequency. They also examined the torque sensitivity of the dynamic response, and showed that the rotational mode response is more sensitive to the driving torque than translational mode response. Parker and Ambarisha [139] also examined the nonlinear dynamic behaviour of planetary gears using two models: a lumped-parameter model and a finite element model. They found that the nonlinear jumps, chaotic motions, and period-doubling bifurcations would occur when the mesh frequency and its higher harmonics are near a natural frequency of the system. These comparisons validated the effectiveness of the lumped-parameter model to simulate the dynamics of planetary gears. Eritenel and Parker [140] investigated the modal properties of a three-dimensional planetary gearbox model. A lumped-parameter model was formulated to obtain the equations of motion, with the inclusion of translational and tilting stiffness. The results showed that the central members rotate and move axially for the rotational-axial modes. Bahk and Parker [141] studied the nonlinear behaviour of a parametrically excited planetary gear, and showed that the

degenerate planet modes cannot experience parametric instability for equally spaced planets and in-phase meshes, and higher applied torque does not prevent teeth contact loss. Moreover, the width of the instability region is not sensitive to the applied torque but to other parameters such as damping, natural frequencies and harmonics of mesh stiffness.

Guo and Parker [142] studied the nonlinear tooth wedging behaviour of planetary gears, and showed the significant impact of tooth wedging on planet bearing forces for a wide range of operating speeds. Furthermore, they found that tooth wedging is mainly caused by gravity forces on translational directions. Parker and Wu [143] provided a dynamic model for planetary gears to study the relationships between the modal properties of planetary gears with equally spaced and diametrically opposed planets. Guo and Parker [144] also studied the dynamics of planetary gears with bearing clearance using the Harmonic Balance Method and the Floquet theory. The results indicated that the bearings of the planetary gear components impact against the bearing races near resonances, and the driving torque can suppress some of the nonlinear effects caused by bearing clearance. Sun and Hu [145] presented a nonlinear dynamic model of a planetary gearbox with multiple clearances taken into account. A lateral-torsional coupled model was established with multiple backlashes, time-varying mesh stiffness, error excitation and sun-gear shaft compliance considered, and solved by using Harmonic Balance Method. They also discussed the effects of the variation of mesh stiffness and static transmission errors on the nonlinear dynamics. Chaari et al. [146] developed a model of a planetary gearbox to study the influence of the manufacturing errors, and demonstrated that the manufacturing errors have large influence on the

dynamic behaviours of planetary gears, and could have dramatic consequences on the transmission.

Hbaieb et al. [147] developed a torsional model of a planetary gearbox. They found that the gear mesh stiffness variation causes parametric instability. The effects of mesh stiffness parameters, including stiffness variation amplitudes, contact ratios, and the mesh phasing on these instabilities were identified. Dhouib et al. [148] studied a compound planetary gearbox. They found that the planets' angular positions do not affect the natural modes, and the eigenfrequencies are sensitive to the gyroscopic effects. Kim, Lee and Chung [149] studied the dynamic responses of a planetary gearbox, which includes the time-varying pressure angles and contact ratios. The time responses for the present and previous studies were compared to show the effects of the time-varying pressure angles and contact ratios on the dynamic behaviours of the planetary gear. Xue et al. [150] presented the torsional stiffness analysis of an involute spur planetary gearbox using the finite element method. A crack coefficient was introduced to the sun-planet and ring-planet meshes to predict the effect and sensitivity of changes to the overall torsional mesh stiffness. The resulting mesh stiffness crack sensitivity of the overall gear system was analysed under quasi-static conditions. They found that the carrier arm stiffness has great influence on the crack sensitivity while the overall stiffness was most sensitive to the crack on the sun-planet mesh. Karray, Feki, Chaari and Haddar [151] developed a 6DOF model for a planetary gear, which is coupled to a 4DOF bevel gear. The natural frequencies of the gear system were determined, and they found that the natural modes can be classified into three major classes according to their displacements and rotations: the bevel mode, planetary mode and the coupled mode.

Kwon, Kahraman, Lee and Suh [152] proposed an approach for an automated design for planetary gearboxes to predict the transmission error amplitudes and contact stresses.

Chapter 3 Wind turbine drivetrain structures

The understanding of wind turbine gearbox components is extremely important to improve the reliability of wind turbine gearboxes. Thus, this chapter presents the general knowledge about the wind turbine gearbox. In particular, Section 3.1 explains the drivetrain configurations, and Section 3.2 describes different gearbox suspension layouts. After that, the two commonly used gearbox types, the parallel-shaft gearbox and planetary gearbox, are introduced in Section 3.3. The general knowledge about the gearbox components, such as gears and bearings, are provided in Sections 3.4 and 3.5.

3.1 Drivetrain configurations

Wind turbines are commonly classified into the vertical-axis wind turbines and the horizontal-axis wind turbines. The vertical-axis wind turbines have the ability to accept wind from every direction, which eliminates the problem of orienting the rotor with respect to the wind. For the horizontal-axis wind turbines as shown in Figure 3.1, they have proven to be more efficient compared with the vertical-axis turbines, and have currently been the most popular design for the modern wind energy industry [18]. Thus, this thesis focuses on the gearbox of horizontal-axis wind turbines.

Figure 3.1. Horizontal-axis wind turbines [153]

The horizontal-axis wind turbines normally consist of three major components: rotor, drivetrain and tower. The drivetrain transforms the mechanical energy generated by the rotor into electrical energy, and the gearbox is located in the middle of the drivetrain. As shown in Figure 3.2, the hub is attached to the nacelle frame. The rotor blades attach to the main shaft, and the gearbox connects the main shaft to the high-speed shaft and converts the low rotor speed and high torque to high speed and low torque to meet the electromechanical requirements of the generator.

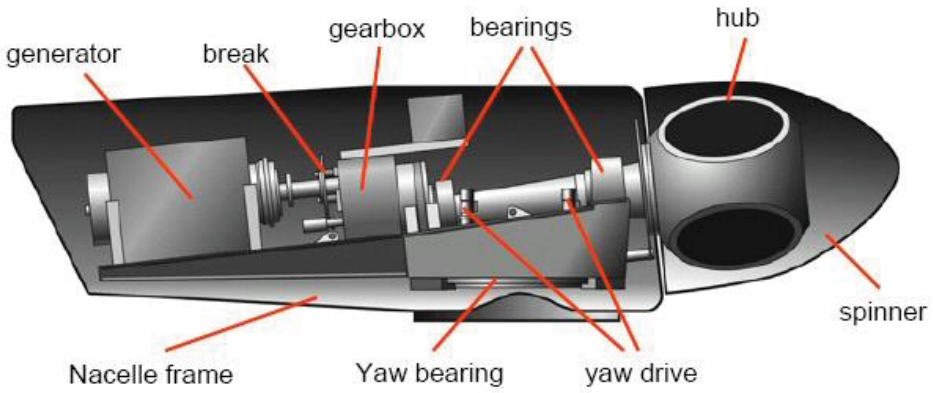

Figure 3.2. Wind turbine drivetrain with gearbox [154]

In this section, three commonly used configurations for wind turbine drivetrain are presented: the modular drivetrain, the integrated drivetrain and the partially integrated drivetrain.

3.1.1 Modular drivetrain

Most modern wind turbine drivetrain designs use modular configuration, which follows a non-vertical design process. It means that different suppliers contribute to the design of individual drivetrain components, such as the main shaft, the gearbox, brakes and the generator, and have them mounted on the bedplate, as shown in Figure 3.3. The advantage of this configuration is that it reduces the overall design cost by fomenting a competitive environment among suppliers, and reduces the in-house requirements of the turbine manufacturers. On the other hand, it increases the difficulty of aligning the different components [18, 52, 155].

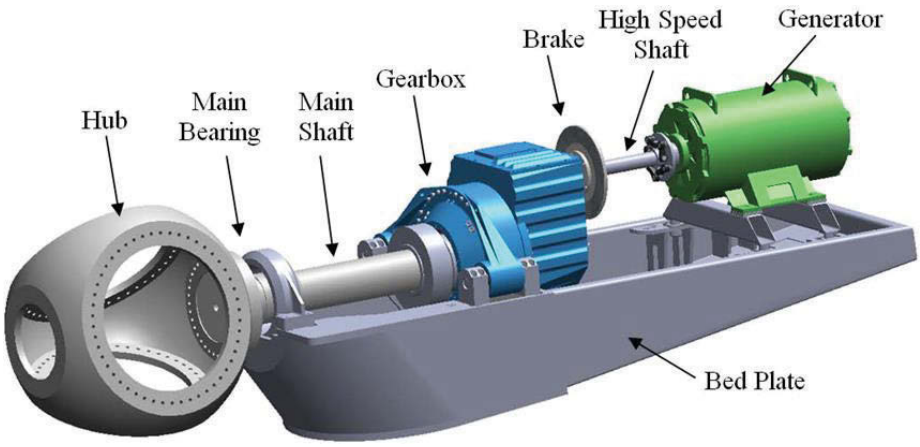

Figure 3.3. Drivetrain of a 750 kW wind turbine [52]

3.1.2 Integrated drivetrain

The integrated drivetrain configuration follows a vertical design process, which means that it is limited to one drivetrain or gearbox design, with the wind turbine manufacturers closely involved throughout the entire design process. This enables the turbine manufacturers own the drivetrain designs. However, the integrated drivetrain configuration is sensitive to the effects of individual components due to the influence of the entire nacelle, which makes the maintenance cost extremely high [18, 155].

3.1.3 Partially integrated drivetrain

The partially integrated drivetrain is a combination of the modular and integrated configurations. It follows the modular design for the use of the bedplate, and follows the integrated design for the surrounding internal components. The two common options for partially integrated drivetrain are the gearbox-generator integration and the gearbox-hub integration. For the generator-gearbox integration, the design is not necessarily to be entirely vertical, thus, only the cooperation between the gearbox supplier and generator providers are needed. For the gearbox-hub integration, the vertical design process must be followed, because the gearbox is a structural component of the wind turbine. For the partially integrated drivetrain configuration, it is difficult to isolate the drivetrain from the tower and rotor hub. Therefore, the external loadings can be transferred to the internal component of drivetrain, which may lead to gearbox failure or reduced component lifetime [18].

3.2 Gearbox suspension layouts

The gearbox suspension is used to fix the gearbox in the nacelle in order to minimize the effect of the non-torque loading caused by the rotor. In this section, three commonly used suspension layouts are presented: the three-point mounting (TPM), the two-bearing mounting (TBC) and the hydraulic suspension (HS).

3.2.1 Three-point mounting configuration

The three-point mounting (TPM) configuration is the most common suspension configuration in the market. As shown in Figure 3.4, the main shaft is connected to the planet carrier arm of the gearbox, supported by the main bearing. The gearbox is fixed to the nacelle by a torque arm supported by two bushings. All non-torque loadings are theoretically transferred to the nacelle through the main bearing and the torque arm, which could help to reduce noises [8, 29, 50, 59].

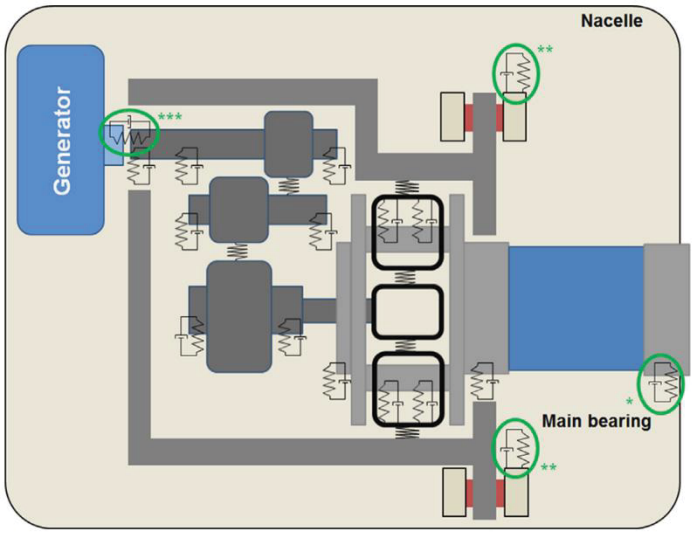

Figure 3.4. Three point mounting configuration [50]

3.2.2 Two-bearing configuration

The two-bearing configuration (TBC) can also be considered as the four-point mounting, due to the use of a second main bearing to support the main shaft at the gearbox side. As shown in Figure 3.5, the gearbox is still fixed to the nacelle by the torque arm through two bushings. Similar to the three-point mounting (TPM) configuration, it can be assumed that all the non-torque loadings are transferred through the two main bearings and torque arm into the nacelle [8, 50].

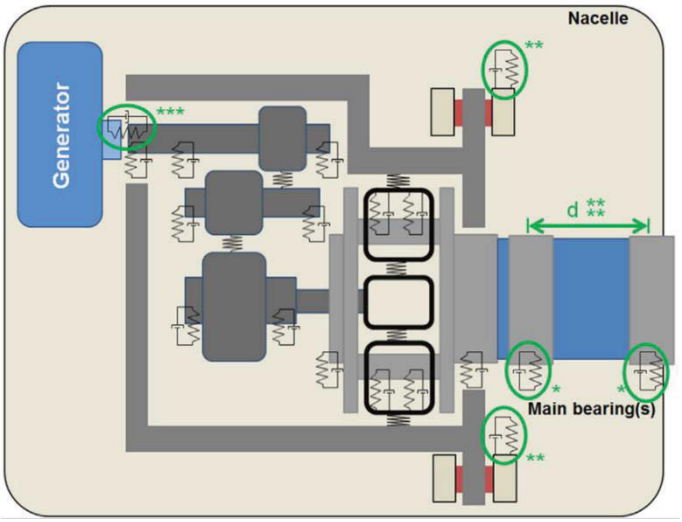

Figure 3.5. Two-point mounting configuration [50]

3.2.3 Hydraulic suspension

In the hydraulic suspension (HS) configuration, the main shaft is supported by two main bearings. The gearbox is not connected to the nacelle by a torque arm. Instead, the upper mount filled with hydraulic fluid on one side is connected to the lower mount by a hydraulic pipe on the other side, as shown in Figures 3.6 and 3.7. This enables the fluid to flow freely from one mount to the other, and the two other mounts are connected in a similar way. Therefore, the gearbox is fixed on the direction of torsion, but is allowed to

move freely upwards and downwards, which could avoid the unfavourable loadings [8, 50].

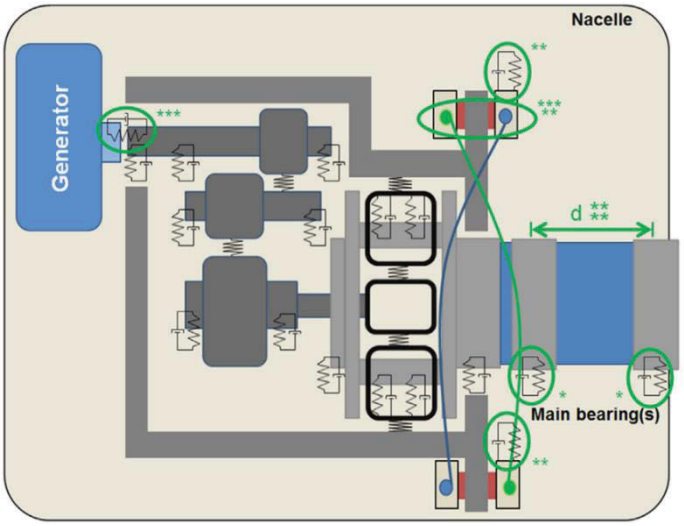

Figure 3.6. Hydraulic suspension system [50]

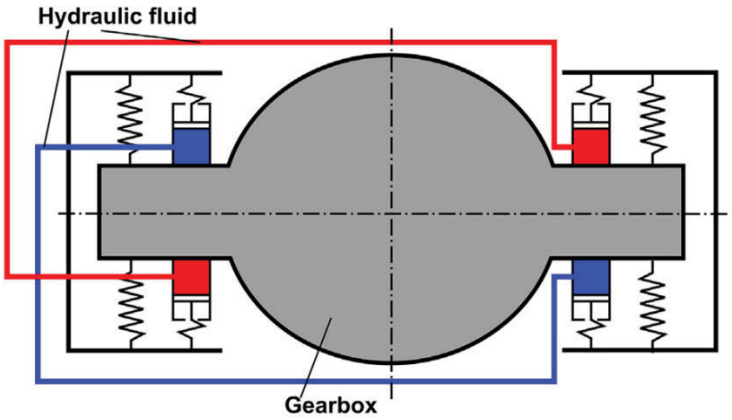

Figure 3.7. Hydraulic suspension system [50]

3.3 Parallel-shaft and planetary gearboxes

Wind turbine gearboxes normally consist of three gear stages, including both the parallel-shaft gear stage and the planetary gear stage. Depending on the capacity requirement of a wind turbine, the arrangement could be either one planetary and two

parallel gear stages or two planetary and one parallel gear stages. As shown in Figure 3.8, the gearbox with one planetary and two parallel gear stages canbe used for small or medium sized wind turbines, and the gearbox with two planetary and one parallel gear stages are normally recommended for large sized wind turbines.

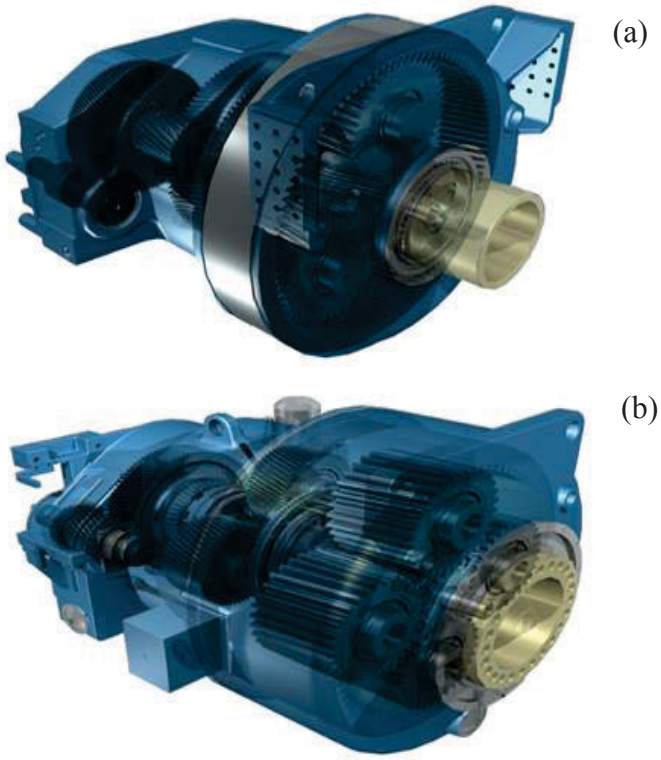

Figure 3.8. Wind turbine gearboxes with (a) one-planetary-two-parallel gear stages (b) two-planetary-one-parallel gear stages [156]

A parallel-shaft gear stage consists of a gear on the input shaft and a pinion on the output shaft. Being the speed-increasing gearbox of wind turbines, the size of the gear is larger than the pinion. The advantage of the use of parallel-shaft gear stages is that they can be modelled with a minimum number of degrees of freedom (DOF) in the design process, this is because the gears are directly attached to the gearbox housing, which results in a simpler calculation for the gearbox analysis. On the other hand, the

disadvantage is that it may require much larger gears compared with the pinion if a large gear ratio is required. This is difficult to produce accurately and are expensive to manufacture.

The planetary gear stage is more complicated than the parallel-shaft gear stage, as it is composed of three moving components, a planet carrier arm, three planet gears and a sun pinion. The stationary ring gear is fixed to the gearbox housing. The teeth of the ring gear are on the inside and mesh with the teeth of the planet gears at all times. The planet carrier arm is responsible to hold the three planet gears, and ensures that the gear meshes of ring-planet and planet-sun gear pairs are properly maintained. The planet gears are supported on the planet carrier arm by the shafts with bearings so that the planet gears can rotate freely with respect to the planet carrier arm. The driving input is applied to the planet carrier arm, which splits the torsional load among the planet gears, and transferred to the sun pinion to become the output of the planetary gear stage.

The planetary gear stage has many advantages compared to the parallel-shaft gear stage, as higher gear ratios can be achieved and they are capable to greater torque loads with less space used. Such configuration has the advantage of reducing the overall mass, which is an important requirement for wind turbine gearboxes. However, planetary gear stages are more complex than the parallel-shaft gear stages. They are more sensitive, and the dynamic behaviour of it can be affected by the internal components, such as the deflection of the planet carrier arm, deformation of the ring gear and bearing clearances [28, 43, 69].

3.4 Spur and helical gears

Spur gears are the most commonly used gears in wind turbines, because they can be simply manufactured with low cost, and they are usually made with an involute tooth profile as shown in Figure 3.9. The nomenclature of a gear tooth is given by Figure 3.10. The gear teeth contact takes place along the line of action controlled by the shape of the active profile of meshing gears, and the length of line of action is defined by the outside diameters of gears. During a full meshing cycle, two pairs of teeth would share the load, and before the first pair of teeth goes out of action the second pair of teeth would pick up their share of the load. This provides a continuous flow of power during gear meshes, and ensures that at least one pair of teeth is in contact at all times [18, 157]. Additional information about gear tooth is provided in Section 8.1.

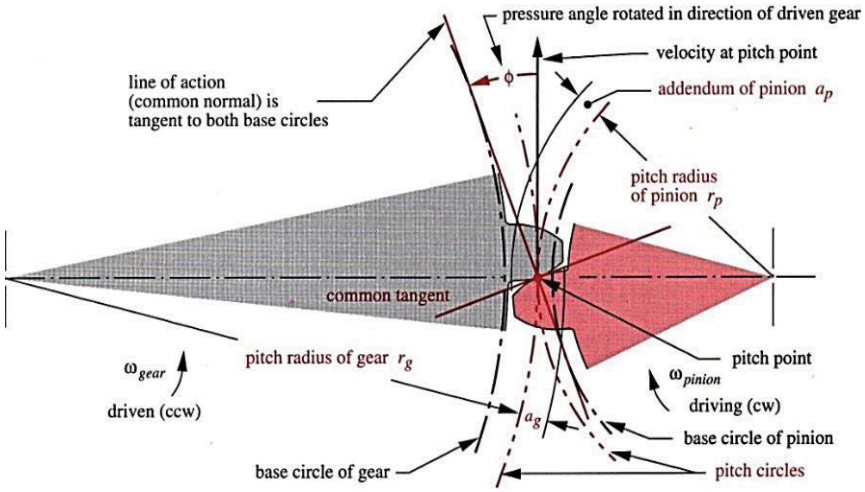

Figure 3.9. Involute tooth nomenclature [18]

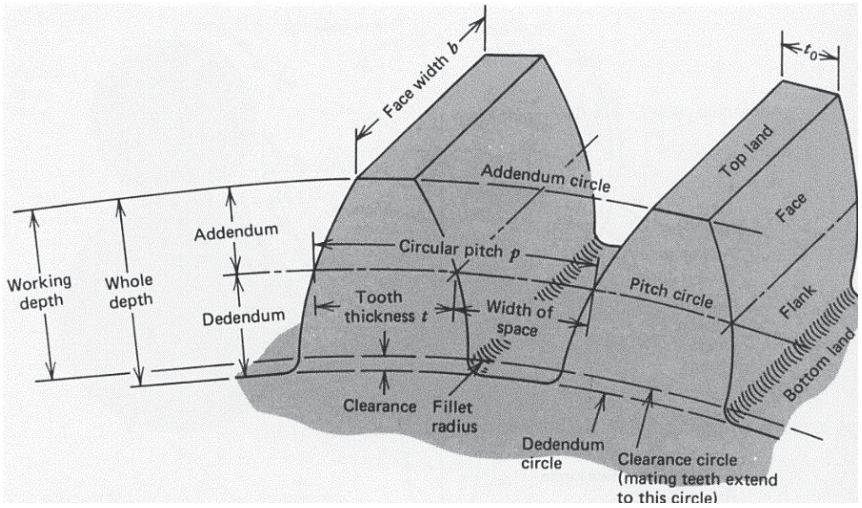

Figure 3.10. Nomenclature of a gear tooth [157]

For the helical gears, their gear teeth are cut at an angle relative to the axis of rotation, as shown in Figure 3.11. This enables the gears to have more teeth in contact in order to share the load, and operate more quietly. On the other hand, the helical gears may produce axial loads due to the normal loading of the tooth, which may lead to premature failures of bearings throughout the gearbox.

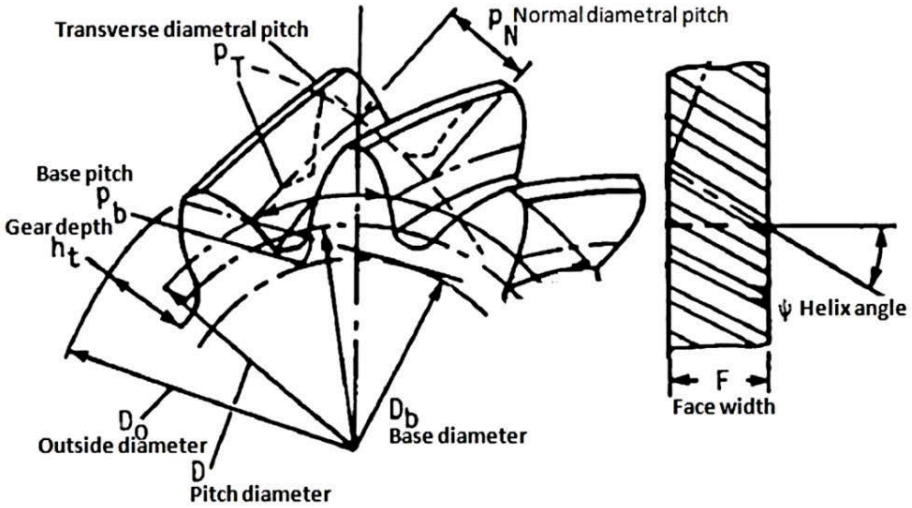

Figure 3.11. Geometry of a helical gear [155]

3.5 Bearings

Bearing is another important component that influence the reliability of a wind turbine gearbox. The majority of gearbox failures appear in bearings, initiating at several specific bearing locations, such as the planetary bearings, intermediate-shaft bearings and high-speed-shaft bearings, which could advance into the gear teeth as bearing debris and excess clearances cause surface wear and misalignments. This is because the accepted design practices for other industrial bearings are deficient when applied to wind turbine gearboxes. Moreover, because of the lack of gearbox models, the root cause analysis of bearing failure has not been performed, thus, there is a need to predict bearing design loads and to understand the effects of dynamic load conditions on bearings [11, 79, 158].

For wind turbine gearboxes, the most commonly used bearings are the rolling element bearings. They are chosen due to their low friction and high load capacity. As an example shown in Figure 3.12, the planet carrier arm is supported by two full-complement cylindrical roller bearings (fcCRB), and each planet gear is supported by two identical cylindrical roller bearings (CRB). In the case of the axial loadings in the gearbox, the tapered roller bearings (TRB) are usually implemented. Thus, the parallel-shaft gear stages, which contains helical gears, are normally supported by the combination of a cylindrical roller bearing (CRB) on the upwind side of the assembly and two back-to-back mounted tapered roller bearings (TRB) on the downwind side [18, 29, 82].

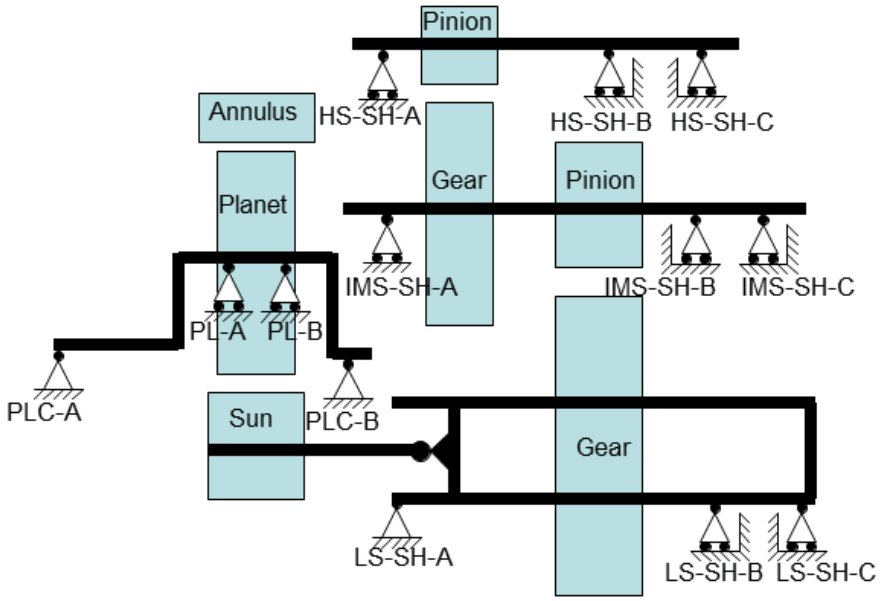

Figure 3.12. Bearing nomenclature and locations [29]

This page intentionally left blank

Chapter 4 Torsional vibrations of wind turbine gearboxes

The dynamic models of wind turbine gearboxes are commonly composed of one planetary and two parallel gear stages [159-163]. Such structure may not be adequate for large capacity wind turbines, as described in Section 3.3. It is known that the planetary gearbox provides higher gear ratios and is capable of carrying higher loads compared with parallel gear arrangement. By considering this feature, this chapter focuses on the study of torsional vibrations of a wind turbine gearbox model, consisting of two planetary and one parallel gear stages.

The proposed torsional model is developed to predict the nonlinear dynamic responses of wind turbine gearbox components. The dynamic responses would be interpreted in terms of harmonic periodic, non-harmonic periodic, sub-harmonic, quasi-periodic and chaotic responses. The effects of the factors on the dynamic responses, such as the static transmission error, the mean-to-alternating force ratio and gear mesh stiffness ratio, would be investigated by using the numerical simulations.

4.1 Mathematical modelling

A wind turbine gearbox, which consists of two planetary and one parallel gear stages, is sketched in Figure 4.1. The first planetary gear stage is the input gear stage, the driving torque is applied on the first planetary gear stage, and the planet carrier arm transfers the driving torque to the three planet gears and maintains the center distances of ring-sun-planet gears. The sun pinion of the first planetary stage is attached to the planet carrier arm of the second planetary gear stage by a shaft, and the sun pinion of the second

planetary gear stage is attached to the low-speed gear of the parallel-shaft gear stage. The high-speed pinion at the parallel gear stage is the output gear of the gearbox.

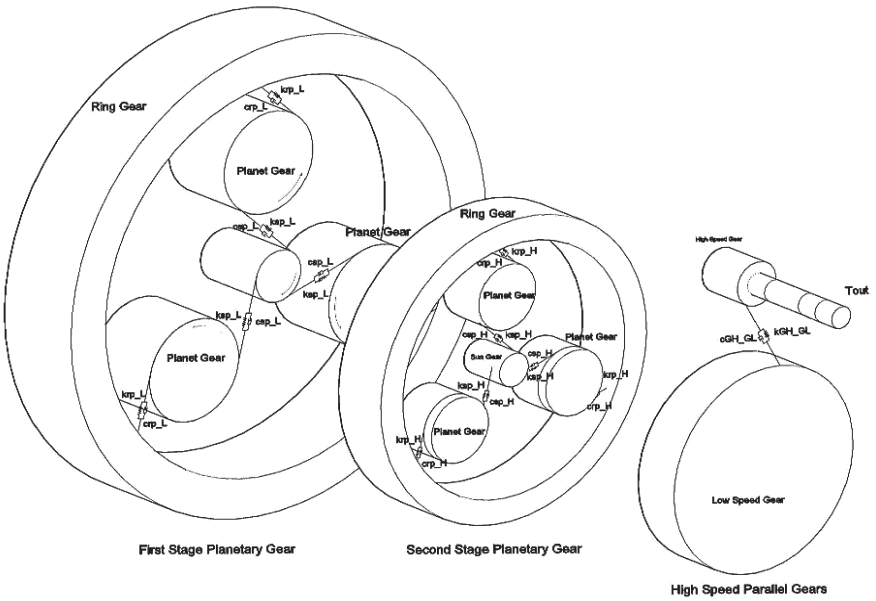

Figure 4.1. Torsional model of a wind turbine gearbox

The proposed gearbox model considers both the low-frequency excitation due to external torque fluctuations and the high-frequency internal excitations due to the static transmission error, and takes into account the some key factors such as time-varying mesh stiffness, damping, static transmission error and gear backlash. The external driving torque is normally caused by wind gust, whereas the static transmission error is the overall kinematic error function of gear pairs under the static conditions, expressed in the form of periodically time-varying displacement functions applied at gear meshes [164]. Damping was neglected in the existing studies as this assumption is reasonable for large wind turbines [159]. However, large influence of damping in the nonlinear behaviour was observed during wind turbine emergency stops [38, 105]. In addition, it was noted that the gear backlash is minimal in wind turbine normal operation, especially

for the modern wind turbine gearboxes with advanced control strategy in energy extractions. However, the gear backlash also exists in emergency stops. Therefore, damping and gear backlash would be included in the proposed model.

A side-view sketch of the proposed torsional model is shown in Figure 4.2. All gears are assumed to be spur gears, and are allowed to rotate only in the torsional direction. The planet gears are interacting with two other components: the ring gear which is fixed to the gearbox housing, and the sun pinion which is constrained to the reference frame but allowed to rotate. The rotational direction of the driving torque is considered to be positive for the angular displacements of gears. Thus, the angular displacements of the planet carrier arm and the sun pinion at the first planetary gear stage ($\theta_{cL},\ \theta_{sL}$), the planet carrier arm and the sun pinion at the second planetary gear stage (θ_{cH}, θ_{sH}), and the low-speed gear at the parallel gear stage (θ_{GL}) is in the positive direction. Whereas the angular displacements of the planet gears at both the first and second planetary gear stages and the high-speed pinion at the parallel gear stage ($\theta_{pL\_n}, \theta_{pH\_n}, \theta_{GL}$) are in the negative direction. The ring gears at the first and second planetary gear stages are fixed with the gearbox housing, which gives the angular displacements (θ_{rL}, θ_{rH}) zero.

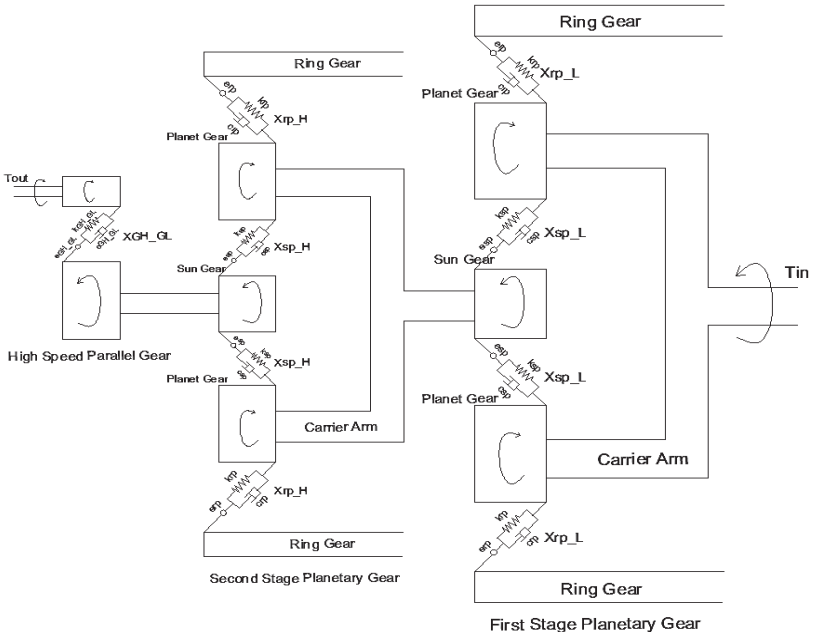

Figure 4.2: Side view of the proposed gearbox

Due to the displacements of the planet carrier arm, the loading conditions of the ring-planet gear meshes can become unfavourable. This could potentially result in non-symmetric planet bearing loading on one of the planet bearings. Thus, this gearbox is designed to have constantly preloaded bearings without bearing backlash, such that non-torque loading would be transferred from the planet carrier arm to the housing through the planet carrier bearings. Therefore, the proposed model is adjusted such that the gear meshes only contribute to the transfer of torque, and not counteract the non-torque loadings [50].

Figure 4.3 illustrates a lumped-parameter model of a ring-planet-sun gear in the gearbox, as an example. The gear deformation during meshing is represented by the time-varying gear mesh stiffness, damping and static transmission error. The gear mesh stiffness, as an important internal excitation source in gearbox, fluctuates as the number of teeth contact changes during gear mesh.

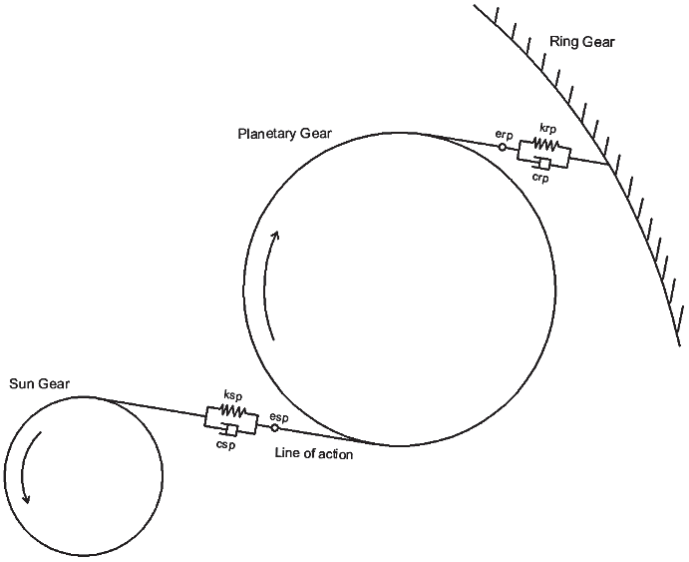

Figure 4.3: A gear pair in planetary gear stage

The non-torque loads such as shaft bending and thrust have been assumed to be uncoupled from the wind turbine gearbox model. The radial direction forces, which are caused by the main shaft bending moment, theoretically pass from the main shaft through the gearbox carrier bearings, gearbox housing, trunnions and into the bedplate [165]. For a more detailed study in the future, gearbox housing flexibility may be considered due to its influence on shaft bore and ring gear misalignment, and planet carrier flexibility may be included for its effects on planet pin misalignment [27, 28, 166]. Thus, the assumptions for the proposed model are listed below:

(1) The housing, planet carrier arm and bedplate are rigid.

(2) The torsional stiffness of the intermediate and high-speed shafts is represented by a spring and damper in the midsection of each shaft.

(3) The main shaft is not included, and the aerodynamic forces on blades are assumed to be applied to the planet carrier arm of the planetary gear stage directly.

(4) The non-torque loads from the blades are assumed to be uncoupled with the gearbox.

(5) The responses of bearings are not included.

4.2 Derivation of equations

Based on the geometry of the gears, the base radius of them is determined as follows:

$$\boldsymbol{r_{bp\_L} = r_{pL}\cos\alpha_{pL},\ r_{bs\_L} = r_{sL}\cos\alpha_{sL},\ r_{bC\_L} = r_{bp\_L} + r_{bs\_L}} \quad (4.1a, b)$$

$$r_{bp\_H} = r_{pH}\cos\alpha_{pH},\ r_{bs\_H} = r_{sH}\cos\alpha_{sH},\ r_{bC\_H} = r_{bp\_H} + r_{bs\_H} \quad (4.1c, d)$$

$$r_{bG\_L} = r_{GL}\cos\alpha_{GL},\ r_{bG\_H} = r_{GH}\cos\alpha_{GH} \quad (4.1e, f)$$

where r_{bp_L}, r_{bs_L} and r_{br_L} are the base radius of the planet gear, sun pinion and ring gear at the first planetary stage; r_{bp_H}, r_{bs_H} and r_{br_H} are the base radius of the planet gear, sun pinion and ring gear at the second planetary stage; r_{bG_L} and r_{bG_H} are the base radius of the low-speed and high-speed gears at the parallel gear stage. Additionally, α_{pL} and α_{sL} are the pressure angles of the planet gear and sun gear at the first planetary gear stage; α_{pH} and α_{sH} are the pressure angles of the planet gear and sun gear at the second planetary gear stage; α_{GL} and α_{GH} are the pressure angles of the low-speed and high-speed gears at the parallel gear stage.

The equivalent transverse displacements of gears in the line of action caused by the rotational displacements are obtained as follows:

$$x_{cL} = r_{bc\_L}\theta_{cL},\ x_{pL\_n} = r_{bp\_L}\theta_{pL\_n},\ x_{sL} = r_{bs\_L}\theta_{sL} \quad (4.2a, b)$$

$$x_{cH} = r_{bc\_H}\theta_{cH},\ x_{pH\_n} = r_{bp\_H}\theta_{pH\_n},\ x_{sH} = r_{bs\_H}\theta_{sH} \quad (4.2c, d)$$

$$x_{GL} = r_{bG\_L}\theta_{GL},\ x_{GH} = r_{bG\_H}\theta_{GH} \quad (4.2e, f)$$

where x_{cL}, x_{pL_n} and x_{sL} respectively represent the equivalent transverse displacements of the planet carrier arm, planet gears and the sun pinion at the first planetary gear stage. x_{cH}, x_{pH_n} and x_{sH} are the equivalent transverse displacements of the planet carrier arm, planet gears and sun pinion at the second planetary gear stage. x_{GL} and x_{GH} are the equivalent transverse displacements of the low-speed gear and the high-speed pinion at the parallel gear stage.

The relative meshing displacements of gears in the line of pressure X_i are obtained as:

$$X_{rp\_L\_n} = x_{pL\_n} - x_{cL}, X_{sp\_L\_n} = x_{sL} - x_{pL\_n} - x_{cL} \quad (4.3a, b)$$

$$X_{cH\_sL} = x_{cH} - x_{sL},\ X_{rp\_H\_n} = x_{pH\_n} - x_{cH} \quad (4.3c, d)$$

$$X_{sp\_H\_n} = x_{sH} - x_{pH\_n} - x_{cH},\ X_{GL\_sH} = x_{GL} - x_{sH} \quad (4.3e, f)$$

$$X_{GH\_GL} = x_{GH} - x_{GL},\ n = 1,2,3 \quad (4.3g)$$

where $X_{rp\_L\_n}$ and $X_{sp\_L\_n}$ are the relative meshing displacements of the ring-planet gears and sun-planet gears at the first planetary gear stage; $X_{rp\_H\_n}$ and $X_{sp\_H\_n}$ are the relative meshing displacements of the ring-planet gears and sun-planet gears at the second planetary gear stage; X_{cH_sL} and X_{GL_sH} are the relative meshing displacements of shafts; X_{GH_GL} is the relative meshing displacements of the low-speed gear and high-speed gear at the parallel gear stage.

In the presence of the effect of gear backlash b, if X_i is used to represent the relative meshing displacements, the non-linear gear mesh displacement function $f(X_i)$ can be expressed by:

$$f(X_i) = \begin{cases} X_i - b, & X_i > b \\ 0, & -b \le X_i \le b \\ X_i + b, & X_i < -b \end{cases} \quad (4.4)$$

The meshing forces of gear pairs shown in Figure 4.3 can be obtained as:

$$F_{rp\_L\_n} = k_{rp\_L} f\left(X_{rp\_L\_n}\right),\ F_{sp\_L\_n} = k_{sp\_L} f\left(X_{sp\_L\_n}\right) \quad (4.5\ a, b)$$

$$F_{cH\_sL} = k_{cH\_sL} X_{cH\_sL},\ F_{rp\_H\_n} = k_{rp\_H} f\left(X_{rp\_H\_n}\right) \quad (4.5c, d)$$

$$F_{sp\_H\_n} = k_{sp\_H} f\left(X_{sp\_H\_n}\right),\ F_{GL\_sH} = k_{GL\_sH} X_{GL\_sH} \quad (4.5e, f)$$

$$F_{GH\_GL} = k_{GHGL} X_{GHGL},\ n = 1,2,3 \quad (4.5g)$$

where k_{rp_L} and k_{sp_L} are the gear mesh stiffness of the ring-planet and sun-planet gear pairs at the first planetary gear stage, k_{rp_H} and k_{sp_H} are the gear mesh stiffness of the ring-planet and sun-planet gear pairs in the second planetary gear stage, and k_{GHGL} is the mesh stiffness of the gears in parallel gear stage. K_{cH_sL} is the torsional stiffness of the shaft that connects the sun pinion in the first planetary gear stage and the planet carrier arm of the second planetary gear stage, K_{GL_sH} is the torsional stiffness of the shaft that links the sun pinion in the second planetary gear stage and the low-speed gear of the parallel gear stage. The equivalent torsional stiffness in the line of action can be calculated as:

$$k_{cH\_sL} = K_{cH\_sL}/{r_{bs\_L}}^2 \,;\; k_{GL\_sH} = K_{GL\_sH}/{r_{bs\_H}}^2 \qquad (4.6\ a,\ b)$$

The damping forces of gear pairs can be written as:

$$D_{rp\_L\_n} = c_{rp\_L}\dot{X}_{rp\_L\_n},\ D_{sp\_L\_n} = c_{sp\_L}\dot{X}_{sp\_L\_n} \qquad (4.7\ a,\ b)$$

$$D_{cH\_sL} = c_{cH\_sL}\dot{X}_{cH\_sL},\ D_{rp\_H\_n} = c_{rp\_H}\dot{X}_{rp\_H\_n} \qquad (4.7c,\ d)$$

$$D_{sp\_H\_n} = c_{sp\_H}\dot{X}_{sp\_H\_n},\ D_{GL\_sH} = c_{GL\_sH}\dot{X}_{GL\_sH} \qquad (4.7e,\ f)$$

$$D_{GH\_GL} = c_{GHGL}\dot{X}_{GH\_GL},\ n = 1,2,3 \qquad (4.7g)$$

where c_{rp_L} and c_{sp_L} are the damping coefficients of the ring-planet and sun-planet at the first planetary gear stage, c_{rp_H} and c_{sp_H} are the damping coefficients of the ring-planet and sun-planet at the second planetary gear stage, and c_{GHGL} is the damping coefficients of the gears at the parallel gear stage. c_{cH_sL} is the damping coefficients of the shaft that links the sun pinion in the first planetary gear stage and the planet carrier arm of the second planetary gear stage, and c_{GL_sH} is the damping coefficient of the shaft that links the sun pinion in the second planetary gear stage and the low-speed gear of the parallel gear stage.

The equations of torsional vibrations can be obtained by applying Newton's second law for different gear stages. For the explanation, the equations of motion are presented according to the gear stages below.

For the first planetary gear stage, the equations of motion are given by Equations 4.8(a) to 4.8(c), which represent the equations of motions for the planet carrier arm, the planet gear and the sun pinion of the first planetary gear stage, respectively.

$$\left(I_{cL} + 3I_{pL\_n}\right)\ddot{\theta}_{cL} - \sum_{n=1}^{3} F_{rp\_L\_n} r_{bC_L} - \sum_{n=1}^{3} D_{rp\_L\_n} r_{bC_L} - \sum_{n=1}^{3} F_{sp\_L\_n} r_{bC_L} - \sum_{n=1}^{3} D_{sp\_L\_n} r_{bC\_L} = -T_{in} \quad (4.8a)$$

$$I_{pL\_n}\ddot{\theta}_{pL\_n} + F_{rp\_L\_n} r_{bp\_L} + D_{rp\_L\_n} r_{bp\_L} - F_{sp\_L\_n} r_{bp_L} - D_{sp\_L\_n} r_{bp_L} = 0 \quad (4.8b)$$

$$I_{sL}\ddot{\theta}_{sL} + \sum_{n=1}^{3} F_{sp\_L\_n} r_{bs\_L} + \sum_{n=1}^{3} D_{sp\_L\_n} r_{bs\_L} - F_{cH\_sL} r_{bs\_L} - D_{cH\_sL} r_{bs\_L} = 0 \quad (4.8c)$$

For the second planetary gear stage, the equations of motion are given by Equations 4.8(d) to 4.8(f), which represent the equations of motions for the planet carrier arm, the planet gear and the sun pinion of the second planetary gear stage, respectively.

$$\left(I_{cH} + 3I_{pH\_n}\right)\ddot{\theta}_{cH} + F_{cH\_sL} r_{bC\_H} + D_{cH\_sL} r_{bC\_H} - \sum_{n=1}^{3} F_{rp\_H\_n} r_{bC\_H} - \sum_{n=1}^{3} D_{rp\_H\_n} r_{bC\_H} - \sum_{n=1}^{3} F_{sp\_H\_n} r_{bC\_H} - \sum_{n=1}^{3} D_{sp\_H\_n} r_{bC\_H} = 0 \quad (4.8d)$$

$$I_{pH_n}\ddot{\theta}_{pH_n} + F_{rp_{H_n}} r_{bp_H} + D_{rp_{H_n}} r_{bp_H} - F_{sp_{H_n}} r_{bp_H} - D_{sp_{H_n}} r_{bp_H} = 0 \quad (4.8e)$$

$$I_{sH}\ddot{\theta}_{sH} + \sum_{n=1}^{3} F_{sp\_H\_n} r_{bs\_H} + \sum_{n=1}^{3} D_{sp\_H\_n} r_{bs\_H} - F_{GL\_sH} r_{bs\_H} - D_{GL\_sH} r_{bs\_H} = 0 \quad (4.8f)$$

For the parallel gear stage, the equations of motion of the gear and pinion can be written as:

$$I_{GL}\ddot{\theta}_{GL} + F_{GL\_sH} r_{bG\_L} + D_{GL\_sH} r_{bG\_L} - F_{GH\_GL} r_{bG\_L} - D_{GH\_GL} r_{bG\_L} = 0 \quad (4.8g)$$

$$I_{GH}\ddot{\theta}_{GH} + F_{GH\_GL} r_{bG\_H} + D_{GH\_GL} r_{bG\_H} = T_{out} \quad (4.8h)$$

Replacing the angular displacements in Equations 4.8(a) to 4.8(h) by the equivalent transverse displacements of gears using Equations 4.2(a) to 4.2(f), yields the equations of motion for the torsional vibrations in terms of equivalent displacement and equivalent mass:

$$M_{cL}\ddot{x}_{cL} - \sum_{n=1}^{3} F_{rp\_L\_n} - \sum_{n=1}^{3} D_{rp\_L\_n} - \sum_{n=1}^{3} F_{sp\_L\_n} - \sum_{n=1}^{3} D_{sp\_L\_n} = -P_{in} \quad (4.9a)$$

$$M_{pL\_n}\ddot{x}_{pL\_n} + F_{rp\_L\_n} + D_{rp\_L\_n} - F_{sp\_L\_n} - D_{sp\_L\_n} = 0 \quad (4.9b)$$

$$M_{sL}\ddot{x}_{sL} + \sum_{n=1}^{3} F_{sp\_L\_n} + \sum_{n=1}^{3} D_{sp\_L\_n} - F_{cH\_sL} - D_{cH\_sL} = 0 \quad (4.9c)$$

$$M_{cH}\ddot{x}_{cH} + F_{cH\_sL} + D_{cH\_sL} - \sum_{n=1}^{3} F_{rp_{Hn}} - \sum_{n=1}^{3} D_{rp_{Hn}} - \sum_{n=1}^{3} F_{sp_{Hn}} - \sum_{n=1}^{3} D_{sp\_H\_n} = 0 \quad (4.9d)$$

$$M_{pH\_n}\ddot{x}_{pH\_n} + F_{rp\_H\_n} + D_{rp\_H\_n} - F_{sp\_H\_n} - D_{sp\_H\_n} = 0 \quad (4.9e)$$

$$M_{sH}\ddot{x}_{sH} + \sum_{n=1}^{3} F_{sp\_H\_n} + \sum_{n=1}^{3} D_{sp\_H\_n} - F_{GL\_sH} - D_{GL\_sH} = 0 \quad (4.9f)$$

$$M_{GL}\ddot{x}_{GL} + F_{GL\_sH} + D_{GL\_sH} - F_{GH\_GL} - D_{GH\_GL} = 0 \quad (4.9g)$$

$$M_{GH}\ddot{x}_{GH} + F_{GH\_GL} + D_{GH\_GL} = P_{out},\ n = 1,2,3 \quad (4.9h)$$

where the equivalent masses are given by:

$$M_{cL} = I_{cL}/{r_{bc\_L}}^2 + 3m_{pL}/cos^2\alpha_{sL}$$

$$M_{pL\_n} = I_{pL\_n}/{r_{bp\_L\_n}}^2$$

$$M_{sL} = I_{sL}/{r_{bs\_L}}^2$$

$$M_{cH} = I_{cH}/{r_{bc\_H}}^2 + 3m_{pH}/cos^2\alpha_{sH}$$

$$M_{pH\_n} = I_{pH\_n}/{r_{bp\_H\_n}}^2$$

$$M_{sH} = I_{sH}/{r_{bs\_H}}^2$$

$$M_{GL} = I_{GL}/{r_{bG\_L}}^2$$

$$M_{GH} = I_{GH}/{r_{bG\_H}}^2, n = 1,2,3$$

By considering the static transmission error e_i, the relative meshing displacements of gears in the direction of line of action X_i in Equations 4.3(a) to 4.3(g) are re-calculated as follows:

$$X_{rp\_L\_n} = x_{pL\_n} - x_{cL} - e_{rp\_L\_n},\ X_{sp\_L\_n} = x_{sL} - x_{pL_n} - x_{cL} - e_{sp\_L\_n} \quad (4.10a, b)$$

$$X_{cH\_sL} = x_{cH} - x_{sL},\ X_{rp\_H\_n} = x_{pH\_n} - x_{cH} - e_{rp\_H\_n} \quad (4.10c, d)$$

$$X_{sp\_H\_n} = x_{sH} - x_{pH_n} - x_{cH} - e_{sp\_H\_n},\ X_{GL\_sH} = x_{GL} - x_{sH} \quad (4.10e, f)$$

$$X_{GH\_GL} = x_{GH} - x_{GL} - e_{GH\_GL},\quad n = 1,2,3 \quad (4.10g)$$

Combining Equations (4.4), (4.5), (4.7), (4.9) and (4.10), the dynamic equations of wind turbine gearbox components can be rewritten in terms of the relative meshing displacements X_i.

$$M_{rp\_L}\ddot{X}_{rp\_L\_n} + \left(M_{rp\_L}/M_{pL}\right)k_{rp\_L}f\left(X_{rp\_L\_n}\right) - \left(M_{rp_L}/M_{pL}\right)k_{sp_L}f\left(X_{sp_{L_n}}\right) +$$

$$\left(M_{rp_L}/M_{cL}\right)\sum_{n=1}^{3} k_{rp_L}f\left(X_{rp_{L_n}}\right) + \left(M_{rp_L}/M_{cL}\right)\sum_{n=1}^{3} k_{sp_L}f\left(X_{sp_{L_n}}\right) +$$

$$\left(M_{rp_L}/M_{pL}\right)c_{rp_L}\dot{X}_{rp_{L_n}} - \left(M_{rp_L}/M_{pL}\right)c_{sp_L}\dot{X}_{sp_{L_n}} + \left(M_{rp_L}/M_{cL}\right)\sum_{n=1}^{3} c_{rp_L}\dot{X}_{rp_{L_n}} +$$

$$\left(M_{rp\_L}/M_{cL}\right)\sum_{n=1}^{3} c_{sp\_L}\dot{X}_{sp\_L\_n} = \left(M_{rp\_L}/M_{cL}\right)P_{in} - M_{rp\_L}\ddot{e}_{rp\_L} \quad (4.11a)$$

$$M_{sp\_L}\ddot{X}_{sp\_L\_n} + \left(M_{sp\_L}/M_{cL}\right)\sum_{n=1}^{3} k_{rp\_L}f\left(X_{rp\_L\_n}\right) + \left(M_{sp\_L}/M_{cL}\right)\sum_{n=1}^{3} c_{rp\_L}\dot{X}_{rp\_L\_n} +$$

$$\left(M_{sp\_L}/M_{sL} + M_{sp\_L}/M_{cL}\right)\sum_{n=1}^{3} k_{sp\_L}f\left(X_{sp\_L\_n}\right) + \left(M_{sp\_L}/M_{sL} +\right.$$

$$\left.M_{sp\_L}/M_{cL}\right)\sum_{n=1}^{3} c_{sp\_L}\dot{X}_{sp\_L\_n} - \left(M_{sp\_L}/M_{sL}\right)k_{cH\_sL}X_{cH\_sL} -$$

$$(M_{sp\_L}/M_{sL})c_{cH\_sL}\dot{X}_{cH\_sL} - (M_{sp\_L}/M_{pL})k_{rp\_L}f\left(X_{rp\_L\_n}\right) -$$

$$(M_{sp\_L}/M_{pL})c_{rp\_L}\dot{X}_{rp\_L\_n} + (M_{sp\_L}/M_{pL})k_{sp\_L}f\left(X_{sp\_L\_n}\right) +$$

$$(M_{sp\_L}/M_{pL})c_{sp\_L}\dot{X}_{sp\_L\_n} = (M_{sp\_L}/M_{cL})P_{in} - M_{sp\_L}\ddot{e}_{sp\_L} \qquad (4.11b)$$

$$M_{cH\_sL}\ddot{X}_{cH\_sL} + (M_{cH\_sL}/M_{cH} + M_{cH\_sL}/M_{sL})k_{cH\_sL}X_{cH\_sL} + (M_{cH\_sL}/M_{cH} +$$

$$M_{cH\_sL}/M_{sL})c_{cH\_sL}\dot{X}_{cH\_sL} - (M_{cH\_sL}/M_{cH})\sum_{n=1}^{3}k_{rp\_H}f\left(X_{rp\_H\_n}\right) -$$

$$(M_{cH\_sL}/M_{cH})\sum_{n=1}^{3}c_{rp\_H}\dot{X}_{rp\_H\_n} - (M_{cH\_sL}/M_{cH})\sum_{n=1}^{3}k_{sp\_H}f\left(X_{sp\_H\_n}\right) -$$

$$(M_{cH\_sL}/M_{cH})\sum_{n=1}^{3}c_{sp\_H}\dot{X}_{sp\_H\_n} - (M_{cH\_sL}/M_{sL})\sum_{n=1}^{3}k_{sp\_L}f\left(X_{sp\_L\_n}\right)$$

$$-(M_{cH\_sL}/M_{sL})\sum_{n=1}^{3}c_{sp\_L}\dot{X}_{sp\_L\_n} = 0 \qquad (4.11c)$$

$$M_{rp\_H}\ddot{X}_{rp\_H\_n} + (M_{rp\_H}/M_{pH})k_{rp\_H}f(X_{rp\_H\_n}) + (M_{rp\_H}/M_{pH})c_{rp\_H}\dot{X}_{rp\_H\_n} -$$

$$(M_{rp\_H}/M_{pH})k_{sp\_H}f(X_{sp\_H\_n}) - (M_{rp\_H}/M_{pH})c_{sp\_H}\dot{X}_{sp\_H\_n} -$$

$$(M_{rp\_H}/M_{cH})k_{cH\_sL}X_{cH\_sL} - (M_{rp\_H}/M_{cH})c_{cH\_sL}\dot{X}_{cH\_sL} +$$

$$(M_{rp\_H}/M_{cH})\sum_{n=1}^{3}k_{rp\_H}f\left(X_{rp\_H\_n}\right) + (M_{rp\_H}/M_{cH})\sum_{n=1}^{3}c_{rp\_H}\dot{X}_{rp\_H\_n} +$$

$$(M_{rp\_H}/M_{cH})\sum_{n=1}^{3}k_{sp\_H}f\left(X_{sp\_H\_n}\right) + (M_{rp\_H}/M_{cH})\sum_{n=1}^{3}c_{sp\_H}\dot{X}_{sp\_H\_n}$$

$$= -M_{rp\_H}\ddot{e}_{rp\_H} \qquad (4.11d)$$

$$M_{sp\_H}\ddot{X}_{sp\_H\_n} + (M_{sp\_H}/M_{sH} + M_{sp\_H}/M_{cH})\sum_{n=1}^{3}k_{sp\_H}f\left(X_{sp\_H\_n}\right) + (M_{sp\_H}/M_{sH} +$$

$$M_{sp\_H}/M_{cH})\sum_{n=1}^{3}c_{sp\_H}\dot{X}_{sp\_H\_n} - (M_{sp\_H}/M_{sH})k_{GL\_sH}X_{GL\_sH} -$$

$$(M_{sp\_H}/M_{sH})c_{GL\_sH}\dot{X}_{GL\_sH} - (M_{sp\_H}/M_{pH})k_{rp\_H}f\left(X_{rp\_H\_n}\right) -$$

$$(M_{sp\_H}/M_{pH})c_{rp\_H}\dot{X}_{rp\_H\_n} + (M_{sp\_H}/M_{pH})k_{sp\_H}f\left(X_{sp\_H\_n}\right) +$$

$$(M_{sp\_H}/M_{pH})c_{sp\_H}\dot{X}_{sp\_H\_n} - (M_{sp\_H}/M_{cH})k_{cH\_sL}X_{cH\_sL} - (M_{sp\_H}/M_{cH})c_{cH\_sL}\dot{X}_{cH\_sL} +$$

$$(M_{sp\_H}/M_{cH})\sum_{n=1}^{3}k_{rp\_H}f\left(X_{rp\_H\_n}\right) + (M_{sp\_H}/M_{cH})\sum_{n=1}^{3}c_{rp\_H}\dot{X}_{rp\_H\_n} =$$

$$-M_{sp\_H}\ddot{e}_{sp\_H} \qquad (4.11e)$$

$$M_{GL\_sH}\dot{X}_{GL\_sH} + (M_{GL\_sH}/M_{GL} + M_{GL\_sH}/M_{sH})k_{GL\_sH}X_{GL\_sH} + (M_{GL\_sH}/M_{GL} + M_{GL\_sH}/M_{sH})c_{GL\_sH}\dot{X}_{GL\_sH} - (M_{GL\_sH}/M_{GL})k_{GH\_GL}f(X_{GH\_GL}) - (M_{GL\_sH}/M_{GL})c_{GH\_GL}\dot{X}_{GH\_GL} - (M_{GL\_sH}/M_{sH})\sum_{n=1}^{3}k_{sp\_H}f(X_{sp\_H\_n}) - (M_{GL\_sH}/M_{sH})\sum_{n=1}^{3}c_{sp\_H}\dot{X}_{sp\_H\_n} = 0 \qquad (4.11f)$$

$$M_{GH\_GL}\dot{X}_{GH\_GL} + (M_{GH\_GL}/M_{GH} + M_{GH\_GL}/M_{GL})k_{GH\_GL}f(X_{GH\_GL}) + (M_{GH\_GL}/M_{GH} + M_{GH\_GL}/M_{GL})c_{GH\_GL}\dot{X}_{GH\_GL} - (M_{GH\_GL}/M_{GL})k_{GL\_sH}f(X_{GL\_sH}) - (M_{GH\_GL}/M_{GL})c_{GL\_sH}\dot{X}_{GL\_sH} = (M_{GH\_GL}/M_{GH})P_{out} - M_{GH\_GL}\ddot{e}_{GH\_GL}, \quad n = 1,2,3 \qquad (4.11g)$$

where

$$M_{rp_L} = M_{pL}M_{cL}/(M_{pL} + M_{cL})$$

$$M_{sp\_L} = M_{sL}M_{pL}M_{cL}/(M_{pL}M_{cL} + M_{sL}M_{pL} + M_{sL}M_{cL})$$

$$M_{cH\_sL} = M_{cH}M_{sL}/(M_{cH} + M_{sL})$$

$$M_{rp\_H} = M_{pH}M_{cH}/(M_{pH} + M_{cH})$$

$$M_{sp\_H} = M_{sH}M_{pH}M_{cH}/(M_{pH}M_{cH} + M_{sH}M_{pH} + M_{sH}M_{cH})$$

$$M_{GL\_sH} = M_{GL}M_{sH}/(M_{GL} + M_{sH})$$

$$M_{GH\_GL} = M_{GH}M_{GL}/(M_{GH+}M_{GL})$$

The torsional dynamic response of the gearbox can be interpreted by the behaviour of solutions of the second-order differential equations 4.11(a) to 4.11(g). The relative meshing displacement vector can then be represented by q as shown below:

$$Q = \{X_{rp\_L\_n}, X_{sp\_L\_n}, X_{cH_{sL}}, X_{rp\_H\_n}, X_{sp\_H\_n}, X_{GL_{sH}}, X_{GH\_GL}\}^T, n = 1,2,3 \quad (4.12)$$

Then Equation (4.11) can be expressed in the concise matrix form:

$$M\ddot{Q} + C\dot{Q} + Kf(Q) = p \quad (4.13)$$

where M is the equivalent mass matrix as shown in Equation (4.14), K is the mesh stiffness matrix, C is the damping matrix and p is the excitation matrix.

$$M = diag[M_{rp_L}, M_{rp_L}, M_{rp_L}, M_{sp_L}, M_{sp_L}, M_{sp_L}, M_{cH_{sL}}, M_{rp\_H},$$
$$M_{rp\_H}, M_{rp\_H}, M_{sp\_H}, M_{sp\_H}, M_{sp\_H}, M_{GL\_sH}, M_{GH\_GL}] \quad (4.14)$$

$f(Q_i)$ is the vector form of the nonlinear gear mesh displacement function.

$$f(Q_i) = \begin{cases} Q_i - b_i, & Q_i > b_i \\ 0, & -b_i \le Q_i \le b_i \\ Q_i + b_i, & Q_i < -b_i \end{cases} \quad (4.15)$$

where the gear backlash $b_i = 0$ for $i = 7, 14$ as no gear backlash exists on shafts, and $b_i = b$ for the rest.

4.3 Specifications

4.3.1 General information

For modern wind turbines, the rotational speed of rotor blades is normally between 5 and 22 rpm, and the required rotational speed of generator is between 1000 and 1600

rpm [156]. The following values for the blade and wind are used in the numerical simulations. The radius of the rotor blades is $36m$, the rotational speed of the blades is $17\ rpm$, the average wind speed is $16m/s$, the density of wind is $1.21kg/m^3$ and the wind power utilization is 0.3. The gear ratio of the wind turbine gearbox is 4.09:19.98:106.53. The mass moment of inertia, radius and pressure angle of each pair of the gearbox are listed in Table 1.

Table 1. Mass moment of inertia, radius and pressure angle of each gear of gearbox

	First Planetary Stage				Second Planetary Stage				Parallel Stage	
	p	s	r	c	p	s	r	c	GH	GL
Inertia (Kgm^2)	36	7		588	2	6		88	0.2	33
Gear radius (m)	0.63	0.378	1.638		0.468	0.324	1.26		0.184	0.752
Pressure Angle (°)	20	20	20		20	20	20		20	20

where the subscripts "p", "s", "r" , "c", "GH" and "GL" represent planet gear, sun pinion, ring gear and planet carrier arm, high-speed gear and low-speed pinion, respectively.

For wind turbine gearboxes, the natural frequencies of gears are always larger than their meshing frequencies. When the rotational speed of the blade is set to be $17\ rpm$ as a constant rather than in a broad speed range, the meshing frequencies at three gear stages are 33.2 Hz, 199.5Hz and 694.4Hz based on Equation (4.16). As the fundamental meshing frequencies play the most important role compared to their harmonics, and it is ensured that the resonance can be avoided in the gearbox when these meshing frequencies are much smaller than their natural frequencies [167].

$$f_i = \omega_g N_g / 60 \tag{4.16}$$

where w_g is the rotational speed of the gear or the rotational speed of the planet carrier arm for the planetary gear stage, and N_g is the gear teeth number or the teeth number of the ring gear for the planetary gear stage [168].

4.3.2 Excitation conditions

The static transmission error $e_i(t)$ is represented by Equation (4.17). As the static transmission error is very small, only the fluctuation term e_{ai} is considered. The high-frequency excitations at the meshing frequency ω_i are expected during gear mesh.

$$e_i(t) = e_{ai} cos(\omega_i t) \tag{4.17}$$

For the excitation term $p_i(t)$, different assumptions would lead to different forms of equations. When only the internal excitation is considered and the excitation is only caused by the static transmission error e_i, the internal excitation $p_i(t)$ is given by Equation (4.18), where F_{ai} is the fluctuating meshing force (N) caused by the static transmission error e_i.

$$p_i(t) = F_{ai} \omega_i^2 \, cos(\omega_i t) \tag{4.18}$$

When both the constant external and fluctuating internal excitations exist, $p_i(t)$ is represented by Equation (4.19), for which the mean term F_{me} of the external load is added [169].

$$p_i(t) = F_{me} + F_{ai}\omega_i{}^2 \, cos(\omega_i t) \tag{4.19}$$

When both the external excitation fluctuation and the internal excitation exist, $p_i(t)$ is expressed by Equation (4.20).

$$p_i(t) = F_{me} + F_{ae} \, cos(\omega_e t) + F_{ai}\omega_i{}^2 \, cos(\omega_i t) \tag{4.20}$$

where F_{ai} is the fluctuating meshing force (N) caused by the static transmission error e_{ai}, F_{me} is the constant external force (N), F_{ae} is the fluctuating external force (N), and ω_e is the external excitation frequency. It can be predicted that the external excitation results in low frequency responses, whereas the internal excitation results in high frequency responses.

In addition, the meshing frequencies of the wind turbine gearbox components, determined by Equation (4.16), remain constant during turbine operation under the constant rotational speed for the simplicity in simulation. The output power of blades can be expressed in terms of the air density ρ_{air}, radius of the blades r_{blade}, the average wind speed V_{wind} and the wind power utilization C_p [170].

$$P_{blade} = \frac{1}{2}\rho_{air}\pi r_{blade}{}^2 V_{wind}{}^3 C_p \tag{4.21}$$

The driving torque of the gearbox is calculated as below:

$$T_{in} = P_{blade}/\omega_{blade} \tag{4.22}$$

where ω_{blade} is the rotational speed of blades. By neglecting the power loss in the gearbox, the output torque of the gearbox T_{out} can be obtained as:

$$T_{out} = T_{in}/Gr \tag{4.23}$$

where Gr is the gear ratio of the gearbox.

4.3.3 Time-varying mesh stiffness

The static transmission error e_i is defined as the difference between the theoretical and actual angular positions of gears, and is commonly used to represent the impact of the internal excitations, caused by manufacturing errors [125]. The gear mesh stiffness variation of each gear pair is assumed to be approximately proportional to the meshing tooth variation, which is periodic over meshing cycles. Each of the gear meshes has the same shape of mesh tooth variation when neglecting the static and dynamic transmission error effects, but they are not in phase with each other. Thus, the time-varying mesh stiffness function $k_{ij}(t)$ is expressed in the periodic forms in terms of the mean and fluctuating mesh stiffnesses as shown in Equation (4.24), which fluctuates with the change of the contact teeth at the meshing frequency ω_i [137].

$$k_{ij}(t) = k_{mij} + k_{aij}cos(\omega_i t) \quad (4.24)$$

where k_{mij} is the mean term of the time-varying mesh stiffness function, k_{aij} is the alternating term, and ω_i is the meshing frequency.

The fluctuating term of the gear mesh stiffness k_{rij} can be calculated by Equations (4.25) and (4.26).

$$k_{aij} = k_{mij}/CR \quad (4.25)$$

$$CR = LA/P_b \quad (4.26)$$

where CR is the contact ratio, P_b is the base pitch and LA is the length of action given by Equation (4.27), which is the distance along the line of action between meshing points. The meshing points are the points of beginning and leaving the teeth contact during tooth mesh.

$$LA = \sqrt{(r_p + a_p)^2 - (r_p \cos\alpha)^2} + \sqrt{(r_g + a_g)^2 - (r_g \cos\alpha)^2} - Cd \sin\alpha \quad (4.27)$$

where r_g and r_p are the pitch radii of the gear and pinion, a_g and a_p are the addendum of the gear and pinion, α is the pressure angle, and Cd is the center distance of the gear pairs [171].

$$Cd = r_p + r_g \quad (4.28)$$

It is assumed that the gear tooth behaves like a cantilever beam, as shown in Figure 4.4. Thus, the mean stiffness k_{mij} can be calculated by Equation (4.30), based on the ISO-6336 standard [172, 173].

$$k_{mij} = P/\left(y_{\max\_gear} - y_{\max\_pinion}\right) \tag{4.29}$$

where $y_{\max\_gear}$ and $y_{\max\_pinion}$ are the maximum deflection of the gear tooth calculated by Equation (4.30), P is the applied load at the tooth tip, L is the tooth depth calculated using the AGMA standard in Table 1 [174], I is the area moment of inertia, and E is the modulus of elasticity.

$$y_{max} = PL^3/3EI \tag{4.30}$$

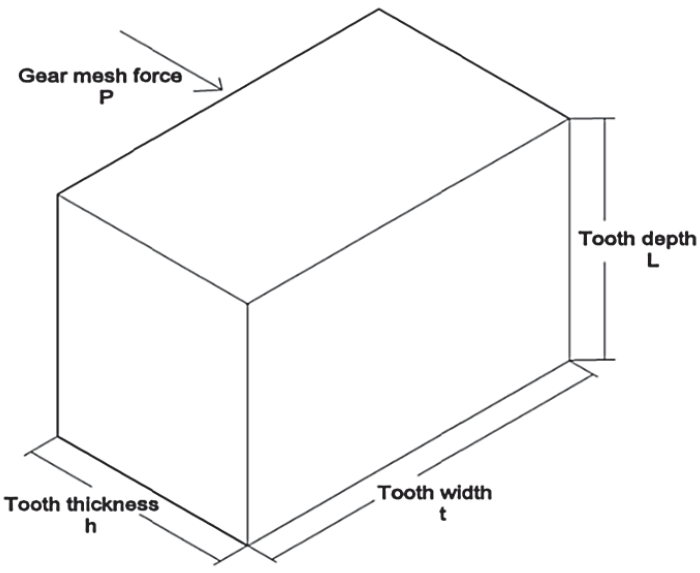

Figure 4.4. Simplified model of a gear tooth

Table 2. AGMA full-depth gear tooth specifications [171]

Parameters	Coarse pitch ($P_d < 20$)
Pressure angle α (°)	20
Addendum a (in)	$1/P_d$
Dedendum b (in)	$1.25/P_d$
Whole depth L (in)	$2.25/P_d$

4.3.4 Damping

The tooth deformation is represented by the time-varying mesh stiffness and damping in the lumped-parameter model, as shown in Figure 4.3. Thus, the damping of the teeth mesh c_j can be expressed by

$$\boldsymbol{c_{ij} = 2\xi\sqrt{k_{ij}m_{gear}m_{pinion}/(m_{gear} + m_{pinion})}} \qquad (4.31)$$

where k_{ij} is the mesh stiffness of the gear pair, ξ is the damping ratio of tooth mesh (varies between 0.03 and 0.17), m_{gear} and m_{pinion} are the masses of gear and pinion.

4.4 Results

The torsional vibrations of wind turbine gearbox are determined by the nonlinear equations shown in Equation (4.13). No explicit solutions to this nonlinear system can be found in the context of mathematics. Thus, numerical integration method is utilised to find the solutions. The *ode45* solver in Matlab is used to solve these nonlinear differential equations. The differential equation solver *ode45* uses a variable step Runge-Kutta Method to solve differential equations numerically. Because the solver *ode45* can only solve first order differential equations, higher order differential

equations would then have to be converted to a set of first order differential equations. The first 1500 periods of integration results are discarded before recording the steady state solutions. In addition, 3600 points are sampled for each meshing cycle in order to capture a sufficient number of meshing frequencies in the response spectra. With the help of time history, FFT spectrum, phase portrait and Poincare map, the effects of the static transmission error, mean-to-alternating force ratio and time-varying mesh stiffness on the dynamic response of the wind turbine gearbox components are investigated. The magnitude of the FFT spectrum has been enlarged so that the frequency can be observed more obvious, thus, it is not the actual magnitude as in the time histories. Even though sufficiently high number of periods are discarded and sufficiently high meshing points are sampled, this is an initial value problem and when time progresses, the numerical errors accumulate and eventually the solutions "blow" and no longer accurate. Detailed numerical analysis is not required because it may be out of the scope of this work.

The possible dynamic responses can be classified into five groups: harmonic periodic, non-harmonic periodic, sub-harmonic, quasi-periodic and chaotic responses. The harmonic periodic responses have circular phase portrait, and repeat themselves at excitation frequencies in Poincare map. The non-harmonic periodic responses have non-circular phase portrait, and repeat themselves at excitation frequencies in Poincare map. The sub-harmonic responses repeat themselves at multiple discrete points in Poincare map. The quasi-periodic responses have non-periodic circles in phase portrait and a closed orbit with combined excitation frequencies in Poincare map. The chaotic responses are non-periodic in time histories and have infinite non-repeating points in Poincare map [175].

4.4.1 Effect of the static transmission error *E*

This section investigates the effects of the static transmission error e_i on gear meshes, for the gearbox under both the constant external excitation and the fluctuating internal excitation, described by Equation (4.19). The dynamic responses of Q_{rp_H}[4] and Q_{GHGL}[5] are presented for three different values of the static transmission error e_i: 10 μm, 100 μm and 300 μm.

The dynamic response of Q_{rp_H} is presented in Figure 4.5 for when the static transmission error e_i is 10 μm. It is shown that the time histories of Q_{rp_H} fluctuates with the meshing frequency f_2, whose amplitude is much larger than f_1, and its harmonics $2f_2$ and $3f_2$ are also observed. A repeated pattern is observed in the phase portrait shown in Figure 4.5(c), and a single point with shifts around it are presented in the Poincare map in Figure 4.5(d), due to the combination of all the frequency components. These indicate that the response of Q_{rp_H} is periodic.

The dynamic responses of Q_{GHGL} is presented in Figure 4.6. It is observed that the time histories of Q_{GHGL} are stable as shown in Figure 4.6(a). Three frequency components f_1, f_2 and its harmonics $2f_2$, and f_3 are observed in Figure 4.6(b). The magnitude of the meshing frequency f_3 is larger than other components. It indicates that both the meshing frequencies of the second and third gear stages f_2 and f_3 contribute on Q_{GHGL}, but the major effects are still caused by its own gear stage. The phase portrait and Poincare map in Figures 4.6(c) and 4.6(d) indicate that the response of Q_{GHGL} is quasi-periodic.

[4] Q_{rp_H} represents the relative displacement of the ring-planet gear mesh at second planetary gear stage.

[5] Q_{GHGL} represents the relative displacement of the gear mesh of the parallel gear stage.

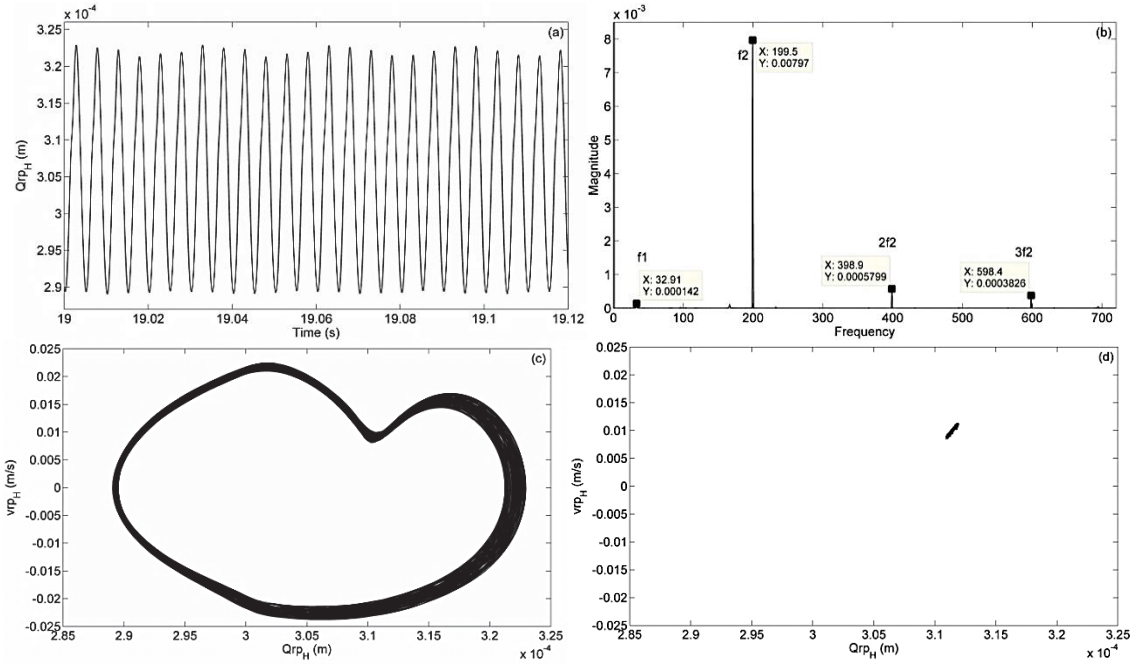

Figure 4.5. The vibrational responses of $\boldsymbol{Q_{rp\_H}}$ caused by $\boldsymbol{e = 10\ \mu m}$ (a) Time histories (b) FFT spectrum (c) Phase Portrait (d) Poincare map

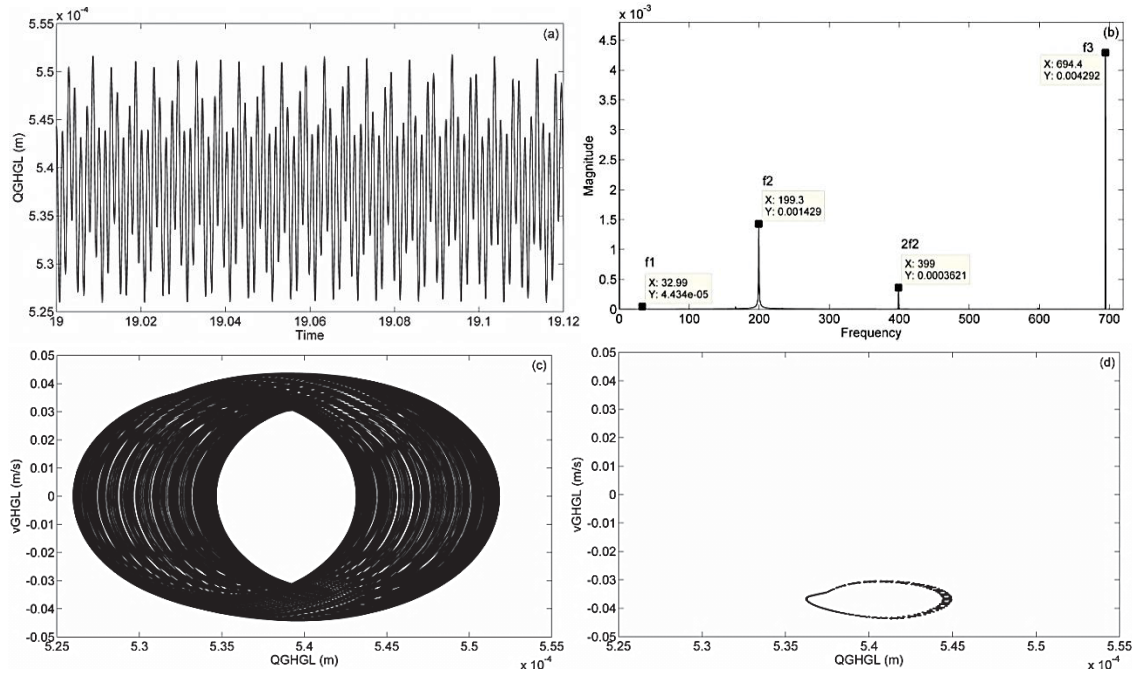

Figure 4.6. The vibrational responses of $\boldsymbol{Q_{GHGL}}$ caused by $\boldsymbol{e = 10\ \mu m}$ (a) Time histories (b) FFT spectrum (c) Phase Portrait (d) Poincare map

The dynamic response of Q_{rp_H} is presented in Figure 4.7 for when the static transmission error e_i is 100 μm. It is observed that the time histories of Q_{rp_H} shown in Figure 4.7(a) fluctuates with the meshing frequency f_2. A repeated circle is observed in the phase portrait in Figure 4.7(c), and a single point is presented in the Poincare map in Figure 4.7(d). These indicate that the response of Q_{rp_H} is periodic.

The dynamic responses of Q_{GHGL} is presented in Figure 4.8. It is observed that the time histories of Q_{GHGL} are stable as shown in Figure 4.8(a). Three frequency components f_1, f_2 and f_3 are shown in Figure 4.8(b). The magnitude of the meshing frequency f_2 is about the same as f_3, which indicates that both the meshing frequencies of the second and third gears stages f_2 and f_3 contribute nearly equally to Q_{GHGL}, due to the effect of the increased transmission error. This affects the phase portrait shown in Figures 4.8(c), and present the shift of points on Poincare map in Figure 4.8(d), which suggest that the response of Q_{rp_H} is periodic.

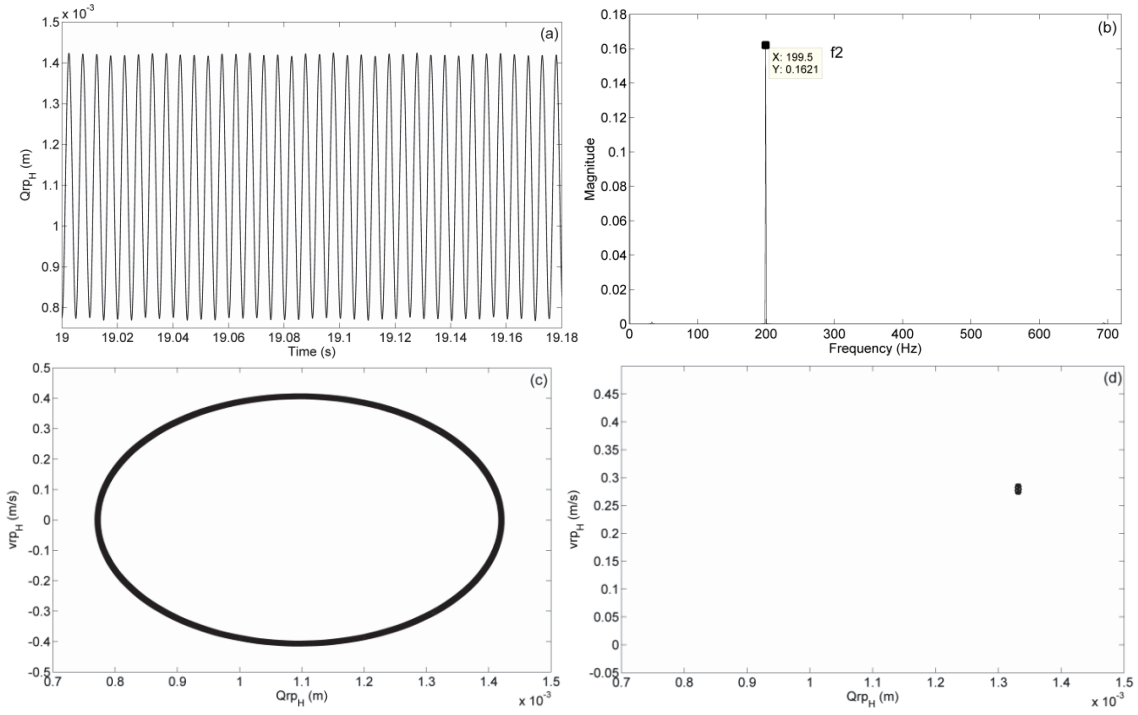

Figure 4.7. The vibrational responses of $\boldsymbol{Q_{rp\_H}}$ caused by $\boldsymbol{e = 100\ \mu m}$ (a) Time histories (b) FFT spectrum (c) Phase Portrait (d) Poincare map

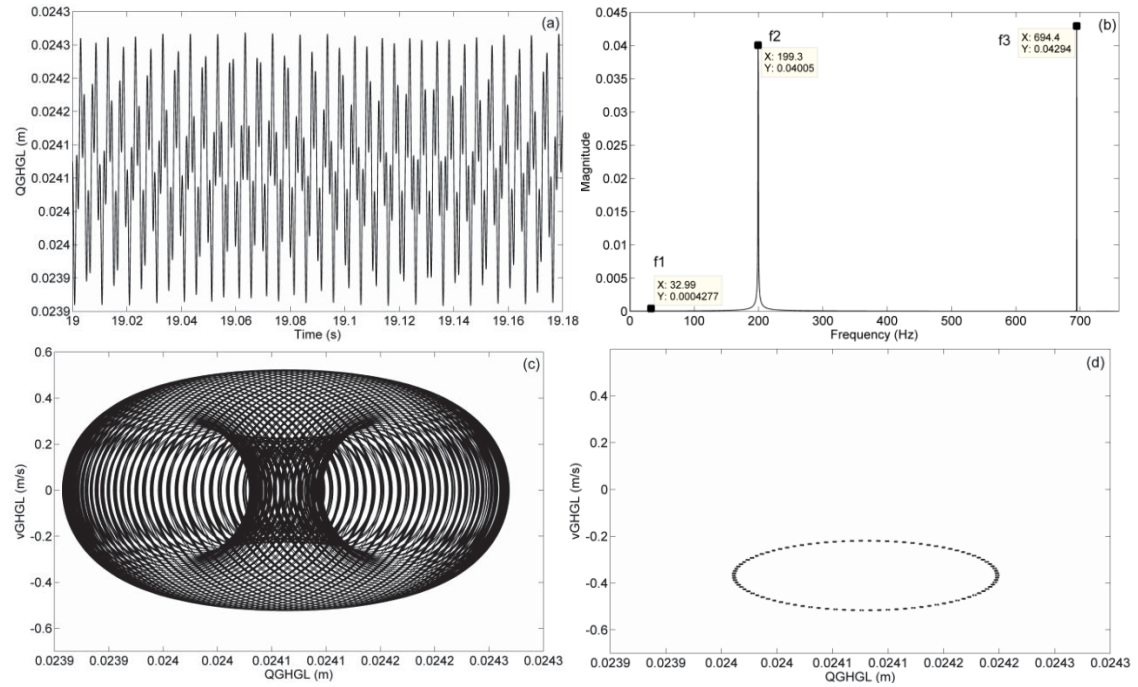

Figure 4.8. The vibrational responses of $\boldsymbol{Q_{GHGL}}$ caused by $\boldsymbol{e = 100\ \mu m}$ (a) Time histories (b) FFT spectrum (c) Phase Portrait (d) Poincare map

When the static transmission error e_i increases to 300 μm, the magnitude of the fluctuation increases compared with that when the transmission error is 100μm as shown previously in Figure 4.7(a). The meshing frequency at its own gear stage f_2 still influences Q_{rp_H} the most, and appears to have harmonics $f_2, 2f_2$ and $3f_2$, as shown in Figure 4.9(b). The phase portrait in Figure 4.9(c) shows a repeating pattern, and the Poincare map in Figure 4.9(d) presents a single point. These indicate that the response of Q_{rp_H} is periodic.

The dynamic responses of Q_{GHGL} is presented in Figure 4.10. It is observed that the time histories of Q_{GHGL} are stable in Figure 4.10(a). Two frequency components f_2 and f_3 are observed in Figure 4.10(b). The magnitude of the meshing frequency f_3 is slightly larger than that of f_2, which indicates that both the meshing frequencies of the second and third gears stages f_2 and f_3 contribute to Q_{GHGL}, and f_3 influences more. The phase portrait and Poincare map in Figures 4.10(c) and 4.10(d) indicate that the response of X_{GHGL} is periodic.

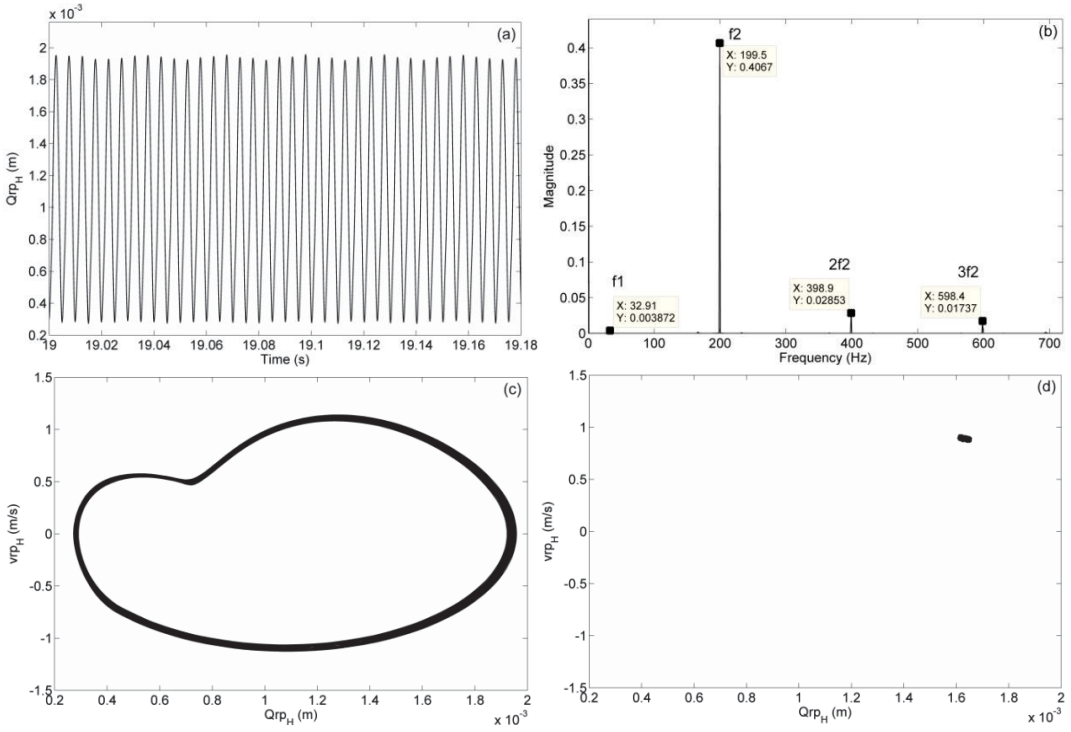

Figure 4.9. The vibrational responses of $\boldsymbol{Q_{rp\_H}}$ caused by $\boldsymbol{e = 300\ \mu m}$ (a) Time histories (b) FFT spectrum (c) Phase Portrait (d) Poincare map

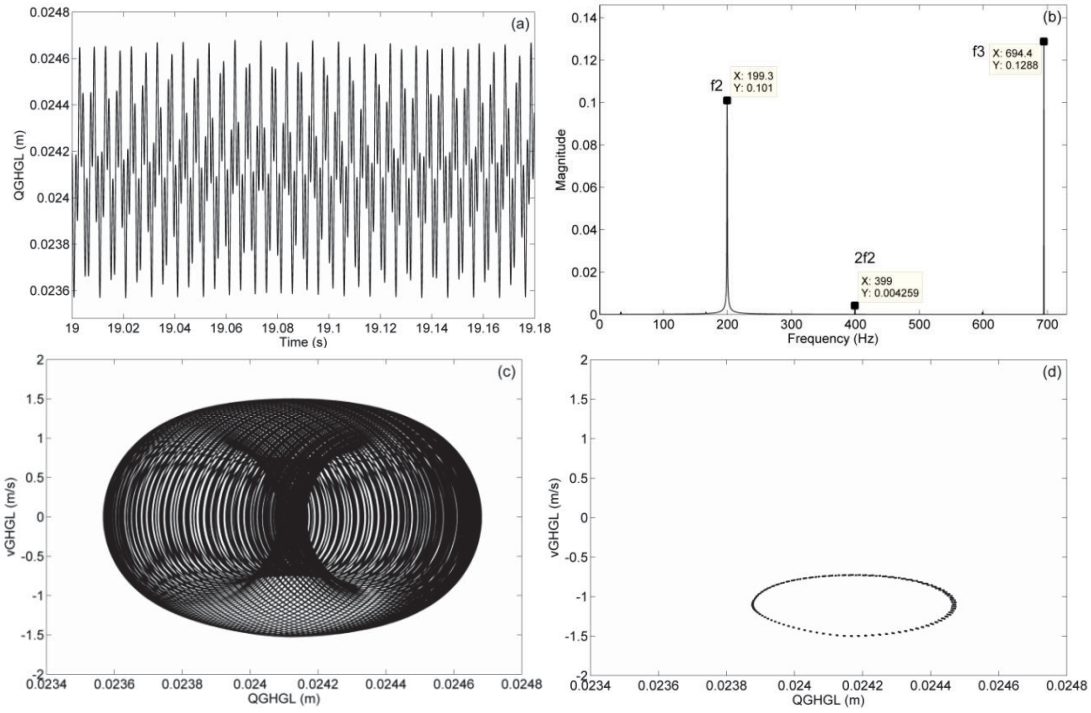

Figure 4.10. The vibrational responses of $\boldsymbol{Q_{GHGL}}$ caused by $\boldsymbol{e = 300\ \mu m}$ (a) Time histories (b) FFT spectrum (c) Phase Portrait (d) Poincare map

4.4.2 Effect of the mesh stiffness *K*

This section studies the effect of the time-varying mesh stiffness on Q_{rp_H} and Q_{GHGL}. To present the extent of variation shown in Equation (4.24), the mean-to-alternating mesh stiffness ratio K_m/K_a is used as the varying parameter. The dynamic response of Q_{rp_H} and Q_{GHGL} are then studied by setting the value of the mean-to-alternating mesh stiffness ratio K_m/K_a to be 10, 3.33 and 2, respectively.

When the mean-to-alternating mesh stiffness ratio K_m/K_a is 10, the dynamic responses of Q_{rp_H} is presented in Figure 4.11, which fluctuates mainly with three meshing frequency components f_1, f_2 and f_3. With the effect of the fluctuating mesh stiffness term K_a, the harmonics of meshing frequency at the first planetary gear stage ($2f_1$ and $3f_1$) are observed. The meshing frequency f_2 is larger than other frequency components, which indicates that it has the most influence on Q_{rp_H}. The meshing frequency of the parallel gear stage f_3 has the least influence. Due to the effects of the combined meshing frequencies, the Phase portrait in Figure 4.11(c) shows unrepeated circles, and the Poincare map in Figure 4.11(d) shows dots around one point. These indicate that the dynamic behaviour of X_{rp_H} is quasi-periodic.

The dynamic responses of Q_{GHGL} is presented in Figure 4.12, which fluctuates with three frequency components f_1, f_2 and f_3. The meshing frequency of the parallel gear stage f_3 has the most influence, as the magnitude of it is larger than other frequency components. Due to the effects of the combined meshing frequencies, the Phase portrait in Figure 4.12(c) shows unrepeated circles, and the Poincare map in Figure 4.12(d)

shows a circle around one point. These indicate that the dynamic behaviour of X_{rp_H} is quasi-periodic.

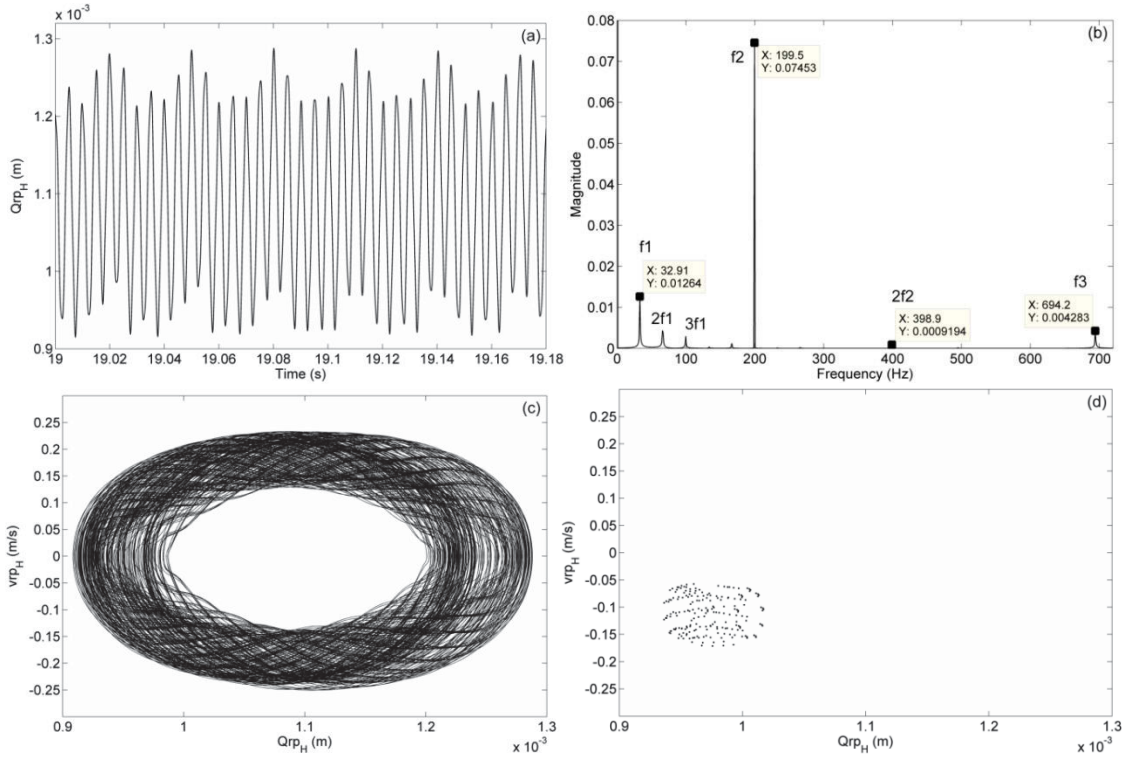

Figure 4.11. The vibrational responses of $\boldsymbol{Q_{rp\_H}}$ caused by $\boldsymbol{K_m/K_a = 10}$ (a) Time histories (b) FFT spectrum (c) Phase Portrait (d) Poincare map

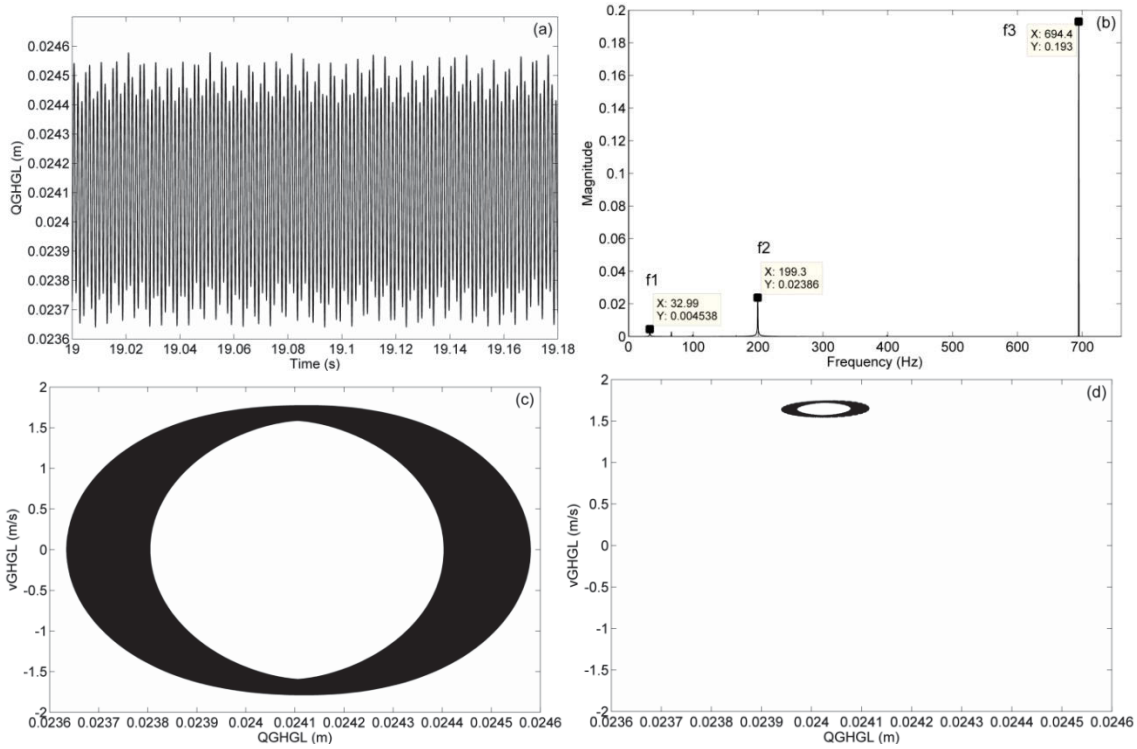

Figure 4.12. The vibrational responses of $\boldsymbol{Q_{GHGL}}$ caused by $\boldsymbol{K_m/K_a = 10}$ (a) Time histories (b) FFT spectrum (c) Phase Portrait (d) Poincare map

When the mean-to-alternating mesh stiffness ratio K_m/K_a is 3.33, the dynamic response of Q_{rp_H} is shown in Figure 4.13. With larger fluctuation of the mesh stiffness K_a, the fundamental meshing frequencies, their harmonics and sidebands appear to be significant. As shown in Figures 4.13(c) and 4.13(d), it does not repeat itself in any pattern, which indicates that the chaotic behaviours on the ring-planet gear pair at the intermediate planetary gear stage Q_{rp_H} exist when the fluctuation of the gear mesh stiffness K_a is increased.

The dynamic responses of Q_{GHGL} is presented in Figure 4.14, it mainly fluctuates with its own meshing frequency f_3. However, due to the effects of the mesh stiffness fluctuation K_a, the harmonics of the meshing frequencies appear more obvious than

those in Figure 4.12(b). The Phase portrait in Figure 4.14(c) shows unrepeated circles, and the Poincare map in Figure 4.14(d) shows a circle around one point. These indicate that the dynamic behaviour of Q_{rp_H} is quasi-periodic.

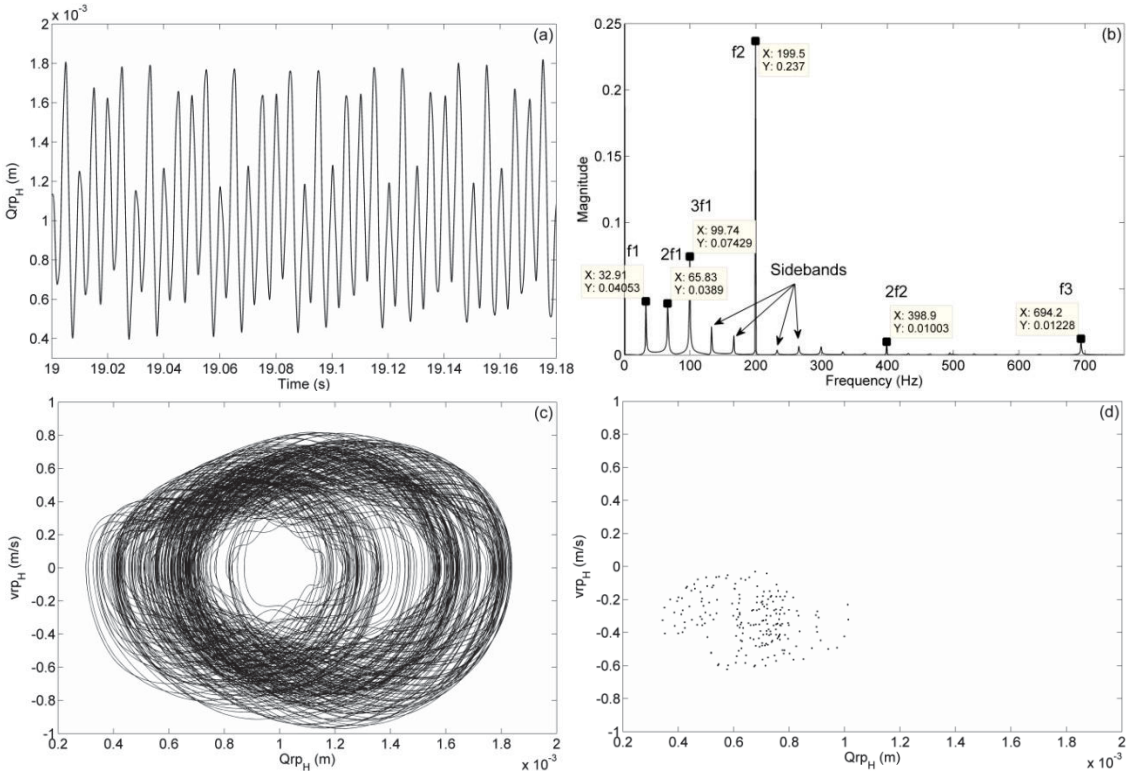

Figure 4.13. The vibrational responses of $\boldsymbol{Q_{rp\_H}}$ caused by $\boldsymbol{K_m/K_a = 3.33}$ (a) Time histories (b) FFT spectrum (c) Phase Portrait (d) Poincare map

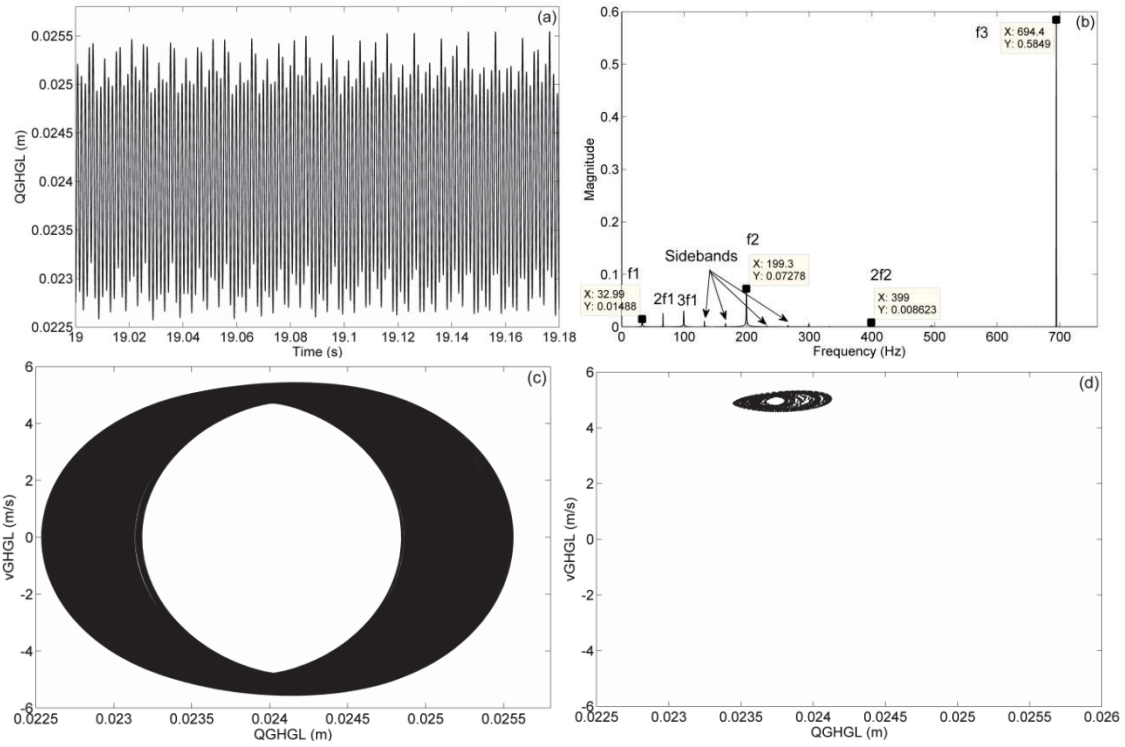

Figure 4.14. The vibrational responses of $\boldsymbol{Q_{GHGL}}$ caused by $\boldsymbol{K_m/K_a = 3.33}$ (a) Time histories (b) FFT spectrum (c) Phase Portrait (d) Poincare map

When the mesh stiffness ratio K_m/K_a is 2, the dynamic responses of Q_{rp_H} is presented in Figure 4.15, which fluctuates with three frequency components f_1, f_2 and f_3 and their harmonics. With the increased varying mesh stiffness, the meshing frequency f_2 is slightly larger than other frequency components, but the meshing frequency and its harmonics at the first planetary gear stage (f_1, $2f_1$, $3f_1$, $4f_1$ and $5f_1$) give larger influence and cannot be ignored. The meshing frequency of the parallel gear stage f_3 has the least influence. Due to the effects of the combined meshing frequencies, the Phase portrait in Figure 4.15(c) and the Poincare map in Figure 4.15(d) show unrepeated patterns, which indicate that the dynamic response of Q_{rp_H} is chaotic.

The dynamic responses of Q_{GHGL} is presented in Figure 4.16, it fluctuates with three frequency components f_1, f_2, f_3 and their harmonics and sidebands. The meshing frequency of the parallel gear stage f_3 has the most influence. The Phase portrait in Figure 4.16(c) shows circles with shifts, and the Poincare map in Figure 4.16(d) shows a circle around one point. These indicate that the dynamic behaviour of X_{rp_H} is quasi-periodic.

It is observed that the gear mesh stiffness is a significant factor for the dynamic response of gears. Compared to the static transmission error, the gear mesh stiffness has more effect on the dynamic response of gearbox components. When the mesh stiffness ratio is large, the response of Q_{rp_L} seems relatively stable. When the mesh stiffness ratio is reduced with an increasing fluctuating term K_a, the response of Q_{rp_L} becomes more unstable. When the fluctuating term K_a is further increased, the response of Q_{rp_L} loses its stability.

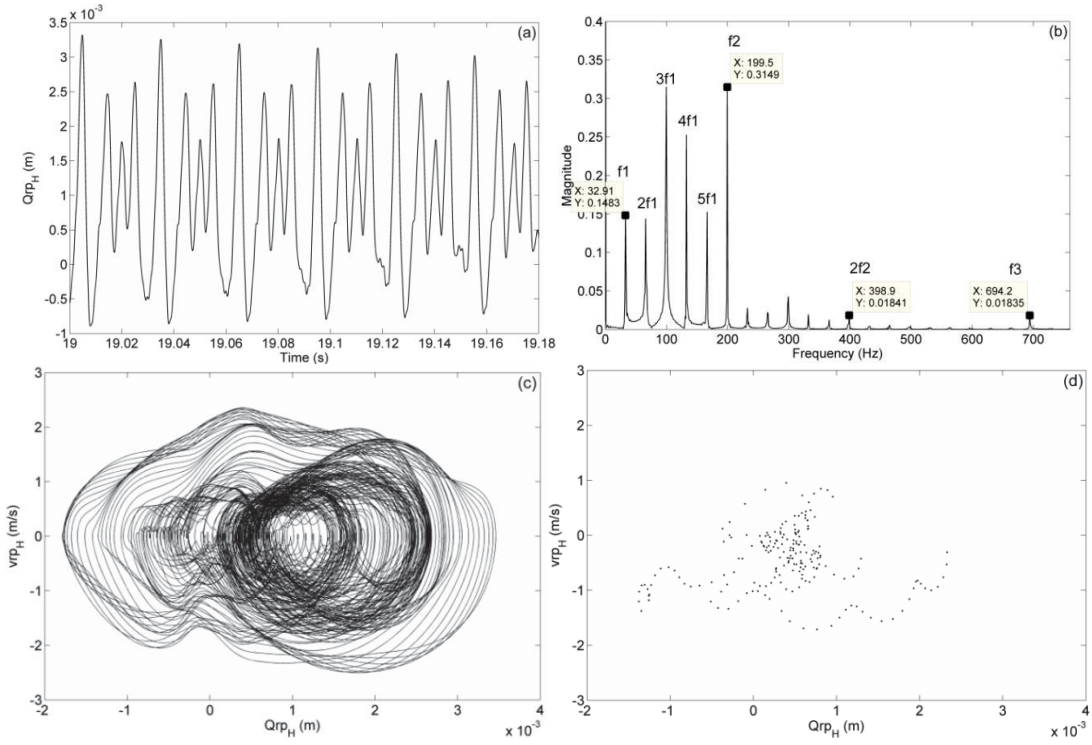

Figure 4.15. The vibrational responses of $\boldsymbol{Q_{rp\_H}}$ caused by $\boldsymbol{K_m/K_a = 2}$ (a) Time histories (b) FFT spectrum (c) Phase Portrait (d) Poincare map

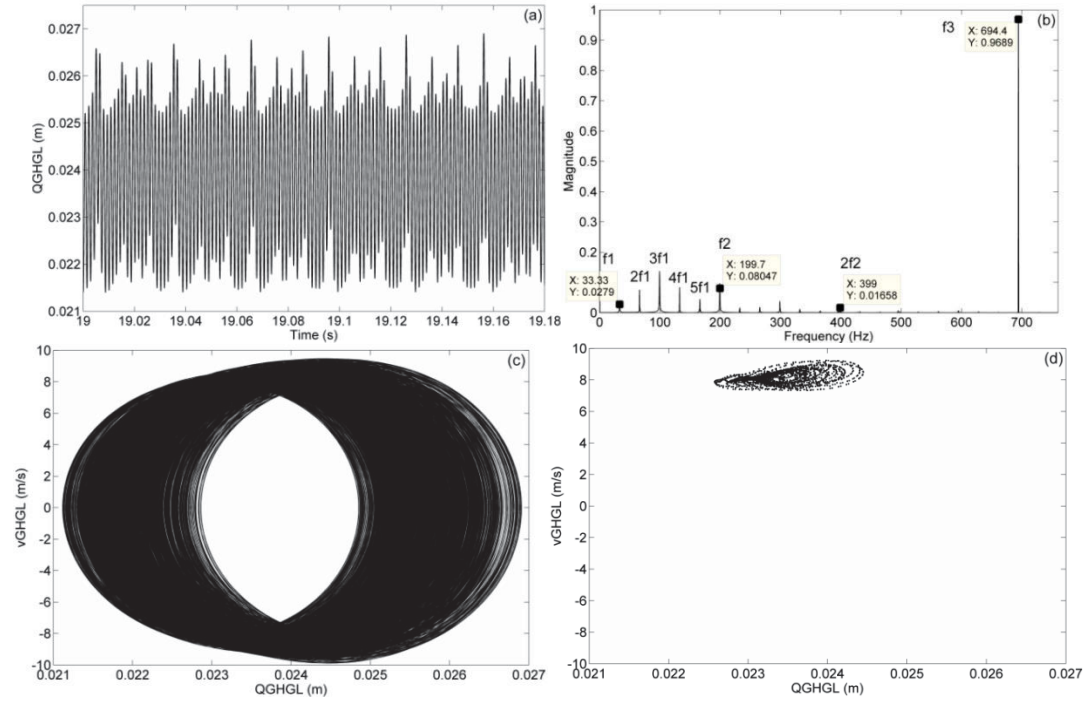

Figure 4.16. The vibrational responses of $\boldsymbol{Q_{GHGL}}$ caused by $\boldsymbol{K_m/K_a = 2}$ (a) Time histories (b) FFT spectrum (c) Phase Portrait (d) Poincare map

4.4.3 Mean-to-alternating force ratio F_m/F_a

This section studies the effect of the external excitation on Q_{rp_H} by setting the mean-to-alternating force ratio F_m/F_a to be 100, 10 and 1.67, respectively. The fluctuation of both the internal and external excitations is considered. As shown in Equation (4.20), the fluctuating external force F_{ae} is adjusted to vary the value of the mean-to-alternating force ratio F_m/F_a while the mean component F_{me} remains constant.

When the mean-to-alternating force ratio F_m/F_a is 100, the dynamic response of Q_{rp_H} is shown in Figure 4.17. Both the external excitation frequency f_e and meshing frequency f_2 affect the responses of Q_{rp_H}, as shown in Figure 4.17(b), and the effects of them cannot be ignored. This results in shifts on the phase portrait and Poincare map. It can be noted that the responses of Q_{rp_H} do not repeat themselves, and thus become quasi-periodic.

Compared with the dynamic response of Q_{rp_H}, a simpler pattern of the dynamic response of Q_{GHGL} is observed in Figure 4.18. The external excitation frequency f_e has the most influence on Q_{GHGL}, as the frequency component f_e is much larger than the other frequency component f_2 and f_3. Due to the large influence of f_e, shifts of points on the phase portrait and Poincare map are observed, and thus the dynamic response is quasi-periodic.

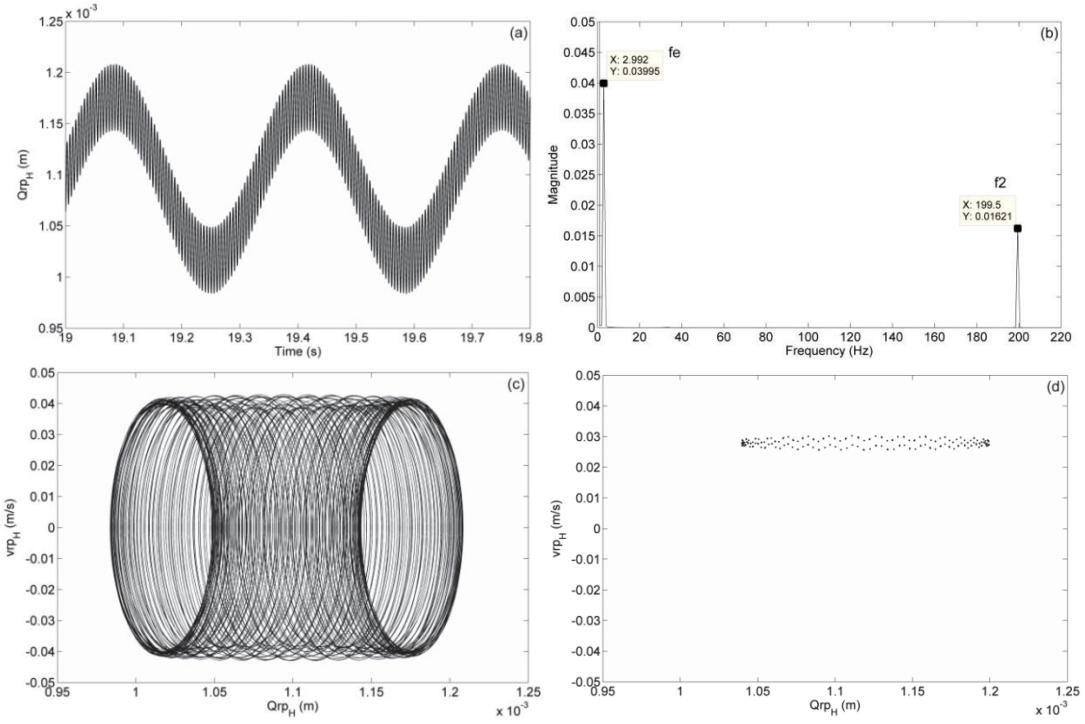

Figure 4.17. The vibrational responses of $\boldsymbol{Q_{rp\_H}}$ caused by $\boldsymbol{F_m/F_a = 100}$ (a) Time histories (b) FFT spectrum (c) Phase Portrait (d) Poincare map

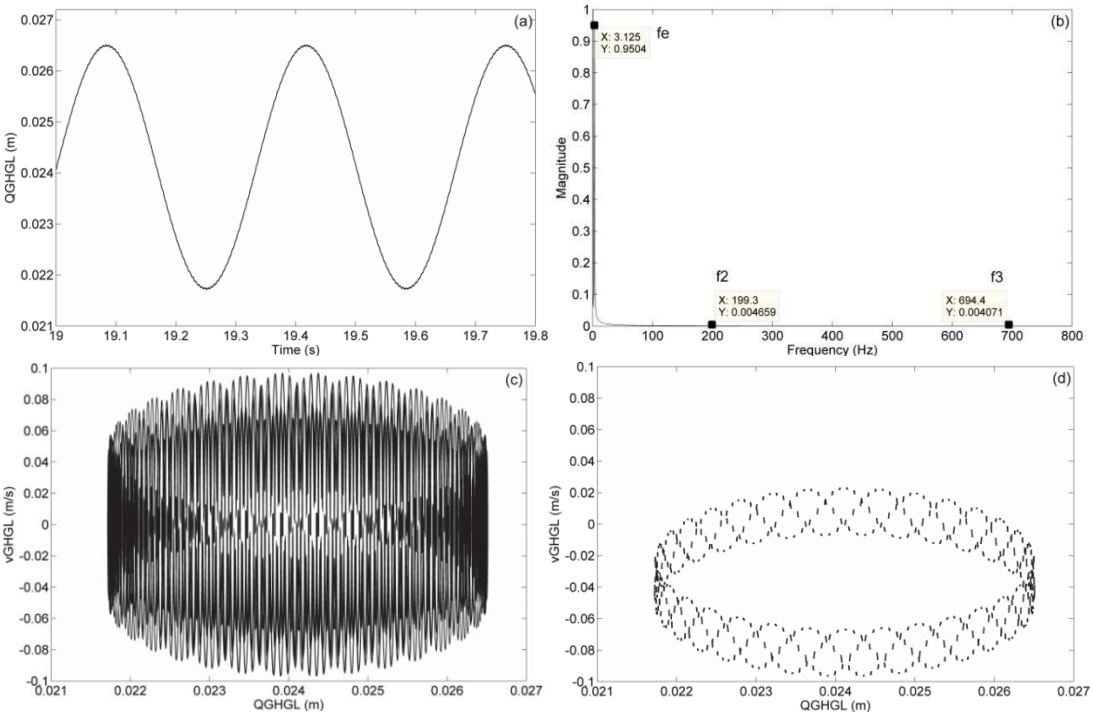

Figure 4.18. The vibrational responses of $\boldsymbol{Q_{GHGL}}$ caused by $\boldsymbol{F_m/F_a = 100}$ (a) Time histories (b) FFT spectrum (c) Phase Portrait (d) Poincare map

When the mean-to-alternating force ratio F_m/F_a is 10, the dynamic response of Q_{rp_H} is shown in Figure 4.19. Both frequencies f_e and f_2 affect the responses of X_{rp_H}, and the effects of them cannot be ignored, as shown in Figure 4.19(b). This results in shifts on the phase portrait and Poincare map. It can be noted that the responses of Q_{rp_H} do not repeat themselves, and thus become quasi-periodic.

Compared with the dynamic response of Q_{rp_H}, it shows a simpler pattern of the dynamic response of Q_{GHGL} in Figures 4.20(a) and 4.20(b). The external excitation frequency f_e has the major influence on Q_{GHGL}, as the frequency component f_e is obviously larger than the other frequency component f_2. Due to the large influence of f_e, it results in shifts on the phase portrait and Poincare map, and thus become quasi-periodic.

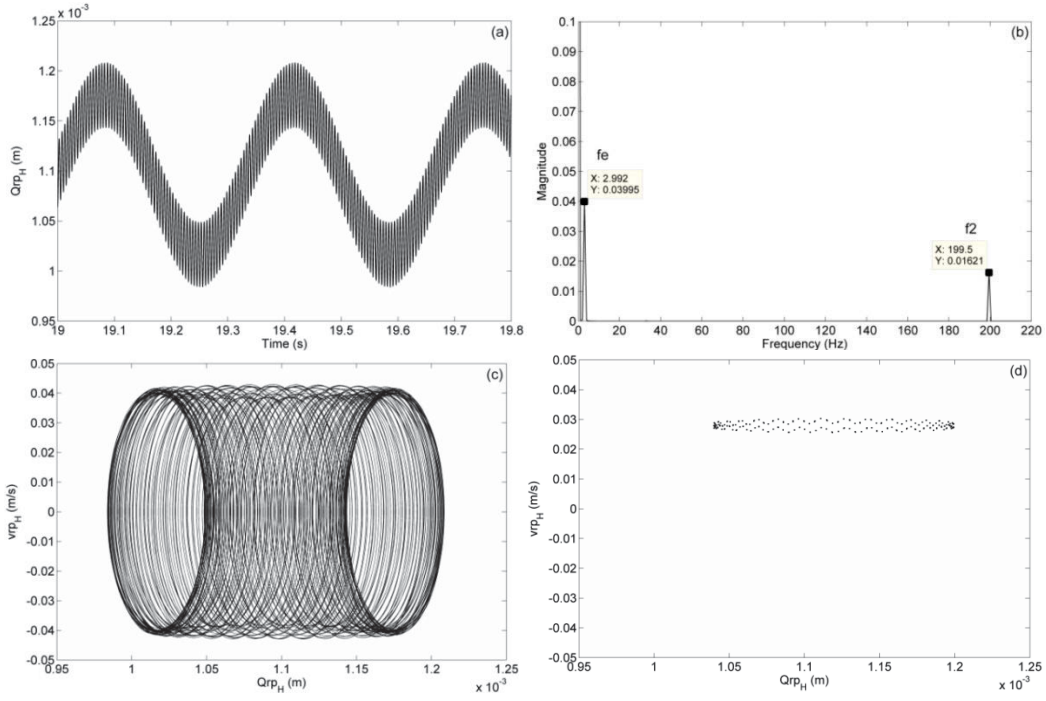

Figure 4.19. The vibrational responses of $\boldsymbol{Q_{rp\_H}}$ caused by $\boldsymbol{F_m/F_a = 10}$ (a) Time histories (b) FFT spectrum (c) Phase Portrait (d) Poincare map

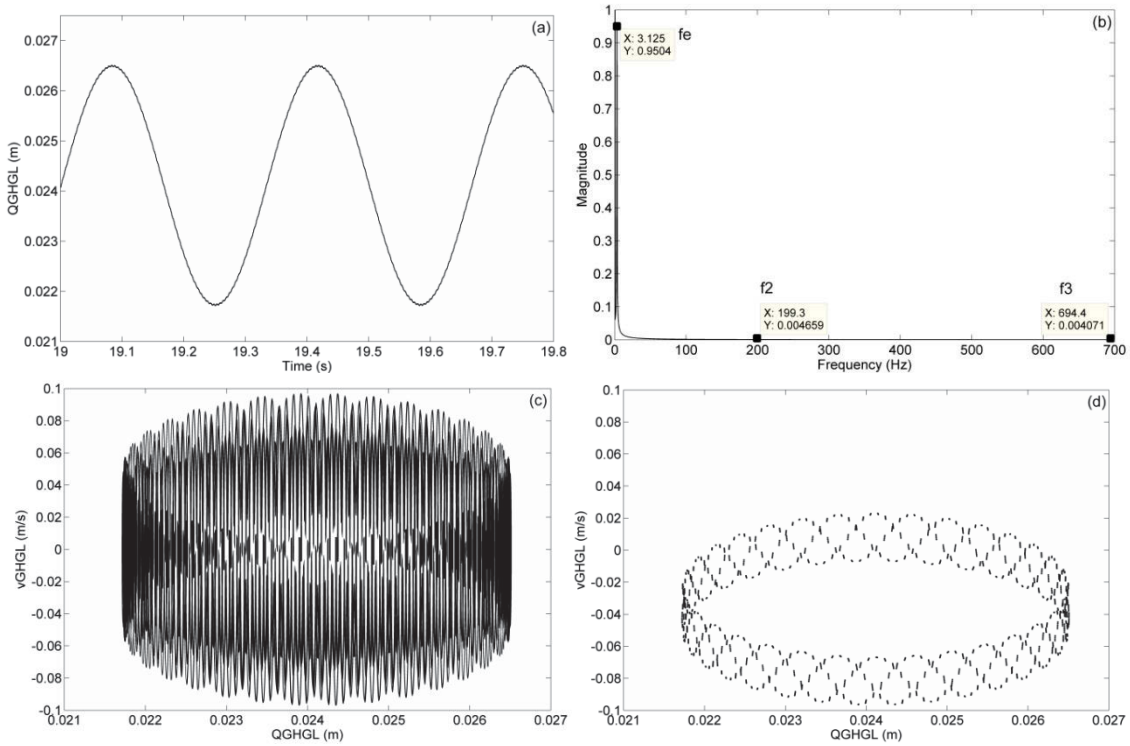

Figure 4.20. The vibrational responses of $\boldsymbol{Q_{GHGL}}$ caused by $\boldsymbol{F_m/F_a = 10}$ (a) Time histories (b) FFT spectrum (c) Phase Portrait (d) Poincare map

When the mean-to-alternating force ratio F_m/F_a is reduced to 1.67, the fluctuating external load F_a plays a more important role on the effect on Q_{rp_H}, as shown in Figure 4.21. It is observed that the low frequency external excitation frequency f_e contributes the most as shown in Figure 4.21(b), and the external excitation influences the responses more compared with the internal excitations. This results in shifts in phase portrait and Poincare map, and indicates that the response of Q_{rp_H} is quasi-periodic.

For the dynamic response of Q_{GHGL} shown in Figure 4.22, the external excitation frequency f_e has the major influence on Q_{GHGL}, and the effect of the internal excitations becomes minor and can be ignored. It results in shifts on the phase portrait and Poincare map due to the effects of f_e, and become quasi-periodic.

In short, the time histories and FFT spectrums of Q_{rp_H} have shown the stability when the mean-to-alternating force ratio is large. As the mean-to-alternating force ratio F_m/F_a is decreased by increasing the fluctuating component F_{ae}, the magnitude of the responses varies significantly. The external excitation plays an important role on wind turbine gearbox, especially when a sudden change of external excitation occurs, which indicates that the dynamic responses of wind turbine gears can be affected and may lead to gear wear [156].

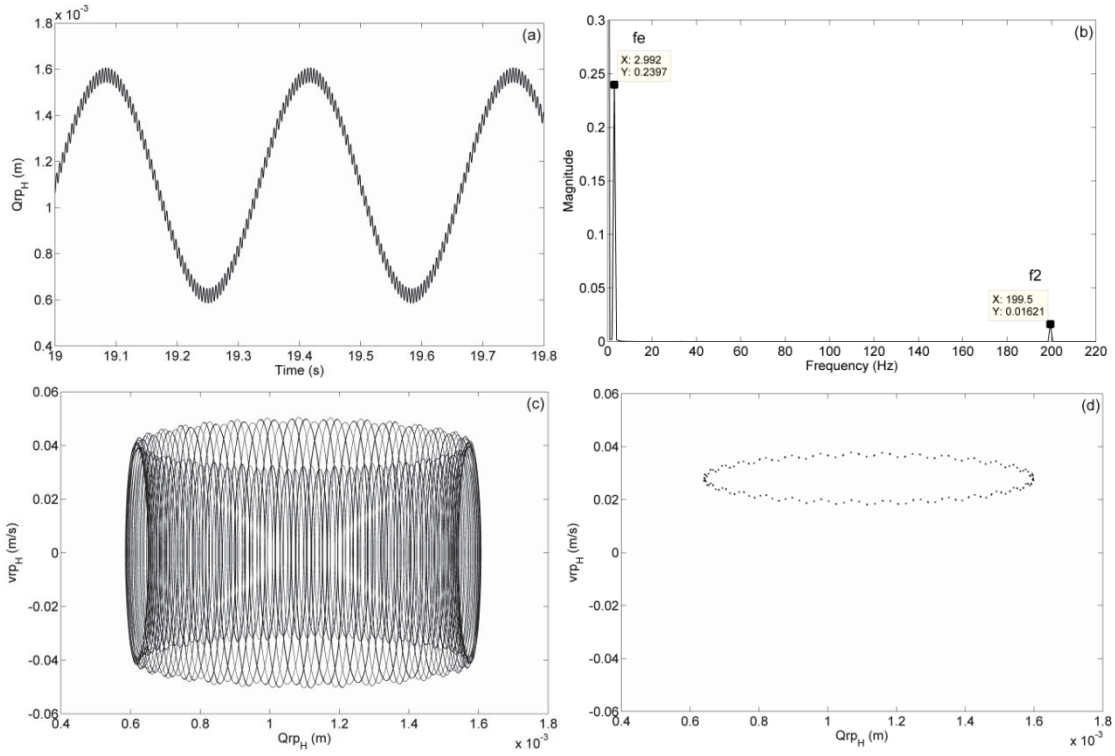

Figure 4.21. The vibrational responses of $\boldsymbol{Q_{rp\_H}}$ caused by $\boldsymbol{F_m/F_a = 1.67}$ (a) Time histories (b) FFT spectrum (c) Phase Portrait (d) Poincare map

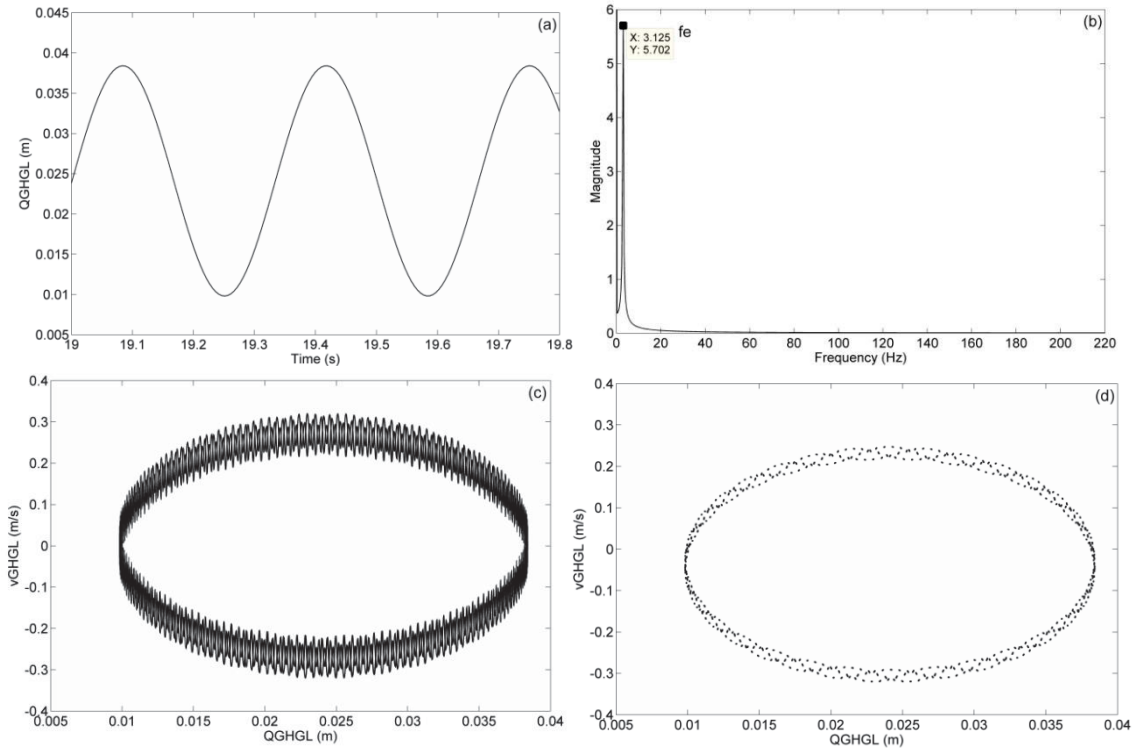

Figure 4.22. The vibrational responses of $\boldsymbol{Q_{GHGL}}$ caused by $\boldsymbol{F_m/F_a = 1.67}$ (a) Time histories (b) FFT spectrum (c) Phase Portrait (d) Poincare map

4.5 Discussions

The torsional dynamic model of a wind turbine gearbox is presented in this chapter by considering the time-varying mesh stiffness, damping, static transmission error and gear backlash. Dynamic responses of gearbox internal components are predicted with the variations of the static transmission error, mean-to-alternating mesh stiffness ratio and mean-to-alternating force ratio.

It was shown from the study of the mean-to-alternating force ratio that the external excitation has more effect than internal excitations on the torsional vibrations of the wind turbine gearbox components. This agrees with the observations that the low-frequency external excitations have a greater contribution to the dynamic response,

rather than the high-frequency internal excitation from gear meshing [43]. The increase of the external excitation fluctuation would lead to the large magnitude variation for gearbox components. In addition, when compared to the static transmission error, the gear mesh stiffness was found to have more effect on the torsional vibrations of gearbox components. Furthermore, the increase of the fluctuating mesh stiffness could change the dynamic responses significantly.

This page intentionally left blank

Chapter 5 Dynamic response of a 4DOF wind turbine gearbox

This chapter studies the dynamic response of a 4DOF dynamic model of a wind turbine gearbox under different excitation conditions. The proposed model would be developed based on the previous torsional model, described in Chapter 4, and takes into account the key factors such as the static transmission error, time-varying mesh stiffness, bearing stiffness, damping and gear backlash. Both the external excitation due to wind and the internal excitation due to the static transmission error are included to represent the gearbox excitation conditions. Three excitation conditions would be presented: the external excitation only condition, the internal and constant external excitation condition; and the internal and fluctuating external excitation condition.

5.1 Modelling

In the proposed gearbox model as shown in Figure 5.1, three gear stages are presented: the low-speed planetary gear stage, the intermediate parallel gear stage and the high-speed parallel gear stage. Theoretically, the aerodynamic loadings are mostly absorbed by the main shaft bearings, and thus have no influence on the gear teeth except for the driving torque. Therefore, the input load of the proposed dynamic model is limited to the torsional load only, and assumed to be applied directly to the planet carrier arm, which transmits the load to planet gears and the sun pinion. The non-torsional loads are assumed to be uncoupled with the gearbox.

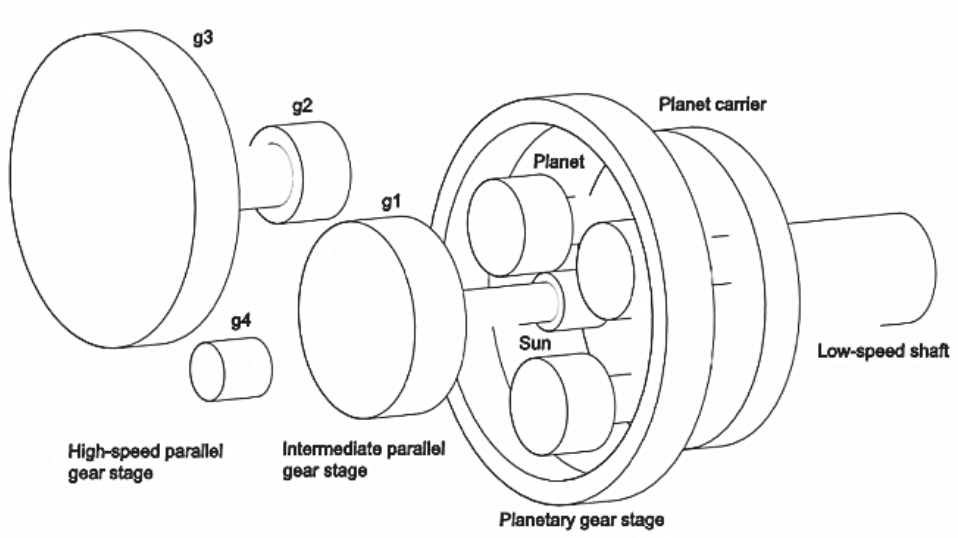

Figure 5.1. Sketch of the proposed wind turbine gearbox

The planetary gear stage includes three moving components: the planet carrier arm, planet gears and the sun pinion. The gearbox housing, planet carrier arm and bedplate are assumed to be rigid, and no relative movements between shafts are allowed. Planetary gears would provide high power density, by splitting the driving torque into multiple parallel sun-planet and ring-planet loads. The planet gears are supported on the planet carrier arm by shafts with bearings, thus the planet gears can rotate freely, and split the input load to reduce the load transmitted at each gear mesh. At parallel gear stages, the gears and pinions are also mounted between bearings [76, 77].

The proposed model can be used to predict the dynamic response of wind turbine gearbox components. Both the low-frequency excitation due to wind fluctuations and the high-frequency excitation due to static transmission errors are considered. The external excitation fluctuation is caused by wind, whereas the static transmission error is the overall kinetic error of gear pairs during gear meshes, expressed in the form of periodically time-varying displacement functions [176]. This model also takes into

account the key factors such as the time-varying mesh stiffness, bearing stiffness, damping and gear backlash. The time-varying mesh stiffness, as an important source of the internal excitation, fluctuates as the number of gears' contacting teeth changes during gear meshes.

The gearbox is mounted with a three-point configuration in which torsional loads are transferred to the gearbox housing through two torque arms, and it is assumed that the non-torque moments and forces are reacted mostly at the main bearing. Each torque arm transfers loads by means of an elastomeric bearing supported by mounts that help isolate and reduce noise. The ring gear serves as part of the gearbox housing, and the sun pinion is set in a floating configuration to equalize the load distribution among the planets [57, 59].

5.2 Derivation of equations

For the derivation of the equations of motions of the wind turbine gearbox components, a lumped-parameter model of a ring-planet-sun gear pair is previously illustrated in Figure 4.3. The gear deformation during gear meshes is represented by the time-varying gear mesh stiffness, damping and the static transmission error. All gears are helical gears in the proposed model, with the helical angle and pressure angle of each gear tooth remaining constant, and are allowed to rotate freely during turbine operation.

Based on the geometry of gears, the base radius of gears is determined by Equation (5.1), where r_{bu} denotes the base radius of gears, r_u denotes the radius of gears and α is the pressure angles.

$$r_{bu} = r_u \cos \alpha \tag{5.1}$$

The equivalent transverse displacements of the gearbox components along the line of action, caused by their rotational displacements, are determined by Equation (5.2).

$$Q_u = r_{bu}\theta_u \tag{5.2}$$

The relative displacement of sun-planet gear mesh on the line of action, caused by rotation, can be expressed as

$$Q_{spn\_\theta} = \left(Q_s - Q_{pn} - Q_c\right) \cos \beta_s \tag{5.3a}$$

The relative displacement of sun-planet gear mesh on the line of action, caused by the translational motions, can be given by

$$Q_{spn\_r} = \left\{x_s \sin \alpha + y_s \cos \alpha - x_{pn} \sin \alpha - y_{pn} \cos \alpha - x_c \sin \alpha - y_c \cos \alpha\right\} \cos \beta_p + \left(z_s - z_{pn} - z_c\right) \sin \beta_s \tag{5.3b}$$

Combining Equations 5.3(a) and 5.3(b), and taking into account the effect of the static transmission error e_{sp}, yields the total relative displacement of sun-planet gear mesh on the line of action, as shown in Equation (5.3c).

$$Q_{spn} = Q_{spn\_\theta} + Q_{spn\_r} - e_{sp} \tag{5.3c}$$

Similarly, the relative displacement of ring-planet gear mesh on the line of action, caused by rotation, can be written as

$$Q_{rpn\_\theta} = \left(Q_{pn} - Q_c\right)\cos\beta_p \qquad (5.4a)$$

The relative displacement of ring-planet gear mesh on the line of action, caused by the translational motions, can be expressed as

$$Q_{rpn\_r} = \left(x_{pn}\sin\alpha + y_{pn}\cos\alpha - x_c\sin\alpha - y_c\cos\alpha\right)\cos\beta_p + \left(z_{pn} - z_c\right)\sin\beta_s \qquad (5.4b)$$

By taking into account the static transmission error of the ring-planet gear mesh, the total relative displacement is

$$Q_{rpn} = Q_{rpn\_\theta} + Q_{rpn\_r} - e_{rp} \qquad (5.4c)$$

The relative displacement between the sun pinion and the gear of the intermediate parallel gear stage can be calculated by

$$Q_{sg1} = Q_{g1} - Q_s \qquad (5.5)$$

The relative displacement of the gear pair at the intermediate parallel gear stage, caused by rotation, can be expressed by

$$Q_{g1g2\_\theta} = \left(Q_{g2} - Q_{g1}\right)\cos\beta_g \qquad (5.6a)$$

The relative displacement of gear pair, caused by the translational motions, is given by

$$Q_{g1g2\_r} = \left(x_{g_2}\sin\alpha + y_{g_2}\cos\alpha - x_{g_1}\sin\alpha - y_{g_1}\cos\alpha\right)\cos\beta_g + \left(z_{g_2} - z_{g_1}\right)\sin\beta_s \qquad (5.6b)$$

By considering the static transmission error between the gear and pinion, the total relative displacement becomes

$$Q_{g1g2} = Q_{g1g2\_\theta} + Q_{g1g2\_r} - e_{g1g2} \qquad (5.6c)$$

The relative displacement between the gears $g2$ and $g3$ can be obtained by

$$Q_{g2g3} = Q_{g3} - Q_{g2} \qquad (5.7)$$

For the high-speed parallel gear stage, the relative displacement of the gear mesh on the line of action, caused by rotation, can be written as

$$Q_{g3g4\_\theta} = \left(Q_{g4} - Q_{g3}\right)\cos\beta_g \qquad (5.8a)$$

The relative displacement of gear pairs on the line of action, caused by the translational motions, can be expressed by

$$Q_{g3g4\_r} = \left(x_{g_4} \sin\alpha + y_{g_4} \cos\alpha - x_{g_3} \sin\alpha - y_{g_3} \cos\alpha\right) \cos\beta_g + \left(z_{g_4} - z_{g_3}\right) \sin\beta_s \quad (5.8b)$$

By including the static transmission error between the gear and pinion, the total relative displacement is

$$Q_{g3g4} = Q_{g3g4\_\theta} + Q_{g3g4\_r} - e_{g3g4} \quad (5.8c)$$

The meshing forces of gear pairs can be determined based on the relative displacements of gear meshes Q_i[6]. By considering the gear backlash, the meshing forces of gear pairs can be calculated by Equations (5.9) and (5.10), where k_i represents the gear mesh stiffness, and $f\left(Q_j\right)$ given by Equation (5.9) is the vector form of the nonlinear gear mesh displacement function. The gear mesh stiffness is obtained by using the method described in Section 4.3.3. Damping forces can be calculated in a similar way.

$$f\left(Q_j\right) = \begin{cases} Q_j - b, & Q_j > b \\ 0, & -b \le Q_j \le b \\ Q_j + b, & Q_j < -b \end{cases} \quad (5.9)$$

$$F_{Q_i} = k_i f(Q_i);\ n = 1,2,3 \quad (5.10)$$

The equations of motion of the gearbox components can be obtained by applying the Newton's laws. For the planet carrier arm, the equations of motion are given by

[6] Q_i represents Q_{rpn}, Q_{spn}, Q_{g1g2} and Q_{g3g4}, where $n = 1,2,3$

$$\left(I_c + 3m_p{}^2\right)\ddot{\theta}_c + \sum_{n=1}^{3}\left(k_{sp}f(Q_{spn}) + c_{sp}\dot{Q}_{spn}\right)\cos\beta_s\, r_{bC} + \sum_{n=1}^{3}\left(k_{rp}f(Q_{rpn}) + c_{rp}\dot{Q}_{rpn}\right)\cos\beta_s\, r_{bC} = T_{in} \quad (5.11a)$$

$$m_c\ddot{x}_c + \left[\sum_{n=1}^{3}\left(k_{sp}f(Q_{spn}) + c_{sp}\dot{Q}_{spn}\right) + \sum_{n=1}^{3}\left(k_{rp}f\left(Q_{rpn}\right) + c_{rp}\dot{Q}_{rpn}\right)\right]\cos\beta_s \sin\alpha - k_{cx}x_c - c_{cx}\dot{x}_c = 0 \quad (5.11b)$$

$$m_c\ddot{y}_c + \left[\sum_{n=1}^{3}\left(k_{sp}f(Q_{spn}) + c_{sp}\dot{Q}_{spn}\right) + \sum_{n=1}^{3}\left(k_{rp}f\left(Q_{rpn}\right) + c_{rp}\dot{Q}_{rpn}\right)\right]\cos\beta_s \cos\alpha - k_{cy}y_c - c_{cy}\dot{y}_c = 0 \quad (5.11c)$$

$$m_c\ddot{z}_c + \left[\sum_{n=1}^{3}\left(k_{sp}f(Q_{spn}) + c_{sp}\dot{Q}_{spn}\right) - \sum_{n=1}^{3}\left(k_{rp}f\left(Q_{rpn}\right) + c_{rp}\dot{Q}_{rpn}\right)\right]\sin\beta_s - k_{cz}z_c - c_{cz}\dot{z}_c = 0 \quad (5.11d)$$

For the sun pinion, the equations of motion are

$$I_s\ddot{\theta}_s - \sum_{n=1}^{3}\left(k_{sp}f(Q_{spn}) + c_{sp}\dot{Q}_{spn}\right)\cos\beta_s\, r_{bs} + \left(k_{sg1}Q_{sg1} + c_{sg1}\dot{Q}_{sg1}\right)\cos\beta_s\, r_{bs} = 0 \quad (5.12a)$$

$$m_s\ddot{x}_s - \sum_{n=1}^{3}\left(k_{sp}f(Q_{spn}) + c_{sp}\dot{Q}_{spn}\right)\cos\beta_s \sin\alpha + k_{sx}x_s + c_{sx}\dot{x}_s = 0 \quad (5.12b)$$

$$m_s\ddot{y}_s - \sum_{n=1}^{3}\left(k_{sp}f(Q_{sp}) + c_{sp}\dot{Q}_{spn}\right)\cos\beta_s \cos\alpha + k_{sy}y_s + c_{sy}\dot{y}_s = 0 \quad (5.12c)$$

$$m_s\ddot{z}_s - \sum_{n=1}^{3}\left(k_{sp}f(Q_{spn}) + c_{sp}\dot{Q}_{spn}\right)\sin\beta_s + k_{sz}z_s + c_{sz}\dot{z}_s = 0 \quad (5.12d)$$

For the planet gears, the equations of motion are given by

$$I_p\ddot{\theta}_{pn} - \left(k_{rp}f(Q_{rpn}) + c_{rp}\dot{Q}_{rpn}\right)cos\,\beta_p + \left(k_{sp}f(Q_{spn}) + c_{sp}\dot{Q}_{spn}\right)cos\,\beta_p = 0 \quad (5.13a)$$

$$m_p\ddot{x}_{pn} - \left[\left(k_{rp}f\left(Q_{rpn}\right) + c_{rp}\dot{Q}_{rpn}\right) - \left(k_{sp}f(Q_{spn}) + c_{sp}\dot{Q}_{spn}\right)\right]cos\,\beta_p\,sin\,\alpha + k_{px}x_{pn} + c_{px}\dot{x}_{pn} = 0 \quad (5.13b)$$

$$m_p\ddot{y}_{pn} - \left[\left(k_{rp}f\left(Q_{rpn}\right) + c_{rp}\dot{Q}_{rpn}\right) - \left(k_{sp}f(Q_{spn}) + c_{sp}\dot{Q}_{spn}\right)\right]cos\,\beta_p\,cos\,\alpha + k_{py}y_{pn} + c_{py}\dot{y}_{pn} = 0 \quad (5.13c)$$

$$m_p\ddot{z}_{pn} - \left[\left(k_{rp}f\left(Q_{rpn}\right) + c_{rp}\dot{Q}_{rpn}\right) - \left(k_{sp}f(Q_{spn}) + c_{sp}\dot{Q}_{spn}\right)\right]sin\,\beta_p + k_{pz}z_{pn} + c_{pz}\dot{z}_{pn} = 0 \quad (5.13d)$$

For the gear g_1 at the intermediate parallel gear stage, the equations of motion are written as

$$I_{g1}\ddot{\theta}_{g1} + \left(k_{g1g2}f(Q_{g1g2}) + c_{g1g2}\dot{Q}_{g1g2}\right)cos\,\beta_g\,r_{bg1} - \left(k_{sg1}Q_{sg1} + c_{sg1}\dot{Q}_{sg1}\right)r_{bg1} = 0 \quad (5.14a)$$

$$m_{g1}\ddot{x}_{g1} + \left(k_{g1g2}f(Q_{g1g2}) + c_{g1g2}\dot{Q}_{g1g2}\right)\cos\beta_g\,\sin\alpha - k_{g1x}x_{g1} - c_{g1x}\dot{x}_{g1} = 0 \quad (5.14b)$$

$$m_{g1}\ddot{y}_{g1} + \left(k_{g1g2}f(Q_{g1g2}) + c_{g1g2}\dot{Q}_{g1g2}\right)\cos\beta_g\,\cos\alpha - k_{g1y}y_{g1} - c_{g1y}\dot{y}_{g1} = 0 \quad (5.14c)$$

$$m_{g1}\ddot{z}_{g1} + \left(k_{g1g2}f(Q_{g1g2}) + c_{g1g2}\dot{Q}_{g1g2}\right)\sin\beta_g - k_{g1z}z_{g1} - c_{g1z}\dot{z}_{g1} = 0 \quad (5.14d)$$

For the pinion g_2 at the intermediate parallel gear stage, the equations of motion are expressed as

$$I_{g2}\ddot{\theta}_{g2} - \left(k_{g1g2}f\left(Q_{g1g2}\right) + c_{g1g2}\dot{Q}_{g1g2}\right)cos\,\beta_g + k_{g2g3}r_{bg2} + \left(k_{g2g3}Q_{g2g3} + c_{g2g3}\dot{Q}_{g2g3}\right)r_{bg2} = 0 \quad (5.15a)$$

$$m_{g2}\ddot{x}_{g2} - \left(k_{g1g2}f(Q_{g1g2}) + c_{g1g2}\dot{Q}_{g1g2}\right)\cos\beta_g \sin\alpha + k_{g2x}x_{g2} + c_{g2x}\dot{x}_{g2} = 0 \quad (5.15b)$$

$$m_{g2}\ddot{y}_{g2} - \left(k_{g1g2}f(Q_{g1g2}) + c_{g1g2}\dot{Q}_{g1g2}\right)\cos\beta_g \cos\alpha + k_{g2y}y_{g2} + c_{g2y}\dot{y}_{g2} = 0 \quad (5.15c)$$

$$m_{g2}\ddot{z}_{g2} - \left(k_{g1g2}f(Q_{g1g2}) + c_{g1g2}\dot{Q}_{g1g2}\right)\sin\beta_g + k_{g2z}z_{g2} + c_{g2z}\dot{z}_{g2} = 0 \quad (5.15d)$$

For the gear g_3 at the high-speed parallel gear stage, the equations of motion are obtained as

$$I_{g3}\ddot{\theta}_{g3} + \left(k_{g3g4}f(Q_{g3g4}) + c_{g3g4}\dot{Q}_{g3g4}\right)cos\,\beta_g\, r_{bg3} - \left(k_{g2g3}Q_{g2g3} + c_{g2g3}\dot{Q}_{g2g3}\right)r_{bg3} = 0 \quad (5.16a)$$

$$m_{g3}\ddot{x}_{g3} + \left(k_{g3g4}f(Q_{g3g4}) + c_{g3g4}\dot{Q}_{g3g4}\right)\cos\beta_g \sin\alpha - k_{g3x}x_{g3} - c_{g3x}\dot{x}_{g3} = 0 \quad (5.16b)$$

$$m_{g3}\ddot{y}_{g3} + \left(k_{g3g4}f(Q_{g3g4}) + c_{g3g4}\dot{Q}_{g3g4}\right)\cos\beta_g \cos\alpha - k_{g3y}y_{g3} - c_{g3y}\dot{y}_{g3} = 0 \quad (5.16c)$$

$$m_{g3}\ddot{z}_{g3} + \left(k_{g3g4}f(Q_{g3g4}) + c_{g3g4}\dot{Q}_{g3g4}\right)\sin\beta_g - k_{g3z}z_{g3} - c_{g3z}\dot{z}_{g3} = 0 \quad (5.16d)$$

For the pinion g_4 at the high-speed parallel gear stage, the equations of motion are given by

$$I_{g4}\ddot{\theta}_{g4} - \left(k_{g3g4}f(Q_{g3g4}) + c_{g3g4}\dot{Q}_{g3g4}\right) cos\,\beta_g\, r_{bg4} = -T_{out} \qquad (5.17a)$$

$$m_{g4}\ddot{x}_{g4} - \left(k_{g3g4}f(Q_{g3g4}) + c_{g3g4}\dot{Q}_{g3g4}\right)\cos\beta_g \sin\alpha + k_{g4x}x_{g4} + c_{g4x}\dot{x}_{g4} = 0 \qquad (5.17b)$$

$$m_{g4}\ddot{y}_{g4} - \left(k_{g3g4}f(Q_{g3g4}) + c_{g3g4}\dot{Q}_{g3g4}\right)\cos\beta_g \cos\alpha + k_{g4y}y_{g4} + c_{g4y}\dot{y}_{g4} = 0 \qquad (5.17c)$$

$$m_{g4}\ddot{z}_{g4} - \left(k_{g3g4}f(Q_{g3g4}) + c_{g3g4}\dot{Q}_{g3g4}\right)\sin\beta_g + k_{g4z}z_{g4} + c_{g4z}\dot{z}_{g4} = 0 \qquad (5.17d)$$

Substituting the relative displacements of gear meshes given by Equations (5.3) to (5.8) into Equations (5.11) to (5.17), yields the transverse and translational displacements of gears.

5.3 Specifications

The proposed 4DOF dynamic model of wind turbine gearbox in this chapter is an extended model based on the previous torsional model, described in Chapter 4. Thus, the general specifications used in the torsional model would be used in the present model. Therefore, the radius of the rotor blades r_{blade} is 36 m, the average wind speed V_{wind} is 16 m/s, the air density ρ_{air} is 1.21 kg/m^3, and the rotational speed of the rotor blades ω_{blade} is 17 rpm. When the rotational speed of the blades is set to be constant, the simulated wind fluctuation results in the fluctuation of the driving torque to the gearbox.

The gear teeth dimensions used for the proposed model are provided in Table 3, where "$7.5L$" and "$14.5R$" in Table 3 represent 7.5° facing left and 14.5° facing right.

Table 3. List of gears and specifications

Gears	Teeth	Module	P_d	$a\ (m)$	$b\ (m)$	$L\ (m)$	$h\ (m)$	$\beta\ (^{o})$
Ring	99	10	2.540	0.0100	0.0125	0.0225	0.0089	7.5L
Planet	39	10	2.540	0.0100	0.0125	0.0225	0.0187	7.5L
Sun	21	10	2.540	0.0100	0.0125	0.0225	0.0172	7.5L
g_1	82	8	3.175	0.0080	0.0100	0.0180	0.0149	14R
g_2	23	8	3.175	0.0080	0.0100	0.0180	0.0137	14L
g_3	76	5.5	4.618	0.0055	0.0069	0.0124	0.0103	14L
g_4	23	5.5	4.618	0.0055	0.0069	0.0124	0.0103	14R

The driving torque T_{in_avg}, that is applied to the planet carrier arm as the input to the system, can be calculated by Equations (4.21) to (4.23) [170]. If only the external excitation is considered, the driving torque can be expressed by Equation (5.18) as a periodic sinusoidal function, where T_{in_avg} is the constant external driving torque, T_{in_e} is the fluctuating external driving torque, and ω_e represents the external excitation frequency[7]. This usually happens when the wind turbine is parked. Under such a condition, the gears in the gearbox are not allowed to rotate.

$$T_{in}(t) = T_{in\_avg} + T_{in\_e}\, cos(\omega_e t) \qquad (5.18)$$

[7] $\omega_e = 2\pi f_e$ and $f_e = 6\,Hz$ (as in the low frequency range) is chosen to be the external excitation frequency.

It can be predicted that the external excitation results in low frequency responses, whereas the internal excitation results in high frequency responses. The static transmission error e_i used in Equations (5.3) to (5.8) is represented by Equation (4.17). As the static transmission error is very small, only the fluctuation term e_{aj} is considered. The high-frequency excitations at the meshing frequency ω_i are expected during gear mesh[8]. When only the internal excitation, caused by the static transmission error e_j, is considered, the internal excitation p_i is given by Equation (4.18). In addition, under the constant rotational speed the meshing frequencies of the wind turbine gearbox components remain constant during operation for the simplicity in simulation [168].

5.4 Results

This section presents the simulation results of the proposed gearbox model. The *ode45* solver in Matlab is used to solve the differential equations. The integration results of the first 1500 periods are discarded prior to recording the steady state solutions. For each meshing cycle, 3600 meshing points are sampled in order to capture the sufficient number of data. The analysis focuses on the effects of the excitation conditions on gears and bearings of the wind turbine gearbox with the help of the time histories and FFT spectrums.

5.4.1 External excitation only

When only the external excitation is considered and the gears are not allowed to rotate, such condition is similar to the situation when the wind turbine is parked. Figures 5.2 to

[8] $\omega_i = 2\pi f_i$ and the meshing frequencies f_i in the proposed dynamic model are 28.05 Hz, 132.8 Hz and 438.7 Hz.

5.6 show the dynamic responses of Q_{rp1}, Q_{sp1}, Q_{g1g2}, X_{g1a} and X_{g4a}, representing the relative displacements of the ring-planet gear meshes, the sun-planet gear meshes, parallel gear meshes, the axial displacement of the gear at the intermediate parallel gear stage and the axial displacement of the pinion at high-speed parallel gear stage.

It is observed that the frequency peak in each FFT spectrum occurs at the external excitation frequency f_e, which indicates that only the external excitation contributes to the vibrations in the gearbox, and the gearbox components only respond to the wind fluctuation. The time histories also show the stability of the dynamic responses of the gearbox components. The magnitude of Q_{rp1} is larger than Q_{sp1} and Q_{g1g2}, and much larger than that of X_{g1a} and X_{g4a}, meaning that the external excitation influences the most on the ring-planet gear meshes than sun-planet gear meshes and that of the parallel gear stage. Moreover, the relative displacement of the gear meshes caused by wind fluctuations is much larger than the axial displacement of the gear when the wind turbine is parked. These observations are in good agreements with Errichelo's findings that the fretting corrosion, as one of the wind turbine gearbox failure modes, normally occurs in gears along a line of action when the turbines are parked [177].

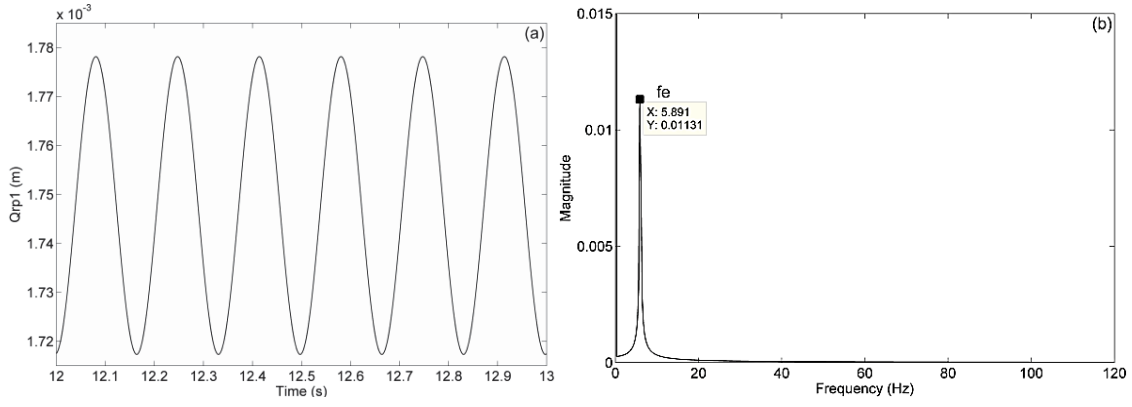

Figure 5.2. The vibrational responses of $\boldsymbol{Q_{rp1}}$ (a) Time histories (b) FFT spectrum

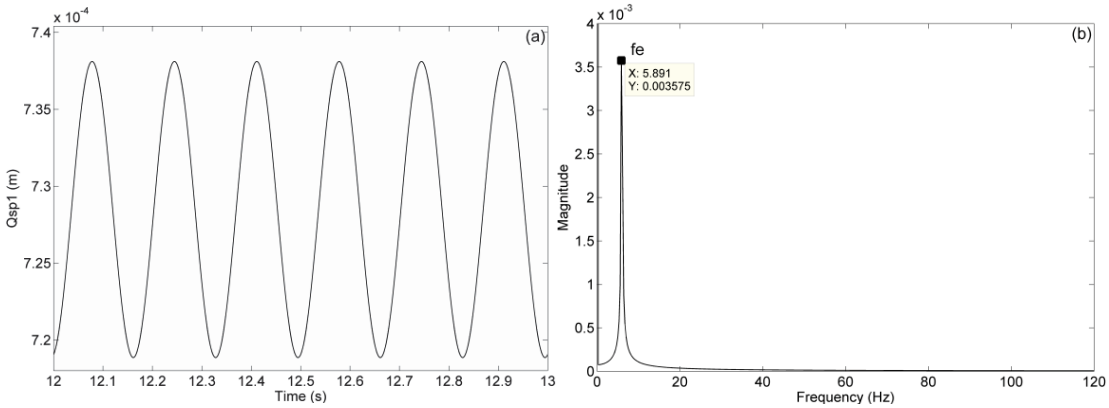

Figure 5.3. The vibrational responses of $\boldsymbol{Q_{sp1}}$ (a) Time histories (b) FFT spectrum

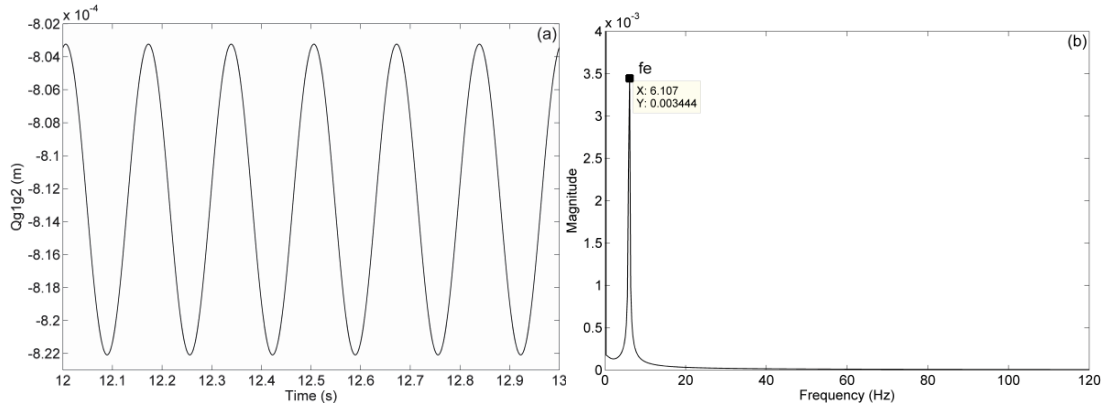

Figure 5.4. The vibrational responses of $\boldsymbol{Q_{g1g2}}$ (a) Time histories (b) FFT spectrum

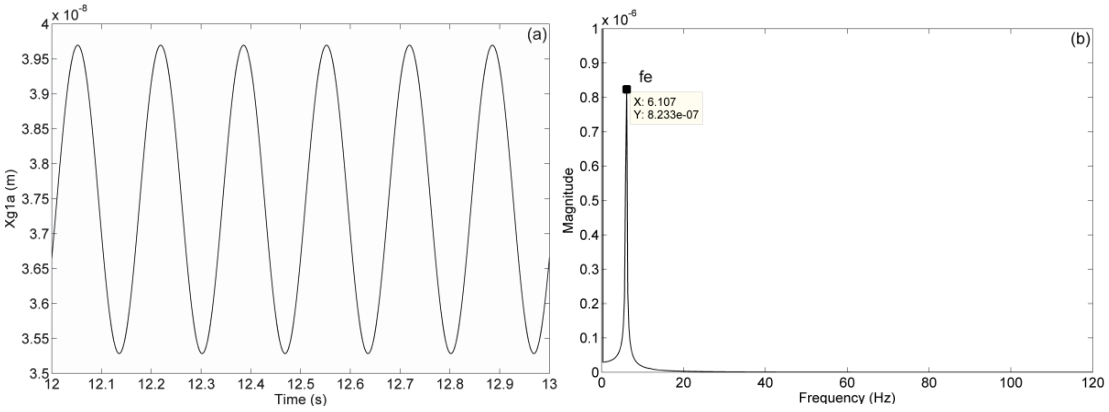

Figure 5.5. The axial vibrational responses $\boldsymbol{X_{g1a}}$ (a) Time histories (b) FFT spectrum

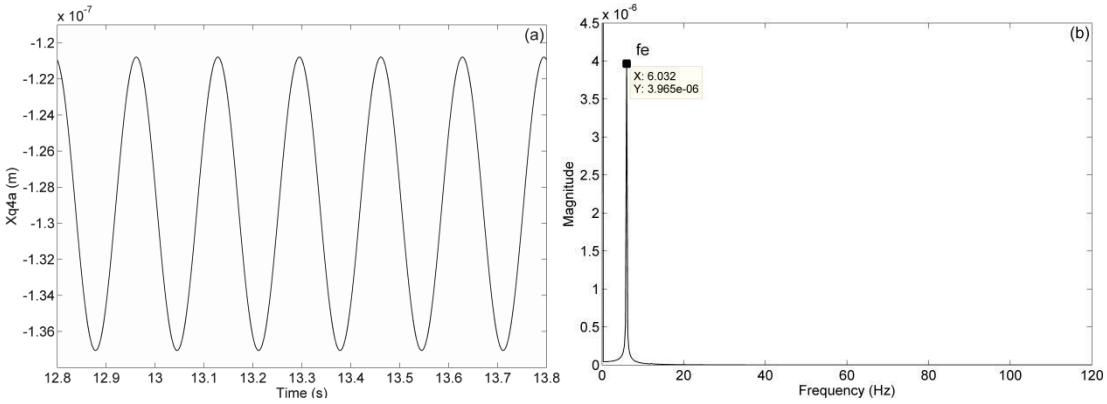

Figure 5.6. The axial vibrational responses $\boldsymbol{X_{g4a}}$ (a) Time histories (b) FFT spectrum

5.4.2 Constant external excitation

When both the internal and constant external excitations are considered, it is assumed that the turbine operates under an ideal condition. The external excitation is constantly applied to the gearbox, and the internal excitation, caused by the static transmission errors e_i, is assumed to fluctuate with the meshing frequencies ω_i. Figures 5.7 to 5.11 show the dynamic responses of Q_{rp1}, Q_{sp1}, Q_{g1g2}, X_{g1a} and X_{g4a}. The internal excitation provides high-frequency vibrations to the gearbox, thus, the dynamic responses under meshing frequencies ω_i are expected to be observed.

Figure 5.7 shows that Q_{rp1} is stable and the meshing frequency of the planetary gear stage f_1 contributes the most on Q_{rp1}, while the magnitude of f_2 is much smaller, thus the effect of it can be ignored. Compared with the dynamic responses of Q_{rp1}, the magnitude of the dynamic responses of Q_{sp1} and Q_{g1g2} are smaller. Similar to Q_{rp1}, the sun-planet gear meshes shown in Figure 5.8 fluctuate with the meshing frequency f_1, and the gear meshes at the parallel gear stage fluctuate with the meshing frequency f_2, as shown in Figure 5.9. The meshing frequencies at their own gear stages influence the

most. Figures 5.10 and 5.11 present the axial displacement of the gear at intermediate parallel gear stage and the pinion at high-speed parallel gear stage. The magnitudes of them are much smaller than that of the relative displacement of gear meshes, and the frequency peaks occur at their own gear stages.

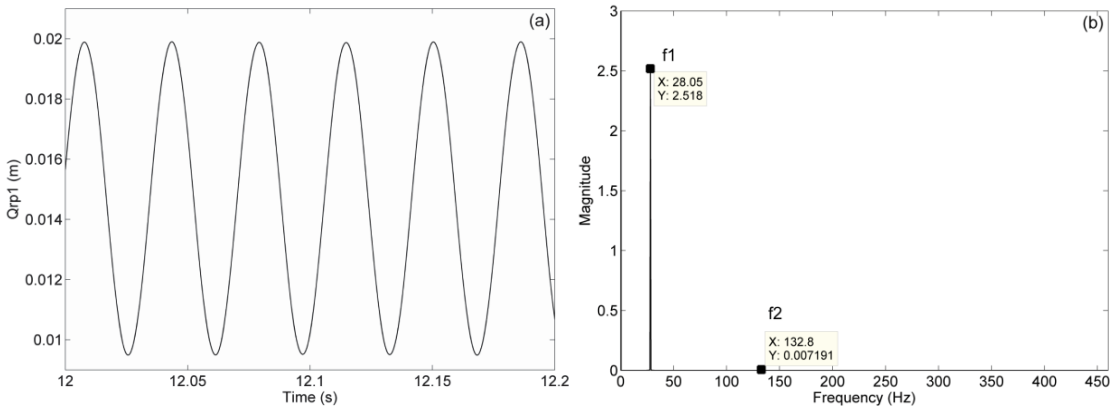

Figure 5.7. The vibrational responses of $\boldsymbol{Q_{rp1}}$ (a) Time histories (b) FFT spectrum

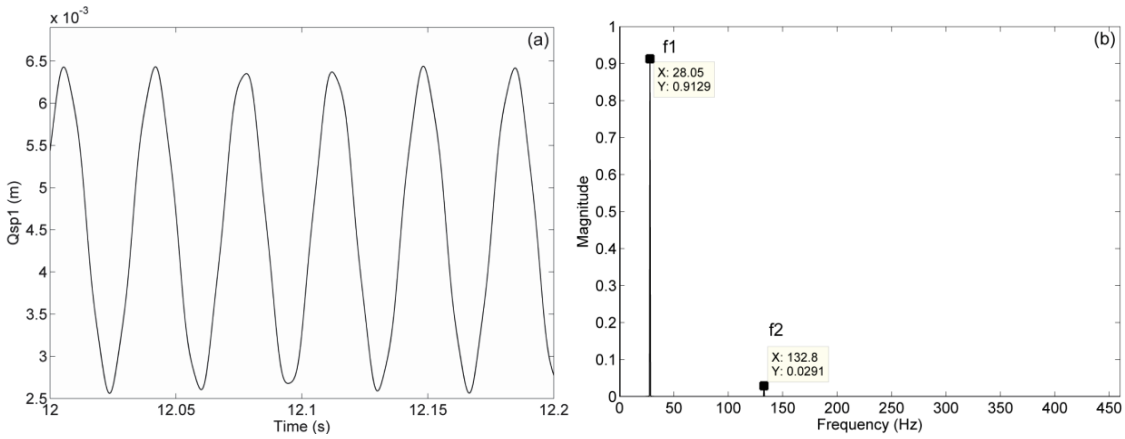

Figure 5.8. The vibrational responses of $\boldsymbol{Q_{sp1}}$(a) Time histories (b) FFT spectrum

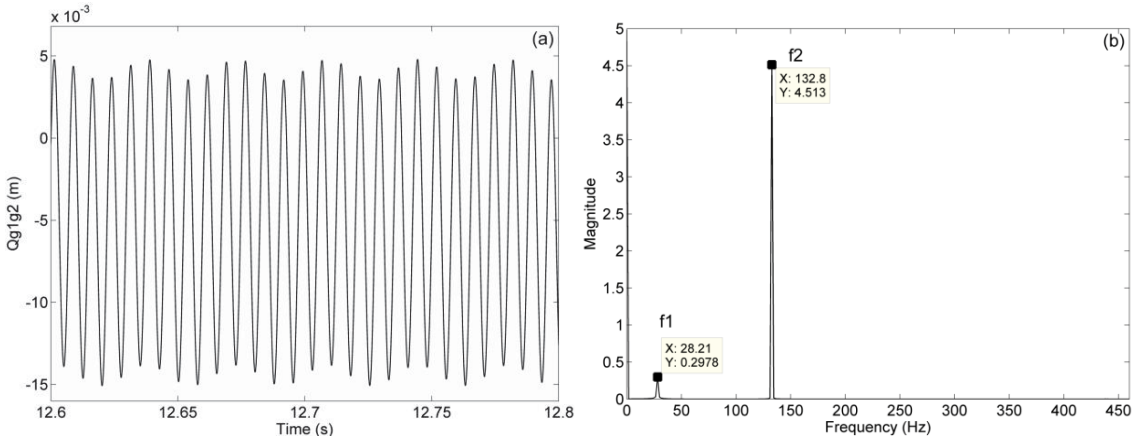

Figure 5.9. The vibrational responses of $\boldsymbol{Q_{g1g2}}$ (a) Time histories (b) FFT spectrum

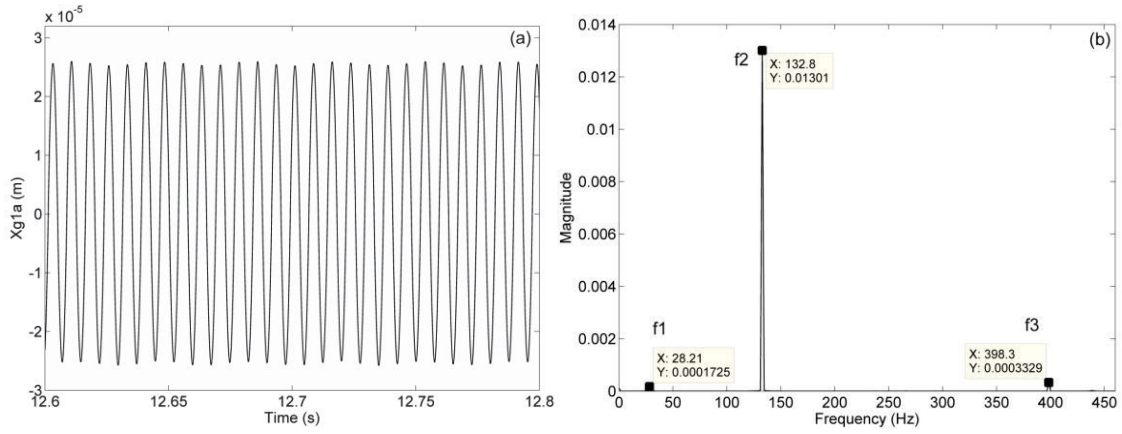

Figure 5.10. The axial vibrational responses $\boldsymbol{X_{g1a}}$ (a) Time histories (b) FFT spectrum

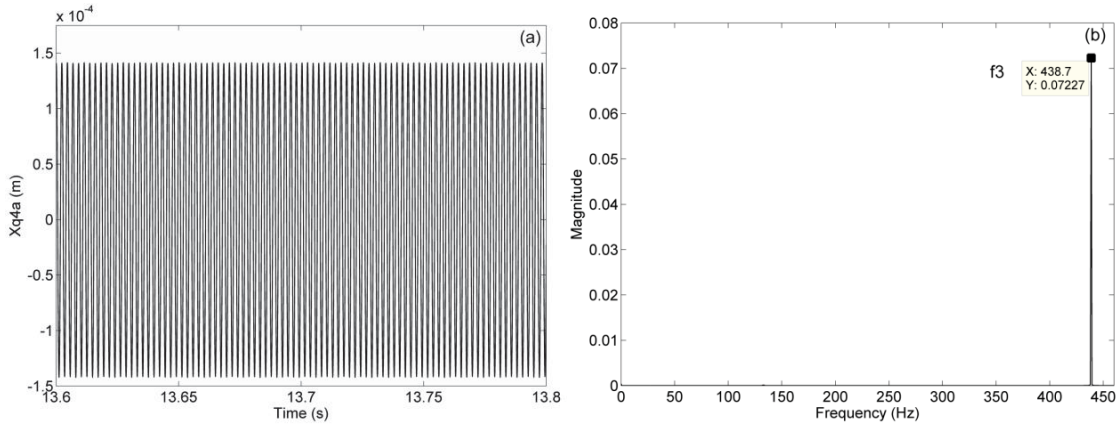

Figure 5.11. The vibrational responses $\boldsymbol{X_{g4a}}$ (a) Time histories (b) FFT spectrum

5.4.3 Mean-to-alternating force ratio F_m/F_a

When both the internal and external excitation fluctuations are taken into account, the effect of the wind fluctuation, the mean-to-fluctuating external force ratio F_m/F_a is used to study the dynamic responses of wind turbine gearbox components. Figures 5.12 to 5.16 show the dynamic responses of Q_{rp1}, Q_{sp1}, Q_{g1g2}, X_{g1a} and X_{g4a}.

As both the external excitation fluctuation (with the mean-to-fluctuating external force ratio of 5) and the internal excitation are considered, the dynamic responses with the external excitation frequency f_e and the meshing frequencies f_i are expected to be observed. It can be seen from Figure 5.12 that both the meshing frequencies and the external excitation frequency exist. The magnitude of the external frequency component f_e is smaller than the meshing frequency at its own gear stage f_1. The magnitudes of f_2 can be ignored. This indicates that the meshing frequency of the planetary gear stage f_1 contributes the most on Q_{rp1}. Figures 5.13 and 5.14 present the dynamic responses of Q_{sp1} and Q_{g1g2}. It is similar as that of Figure 5.12 that both the meshing frequencies and the external excitation frequency exist, and the relative displacement of gear meshes fluctuate at their own meshing frequencies, and having smaller magnitudes than that of the ring-planet gear meshes. The axial displacement of the gear and pinion at the intermediate and high-speed parallel gear stage (X_{g1a} and X_{g4a}) are shown in Figures 5.15 and 5.16.

In short, the gear meshes at all three gear stages are relatively stable when the external fluctuation is small. However, the harmonics and their sidebands exist on the dynamic

responses of the gears. When with the external fluctuations, the sidebands appeared in the FFT spectrum can be used to estimate the gear and bearing damage conditions.

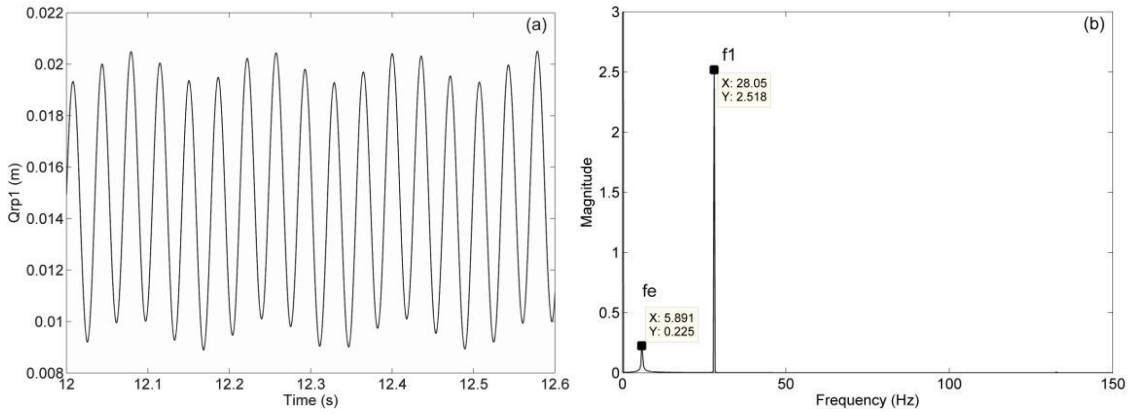

Figure 5.12. The vibrational responses of $\boldsymbol{Q_{rp1}}$ with the mean-to-fluctuating external force ratio $\boldsymbol{F_m/F_a}$ of 5 (a) Time histories (b) FFT spectrum

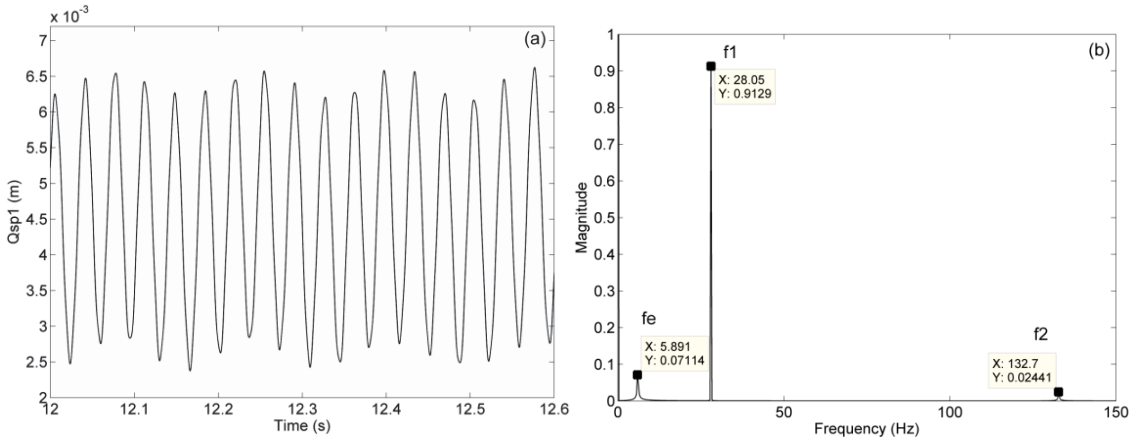

Figure 5.13. The vibrational responses of $\boldsymbol{Q_{sp1}}$ with the mean-to-fluctuating external force ratio $\boldsymbol{F_m/F_a}$ of 5 (a) Time histories (b) FFT spectrum

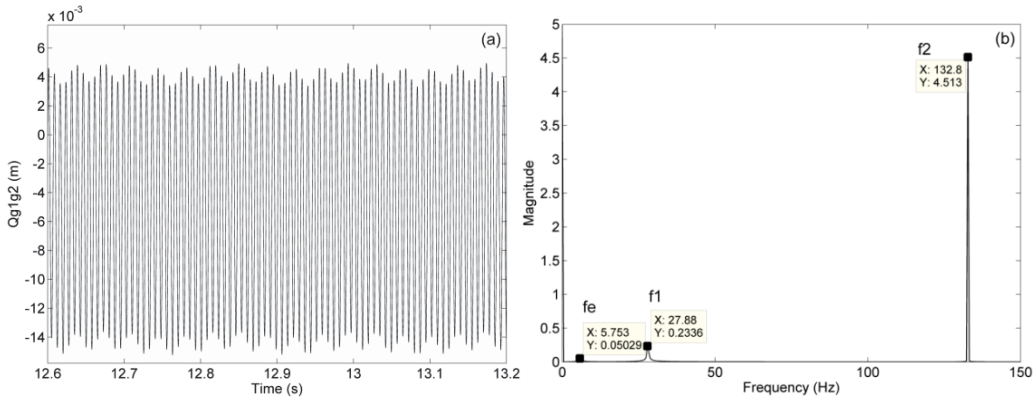

Figure 5.14. The vibrational responses of $\boldsymbol{Q_{g1g2}}$ with the mean-to-fluctuating external force ratio $\boldsymbol{F_m/F_a}$ of 5 (a) Time histories (b) FFT spectrum

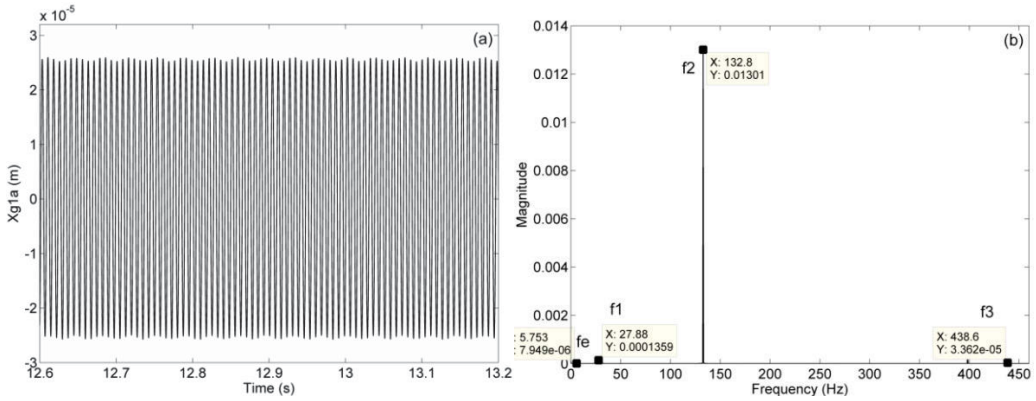

Figure 5.15. The axial vibrational responses $\boldsymbol{X_{g1a}}$ with the mean-to-fluctuating external force ratio $\boldsymbol{F_m/F_a}$ of 5 (a) Time histories (b) FFT spectrum

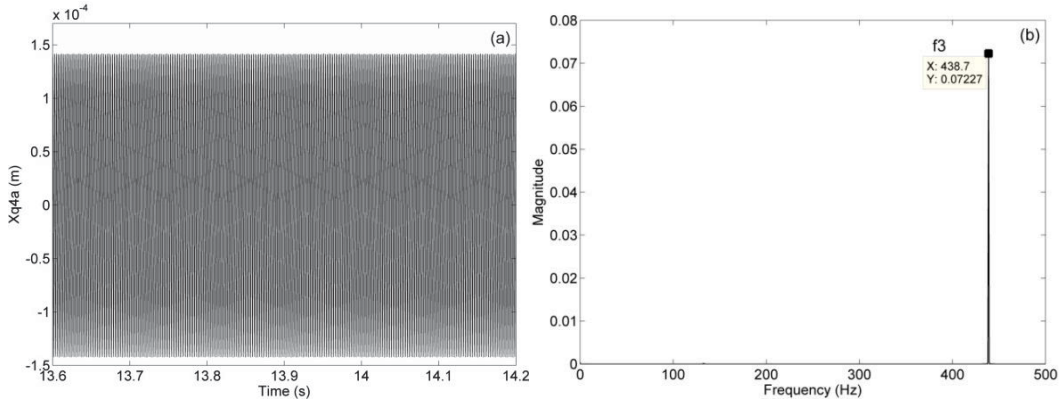

Figure 5.16. The vibrational responses of $\boldsymbol{X_{g4a}}$ with the mean-to-fluctuating external force ratio $\boldsymbol{F_m/F_a}$ of 5 (a) Time histories (b) FFT spectrum

The increased external excitation fluctuation (with the mean-to-fluctuating external force ratio of 2) and the internal excitation are considered below, as shown in Figures 5.17 to 5.21. The dynamic response of Q_{rp1} starts to have more fluctuations. The magnitude of the external frequency f_e is still smaller than the meshing frequency at its own gear stage f_1, but contributes more compared with that in Figure 5.12. The magnitude of f_2 is much smaller than f_1, which means that it provides limited effects on Q_{rp1}. Figures 5.18 and 5.19 present the dynamic responses of Q_{sp1} and Q_{g1g2}. It is similar to those in Figures 5.13 and 5.14, the relative displacement of gear meshes fluctuate at their own meshing frequencies, but larger influence from the external excitation frequency f_e. Figures 5.20 presents the axial displacement of gear at the intermediate parallel gear stage X_{g1a}, which is very similar to that of Figure 5.15. This indicates that the increased external fluctuation does not have significant effects on the axial displacement at the intermediate parallel gear stage. Figures 5.21 presents the axial displacement of pinion at the high-speed parallel gear stage X_{g4a}. The frequency peak occurs at f_3 and its magnitude is much larger than f_e, f_1 and f_2. This shows that f_3 contributes the most at the high-speed parallel gear stage. Its harmonics $2f_3$ and sidebands are also observed. Compared with Figure 5.16 for when the mean-to-fluctuating force ratio f_m/f_a is 5, the external excitation has larger influence on both the gears and bearings, which simulates the condition for a sudden change of external excitation on turbines.

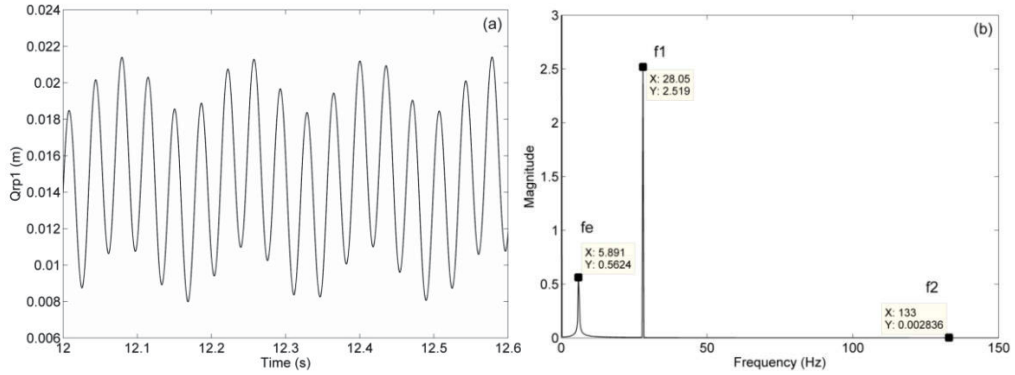

Figure 5.17. The vibrational responses of $\boldsymbol{Q_{rp1}}$ with the mean-to-fluctuating external force ratio $\boldsymbol{F_m/F_a}$ of 2 (a) Time histories (b) FFT spectrum

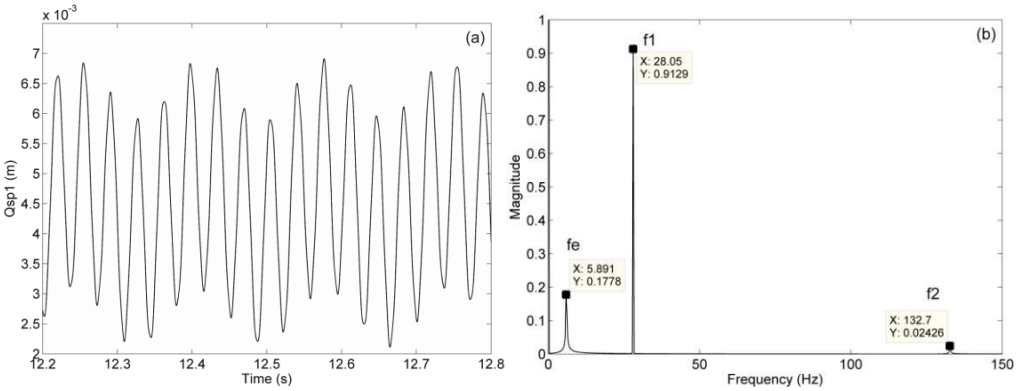

Figure 5.18. The vibrational responses of $\boldsymbol{Q_{sp1}}$ with the mean-to-fluctuating external force ratio $\boldsymbol{F_m/F_a}$ of 2 (a) Time histories (b) FFT spectrum

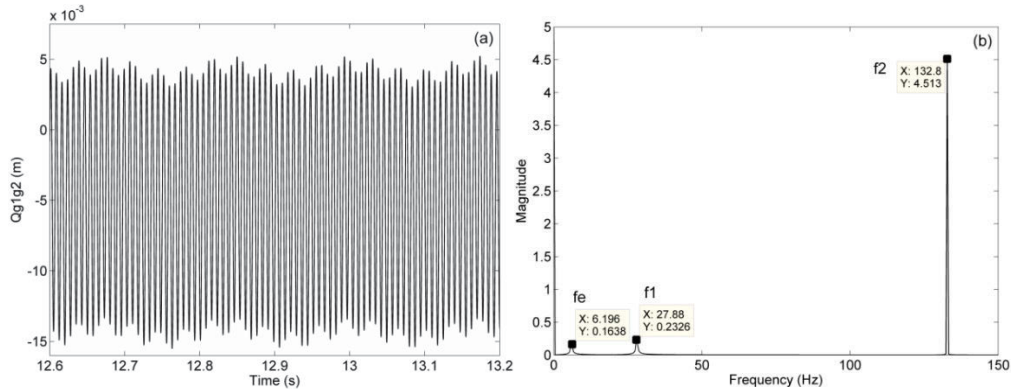

Figure 5.19. The vibrational responses of $\boldsymbol{Q_{g1g2}}$ with the mean-to-fluctuating external force ratio $\boldsymbol{F_m/F_a}$ of 2 (a) Time histories (b) FFT spectrum

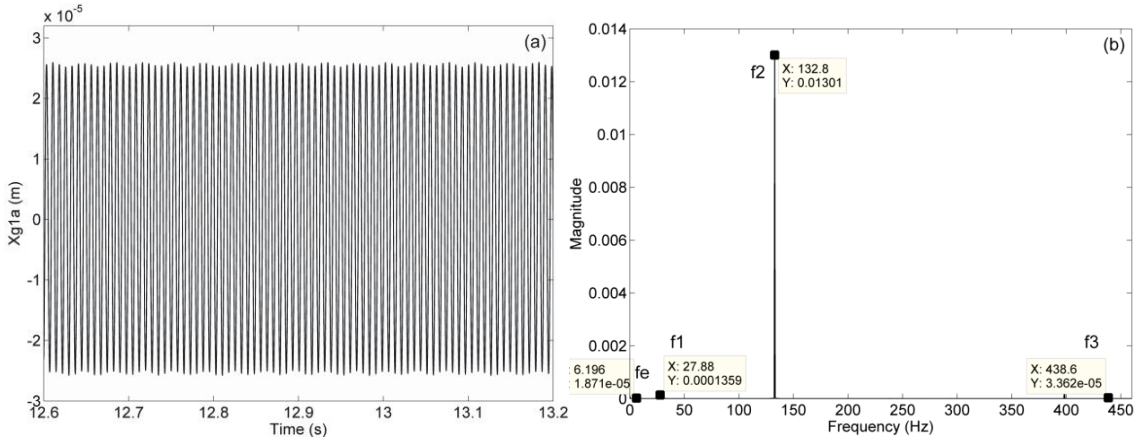

Figure 5.20. The axial vibrational responses $\boldsymbol{X_{g1a}}$ with the mean-to-fluctuating external force ratio $\boldsymbol{F_m/F_a}$ of 2 (a) Time histories (b) FFT spectrum

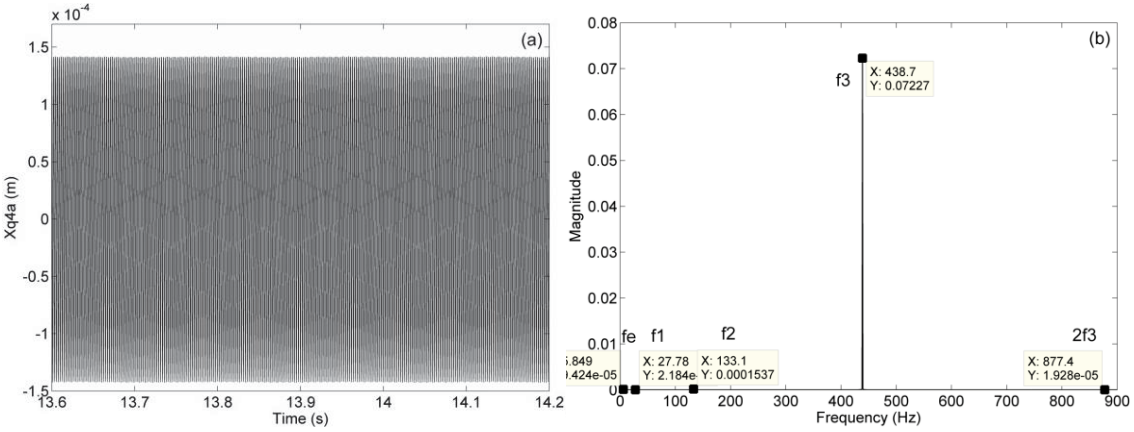

Figure 5.21. The axial vibrational responses $\boldsymbol{X_{g4a}}$ with the mean-to-fluctuating external force ratio $\boldsymbol{F_m/F_a}$ of 2 (a) Time histories (b) FFT spectrum

5.5 Discussions

In the study of the dynamic responses of the wind turbine gearbox components, when considering the external excitation only and disallowing gears to rotate, such a condition is similar to that when the wind turbine is parked. The results showed that the magnitude of the relative displacements of gear meshes is much larger than the elastic displacement of gearbox bearings. This explains why the fretting corrosion, as one of

the wind turbine gearbox failure modes, occurs in gears along the line of action when the wind turbine is parked.

When both the internal and external excitations were considered, it was observed that the gear meshes at all gear stages are relatively stable. When the external excitation fluctuation is small, the stability of gears is not affected. However, the dynamic responses of gears were observed to have more fluctuation. When the external excitation fluctuation is increased, the external excitation fluctuation has large influence on wind turbine gearbox components, especially when a sudden change of external excitation is added, such as emergency stops which may happen about 10-20 emergency stops per year. During such emergency stops it is possible for the torque to vary very dynamically. As a result, the dynamic responses of wind turbine gearbox components can be affected and may lead to gear wear and bearing failures.

This page intentionally left blank

Chapter 6 Effect of bending moment on a 6DOF wind turbine planetary gearbox

Non-torque load is one of the major sources of gearbox reliability issues for wind turbines, such as premature gearbox damages and failures [50, 76]. Thus, this chapter studies the effects of the non-torque load, especially the effect of bending moments, on the dynamic responses of a wind turbine planetary gearbox. To complete the full dynamic model of the wind turbine gearbox, the proposed 6DOF dynamic model is developed based on the torsional and the 4DOF models, described previously in Chapters 4 and 5, and takes into account the key factors such as bearing clearances, bearing stiffness, the gear mesh stiffness, damping, gear backlash and static transmission error. Both the external excitation due to wind and the internal excitation due to the static transmission error are included in the proposed dynamic model, and the study of the effect of the bending moments is emphasised in this chapter. The dynamic responses of wind turbine planetary gearbox components are studied with the help of the time history, FFT spectrum, Phase portrait, Poincare map and load share ratio.

6.1 Modelling

A wind turbine planetary gear stage is shown in Figure 6.1. The ring gear is fixed at the gearbox housing, remaining non-rotating, and three planet gears are included in the gearbox. The floating-sun configuration is implemented to improve the load share in the planetary gear stage [52]. The driving torque is the major loading transmitted into the gearbox, and non-torque loads occur in the other five degrees of freedom (5DOF).

Theoretically, the planet carrier arm bearings would hold the majority of non-torque loads, for example, the radial reaction forces caused by the bending moments would pass through the main shaft through the carrier bearings, torque arms and trunnions into the gearbox housing. Only a small fraction of the non-torque loads are transmitted into gear meshes, thus, the gear teeth only carry the driving torque [41]. However, the gearbox would transmits significant main-shaft bending loads into the gearbox in reality, which can alter shaft alignment to the gearbox and gear mesh patterns in planetary gear stage [76, 178].

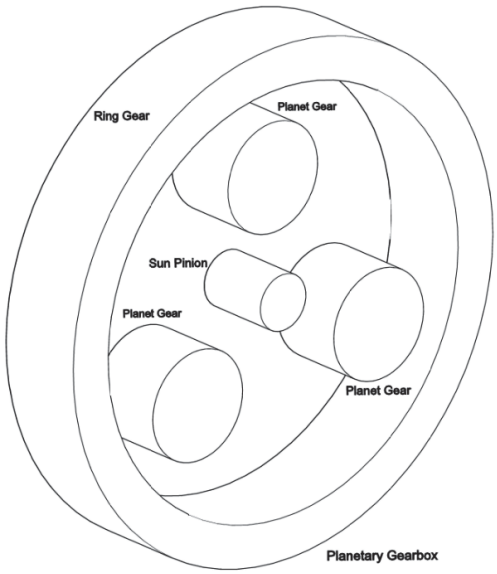

Figure 6.1. A wind turbine planetary gearbox

6.2 Derivation of equations

The equivalent transverse displacements of the gearbox components on x, y and z axes, caused by their rotational displacements Q_j, can be obtained by using Equations (6.1) and (6.2), where j denotes the gearbox components such as the planet carrier arm,

planet gears and the sun pinion respectively, θ represent the rotational displacements, r_{bj} represents the base radius of the gearbox components, and α is the pressure angle.

$$Q_{xj} = r_{bj}\theta_{xj};\ Q_{yj} = r_{bj}\theta_{yj};\ Q_{zj} = r_{bj}\theta_{zj}; \qquad (6.1a, b, c)$$

$$r_{bj} = r_j \cos \alpha \qquad (6.2)$$

The locations of planet gears are taken into account for finding the translational displacements of the planet gears and sun pinion, as shown in Figures 6.2 and 6.3. Considering the configuration of the planetary gear stage, three planet gears are located with angles of 0°, 120° and 240°, notated as ϕ_i with respect to the negative x-axis.

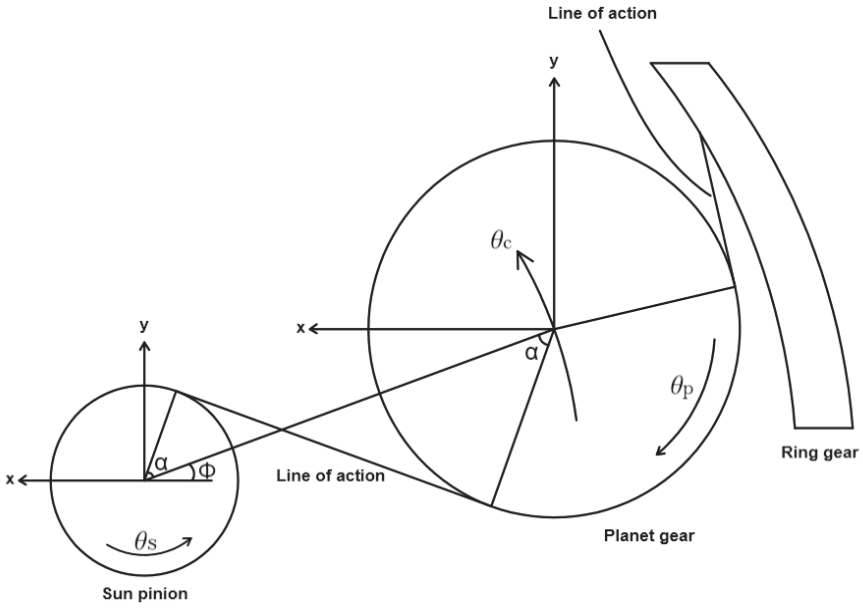

Figure 6.2. A sun-planet gear pair

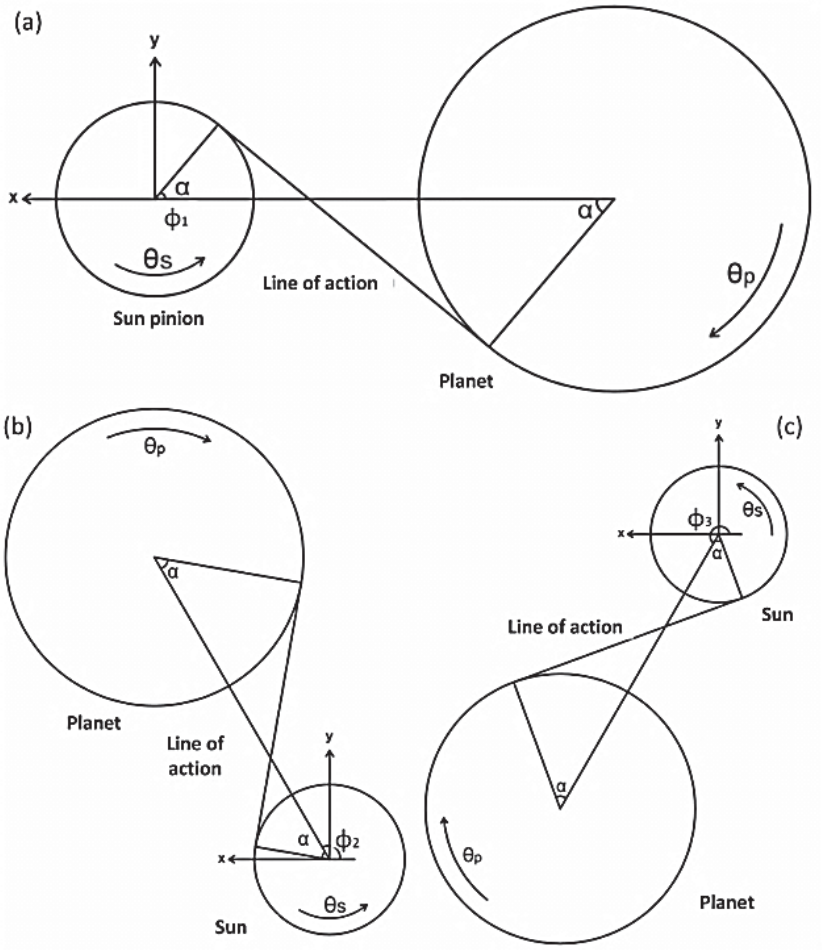

Figure 6.3. A sun-planet gear pair (a) with $\boldsymbol{\phi_1 = 0^\circ}$ (b) with $\boldsymbol{\phi_2 = 120^\circ}$ (c) with $\boldsymbol{\phi_3 = 240^\circ}$

The relative displacement of sun-planet gear mesh on the line of action, caused by rotation, can be expressed by

$$Q_{spn\_\theta} = \left(Q_{xs} - Q_{xpn} - Q_{xc}\right)[-\sin\beta_s \sin(\phi_n + \alpha) + \tan\alpha \sin\beta_s \cos(\phi_n + \alpha)] + \left(Q_{ys} - Q_{ypn} - Q_{yc}\right)[-\sin\beta_s \cos(\phi_n + \alpha) - \tan\alpha \sin\beta_s \sin(\phi_n + \alpha)] + \left(Q_{zs} - Q_{zpn} - Q_{zc}\right)\cos\beta_s \quad (6.3a)$$

The relative displacement of sun-planet gear mesh on the line of action, caused by the translational motions, can be found by

$$Q_{spn\_t} = \left(x_s - x_{pn} - x_c\right)\cos\beta_p \sin(\phi_n + \alpha) + \left(y_s - y_{pn} - y_c\right)\cos\beta_p \cos(\phi_n + \alpha) + \left(z_s - z_{pn} - z_c\right)\sin\beta_p \quad (6.3b)$$

By combining Equations (6.3a) and (6.3b), and taking into account the effect of the static transmission error e_{sp}, the total relative displacement of sun-planet gear mesh on the line of action becomes

$$Q_{spn} = Q_{spn\_\theta} + Q_{spn\_t} - e_{sp} \quad (6.3c)$$

Similarly, the relative displacement of ring-planet gear mesh on the line of action, caused by rotation, can be obtained as

$$Q_{rpn_\theta} = \left(Q_{xpn} - Q_{xc}\right)[-\sin\beta_s \sin(\phi_n - \alpha) + \tan\alpha \sin\beta_s \cos(\phi_n - \alpha)] + \left(Q_{ypn} - Q_{yc}\right)[-\sin\beta_s \cos(\phi_n - \alpha) - \tan\alpha \sin\beta_s \sin(\phi_n - \alpha)] + \left(Q_{zpn} - Q_{zc}\right)\cos\beta_p \quad (6.4a)$$

The relative displacement of ring-planet gear mesh on the line of action, caused by the translational motions, is found by

$$Q_{rpn\_t} = \left(x_{pn} - x_c\right)\cos\beta_p \sin(\phi_n - \alpha) + \left(y_{pn} - y_c\right)\cos\beta_p \cos(\phi_n - \alpha) + \left(z_{pn} - z_c\right)\sin\beta_p \quad (6.4b)$$

By taking into account the static transmission error of the ring-planet gear mesh, the total relative displacement becomes

$$Q_{rpn} = Q_{rpn\_\theta} + Q_{rpn\_t} - e_{rp} \tag{6.4c}$$

The meshing forces of the gear pairs of the wind turbine gearbox can be determined by Equations (6.5a) and (6.5b), where k_{rp} and k_{sp} represent the gear mesh stiffness of the ring-planet and sun-planet gear pairs.

$$F_{rpn} = k_{rp}Q_{rpn};\ F_{spn} = k_{sp}Q_{spn};\ n = 1,2,3 \tag{6.5a, b}$$

Damping forces are calculated in a similar way by Equations (6.6a) and (6.6b), where c_{rp} and c_{sp} are the damping of the ring-planet and sun-planet gear pairs.

$$D_{rpn} = c_{rp}\dot{Q}_{rpn};\ D_{spn} = c_{sp}\dot{Q}_{spn};\ \ n = 1,2,3 \tag{6.6a, b}$$

The gear mesh stiffness and damping are obtained based on the previous work described in Sections 4.3 and 5.3 [95]. By taking into account the gear backlash b, $f(Q_j)$ is the vector form of the gear mesh displacement function (piecewise linear characteristics), where Q_j represents Q_{rpn} and Q_{spn}.

$$f(Q_j) = \begin{cases} Q_j - b, & Q_j > b \\ 0, & -b \le Q_j \le b \\ Q_j + b, & Q_j < -b \end{cases} \tag{6.7}$$

The bearing stiffness has large influence on the dynamic behaviours of bearings. The elastic displacement of bearings, during the wind turbine operation, would affect the dynamic responses of other gearbox components. The bearings used in the proposed wind turbine planetary gear stage are the roller bearings, due to their nature of low friction and high load capacity. The planet carrier arm is supported by two full-complement cylindrical roller bearings and each planet gear supported by two cylindrical roller bearings. Each shaft in the gearbox is supported by a cylindrical roller bearing and two tapered roller bearings. Tapered roller bearings are mostly used to support the axial loading [174, 179, 180].

For cylindrical roller bearings, the radial elastic displacement δ_r can be calculated by

$$\delta_r = 0.000077\, {F_{r\_max}}^{0.9} / {L_{we}}^{0.8} \tag{6.8}$$

$$F_{r\_max} = (4.08/iZ)F_r \tag{6.9}$$

where F_{r_max} is the maximum rolling element load, L_{we} is the effective contact length of roller, i is the number of the rows of rollers, Z is the number of rollers per row, and F_r is the radial load [181].

The elastic displacement δ_r of the cylindrical roller bearing varies with the changes of the radial load F_r during gear mesh. Thus, the radial stiffness k_r, as the input of the dynamic model, should be calculated prior to the simulation by

$$k_r = F_r/\delta_r \tag{6.10}$$

For tapered roller bearings, the axial deformation δ_a can be calculated by

$$\delta_a = 0.000077{F_L}^{0.9}/(\sin\gamma\,{L_{we}}^{0.8}) \quad (6.11)$$

$$F_L = F_a/Z\sin\gamma \quad (6.12)$$

where F_L is the load on rolling elements, γ is the contact angle, L_{we} is the effective contact length of roller, Z is the number of rollers, and F_a is the axial load [181].

In order to include the radial clearance for the bearing model, nonlinear input functions shown below are used for the diagonal terms.

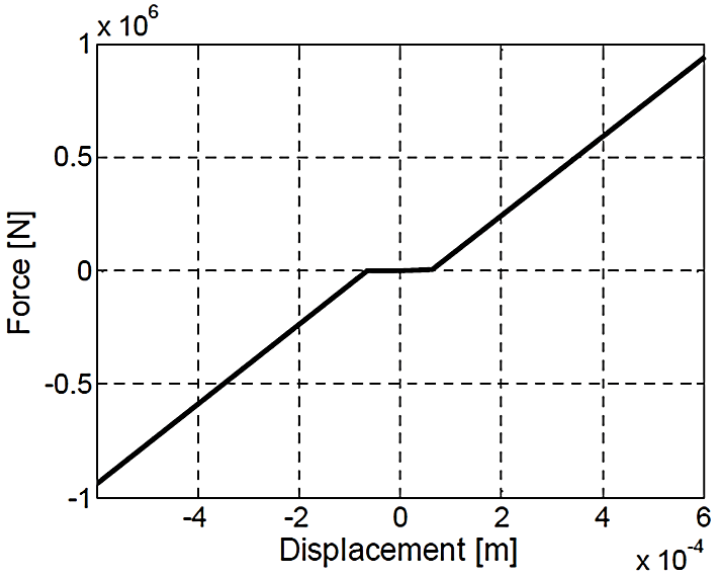

Figure 6.4. Bearing stiffness function with clearance [53]

The radial forces, expressed in terms of the translational displacements X_k (e.g. x_{pn} and y_{pn}, $n = 1,2,3$), exist only when the relative displacement between the connected gear teeth exceeds a specified clearance c. Taking into account the radial clearance of the

planet bearings, $f(X_k)$ is the vector form of the nonlinear translational displacement function (piecewise linear characteristics).

$$f(X_k) = \begin{cases} X_k - c, & X_k > c \\ 0, & -c \le X_k \le c \\ X_k + c, & X_k < -c \end{cases} \tag{6.13}$$

The motions of the gearbox components can be governed by applying the Newton's laws. For planet carrier arm, the equations of motion are given by

$$\left(I_{xc} + 3m_p {r_c}^2\right)\ddot{\theta}_{xc} - \sum_{n=1}^{3}\left(k_{rp} f\left(Q_{rpn}\right) + c_{rp}\dot{Q}_{rpn}\right)\sin\beta_s \sin(\phi_n + \alpha)\, r_{bC} - \sum_{n=1}^{3}\left(k_{sp} f\left(Q_{spn}\right) + c_{sp}\dot{Q}_{spn}\right)\sin\beta_s \sin(\phi_n + \alpha)\, r_{bC} - K_{xc}\theta_{xc} - C_{xc}\dot{\theta}_{xc} = M_{xx} \tag{6.14a}$$

$$\left(I_{yc} + 3m_p {r_c}^2\right)\ddot{\theta}_{yc} - \sum_{n=1}^{3}\left(k_{rp} f\left(Q_{rpn}\right) + c_{rp}\dot{Q}_{rpn}\right)\sin\beta_s \cos(\phi_n + \alpha)\, r_{bC} - \sum_{n=1}^{3}\left(k_{sp} f\left(Q_{spn}\right) + c_{sp}\dot{Q}_{spn}\right)\sin\beta_s \cos(\phi_n + \alpha)\, r_{bC} - K_{yc}\theta_{yc} - C_{yc}\dot{\theta}_{yc} = M_{yy} \tag{6.14b}$$

$$\left(I_{zc} + 3m_p {r_c}^2\right)\ddot{\theta}_{zc} + \sum_{n=1}^{3}\left(k_{sp} f\left(Q_{spn}\right) + c_{sp}\dot{Q}_{spn}\right)\cos\beta_s\, r_{bC} + \sum_{n=1}^{3}\left(k_{rp} f\left(Q_{rpn}\right) + c_{rp}\dot{Q}_{rpn}\right)\cos\beta_s\, r_{bC} = T_{in} \tag{6.14c}$$

$$m_c\ddot{x}_c + \sum_{n=1}^{3}\left(k_{sp} f\left(Q_{spn}\right) + c_{sp}\dot{Q}_{spn}\right)\cos\beta_s \sin(\phi_n + \alpha) + \sum_{n=1}^{3}\left(k_{rp} f\left(Q_{rpn}\right) + c_{rp}\dot{Q}_{rpn}\right)\cos\beta_s \sin(\phi_n - \alpha) - k_{cx}x_c - c_{cx}\dot{x}_c = 0 \tag{6.14d}$$

$$m_c\ddot{y}_c - \sum_{n=1}^{3}\left(k_{sp}f(Q_{spn}) + c_{sp}\dot{Q}_{spn}\right)\cos\beta_s\cos(\phi_n + \alpha) +$$

$$\sum_{n=1}^{3}\left(k_{rp}f\left(Q_{rpn}\right) - c_{rp}\dot{Q}_{rpn}\right)\cos\beta_s\cos(\phi_n - \alpha) - k_{cy}y_c$$

$$-c_{cy}\dot{y}_c = 0 \qquad (6.14e)$$

$$m_c\ddot{z}_c - \sum_{n=1}^{3}\left(k_{sp}f(Q_{spn}) + c_{sp}\dot{Q}_{spn}\right)\sin\beta_s +$$

$$\sum_{n=1}^{3}\left(k_{rp}f\left(Q_{rpn}\right) + c_{rp}\dot{Q}_{rpn}\right)\sin\beta_s - k_{cz}z_c - c_{cz}\dot{z}_c = 0 \qquad (6.14f)$$

For the planet gears, the equations of motion are expressed by

$$I_{xp}\ddot{\theta}_{ypn} - \left(k_{rp}f\left(Q_{rpn}\right) + c_{rp}\dot{Q}_{rpn}\right)\sin\beta_p\sin(\phi_n + \alpha)\,r_{bp}$$

$$-\left(k_{sp}f(Q_{spn}) + c_{sp}\dot{Q}_{spn}\right)\sin\beta_p\sin(\phi_n + \alpha)\,r_{bp} = 0 \qquad (6.15a)$$

$$I_{yp}\ddot{\theta}_{ypn} - \left(k_{rp}f\left(Q_{rpn}\right) + c_{rp}\dot{Q}_{rpn}\right)\sin\beta_p\cos(\phi_n + \alpha)\,r_{bp}$$

$$-\left(k_{sp}f\left(Q_{spn}\right) + c_{sp}\dot{Q}_{spn}\right)\sin\beta_p\cos(\phi_n + \alpha)\,r_{bp} = 0 \qquad (6.15b)$$

$$I_{zp}\ddot{\theta}_{xpn} - \left(k_{rp}f(Q_{rpn}) + c_{rp}\dot{Q}_{rpn}\right)\cos\beta_p r_{bp} +$$

$$\left(k_{sp}f(Q_{spn}) + c_{sp}\dot{Q}_{spn}\right)\cos\beta_p r_{bp} = 0 \qquad (6.15c)$$

$$m_p\ddot{x}_{pn} - \left(k_{rp}f\left(Q_{rpn}\right) + c_{rp}\dot{Q}_{rpn}\right)\cos\beta \quad \sin(\varphi_n - \alpha)$$

$$-\left(k_{sp}f\left(Q_{spn}\right) + c_{sp}\dot{Q}_{spn}\right)\cos\beta_p\sin(\phi_n + \alpha) - k_{px}x_{pn} - c_{px}\dot{x}_{pn} = 0 \qquad (6.15d)$$

$$m_p\ddot{y}_{pn} + \left(k_{rp}f\left(Q_{rpn}\right) + c_{rp}\dot{Q}_{rpn}\right)\cos\beta_p\cos(\varphi_n - \alpha)$$

$$+\left(k_{sp}f(Q_{spn}) + c_{sp}\dot{Q}_{spn}\right)\cos\beta_p\cos(\phi_n + \alpha) - k_{py}y_{pn} - c_{py}\dot{y}_{pn} = 0 \qquad (6.15e)$$

$$m_p\ddot{z}_{pn} - \left(k_{rp}f\left(Q_{rpn}\right) + c_{rp}\dot{Q}_{rpn} - k_{sp}f\left(Q_{spn}\right) - c_{sp}\dot{Q}_{spn}\right)\sin\beta_p$$
$$-k_{pz}z_{pn} - c_{pz}\dot{z}_{pn} = 0 \qquad (6.15f)$$

For the sun pinion, the equations of motion are given by

$$I_{xs}\ddot{\theta}_{xs} - \sum_{n=1}^{3}\left(k_{sp}f\left(Q_{spn}\right) + c_{sp}\dot{Q}_{spn}\right)\sin\beta_s\sin(\phi_n + \alpha)\,r_{bs} = 0 \qquad (6.16a)$$

$$I_{ys}\ddot{\theta}_{ys} - \sum_{n=1}^{3}\left(k_{sp}f\left(Q_{spn}\right) + c_{sp}\dot{Q}_{spn}\right)\sin\beta_s\cos(\phi_n + \alpha)\,r_{bs} = 0 \qquad (6.16b)$$

$$I_{zs}\ddot{\theta}_{zs} - \sum_{n=1}^{3}\left(k_{sp}f\left(Q_{spn}\right) + c_{sp}\dot{Q}_{spn}\right)\cos\beta_s\,r_{bs} = -T_{out} \qquad (6.16c)$$

$$m_s\ddot{x}_s - \sum_{n=1}^{3}\left(k_{sp}f\left(Q_{spn}\right) + c_{sp}\dot{Q}_{spn}\right)\cos\beta_s\sin(\phi_n + \alpha) = 0 \qquad (6.16d)$$

$$m_s\ddot{y}_s - \sum_{n=1}^{3}\left(k_{sp}f\left(Q_{spn}\right) + c_{sp}\dot{Q}_{spn}\right)\cos\beta_s\cos(\phi_n + \alpha) = 0 \qquad (6.16e)$$

$$m_s\ddot{z}_s - \sum_{n=1}^{3}\left(k_{sp}f\left(Q_{spn}\right) + c_{sp}\dot{Q}_{sn}\right)\sin\beta_s = 0 \qquad (6.16f)$$

Substituting the relative displacements of gear meshes given by Equations (6.3) to (6.13) into Equations (6.14) to (6.16), yields the transverse and translational displacements of gearbox components.

6.3 Simulation and results

The external excitations include the driving torque T_{in} and the aerodynamic bending moment (e.g. M_y), which are expected to locate at the low frequency range. Thus, in this chapter the torsional frequency is chosen to be 5Hz, and the bending moment frequency is chosen to be 12Hz. Under the constant rotational speed, the meshing frequency of the planetary gearbox is 28Hz. The external excitation condition is described in Chapters 4 and 5 [94, 95].

To investigate the effects of the bending moments, a non-dimensional quantity M_y/T_{in} is introduced to address the combined external loading transmitted on the planet carrier arm. With the help of time histories, FFT spectrum, Portrait phase, Poincare map and load share ratios (LSR), the dynamic responses of the planetary components are studied in the following five sections: (1) driving torque only; (2) driving torque and bending moment with $M_y/T_{in} = 0.5$; (3) driving torque and bending moment with $M_y/T_{in} = 1$; (4) driving torque and bending moment with $M_y/T_{in} = 5$; (5) increased driving torque and bending moment with $M_y/T_{in} = 0.5$. In Section 6.3.6, a comparison of the conditions with and without the bearing clearances is presented and discussed.

6.3.1 Constant external excitations

In this section, the only external excitation is the driving torque. The dynamic response include the ring-planet gear mesh Q_{rp1} shown in Figure 6.5, the sun-planet gear mesh Q_{sp1} shown in Figure 6.6, the load share ratio (LSR) of one of the planet gears shown in Figure 6.7, and the radial and axial displacement of one of the planet gears X_p and X_{pa} presented in Figures 6.8 and 6.9.

For the the ring-planet gear mesh Q_{rp1}, the FFT spectrum shown in Figure 6.5(b) presents two frequency components f_t and f_1. The meshing frequency peak f_1[9] is larger than f_t[10], which indicates that the meshing frequency f_1 has more effects on Q_{rp1} than f_t. Figures 6.5(c) and 6.5(d) present the phase portrait and Poincare map of Q_{rp1}, which repeat themselves with slight shifts due to the combination of the two excitation frequencies f_t and f_1. This indicates that the response of Q_{rp1} is periodic.

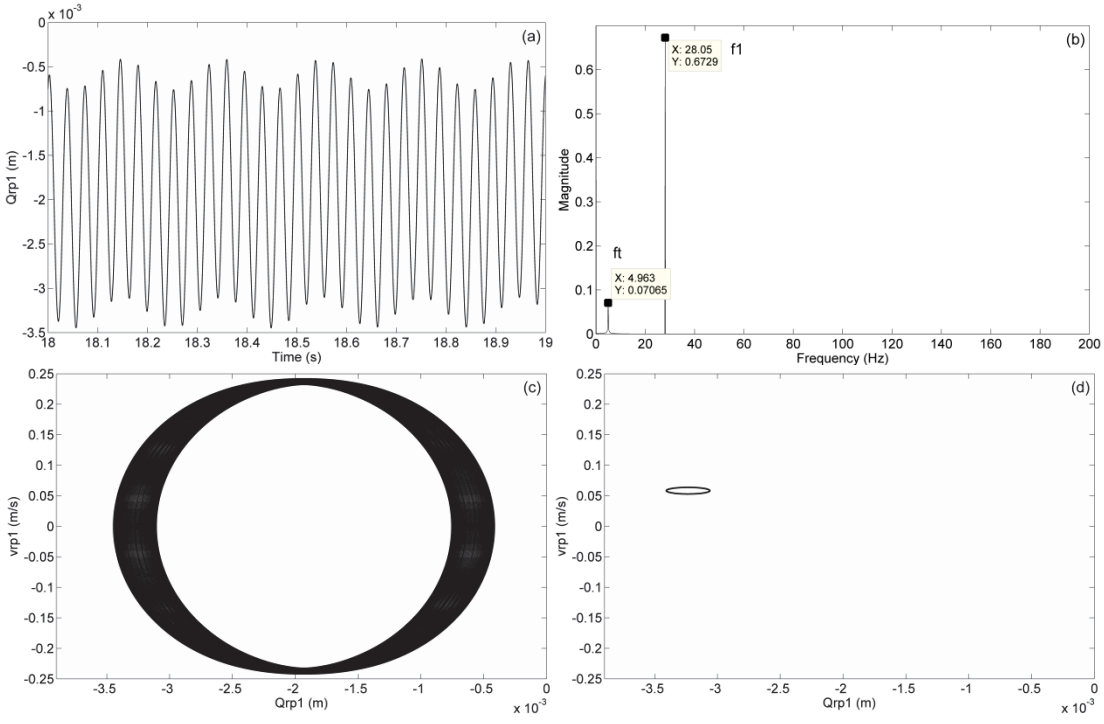

Figure 6.5. The vibrational responses of $\boldsymbol{Q_{rp1}}$ (a) Time histories (b) FFT spectrum (c) Phase Portrait (d) Poincare map

[9] The planetary gearbox is normally the first gear stage in wind turbine gearbox, thus the meshing frequency of the planetary gearbox is set to be f_1 throughout this chapter.

[10] f_t represents the external excitation frequency (torque).

It is observed in Figure 6.6(a) that the time histories of Q_{sp1} are stable, but fluctuate less than Q_{rp1} shown in Figure 6.5(a). Two frequency components f_t and f_1 are observed in Figure 6.6(b). The peak of f_1 is larger than f_t, this indicates that the meshing frequency f_1 has more effects on Q_{sp1} than f_t does. The magnitude of the meshing frequency peak f_1 is smaller than that for Q_{rp1} shown in Figure 6.5(b), this suggests that the meshing frequency f_1 has slightly less influence on Q_{sp} than it does on Q_{rp}. Figures 6.6(c) and 6.6(d) present the phase portrait and Poincare map, which repeat themselves with slight shifts due to the two excitation frequencies f_t and f_1. This indicates that the response of Q_{sp1} is periodic.

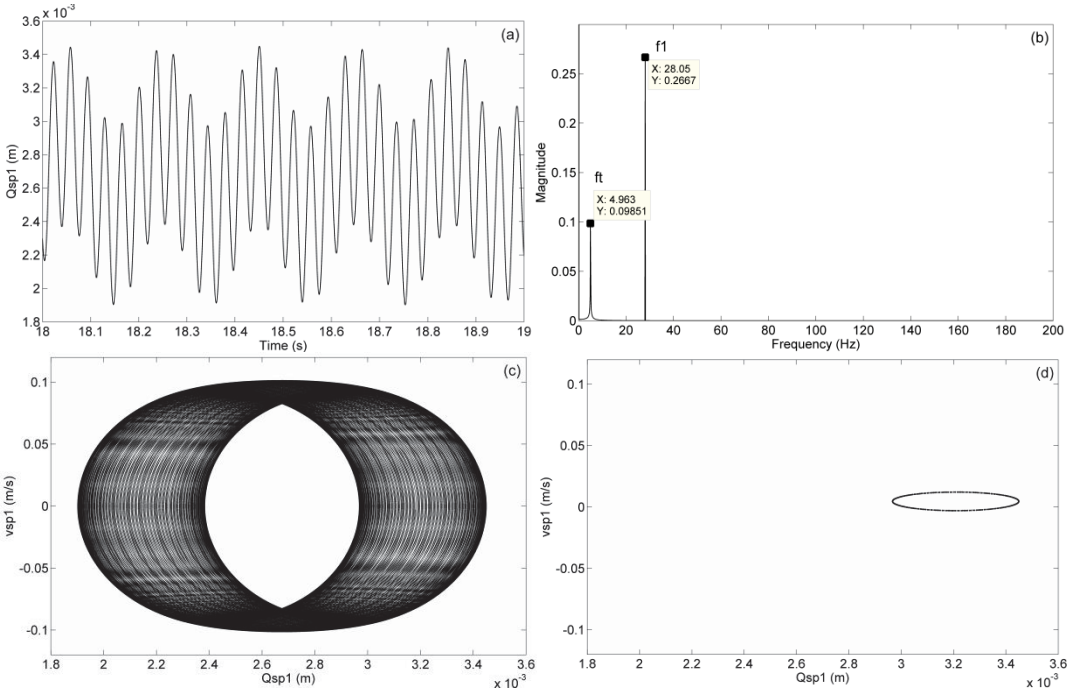

Figure 6.6. The vibrational responses of $\boldsymbol{Q_{sp1}}$ (a) Time histories (b) FFT spectrum (c) Phase Portrait (d) Poincare map

The load share ratio shown in Figure 6.7 is influenced by both the external excitation frequency f_t and meshing frequency f_1, and the value fluctuates between 0.18 and 0.49

around the ideal value $1/3$. The *LSRs* of the other two planet gears are similar to that as shown in Figure 6.7 but with phase shifts of $2\pi/3$. This suggests that the loads on the planet gears are equally shared.

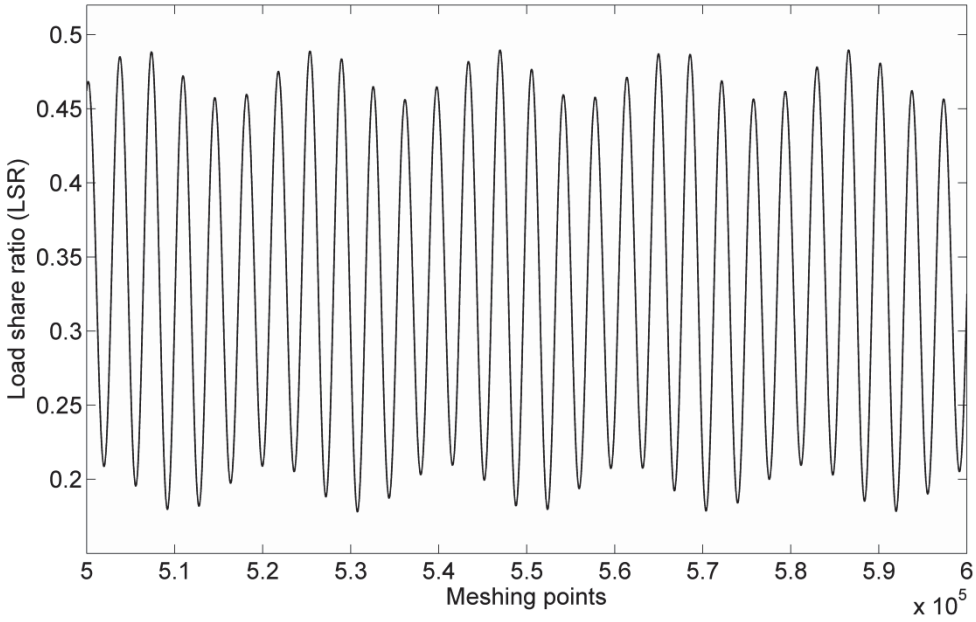

Figure 6.7. Load share ratio (LSR)

The magnitude of the radial and axial displacements of the planet gear in the time histories are smaller than those of the gear meshes, as shown previously in Figures 6.8 and 6.9. The two frequency peaks f_t and f_1 are observed. The peak of f_1 is larger than f_t, this indicates that the meshing frequency f_1 has more effect on the radial X_p and axial displacement X_{pa} than f_t does.

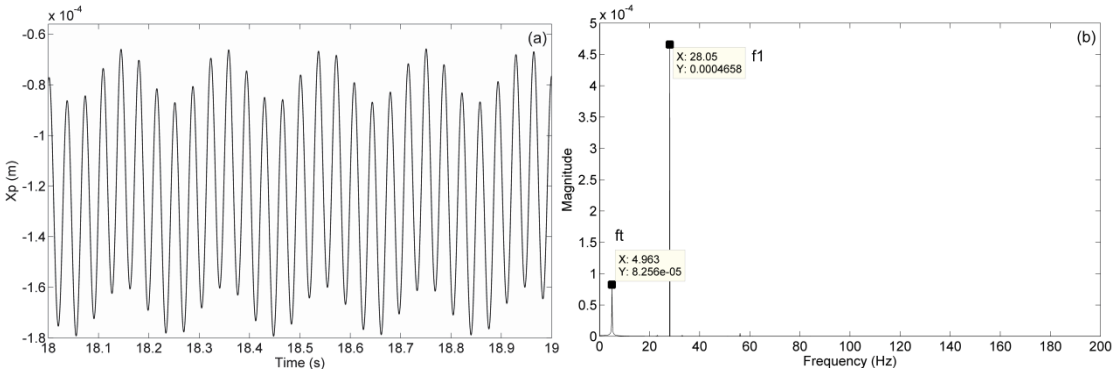

Figure 6.8. The radial vibrational responses of planet gear $\boldsymbol{X_p}$ (a) Time histories (b) FFT spectrum

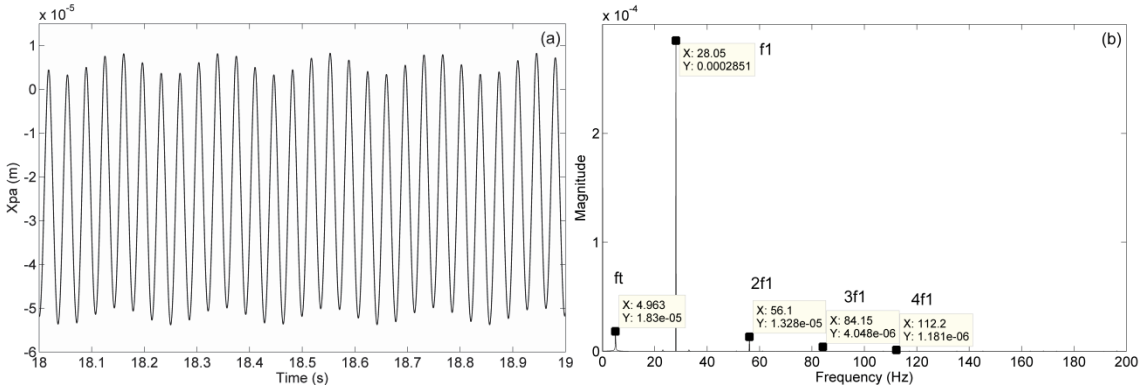

Figure 6.9. The axial vibrational responses of planet gear $\boldsymbol{X_{pa}}$ (a) Time histories (b) FFT spectrum

6.3.2 Wind fluctuation and bending moment with $M_y/T_{in} = 0.5$

The effect of the bending moment with $M_y/T_{in} = 0.5$ is studied in this section. Figure 6.10 presents the dynamic response of Q_{p1}. Figure 6.11 presents the dynamic response of the sun-planet gear meshes Q_{sp1}. The LSR is presented in Figure 6.12. The radial and axial displacement of one of the planets X_p and X_{pa} are presented in Figures 6.13 and 6.14.

Figure 6.10 (a) presents the time histories of Q_{rp1}. It shows that the magnitudes of the time histories are larger than Q_{rp1} shown in Figure 6.5(a). Compared with the dynamic response of the ring-planet gear meshes for when bending moment $\mathrm{M_y}$ is not included, the gear mesh pattern has changed. The FFT spectrum shows three frequency peaks f_t, f_b[11] and f_1. With the $\mathrm{M_y/T_{in}}$ ratio set to be 0.5, it is observed that the meshing frequency f_1 has the largest influence on the ring-planet gear meshes Q_{rp1}, and the applied bending moment frequency f_b has larger influence than f_t. Figures 6.10(c) and 6.10(d) present the phase portrait and Poincare map, which repeat themselves with slight shifts due to the three excitation frequencies. This indicates that the response of Q_{rp1} is periodic.

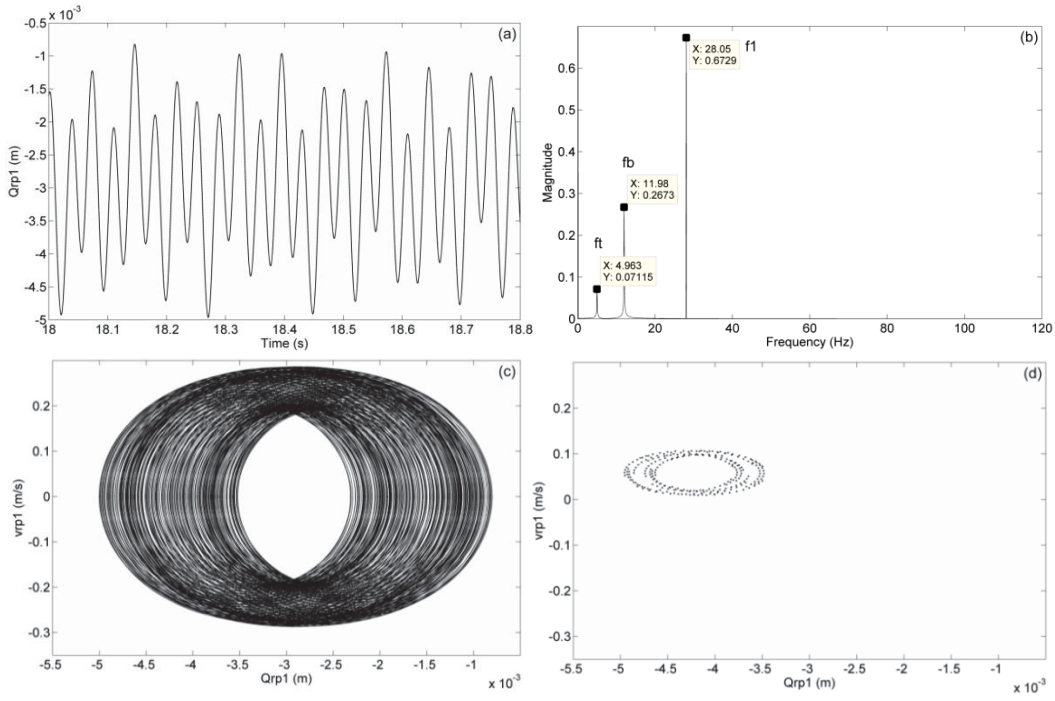

Figure 6.10. The vibrational responses of $\boldsymbol{Q_{rp1}}$ (a) Time histories (b) FFT spectrum (c) Phase Portrait (d) Poincare map

[11] f_b represents the excitation frequency caused by the bending moment, and it not chosen to be 12Hz to differ from the excitation frequency caused by torque (5Hz) and meshing frequency (28Hz).

Figure 6.11(a) shows the time histories of Q_{sp1}, the gear mesh pattern is very similar to the Q_{sp1} shown in Figure 6.6(a). In Figure 6.11(b), the bending moment frequency peak f_b is observed to be much smaller than the other two frequency components f_t and f_1. These suggest that the sun-planet gear meshes Q_{sp1} are less affected by the bending moments compared to the ring-planet gear meshes Q_{rp1} when the M_y/T_{in} ratio is 0.5. Figures 6.11(c) and 6.11(d) present the phase portrait and Poincare map, which repeat themselves with slight shifts due to the three excitation frequencies. This indicates that the response of Q_{sp1} is periodic.

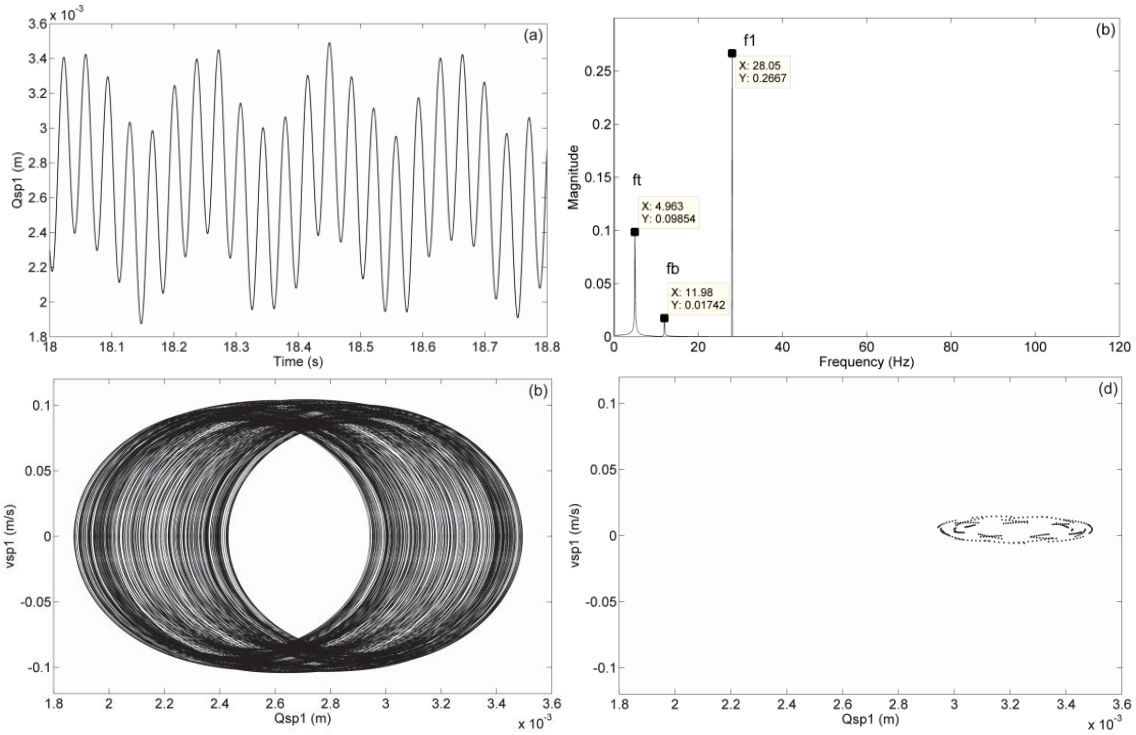

Figure 6.11. The vibrational responses of $\boldsymbol{Q_{sp1}}$ (a) Time histories (b) FFT spectrum (c) Phase Portrait (d) Poincare map

The value varies between 0.18 and 0.49 caused by the combination of the external excitation frequency f_t, the bending moment frequency f_b and meshing frequency f_1.

The *LSRs* of the other planets are similar to that shown in Figure 6.12 with phase shifts of $2\pi/3$. It is considered that the loads on the planet gears are equally shared.

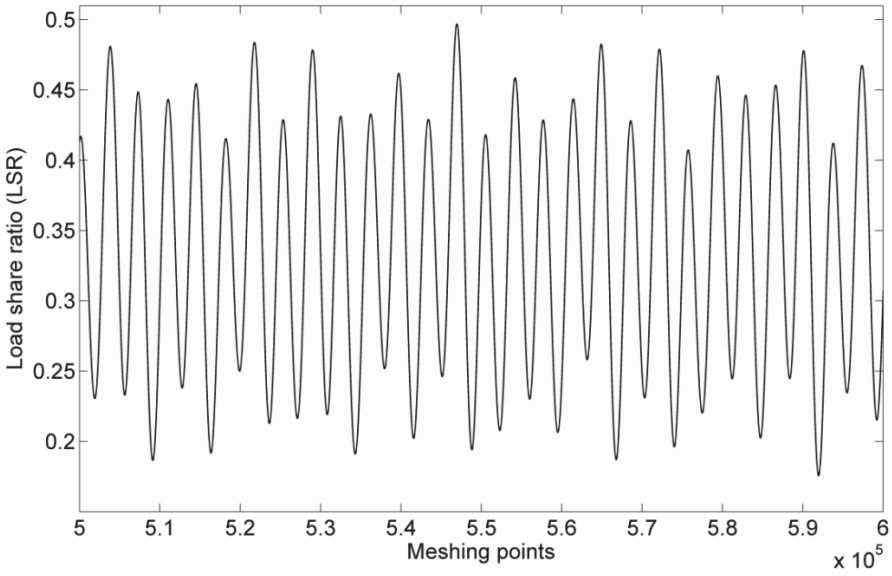

Figure 6.12. Load share ratio (LSR)

The following two figures present the radial and axial displacement of the planet gear, as shown in Figures 6.13 and 6.14. They have shown similar patterns, and the peak of f_1 is larger than the other two frequency components f_b and f_t, which means the meshing frequency f_1 still has more effect on X_p and X_{pa}.

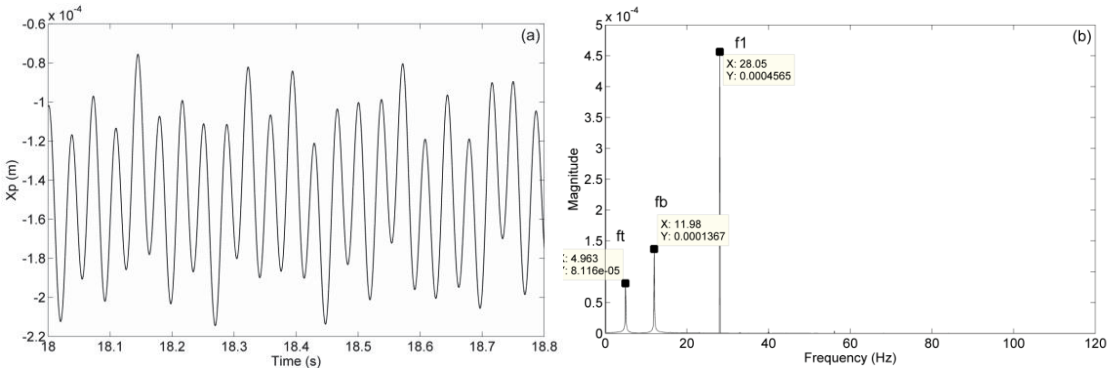

Figure 6.13. The radial vibrational responses of planet gears $\boldsymbol{X_p}$ (a) Time histories (b) FFT spectrum

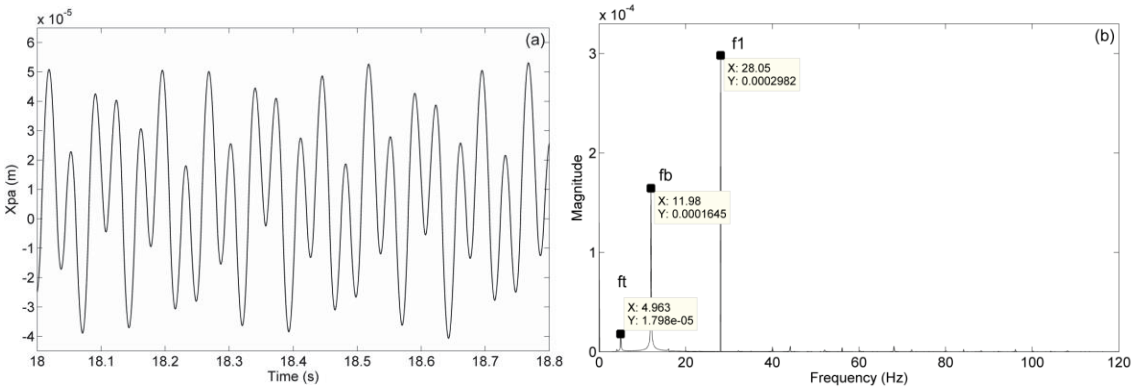

Figure 6.14. The axial vibrational responses of planet gears $\boldsymbol{X_{pa}}$ (a) Time histories (b) FFT spectrum

More simulations with different fluctuation ratio (mean-to-alternating force ratio) are provided in Appendix (Chapter 8).

6.3.3 Wind fluctuation and bending moment with $M_y/T_{in} = 1$

In this section, an increasing bending moment is applied to the main shaft for $\mathrm{M_y/T_{in}} = 1$. The dynamic response of Q_{rp1} and Q_{sp1} are shown in Figures 6.15 and 6.16. The LSR is presented in Figure 6.17. The radial and axial displacement X_p and X_{pa} are presented in Figures 6.18 and 6.19.

In Figure 6.15, the time histories of Q_{rp1} has shown larger magnitudes than that in Figure 6.10(a), due to the increased bending moment. The meshing frequency f_1 still has the largest influence on Q_{rp1}, but the bending moment starts to affect more on the ring-planet gear meshes Q_{rp}. The external torsional frequency f_t is observed with smaller magnitude, which indicates that the driving torque does not have the major influence on Q_{rp1}. Figures 6.15(c) and 6.15(d) present non-periodic circles in phase

portrait and a closed orbit with combined excitation frequencies in Poincare map. These suggest Q_{rp1} to be quasi-periodic.

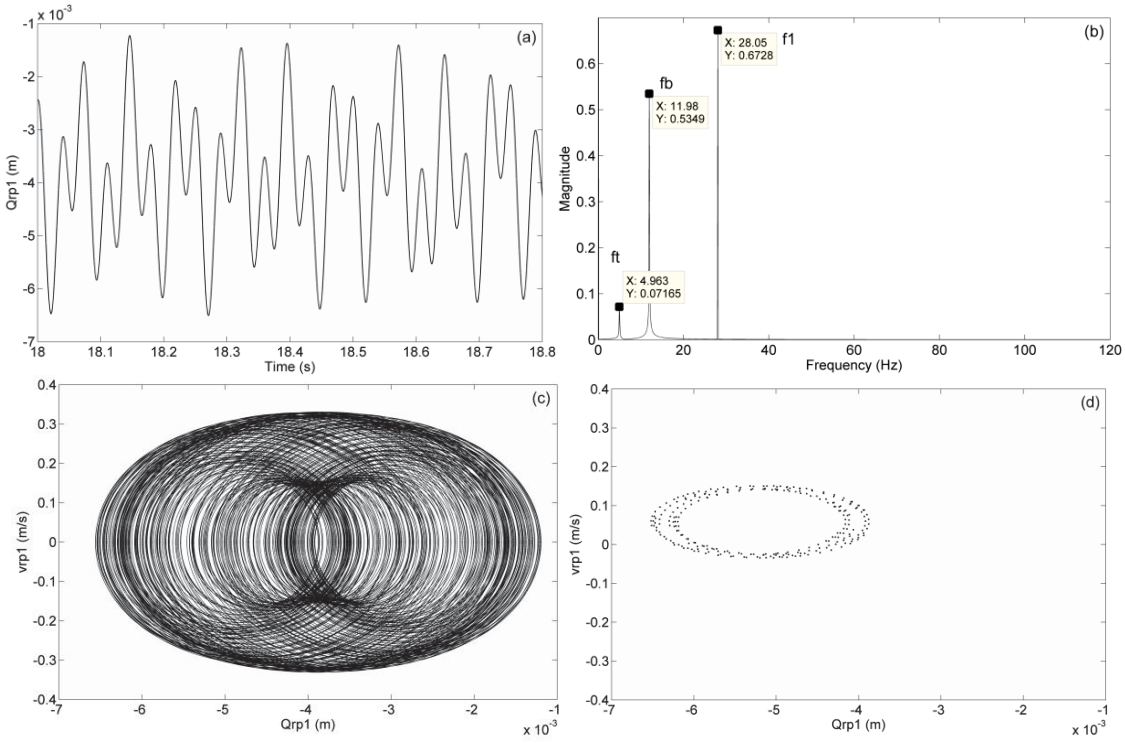

Figure 6.15. The vibrational responses of $\boldsymbol{Q_{rp1}}$ (a) Time histories (b) FFT spectrum (c) Phase Portrait (d) Poincare map

The time histories of the Q_{sp1} in Figure 6.16(a) present similar patterns as shown in Figure 6.11(a). The FFT spectrum present three frequency components f_t, f_b and f_1. It is observed that the meshing frequency f_1 has the largest influence on the sun-planet gear meshes Q_{sp1}, and the effect of the bending moment is increased compared with that in Figure 6.11(b) but still affects the least on Q_{sp1} among the three existing excitation frequencies. On the other hand, the bending moment has less effects than the driving torque, which is different from the dynamic response of the ring-planet gear meshes Q_{rp1} shown in Figure 6.15(b). Figures 6.16(c) and 6.16(d) present the phase

portrait and Poincare map, which repeat themselves with three excitation frequencies. These indicate that the response of Q_{sp1} is periodic.

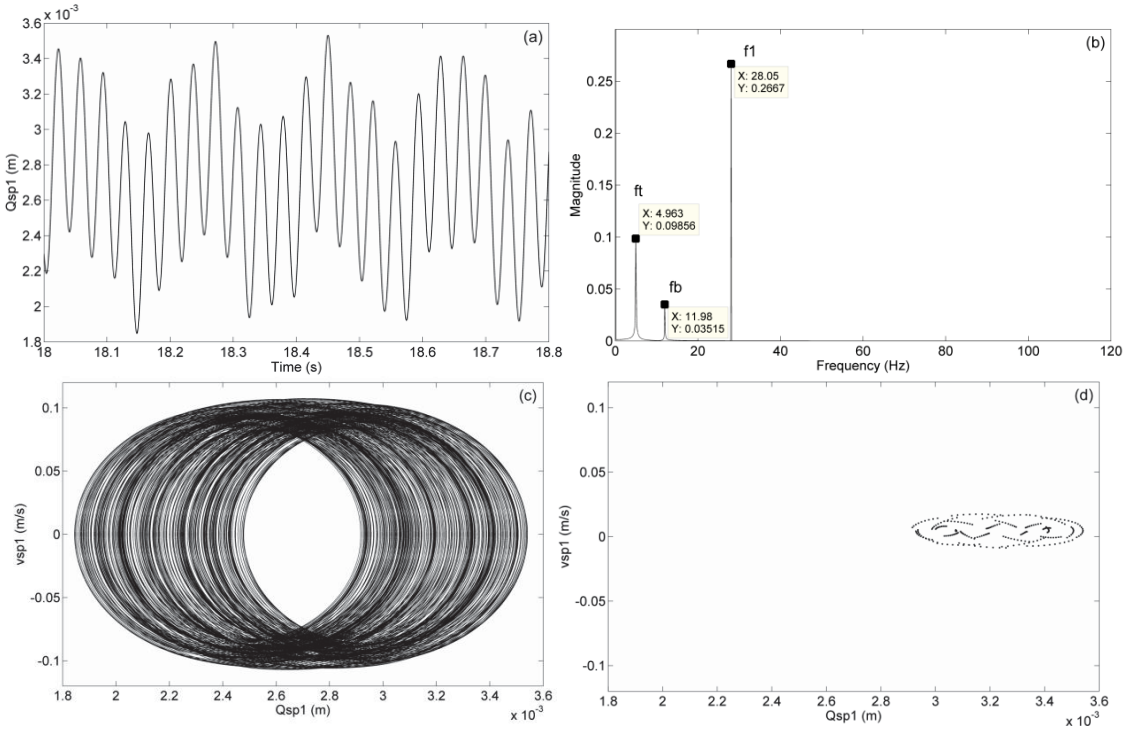

Figure 6.16. The vibrational responses of $\boldsymbol{Q_{sp1}}$ (a) Time histories (b) FFT spectrum (c) Phase Portrait (d) Poincare map

The ratio fluctuates between 0.18 and 0.5 with the external excitation frequency f_t, the bending moment frequency f_b and meshing frequency f_1. Due to the increased influence of the bending moment, the pattern of LSR has slightly changed.

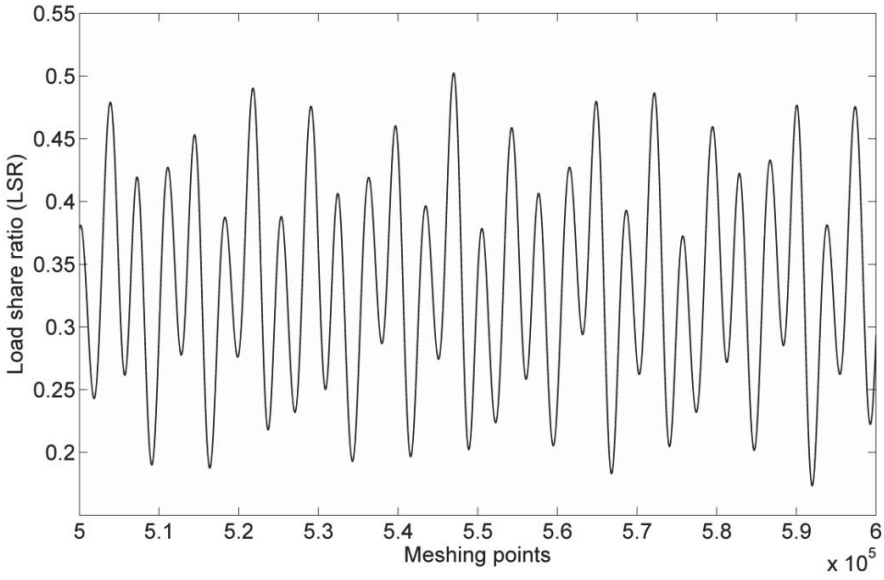

Figure 6.17. Load share ratio (LSR)

The radial displacement of planet gear is shown in Figure 6.18. Three frequency components f_t, f_b and f_1 are observed. The peak of f_1 is larger than the other two frequency components f_b and f_t, which means the meshing frequency f_1 has the most effect on X_p. Compared with the radial displacement, the axial displacement of the planet gear is shown in Figure 6.19. The bending moment frequency f_b contributes the most among all the excitation frequencies, and the meshing frequency f_1 affects slightly less than the bending moment.

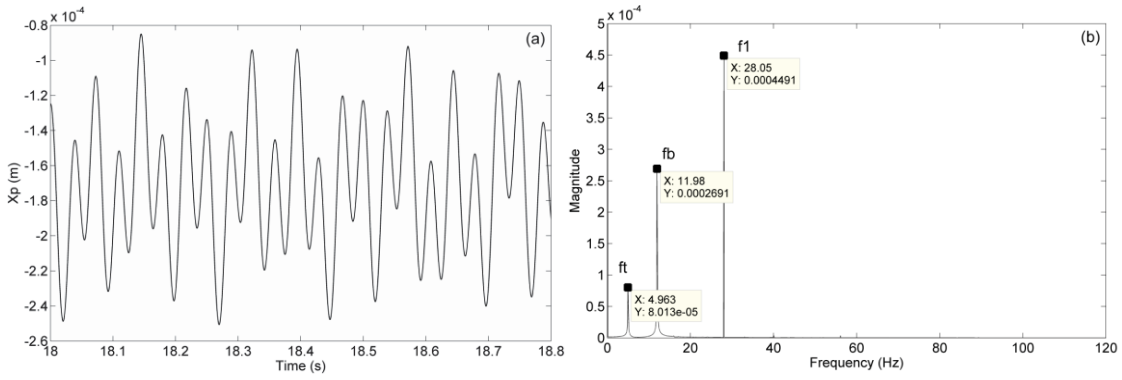

Figure 6.18. The radial vibrational responses $\boldsymbol{X_p}$ (a) Time histories (b) FFT spectrum

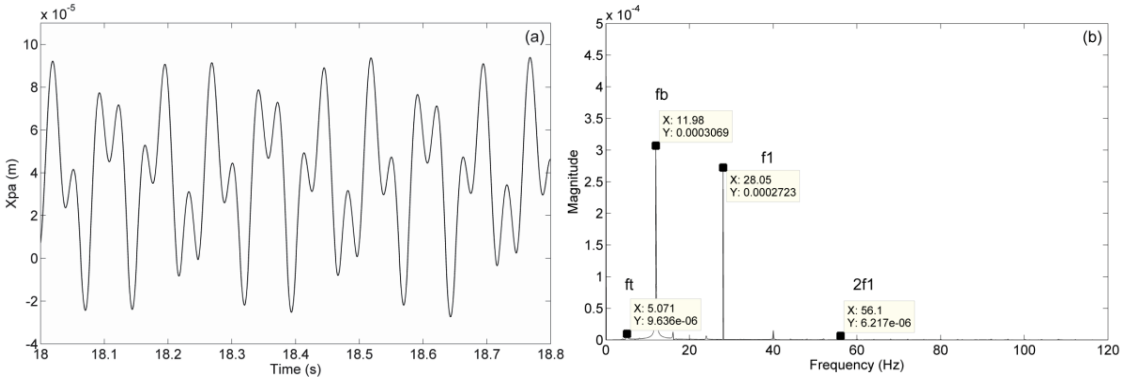

Figure 6.19. The axial vibrational responses $\boldsymbol{X_{pa}}$ (a) Time histories (b) FFT spectrum

6.3.4 Wind fluctuation and bending moment with $M_y/T_{in} = 5$

When non-dimensional quantity M_y/T_{in} is increased to 5, the time histories of Q_{rp1} in Figure 6.20(a) has shown much larger magnitudes compared with that in Figure 6.15(a). The meshing frequency f_1 no longer has the largest influence on the ring-planet gear meshes Q_{rp1}, instead the bending moment affects the most on Q_{rp}, and the external torsional frequency f_t is observed with much smaller magnitude. Figures 6.20(c) and 6.20(d) present non-periodic circles in phase portrait and a closed orbit with combined excitation frequencies in Poincare map. These suggest Q_{rp1} to be quasi-periodic

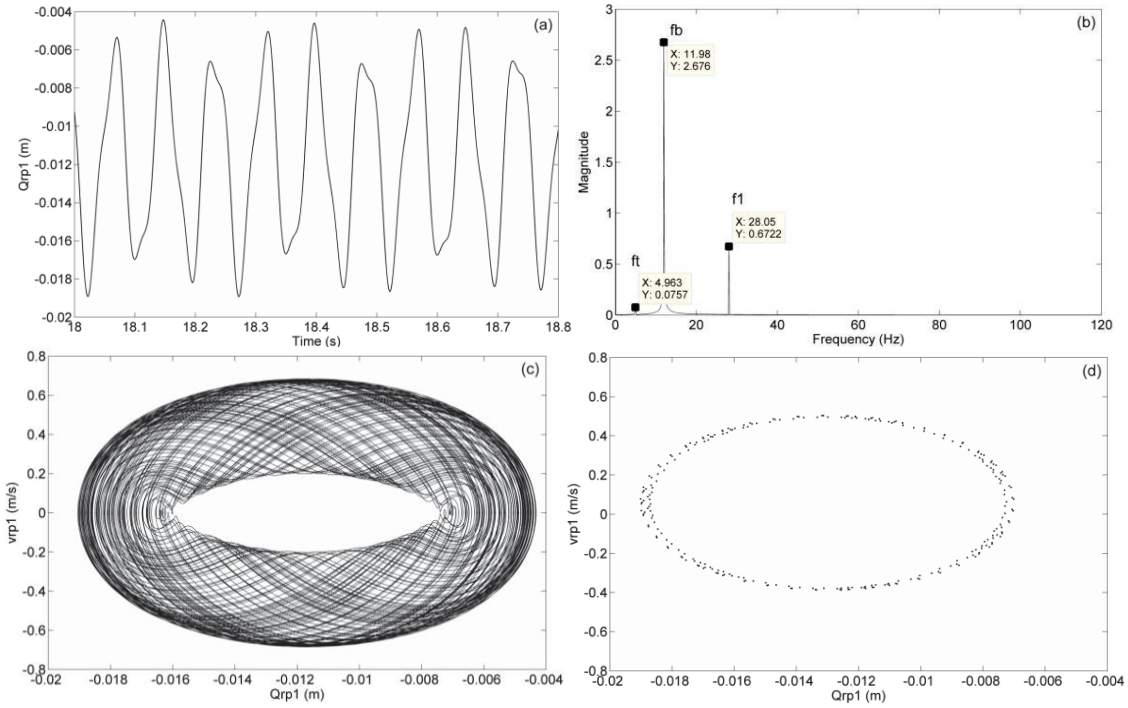

Figure 6.20. The vibrational responses of $\boldsymbol{Q_{rp1}}$ (a) Time histories (b) FFT spectrum (c) Phase Portrait (d) Poincare map

The time histories present similar patterns as the Q_{sp1} as shown in Figure 6.21(a). The FFT spectrum present three frequency components f_t, f_b and f_1. It is observed that the meshing frequency f_1 has the largest influence on the sun-planet gear meshes Q_{sp1}, and the effect of the bending moment is increased compared with that in Figure 6.16(b), which affects the least on Q_{sp1} among the three existing excitation frequencies. On the other hand, the bending moment has the second largest effect than the driving torque, which is different from the dynamic response of the ring-planet gear meshes Q_{rp1}. Figures 6.21(c) and 6.21(d) present the phase portrait and Poincare map, which repeat themselves with three excitation frequencies. These indicate that the response of Q_{sp1} is periodic.

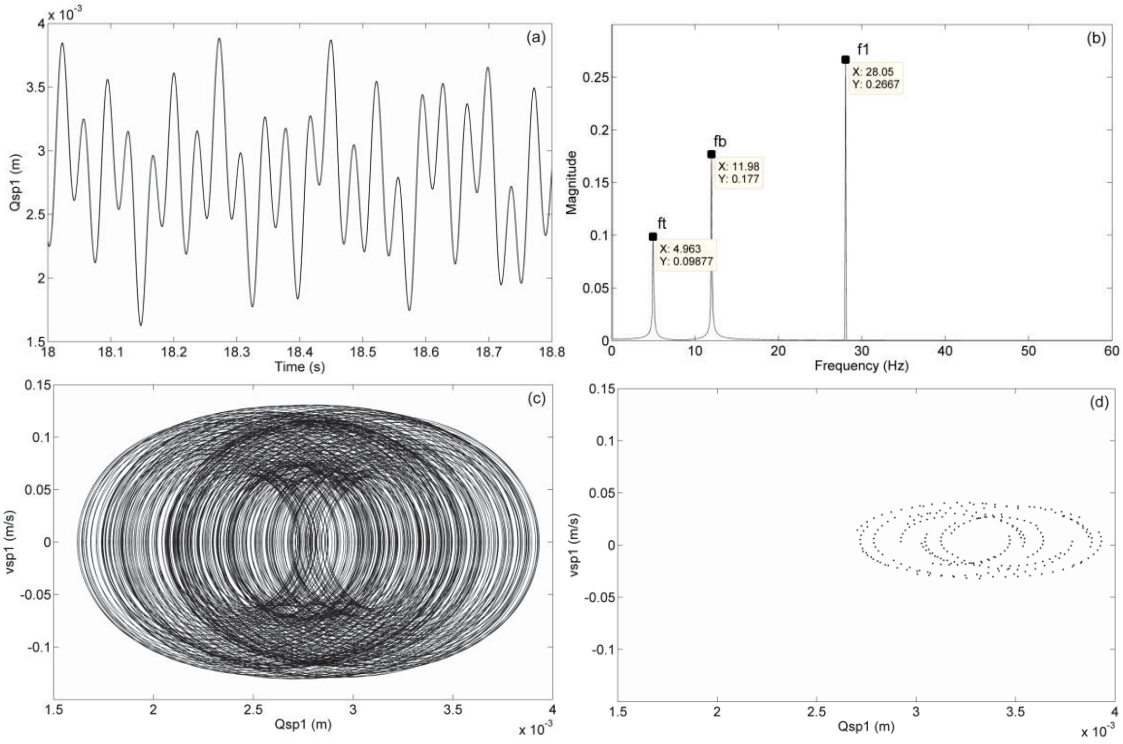

Figure 6.21. The vibrational responses of $\boldsymbol{Q_{sp1}}$ (a) Time histories (b) FFT spectrum (c) Phase Portrait (d) Poincare map

The ratio fluctuates between 0.15 and 0.53 with the external excitation frequency f_t, the bending moment frequency f_b and meshing frequency f_1. Due to the increased influence of the bending moment, the pattern of LSR has changed.

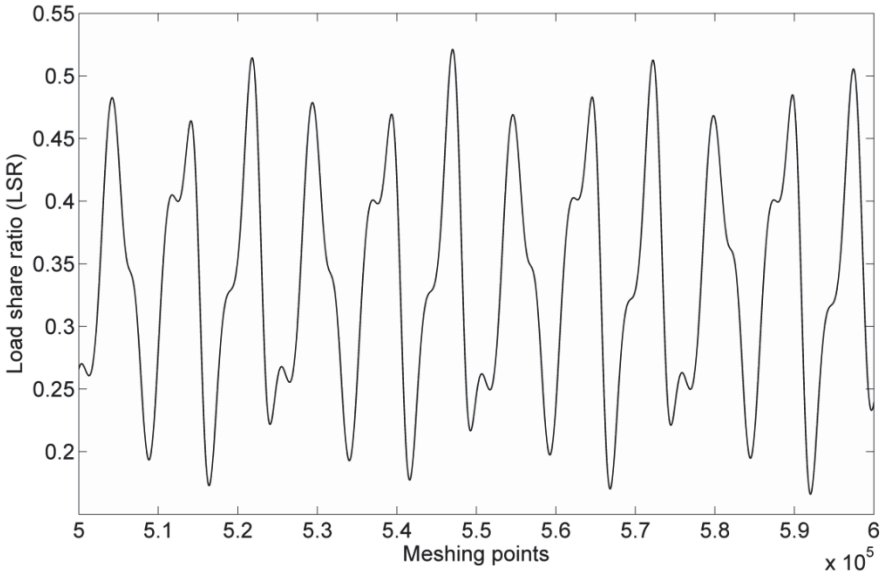

Figure 6.22. Load share ratio (LSR)

The radial displacement of planet gear is shown in Figure 6.23. Three frequency components f_t, f_b and f_1 are observed. The peak of f_b is larger than the other two frequency components f_t and f_1, which means the bending moment frequency f_b has the most effect on X_p. Similarly, the axial displacement of the planet gear is shown in Figure 6.24. The bending moment frequency f_b contributes the most among all the excitation frequencies, and the meshing frequency f_1 affects less than the bending moment.

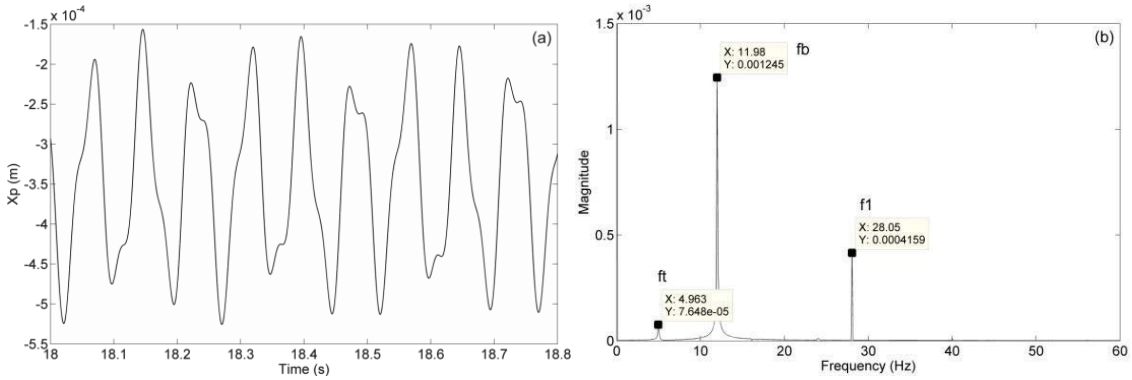

Figure 6.23. The radial vibrational responses $\boldsymbol{X_p}$ (a) Time histories (b) FFT spectrum

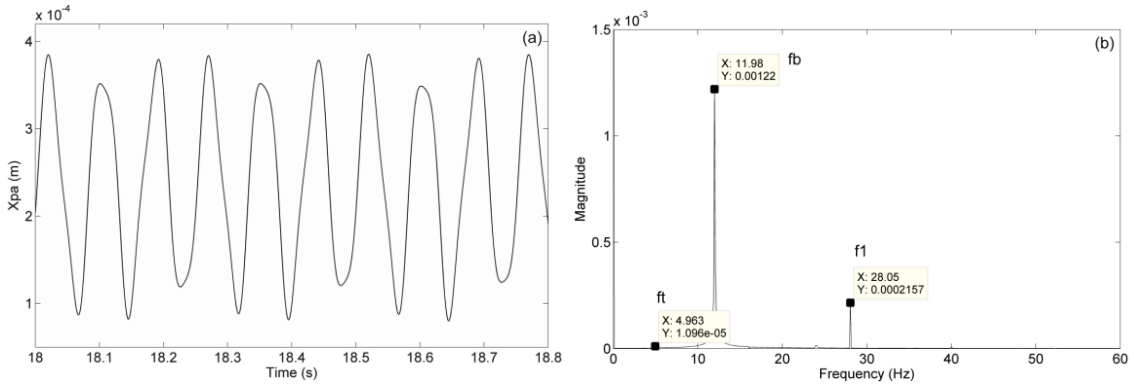

Figure 6.24. The axial vibrational responses $\boldsymbol{X_{pa}}$ (a) Time histories (b) FFT spectrum

6.3.5 Increased driving torque and bending moment with $M_y/T_{in} = 1$

When the driving torque is increased, the time histories of Q_{rp1} is presented in Figure 6.25(a). Compared with Figure 6.15, the magnitude of Q_{rp1} is increased. However, because the M_y/T_{in} ratio remains at 1, the bending moment frequency f_b has the largest influence on the ring-planet gear meshes Q_{rp1}. The external torsional frequency f_t is observed with smaller magnitude. Figures 6.25 (c) and 6.25(d) present non-periodic circles in phase portrait and a closed orbit with combined excitation frequencies in Poincare map. These suggest Q_{rp1} to be quasi-periodic

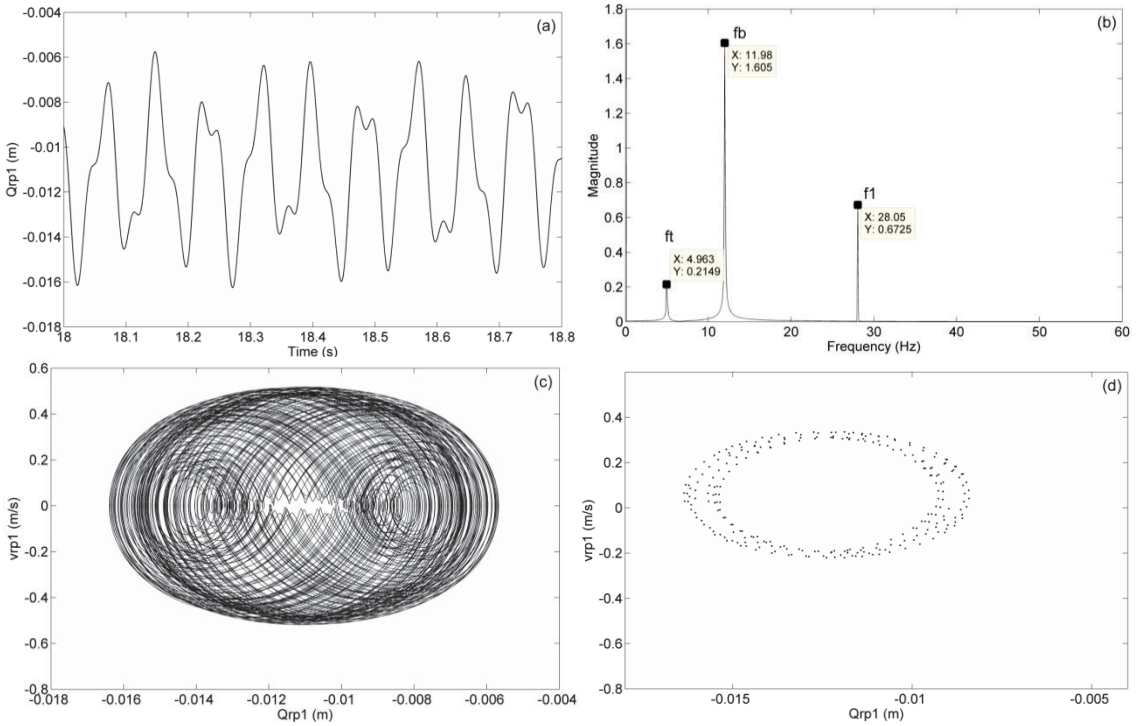

Figure 6.25. The vibrational responses of $\boldsymbol{Q_{rp1}}$ (a) Time histories (b) FFT spectrum (c) Phase Portrait (d) Poincare map

In Figure 6.26, the time histories of Q_{sp1} has shown larger magnitudes compared with that in Figure 6.16(a). The driving torque and the meshing frequency have the equally influence on Q_{sp1}, and the bending moment affect less on the ring-planet gear meshes Q_{rp}. Figures 6.26(c) and 6.26(d) present non-periodic circles in phase portrait and a closed orbit with combined excitation frequencies in Poincare map. These suggest Q_{sp1} to be quasi-periodic.

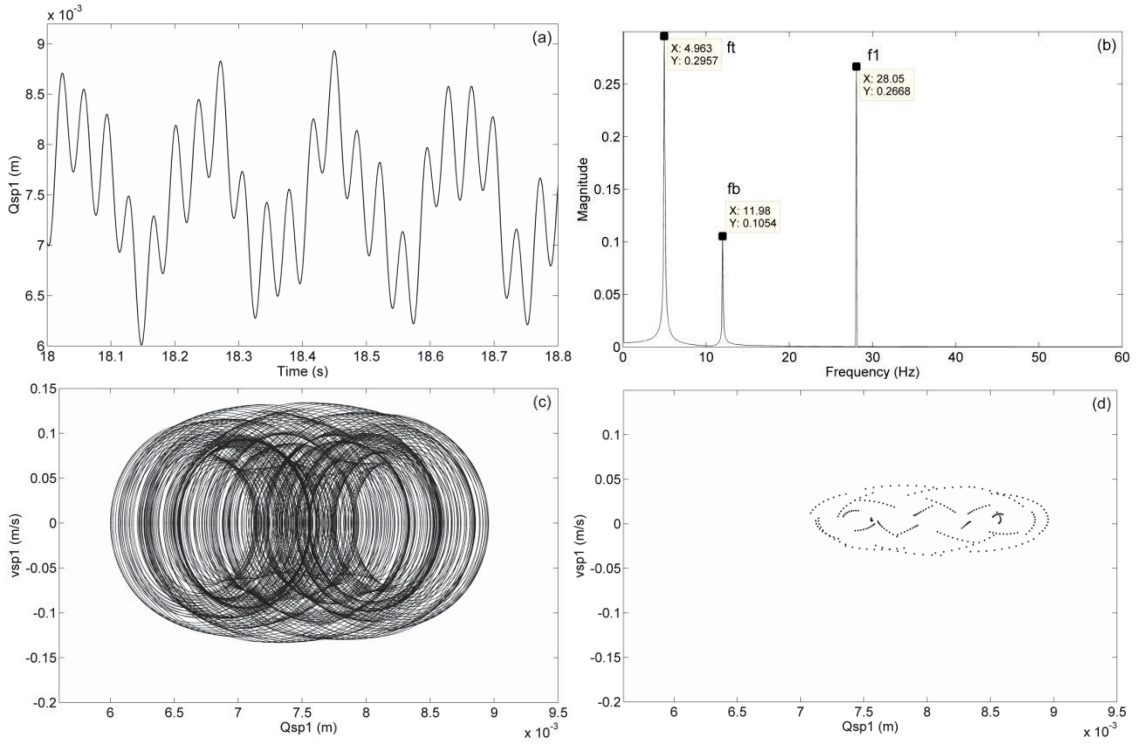

Figure 6.26. The vibrational responses of $\boldsymbol{Q_{sp1}}$ (a) Time histories (b) FFT spectrum (c) Phase Portrait (d) Poincare map

The ratio fluctuates between 0.23 and 0.435 with the external excitation frequency f_t, the bending moment frequency f_b and meshing frequency f_1. Due to the increased influence of the bending moment, the pattern of LSR has slightly changed.

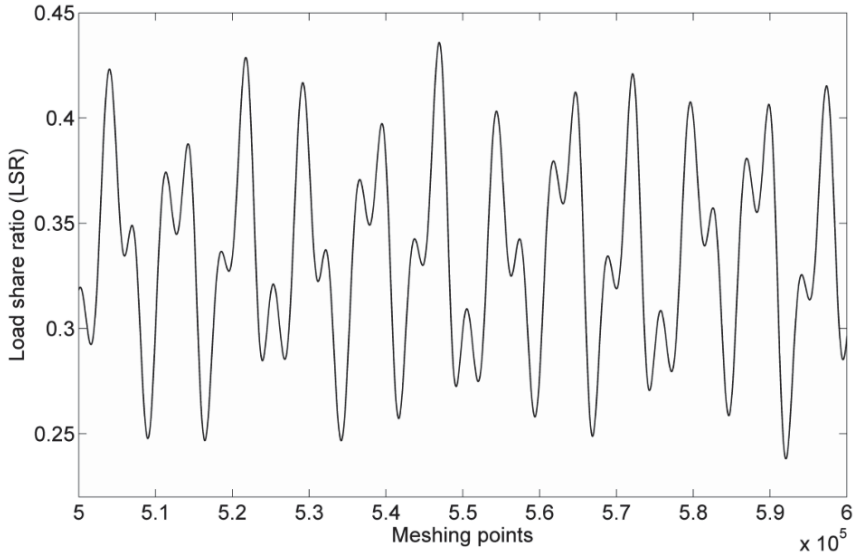

Figure 6.27. Load share ratio (LSR)

The radial displacement of planet gear is shown in Figure 6.28. Three frequency components f_t, f_b and f_1 are observed. The peak of f_b is larger than the other two frequency components f_t and f_1. Compared with the radial displacement, the axial displacement of the planet gear is shown in Figure 6.29. The bending moment frequency f_b still contributes the most among all the excitation frequencies, and the effect of the driving torque frequency f_t affects little, and can be ignored.

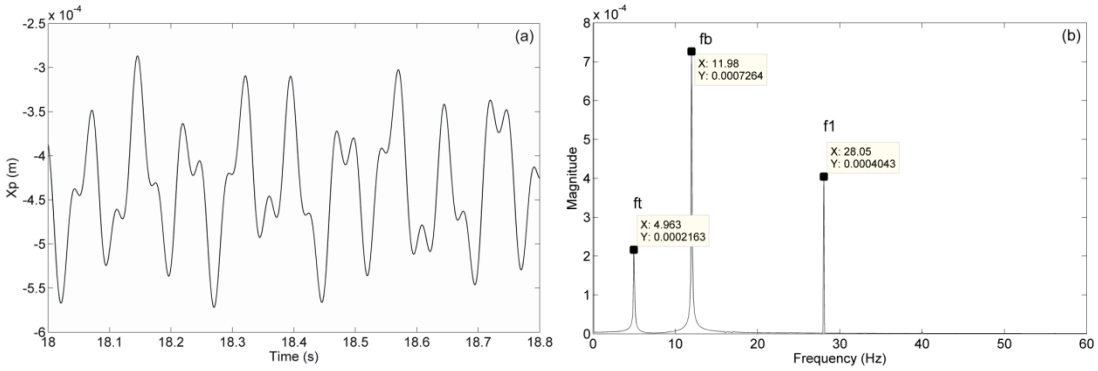

Figure 6.28. The radial vibrational responses $\boldsymbol{X_p}$ (a) Time histories (b) FFT spectrum

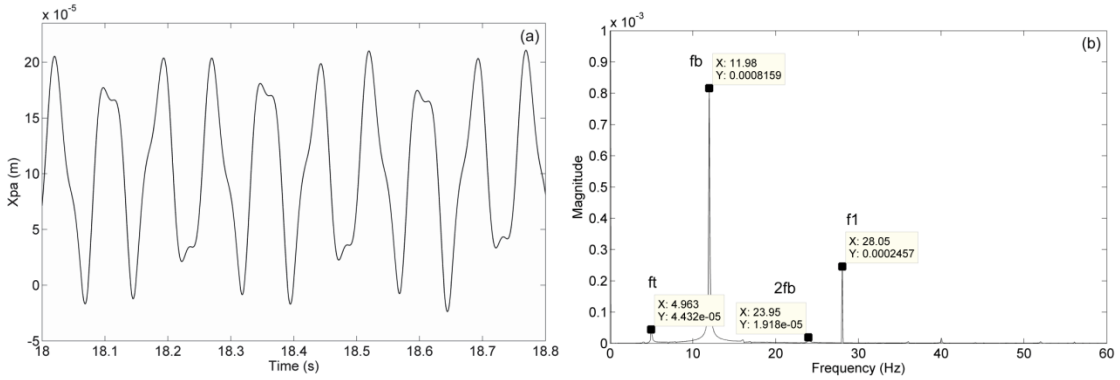

Figure 6.29. The axial vibrational responses $\boldsymbol{X_{pa}}$ (a) Time histories (b) FFT spectrum

6.3.6 Effects of the bearing clearances

In this section, the effects of bearing clearance studied. Only the dynamic responses of the ring-planet gear meshes Q_{rp1} are presented in Figure 6.30. When the bearing clearance taken into account, the loads are transferred to the gear meshes, thus the gear loads are increased. Gearbox may have the gear misalignments as the radial and axial displacements exist. When the bearing clearance is not considered, the bearings are used to support the non-torque loadings. The loads are better shared among gears, but the bearings would support more, which increases the possibility of the bearing fatigue and may lead to failures. The gear tooth patterns have very little differences between the conditions with and without bearing clearances, and thus the bearing clearance has negligible effects on gear meshes.

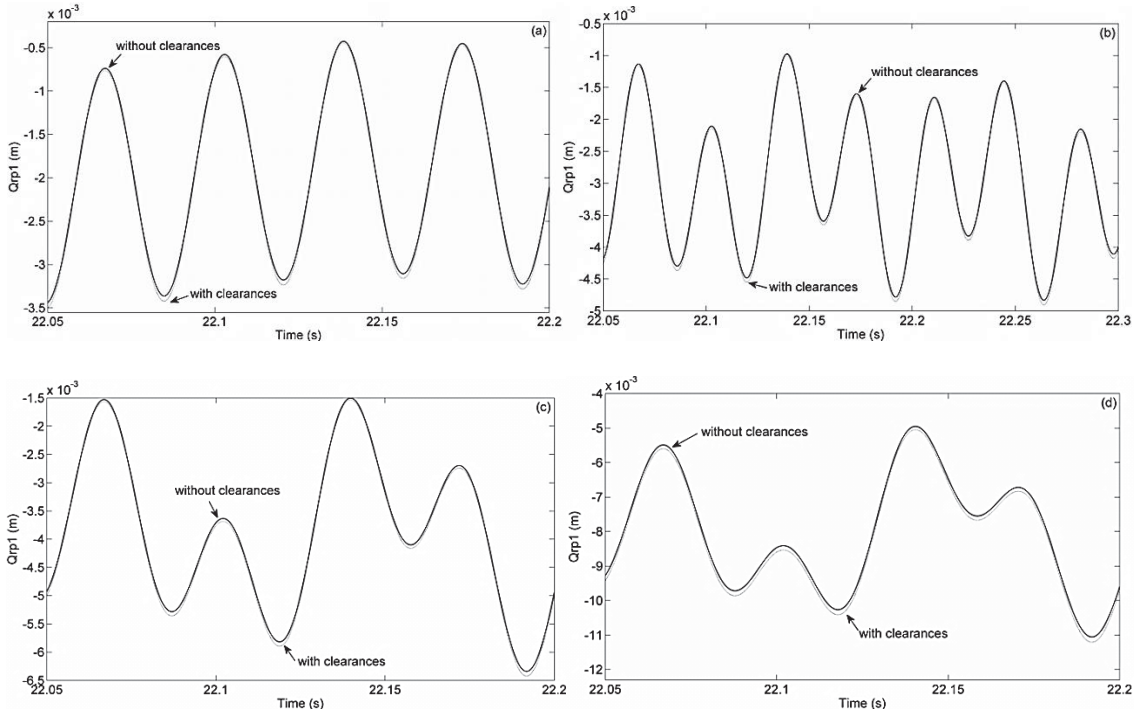

Figure 6.30. Comparison between the vibrational responses Q_{rp1} with and without bearing clearances. (a) Driving torque only; (b) $M_y/T_{in} = 0.5$; (c) $M_y/T_{in} = 1$; (d) with increased T_{in} at $M_y/T_{in} = 0.5$

6.4 Discussions

This chapter established a 6DOF dynamic model of a wind turbine planetary gearbox. When only the driving torque is considered as the main loading, it was found that the radial and axial displacements of the planet gear are smaller than their gear meshes, because the movement of the planet gears are nearly balanced by the self-equilibrating tooth loads at the sun-planet and ring-planet meshes. On the other hand, the meshing frequency f_m has the most influence on gear meshes (e.g. Q_{rp} and Q_{sp}), and the ring-planet gear mesh Q_{rp} is more influenced compared with the sun-planet gear mesh Q_{sp}.

Theoretically, carrier bearings with high load capacities carry the majority of these loads so that only a small fraction of the non-torque loads are transmitted into gears. Therefore, in the ideal case, the gear teeth only carry the driving torque. However, it has been proved that the bending moment affects the dynamic response of gearbox components, and plays an important role in gearbox reliability. When both the driving torque and the bending moment are taken into account, a nondimensional quantity M_y/T_{in} is introduced to address the combined loading, where M_y is the bending moment and T_{in} is the driving torque. It was observed that the effects of the bending moments are transmitted into gear meshes, and the results showed that the bending moment could affect gearbox internal responses such as the tooth contact patterns, especially the ring-planet gear meshes, and increases the tooth loads significantly in the planetary gear stage, which could cause the dynamic forces on planet bearings to shorten the gearbox life.

The bending moment and driving torque are found to be the decisive parameters for the dynamic responses of wind turbine gearbox components. The ring-planet gear meshes Q_{rp} are more sensitive to the bending moments compared to the sun-planet gear mesh Q_{sp}. Due to the fact that the dynamic response of the proposed gearbox is coupled in the different degrees of freedoms (DOFs), the driving torque also influences the non-torque DOFs, and the effect of bending moments on planetary gear loads depends upon driving torque. It can be seen that when the driving torque is increased, the tooth pattern has been changed significantly, and the increased driving torque has changed the effect of bending moments on the bearing loads and tooth-contact patterns.

In addition, the bearing clearances in the planetary gear stage have negligible effect, but it is suggested that a well-balanced design is important for the wind turbine planetary gear stage.

This page intentionally left blank

Chapter 7 Conclusions and future research

This thesis focuses on the study of wind turbine gearbox components. The background and challenges of wind energy industry are firstly introduced. A literature review regarding the wind turbine gearboxes and gear dynamics is provided, and the general information of wind turbines, including the drivetrain configurations, gearbox suspension layouts, gearbox types and components are also presented.

For the analysis of wind turbine gearboxes, the torsional vibrations of gearbox components were firstly studied. The nonlinear dynamic model developed considers the factors such as time-varying mesh stiffness, damping, static transmission error and gear backlash. Both the external excitation due to wind gust and the internal excitation due to static transmission error are included. With the help of time history, FFT spectrum, phase portrait, Poincare map and the effects of the static transmission error, mean-to-alternating force ratio and time-varying mesh stiffness on the dynamic behaviour of wind turbine gearbox components are investigated by using the numerical integration method. It is found that the external excitation has the most influence on the torsional vibrations of the wind turbine gearbox components. The mesh stiffness, being another significant factor, has more influence than the other internal excitation source, the static transmission error. The static transmission error has the least influence.

After that, the dynamic response of a wind turbine gearbox under different excitation conditions was studied. The proposed four-degree-of-freedom (4DOF) dynamic model takes into account the key factors such as the time-varying mesh stiffness, bearing stiffness, damping, static transmission error and gear backlash. It explains under which conditions the fretting corrosion, as one of the wind turbine gearbox failure modes, may

occur. Furthermore, it is observed that the external excitation fluctuation has large influence on the dynamic responses of both the gears and bearings.

Lastly, the effects of bending moments on the dynamic responses of a wind turbine planetary gearbox were explored. The proposed six-degree-of-freedom (6DOF) dynamic model takes into account the key factors such as the time-varying mesh stiffness, bearing stiffness, damping, static transmission error, gear backlash and bearing clearances. When only the driving torque is considered as the main loading, it was found that the radial and axial displacements of the planet gear are smaller than their gear meshes, and the meshing frequency has the most influence on gear meshes. What is more, it has been proved that the bending moment affect the dynamic response of gearbox components, and plays an important role in gearbox reliability. When both the driving torque and the bending moment are taken into account, it was observed that the effects of the bending moments are transmitted into gear meshes, and the results showed that the bending moment could affect gearbox internal responses such as the tooth contact patterns, especially the ring-planet gear meshes, and increases the tooth loads significantly in the planetary gear stage. Furthermore, the effect of bending moments on planetary gear loads depends upon driving torque. When the driving torque is increased, the tooth pattern has been changed significantly, and the increased driving torque has changed the effect of bending moments on the bearing loads and tooth-contact patterns. In addition, the bearing clearances in the planetary gear stage have negligible effect, but it is suggested that a well-balanced design is important for the wind turbine planetary gear stage.

For the research in the future, the study of the offshore wind turbines would be important. Although there are many similarities between the designs of onshore and offshore wind turbines, the configuration of the offshore wind turbines is similar to that of the land-based wind turbines, but with much larger capacity and more complicated loadings. On the other hand, there are still differences between them that result from the particular operating environment. For example, the installation in water is more difficult than on land and becomes increasingly harder with deeper water. Based on the gearbox models presented in this thesis, the study of the offshore wind turbine gearbox and drivetrain would be the next research topic.

Furthermore, the floating platform for offshore wind turbines would be another important topic in the future, because designing an offshore wind turbine is a multi-disciplinary research topic. Currently, there are a number of permutations and combinations of platforms and wind turbine configurations being researched, and the platforms would be designed to accommodate single or multiple turbines, with two or three blades suitable for upwind, downwind, vertical or horizontal mounting.

What is more, the load study and the optimization of wind turbine bearings would be one of the major research topics in the future. These include the design of the bearings for the blade pitch, nacelle yaw system, support bearings on the main shaft, and the bearings inside the gearbox and the generator.

In addition, the study of the direct drivetrain would be another topic in the future. As the generator is directly driven by the rotor, a high number of pole pairs would be needed to provide the given electrical grid frequency using the low rotational speed from the rotor.

To transfer the power at low rotational speed conditions, a high torque would then be required.

Chapter 8 Appendices

8.1 Gear

Sketches of a spur gear tooth are presented in Figures 8.1 and 8.2.

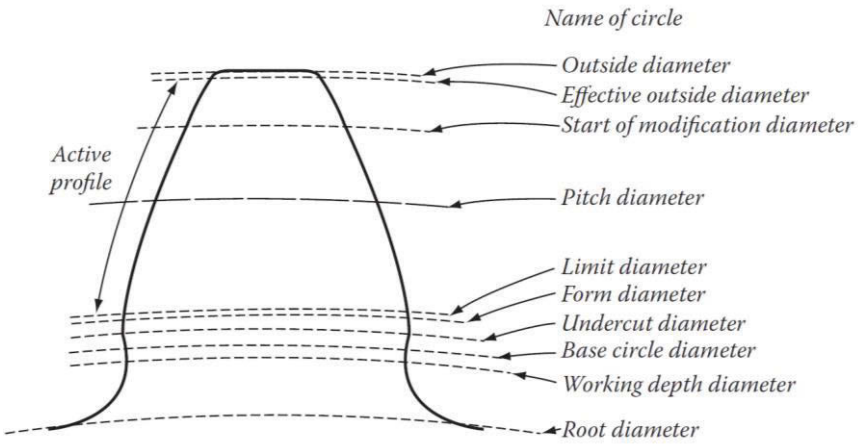

Figure 8.1. Nomenclature of a gear tooth [182]

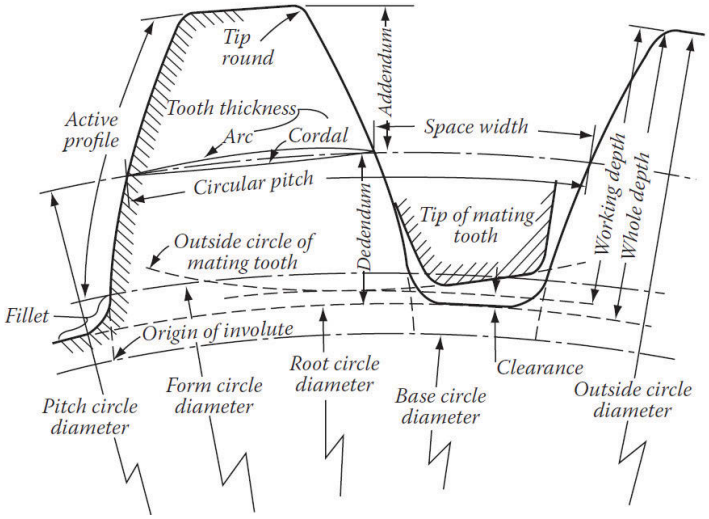

Figure 8.2. Gear tooth nomenclature [182]

- Base circle - the cylinder from which the involute curve originates.
- Pitch point - the point between the axes of the gear set at which the teeth

contact. It defines the dimension of the pitch circle.

- Pitch circle - divides the tooth profile in two sections, generally at five-ninths of the height of the tooth. The portion of the tooth extending from the pitch circle is called the addendum and the section below is called the dedendum.
- Line of action - a line described by the points of contact of the gear tooth as it rotates. The line of action is tangent to both base circles of the gear set and passes through the pitch point.
- Pressure angle - the angle between the tangent of the pitch circle and the line of action.

Control of the continuity of action can be obtained by varying following factors:

(1). The slope of the line of action.

(2). The outside diameters of the gear and pinion.

(3). The shape of the active profile.

(4). The relative sizes of the limit diameter and undercut diameter circles.

8.2 Wind fluctuation and bending moment with $M_y/T_{in} = 0.5$

8.2.1 Mean-to-alternating force ratio $F_m/F_a = 10$

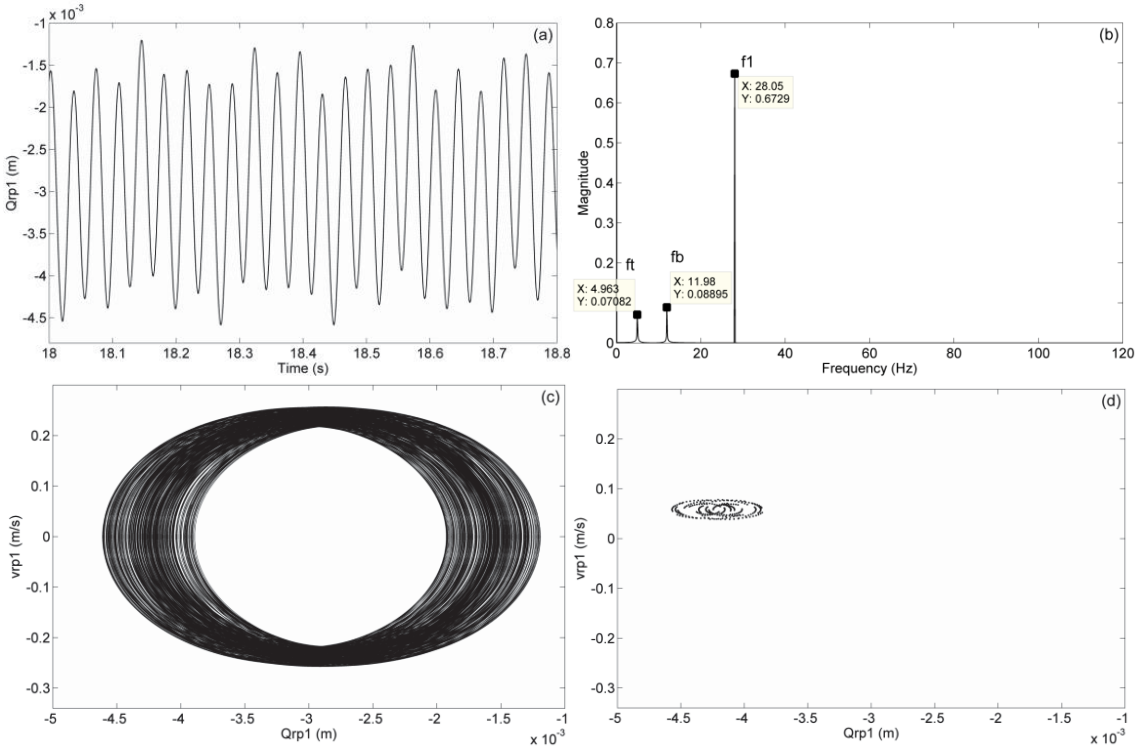

Figure 8.3. The vibrational responses of Q_{rp} (a) Time histories (b) FFT spectrum (c) Phase Portrait (d) Poincare map

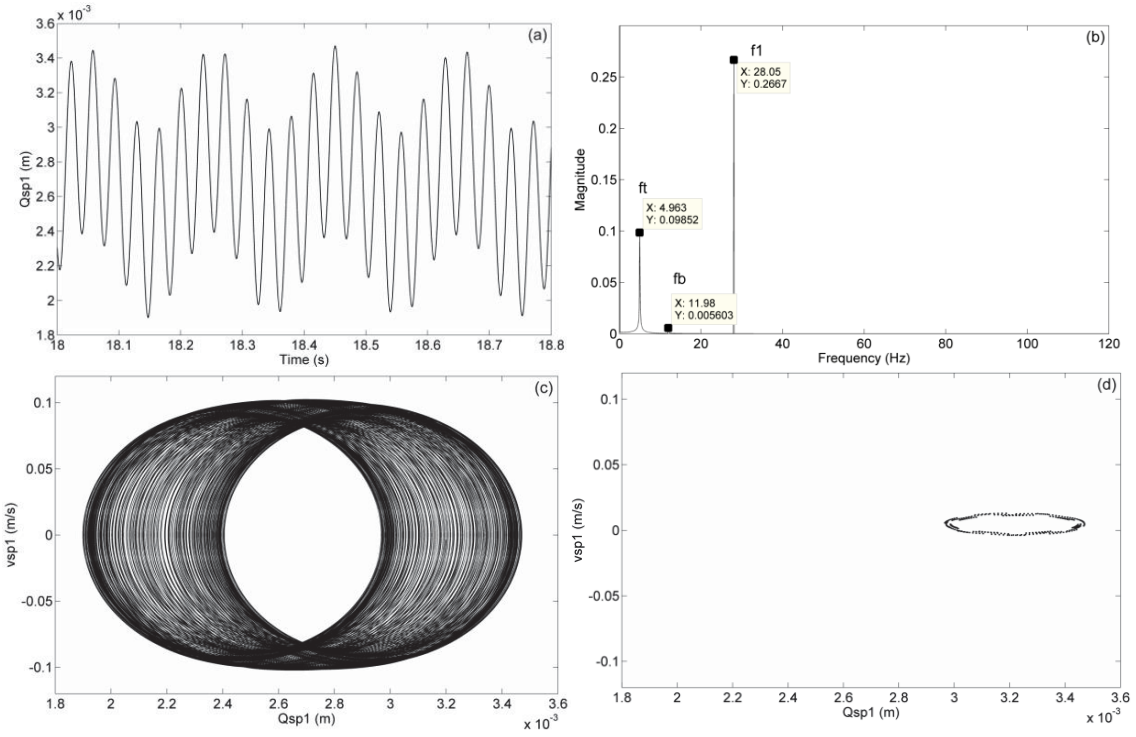

Figure 8.4. The vibrational responses of Q_{sp} (a) Time histories (b) FFT spectrum (c) Phase Portrait (d) Poincare map

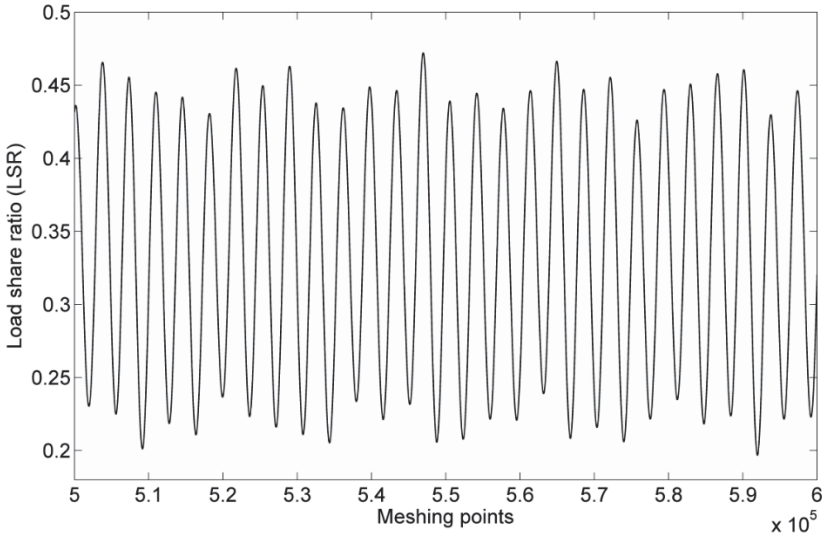

Figure 8.5. Load share ratio (LSR)

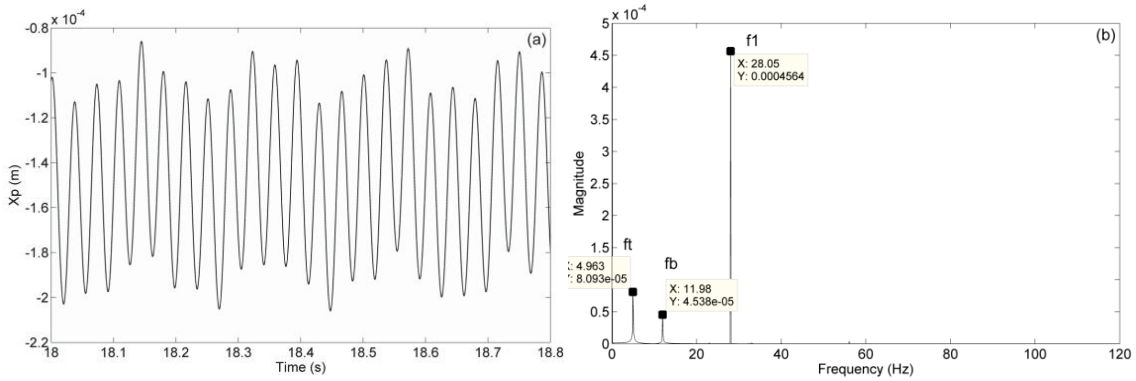

Figure 8.6. The radial vibrational responses of planet gears X_p (a) Time histories (b) FFT spectrum

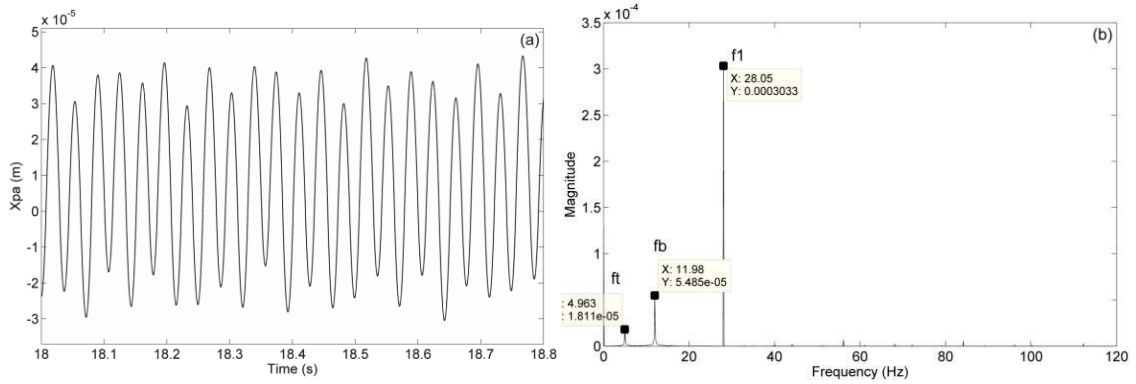

Figure 8.7. The axial vibrational responses of planet gears X_{pa} (a) Time histories (b) FFT spectrum

8.2.2 Mean-to-alternating force ratio $F_m/F_a = 2$

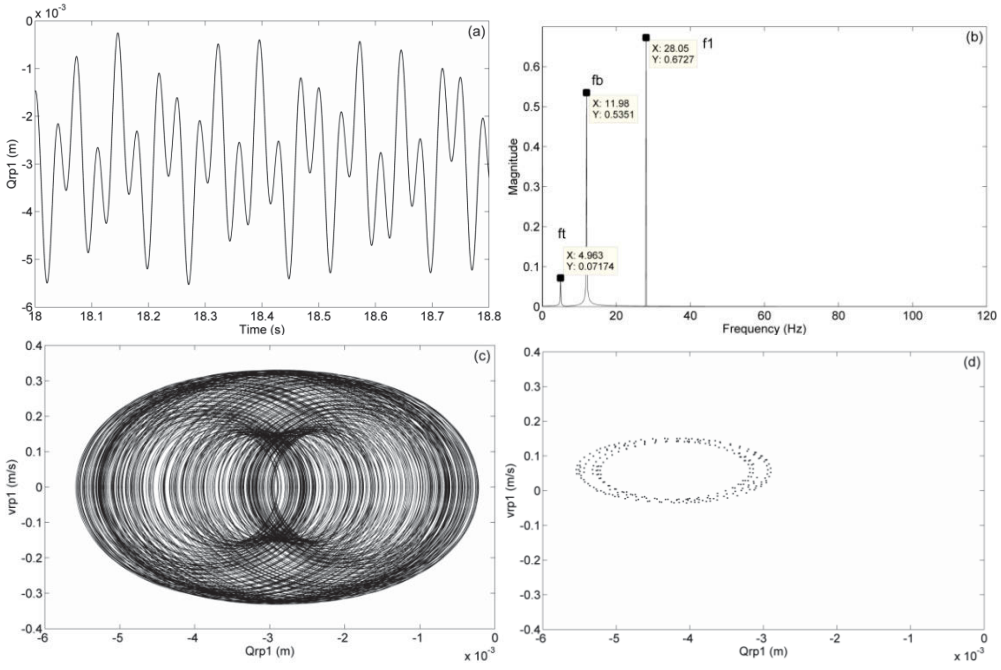

Figure 8.8. The vibrational responses of Q_{rp} (a) Time histories (b) FFT spectrum (c) Phase Portrait (d) Poincare map

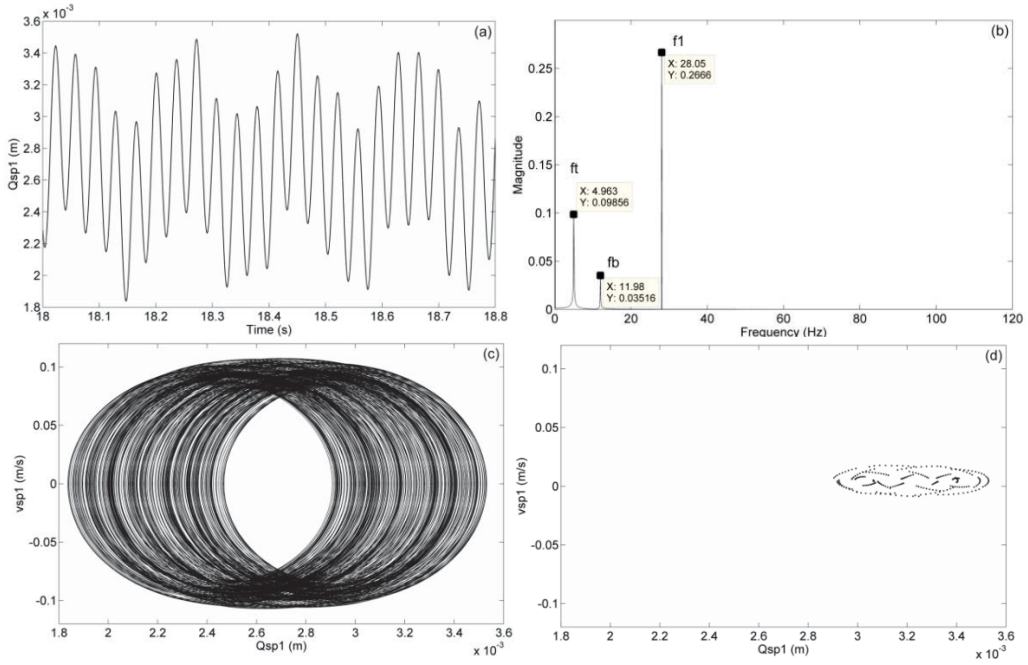

Figure 8.9. The vibrational responses of Q_{sp} (a) Time histories (b) FFT spectrum (c) Phase Portrait (d) Poincare map

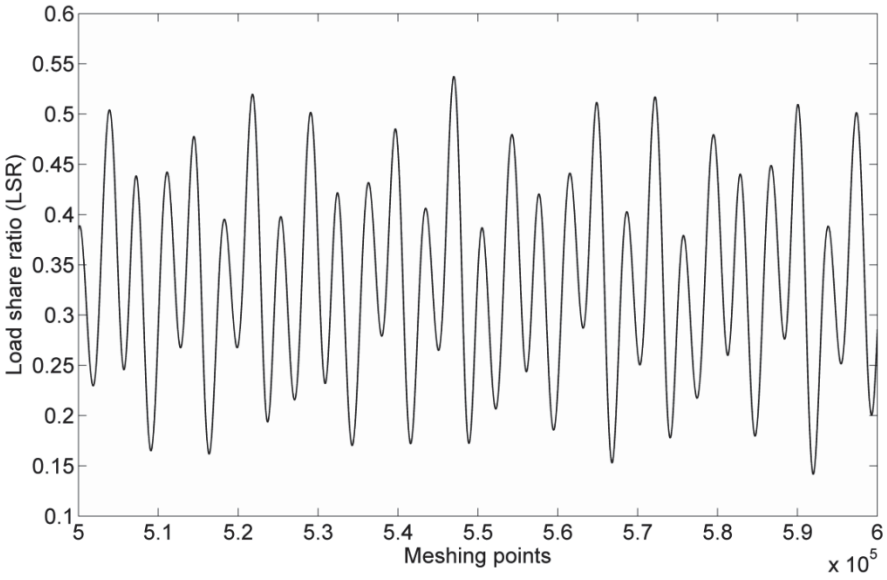

Figure 8.10. Load share ratio (LSR)

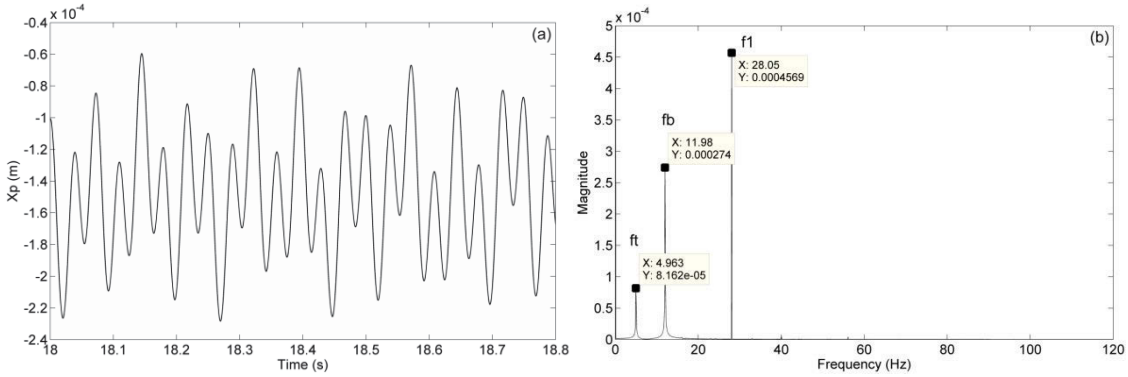

Figure 8.11. The radial vibrational responses of X_p (a) Time histories (b) FFT spectrum

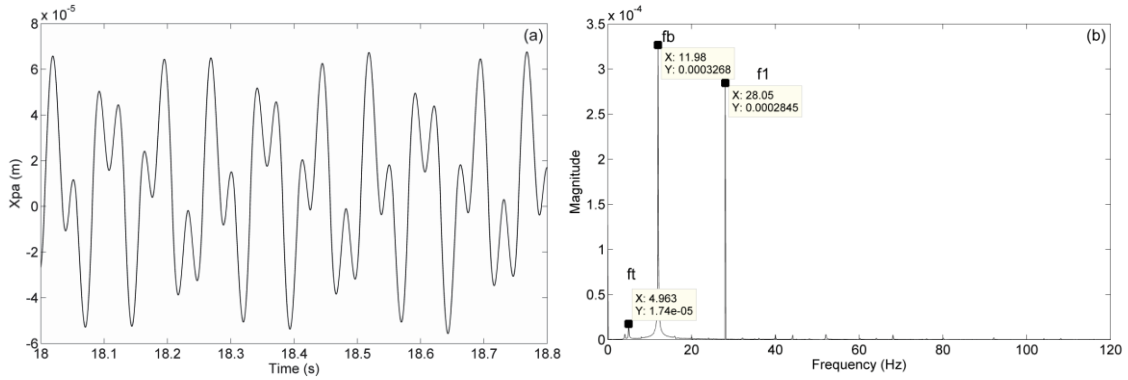

Figure 8.12. The axial vibrational responses of X_{pa} (a) Time histories (b) FFT spectrum

8.3 Wind fluctuation and bending moment with $M_y/T_{in} = 1$

8.3.1 Mean-to-alternating force ratio $F_m/F_a = 10$

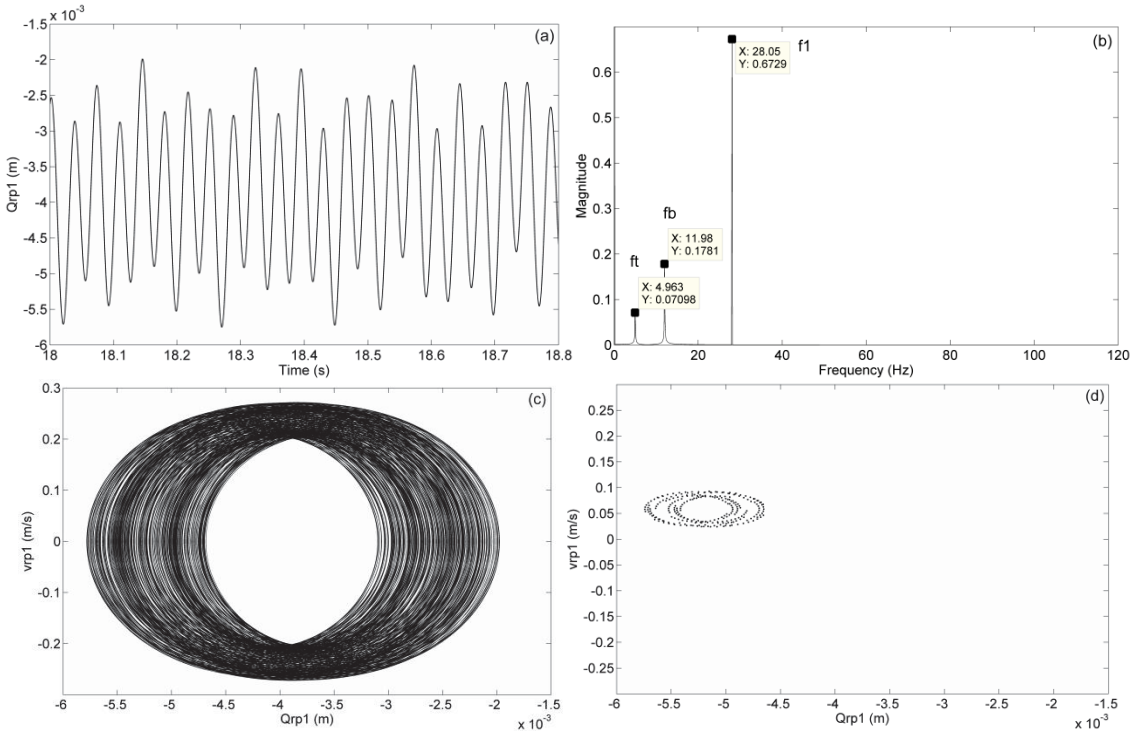

Figure 8.13. The vibrational responses of Q_{rp} (a) Time histories (b) FFT spectrum (c) Phase Portrait (d) Poincare map

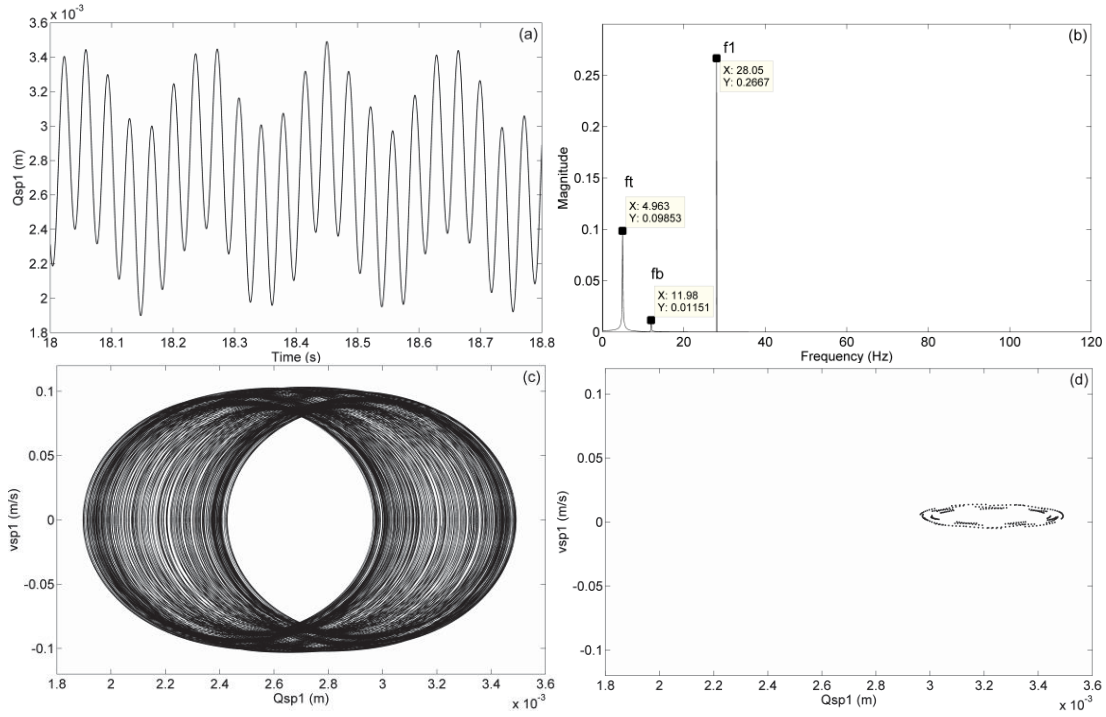

Figure 8.14. The vibrational responses of Q_{sp} (a) Time histories (b) FFT spectrum (c) Phase Portrait (d) Poincare map

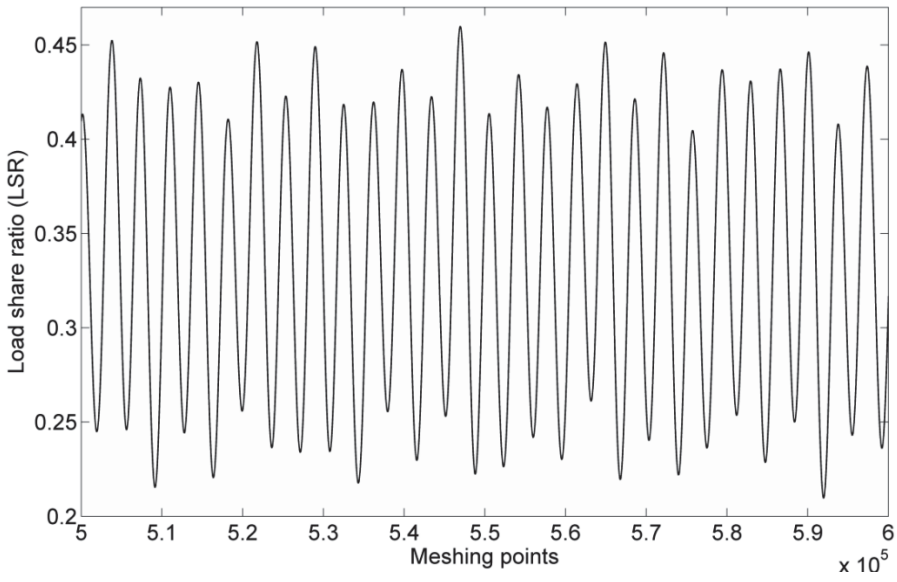

Figure 8.15. Load share ratio (LSR)

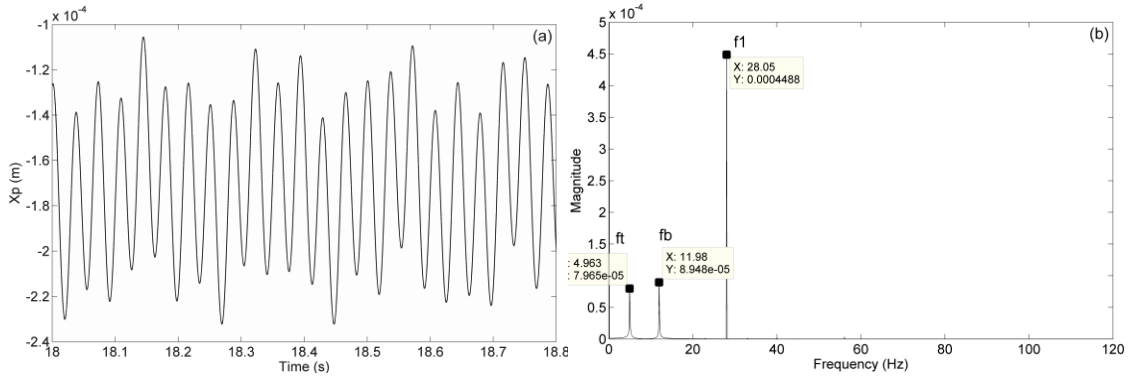

Figure 8.16. The radial vibrational responses X_p (a) Time histories (b) FFT spectrum

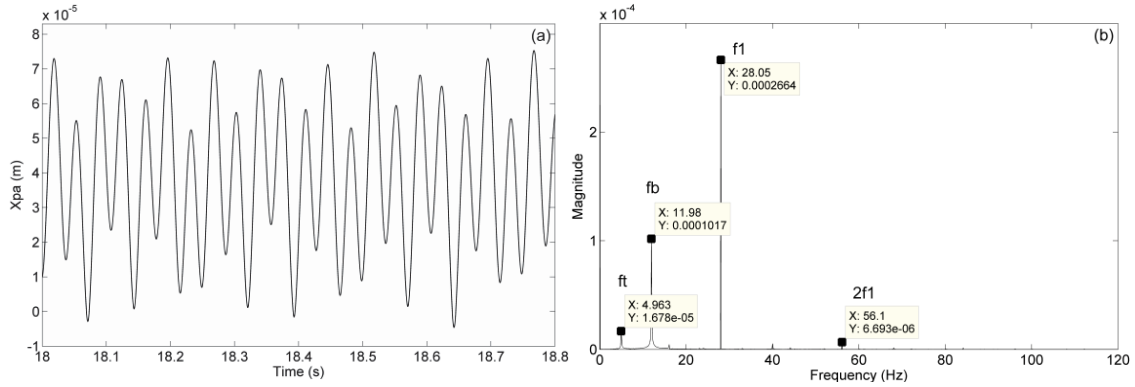

Figure 8.17. The axial vibrational responses (a) Time histories (b) FFT spectrum

8.3.2 Mean-to-alternating force ratio $F_m/F_a = 2$

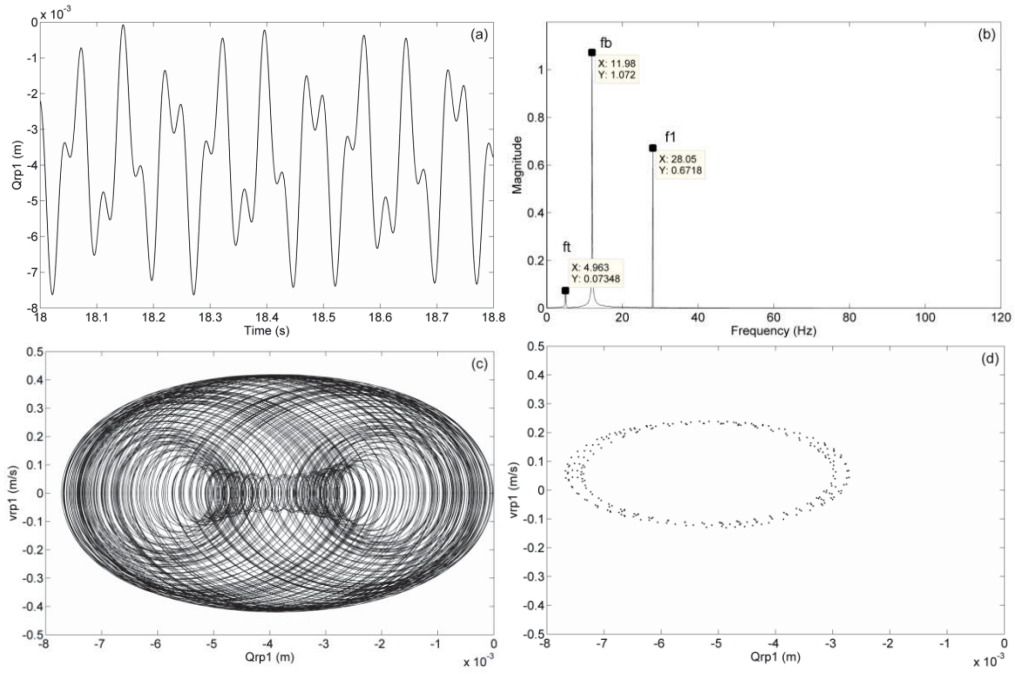

Figure 8.18. The vibrational responses of Q_{rp} (a) Time histories (b) FFT spectrum (c) Phase Portrait (d) Poincare map

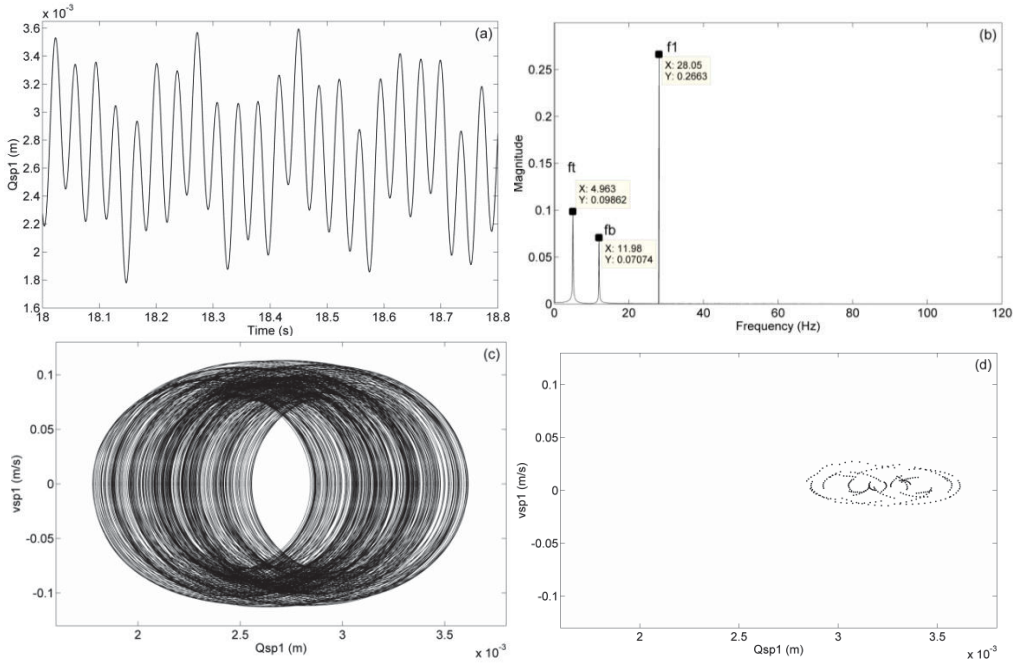

Figure 8.19. The vibrational responses of Q_{sp} (a) Time histories (b) FFT spectrum (c) Phase Portrait (d) Poincare map

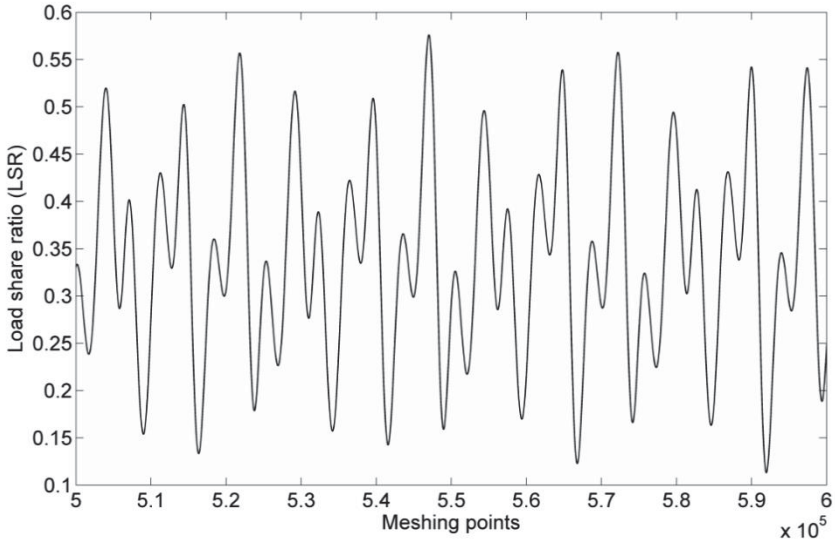

Figure 8.20. Load share ratio (LSR)

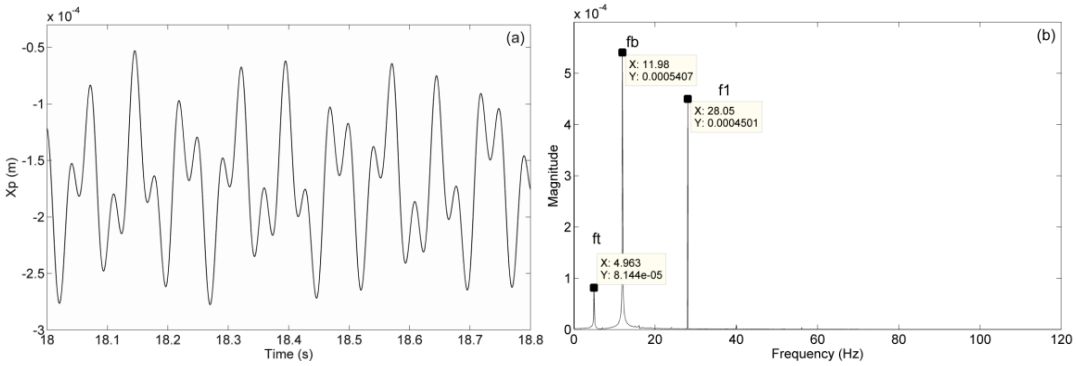

Figure 8.21. The radial vibrational responses X_p (a) Time histories (b)

FFT spectrum

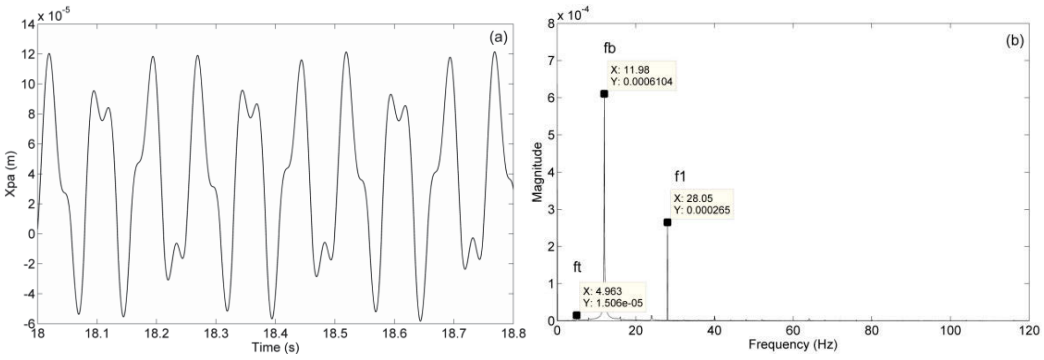

Figure 8.22. The axial vibrational responses X_{pa} (a) Time histories (b)

FFT spectrum

8.4 Wind fluctuation and bending moment with $M_y/T_{in} = 5$

8.4.1 Mean-to-alternating force ratio $F_m/F_a = 10$

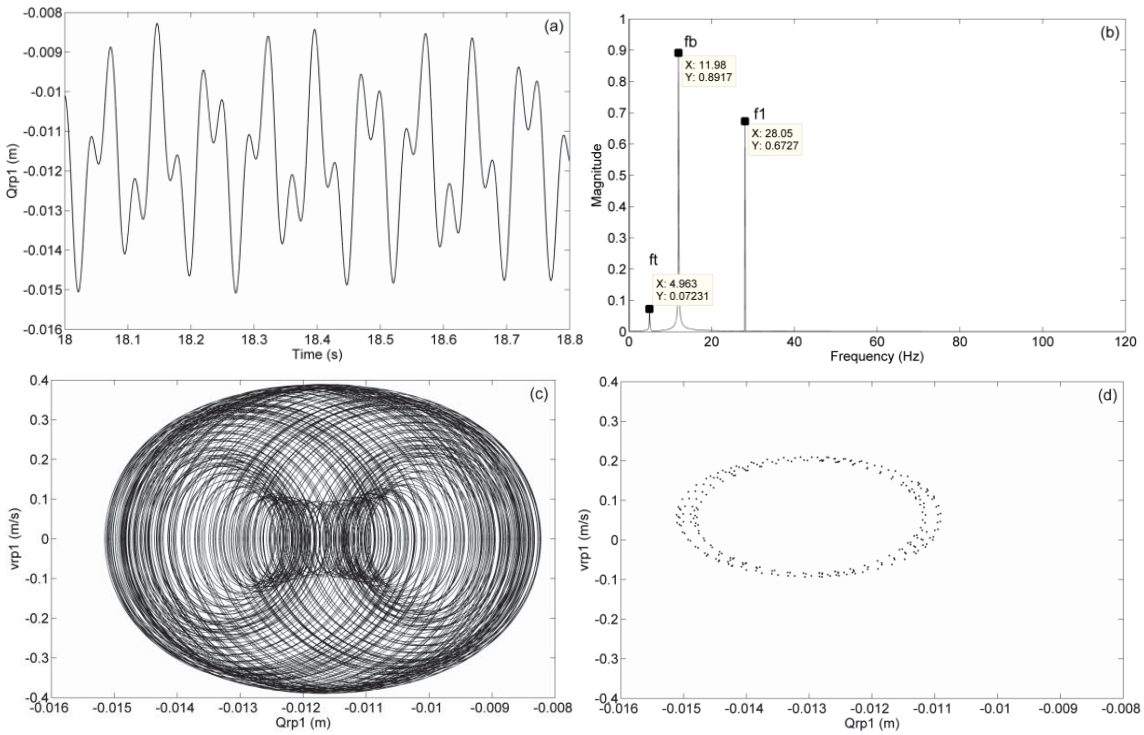

Figure 8.23. The vibrational responses of Q_{rp} (a) Time histories (b) FFT spectrum (c) Phase Portrait (d) Poincare map

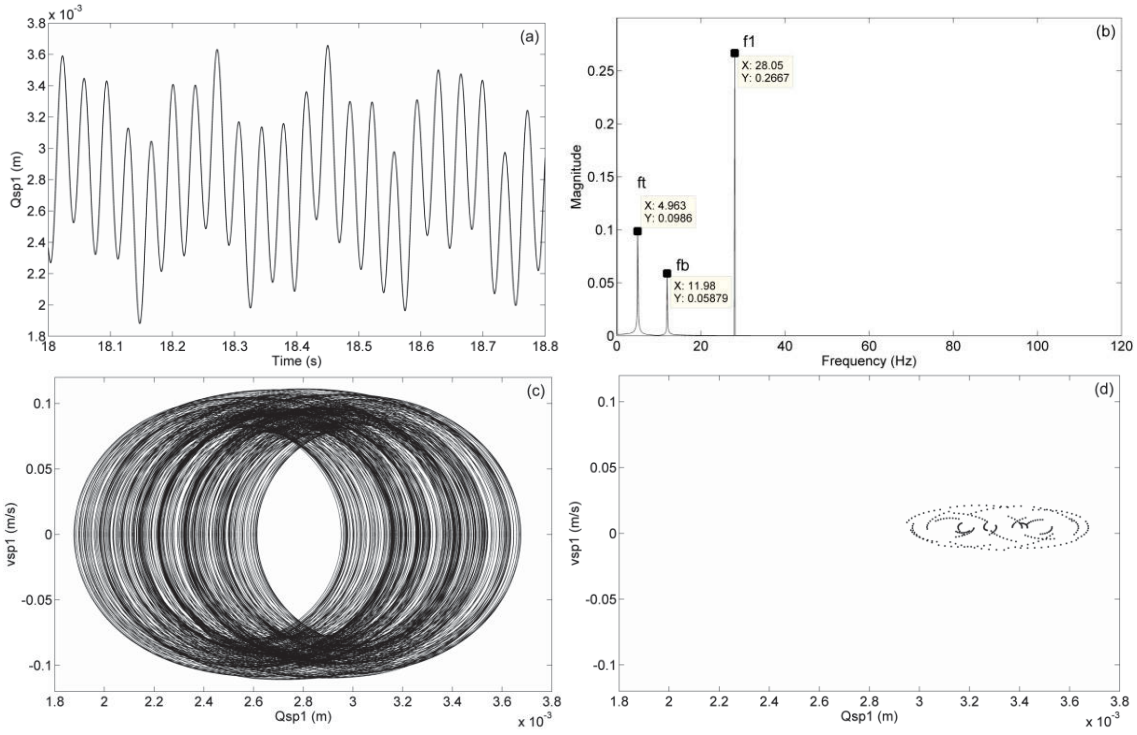

Figure 8.24. The vibrational responses of Q_{sp} (a) Time histories (b) FFT spectrum (c) Phase Portrait (d) Poincare map

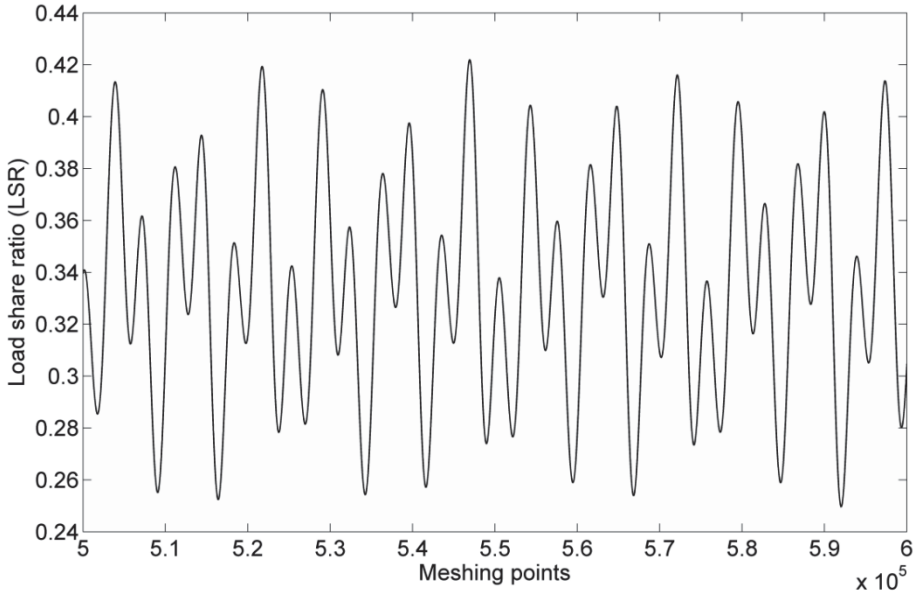

Figure 8.25. Load share ratio (LSR)

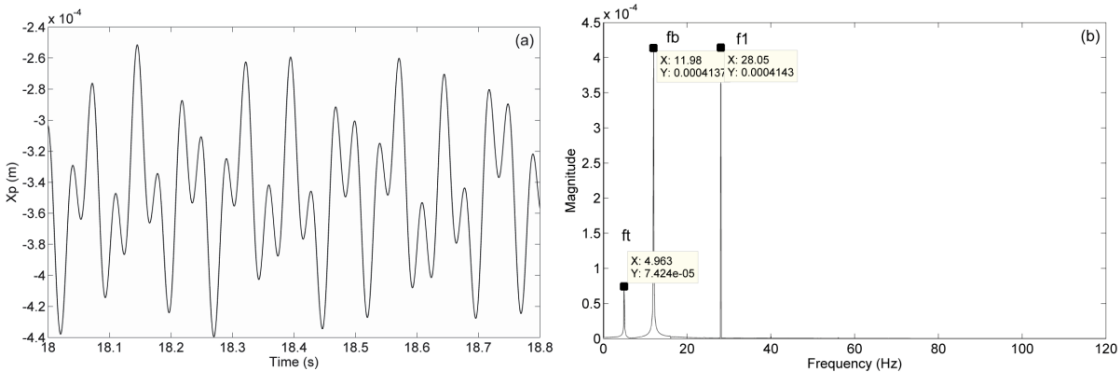

Figure 8.26. The radial vibrational responses X_p (a) Time histories (b)

FFT spectrum

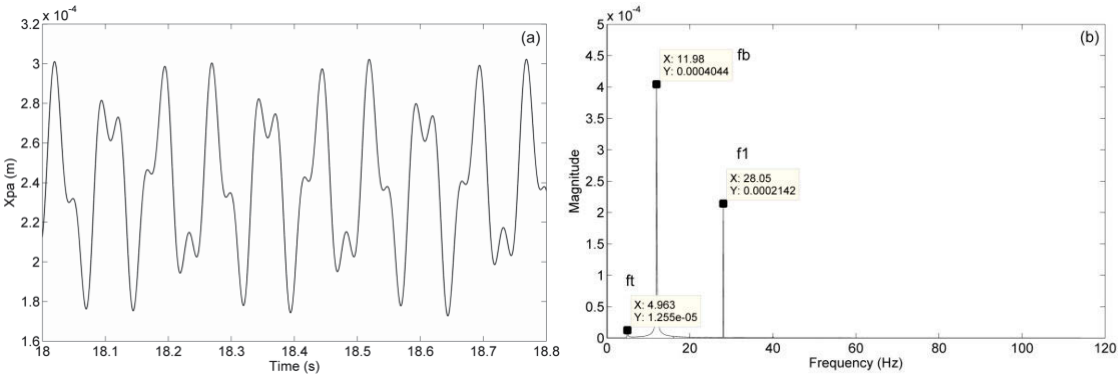

Figure 8.27. The axial vibrational responses X_{pa} (a) Time histories (b)

FFT spectrum

8.4.2 Mean-to-alternating force ratio $F_m/F_a = 2$

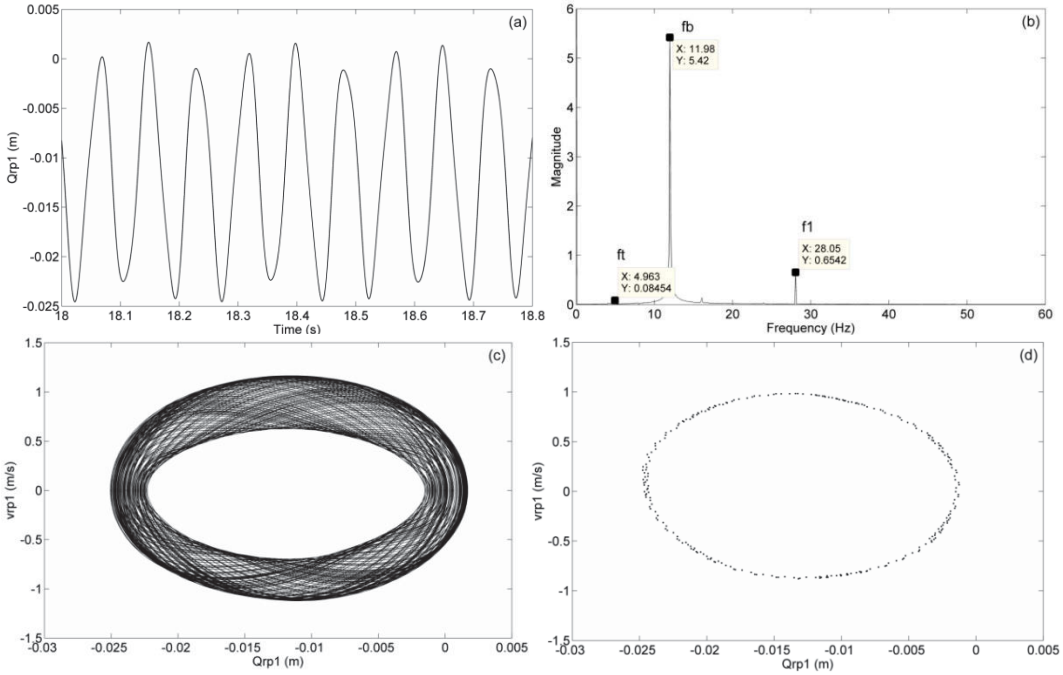

Figure 8.28. The vibrational responses of Q_{rp} (a) Time histories (b) FFT spectrum (c) Phase Portrait (d) Poincare map

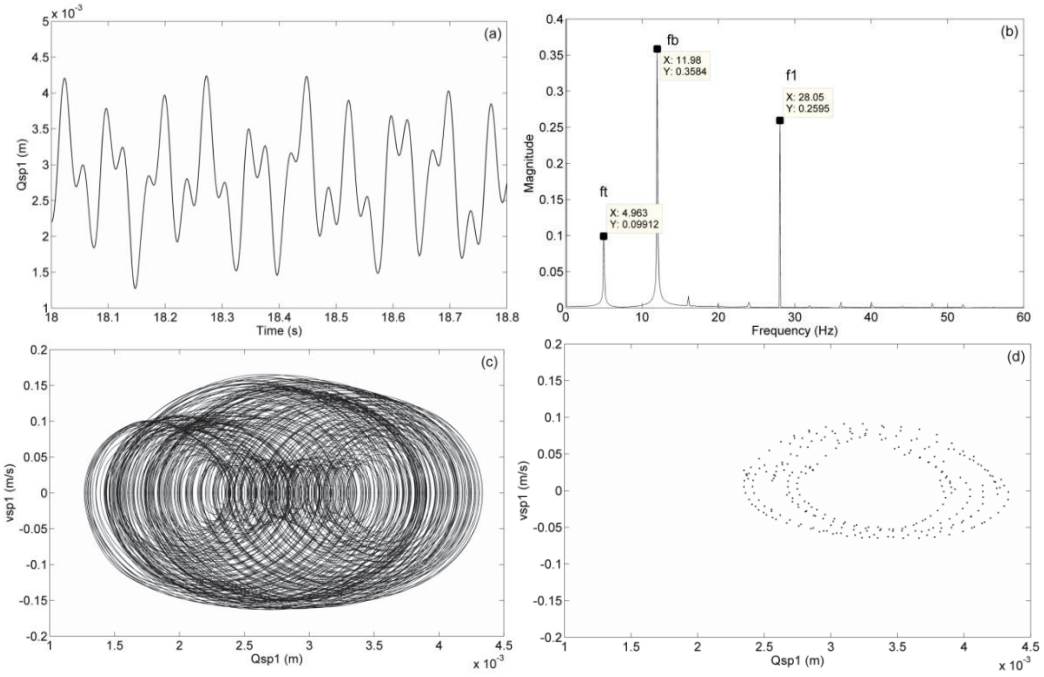

Figure 8.29. The vibrational responses of Q_{sp} (a) Time histories (b) FFT spectrum (c) Phase Portrait (d) Poincare map

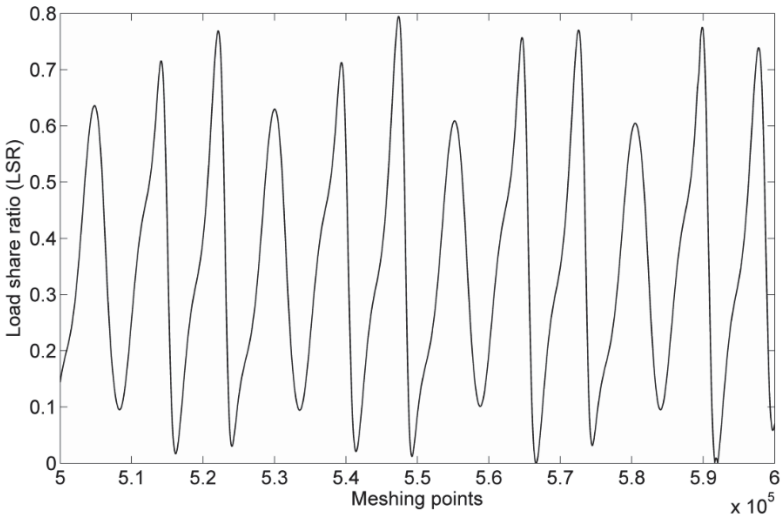

Figure 8.30. Load share ratio (LSR)

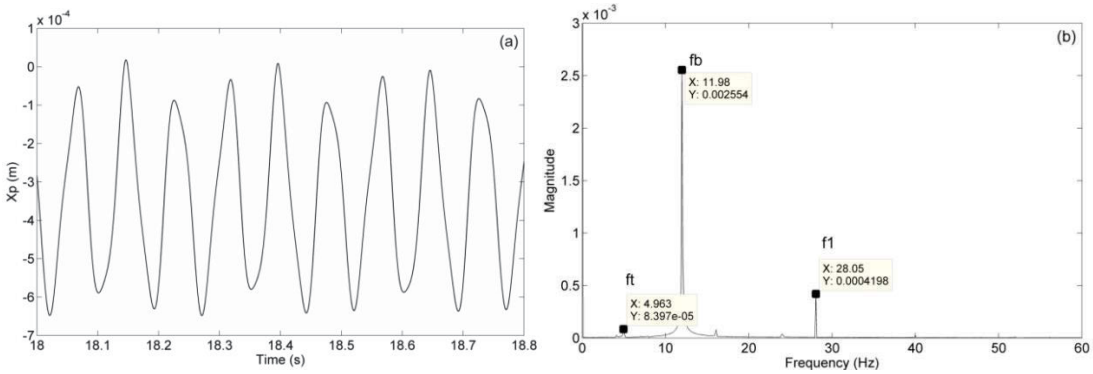

Figure 8.31. The radial vibrational responses X_p (a) Time histories (b)

FFT spectrum

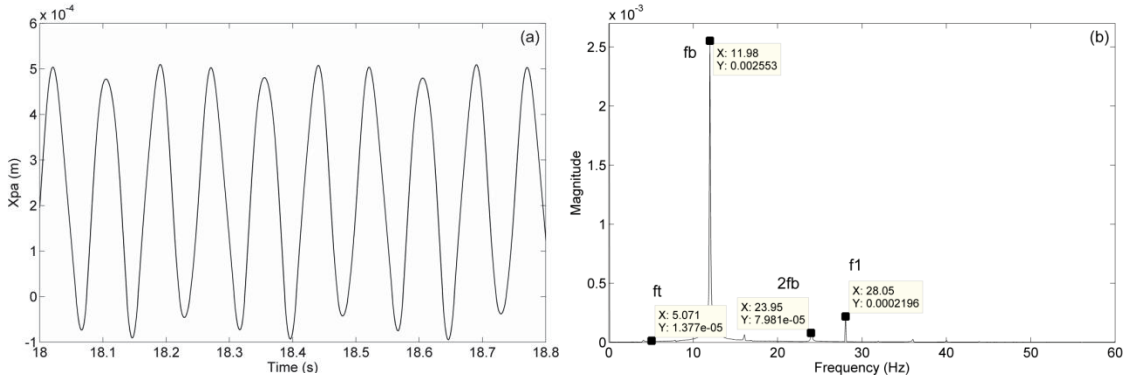

Figure 8.32. The axial vibrational responses X_{pa} (a) Time histories (b)

FFT spectrum

8.5 Increased wind fluctuation and bending moment with $M_y/T_{in} = 1$

8.5.1 Mean-to-alternating force ratio $F_m/F_a = 10$

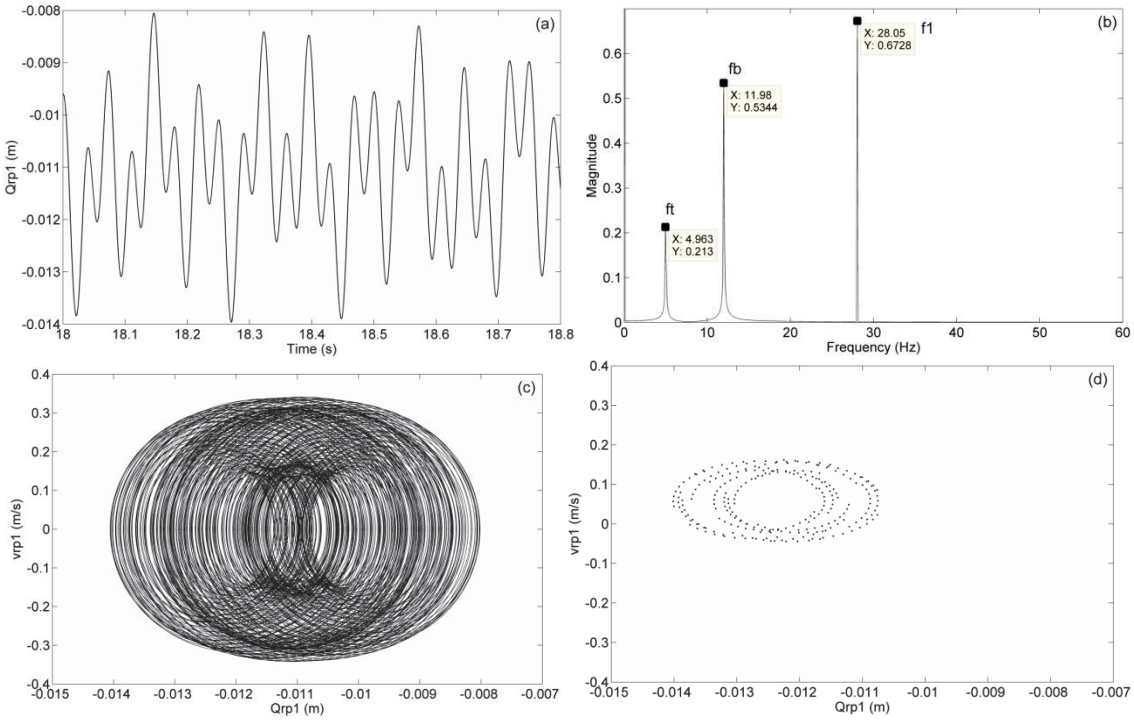

Figure 8.33. The vibrational responses of Q_{rp} (a) Time histories (b) FFT spectrum (c) Phase Portrait (d) Poincare map

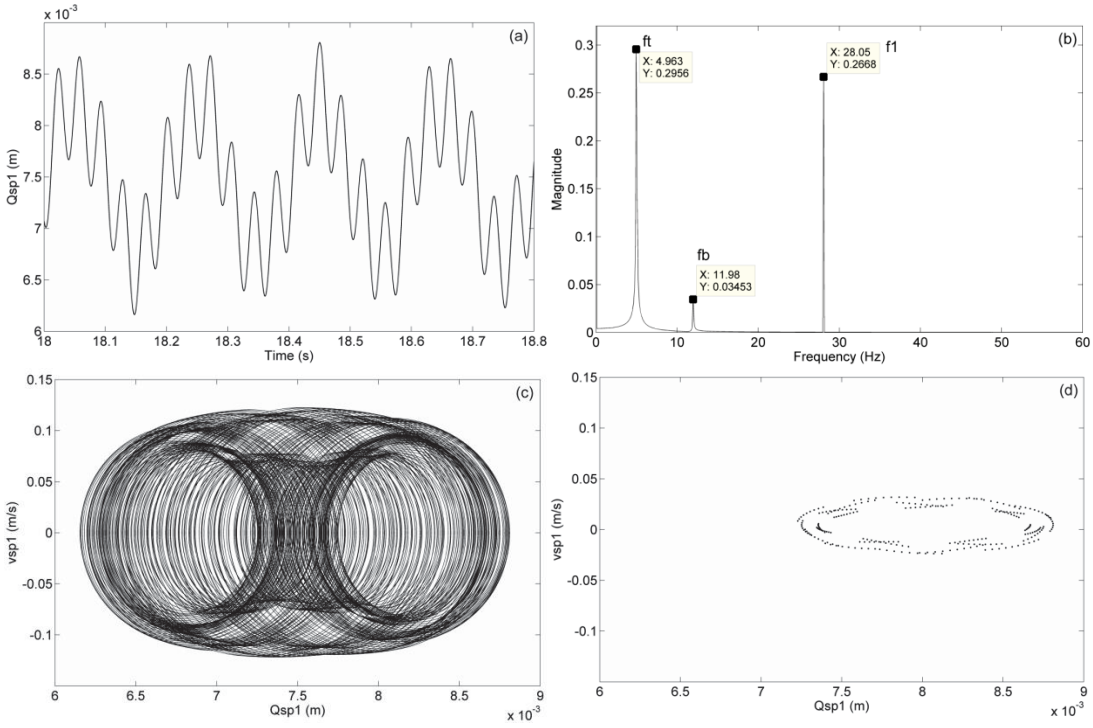

Figure 8.34. The vibrational responses of Q_{sp} (a) Time histories (b) FFT spectrum (c) Phase Portrait (d) Poincare map

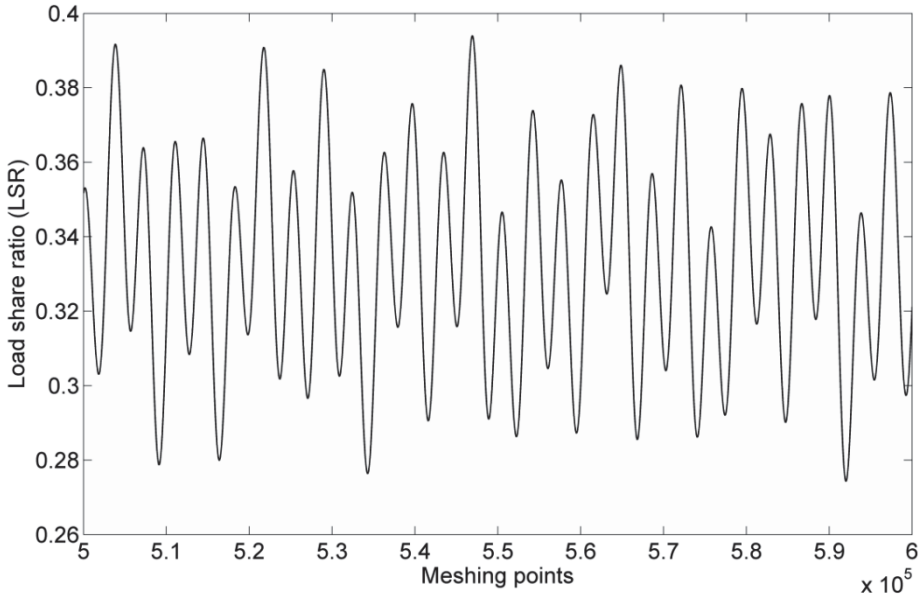

Figure 8.35. Load share ratio (LSR)

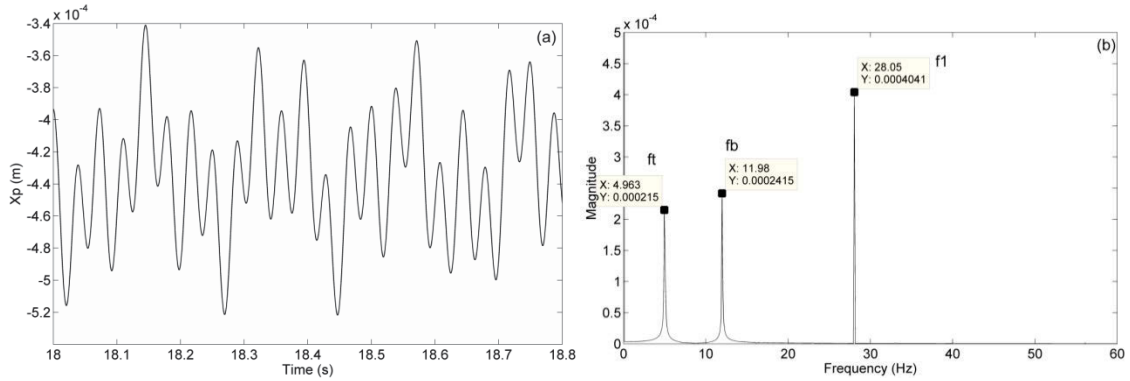

Figure 8.36. The radial vibrational responses X_p (a) Time histories (b)

FFT spectrum

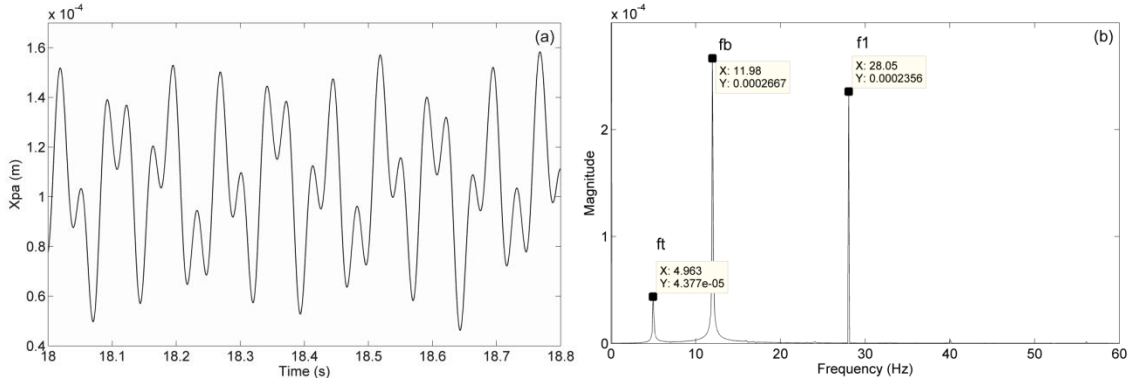

Figure 8.37. The axial vibrational responses X_{pa} (a) Time histories (b)

FFT spectrum

8.5.2 Mean-to-alternating force ratio $F_m/F_a = 2$

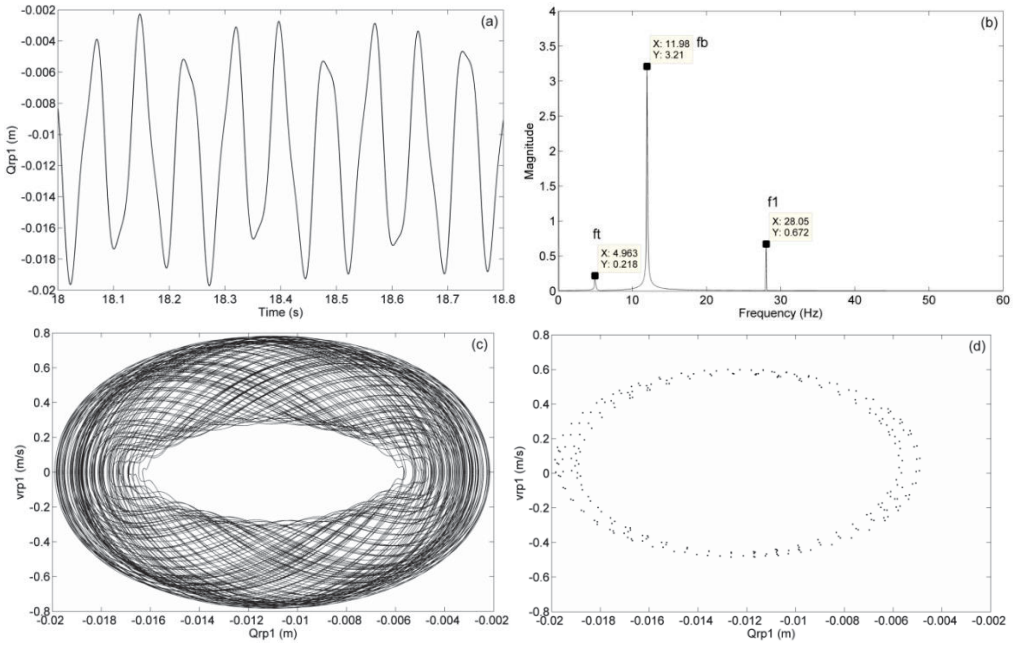

Figure 8.38. The vibrational responses of Q_{rp} (a) Time histories (b) FFT spectrum (c) Phase Portrait (d) Poincare map

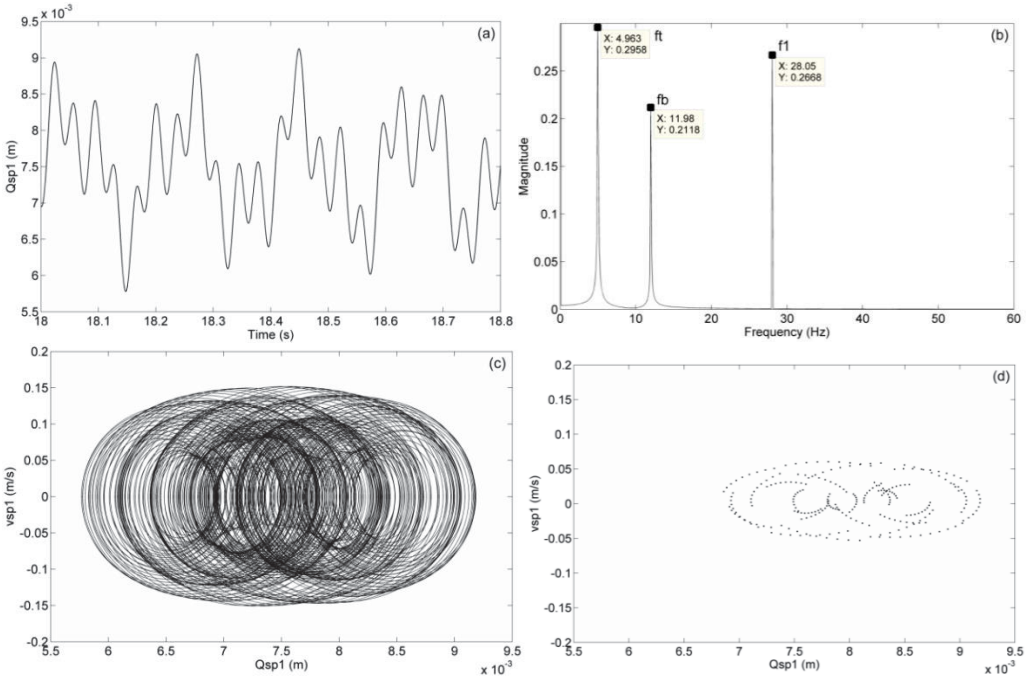

Figure 8.39. The vibrational responses of Q_{sp} (a) Time histories (b) FFT spectrum (c) Phase Portrait (d) Poincare map

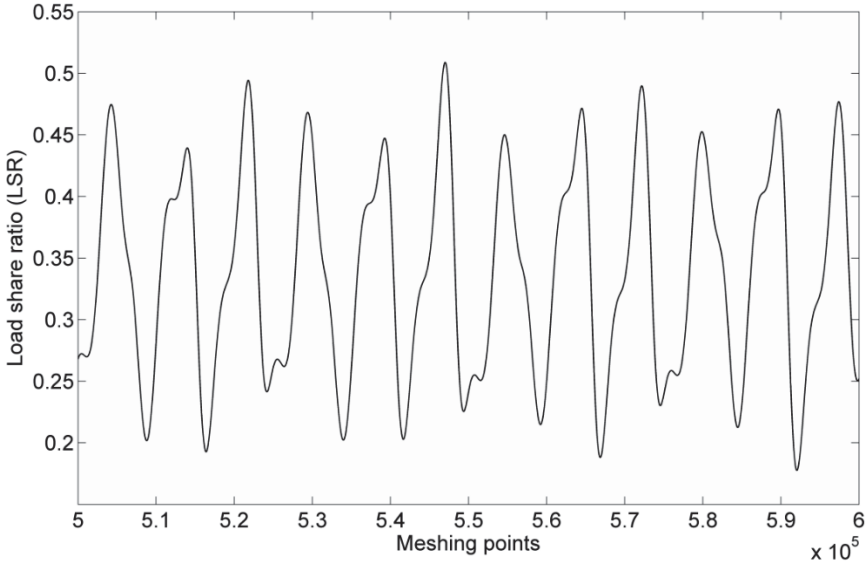

Figure 8.40. Load share ratio (LSR)

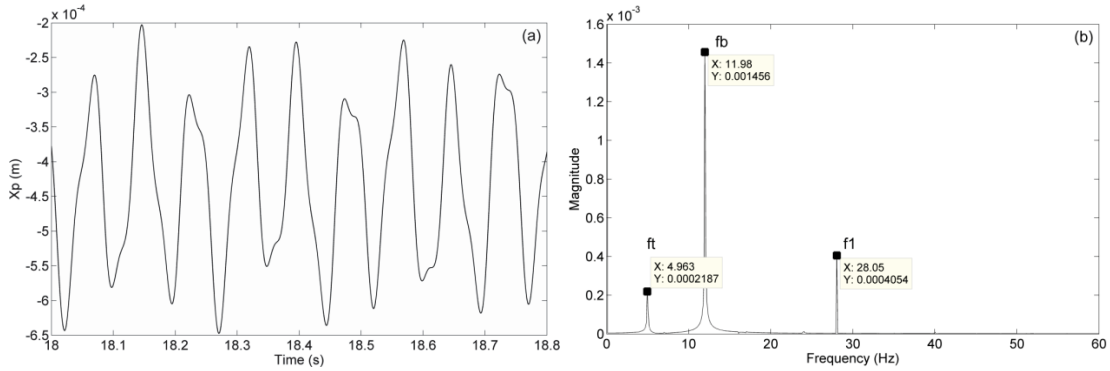

Figure 8.41. The radial vibrational responses X_p (a) Time histories (b) FFT spectrum

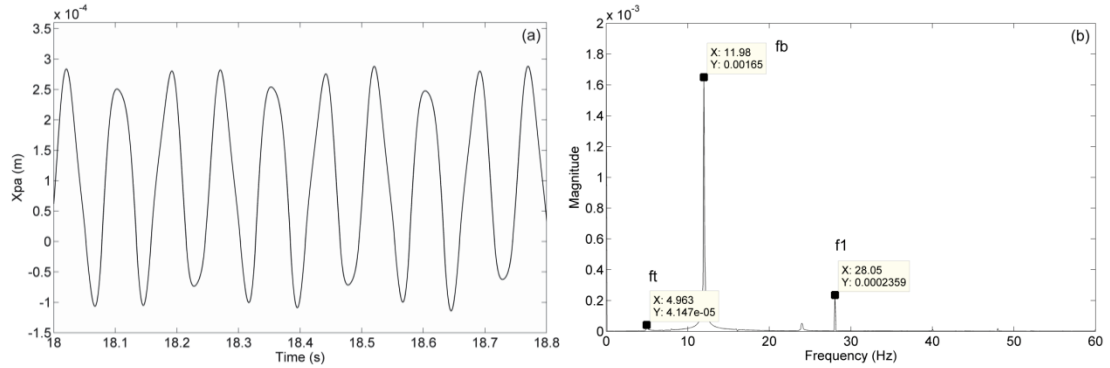

Figure 8.42. The axial vibrational responses X_{pa} (a) Time histories (b) FFT spectrum

References

1. Sandu, S., et al. *Australian energy resource assessment*. In *proc. World Computer Congress*. 2010. ABARE.
2. Ca, A.I., *20% Wind Energy By 2030*. 2008.
3. DECCW. *The wind energy fact sheet*. 2010 [cited 2012 16th Sep].
4. OEH. *NSW Wind Farm Greenhouse Gas Savings Tool*. Available from: http://www.environment.nsw.gov.au/ggecapp/.
5. UNEP. *United Nations Environment Programme (UNEP)*. [cited 2014 29th Jun]; Available from: http://www.un-energy.org/members/unep.
6. AGCER. *About the Renewable Energy Target*. 2015; Available from: http://www.cleanenergyregulator.gov.au/RET/About-the-Renewable-Energy-Target.
7. EPA. *Wind farms environmental noise guidelines*. 2009; Available from: file:///C:/Users/Mingming%20Zhao/Downloads/47788_windfarms.pdf.
8. Helsen, J., et al. *Some trends and challenges in wind turbine upscaling*. In *proc. International Conference On Noise And Vibration (ISMA)*. 2012. pp. 4335-4350.
9. Alemayehu, F.M. and S. Ekwaro-Osire, *Loading and design parameter uncertainty in the dynamics and performance of high-speed-parallel-helical-stage of a wind turbine gearbox.* Journal of Mechanical Design, 2014. **136**(9): pp. 091002-091002.
10. Musial, W., S. Butterfield, and B. McNiff. *Improving wind turbine gearbox reliability*. In *proc. European Wind Energy Conference, Milan, Italy*. 2007. pp. 7-10.
11. Felker, F. *NREL Gearbox study aims to grease wind power's future*. Power Engineering, 2010. **114**, 12-12.

12. Cho, J.R., et al., *Dynamic response analysis of wind turbine gearbox using simplified local tooth stiffness of internal gear system.* Journal of Computational and Nonlinear Dynamics, 2015. **10**(4): pp. 041001-041001.

13. Coultate, J., et al. *An investigation into the effect of lateral and axial aerodynamic loads on wind turbine gearbox reliability*. In *proc. European Wind Energy Conference and Exhibition (EWEC), Marseille*. 2009.

14. Wei, J., et al., *A study on optimum design method of gear transmission system for wind turbine.* International Journal of Precision Engineering and Manufacturing, 2013. **14**(5): pp. 767-778.

15. Whittle, M., et al., *Improving wind turbine drivetrain bearing reliability through pre-misalignment.* Wind Energy, 2014. **17**(8): pp. 1217-1230.

16. Todorov, M., I. Dobrev, and F. Massouh, *Analysis of torsional oscillation of the drive train in horizontal-axis wind turbine*, in *Advanced Electromechanical Motion Systems & Electric Drives Joint Symposium, 2009. ELECTROMOTION 2009. 8th International Symposium on*2009. pp. 1-7.

17. Musial, W., S. Butterfield, and B. McNiff. *Improving Wind Turbine Gearbox Reliability*. In *proc. Proceedings of the European Wind Energy Conference*. 2007.

18. Oyague, F., *Gearbox modeling and load simulation of a baseline 750-kW wind turbine using state-of-the-art simulation codes*2009: National Renewable Energy Laboratory Golden, CO.

19. Oyague, F., D. Gorman, and S. Sheng. *Progressive dynamical drive train modeling as part of NREL gearbox reliability collaborative*. In *proc. Windpower 2008 Conference and Exhibition*. 2008.

20. Zhang, Z., et al., *The effect of transient loading on the stresses of wind turbine drivetrain components*, in *EWEC*2009.

21. Peeters, J., et al., *Comparison of analysis techniques for the dynamic behaviour of an integrated drivetrain in a wind turbine*, in *International Conference on Noise and Vibration Engineering*2002: Belgium. pp. 1397-1405.

22. Peeters, J., D. Vandepitte, and P. Sas. *Flexible multibody model of a three-stage planetary gearbox in a wind turbine*. In *proc. Proc. ISMA*. 2004. Leuven, Belgium. pp. 3923-3941.

23. Peeters, J., D. Vandepitte, and P. Sas, *Structural analysis of a wind turbine and its drive train using the flexible multibody simulation technique*, in *Proceedings of ISMA*2006. pp. 3665-3679.

24. Peeters, J.L.M., D. Vandepitte, and P. Sas, *Analysis of internal drive train dynamics in a wind turbine.* Wind Energy, 2006. **9**(1-2): pp. 141-161.

25. Heege, A., J. Betran, and Y. Radovcic, *Fatigue load computation of wind turbine gearboxes by coupled finite element, multi-body system and aerodynamic analysis.* Wind Energy, 2007. **10**(5): pp. 395-413.

26. Helsen, J., et al., *The influence of flexibility within multibody modeling of multi-megawatt wind turbine gearboxes*, in *Proceedings of the ISMA International Conference on Noise & Vibration Engineering*2008. pp. 2045-2071.

27. Oyague, F., C. Butterfield, and S. Sheng, *Gearbox reliability collaborative analysis round robin.* National Renewable Energy Laboratory, Golden, CO, Report No. NREL/CP-500-45325, 2009.

28. Oyague, F., D. Gorman, and S. Sheng. *NREL gearbox reliability collaborative experimental data overview and analysis*. In *proc. Windpower Conference and Exhibition*. 2010.

29. Oyague, F., *Gearbox reliability collaborative (GRC) description and loading*, 2011. pp. 275-3000.

30. Coultate, J., et al. *The impact of gearbox housing and planet carrier flexibility on wind turbine gearbox durability*. In *proc. Proc of European Wind Energy Conference*. 2009. pp. 1-8.

31. Crowther, A., et al., *Sources of time-varying contact stress and misalignments in wind turbine planetary sets.* Wind Energy, 2011. **14**(5): pp. 637-651.

32. Spinato, F., et al., *Reliability of wind turbine subassemblies.* Renewable Power Generation, IET, 2009. **3**(4): pp. 387-401.

33. Todorov, M. and G. Vukov, *Parametric torsional vibrations of a drive train in horizontal axis wind turbine.* Proceedings of CFSER-2010, 2010.

34. De Coninck, F., et al. *Reproduction of dynamic load cases on a 13.2 MW test facility for wind turbine gearboxes*. In *proc. Proceedings of ISMA*. 2010.

35. Abboudi, K., et al., *Dynamic behaviour of a two-stage gear train used in a fixed-speed wind turbine.* Mechanism and Machine Theory, 2011. **46**(12): pp. 1888-1900.

36. Allen, M.S., et al., *Output-only modal analysis of linear time-periodic systems with application to wind turbine simulation data.* Mechanical Systems and Signal Processing, 2011. **25**(4): pp. 1174-1191.

37. Haastrup, M., M.R. Hansen, and M.K. Ebbesen, *Modeling of wind turbine gearbox mounting.* Modeling, Identification and Control, 2011. **32**: pp. 141-149.

38. Helsen, J., et al., *Insights in Wind Turbine Drive Train Dynamics Gathered by Validating Advanced Models on a Newly Developed 13.2 MW Dynamically Controlled Test-rig.* Mechatronics, 2011. **21**(4): pp. 737-752.

39. Helsen, J., et al., *Multibody modelling of varying complexity for modal behaviour analysis of wind turbine gearboxes.* Renewable Energy, 2011. **36**(11): pp. 3098-3113.

40. Jain, S. and H. Hunt, *Vibration response of a wind-turbine planetary gear set in the presence of a localized planet bearing defect*, in *ASME 2011 International Mechanical Engineering Congress and Exposition (IMECE2011), Denver, Colorado, USA*2011. pp. 943-952.

41. Keller, J., et al., *Gearbox reliability collaborative phase 1 and 2: testing and modeling results*, in *Conference on Noise and Vibration Engineering*2011, National Renewable Energy Laboratory: Leuven, Belgium.

42. Guo, Y., J. Keller, and W. LaCava. *Combined effects of gravity, bending moment, bearing clearance, and input torque on wind turbine planetary gear load sharing*. In *proc. AGMA Fall technical meeting*. 2012. Dearborn, Michigan.

43. Guo, Y., J. Keller, and R. Parker, *Dynamic analysis of wind turbine planetary gears using an extended harmonic balance approach*, in *International Conference on Noise and Vibration Engineering*2012: Leuven, Belgium.

44. Villa, L.F., et al., *Angular resampling for vibration analysis in wind turbines under non-linear speed fluctuation.* Mechanical Systems and Signal Processing, 2011. **25**(6): pp. 2157-2168.

45. Dong, W., Y. Xing, and T. Moan *Time domain modeling and analysis of dynamic gear contact force in a wind turbine gearbox with respect to fatigue assessment*. Energies (19961073), 2012. **5**, 4350-4371 DOI: http://dx.doi.org/10.3390/en5114350.

46. Haastrup, M., et al., *Modeling and parameter identification of deflections in planetary stage of wind turbine gearbox.* Modeling, Identification and Control, 2012. **33**: pp. 1-11.

47. Hall, J.F. and D. Chen, *Dynamic optimization of drivetrain gear ratio to maximize wind turbine power generation—Part 1: System model and control framework.*

Journal of Dynamic Systems, Measurement, and Control, 2012. **135**(1): pp. 011016-011016.

48. Hall, J.F. and D. Chen, *Performance of a 100 kW wind turbine with a variable ratio gearbox.* Renewable Energy, 2012. **44**: pp. 261-266.
49. Helsen, J., et al., *Assessment of excitation mechanisms and structural flexibility influence in excitation propagation in multi-megawatt wind turbine gearboxes: Experiments and flexible multibody model optimization.* Mechanical Systems and Signal Processing, 2013. **40**(1): pp. 114-135.
50. Helsen, J., et al., *The dynamic behaviour induced by different wind turbine gearbox suspension methods assessed by means of the flexible multibody technique.* Renewable Energy, 2014. **69**: pp. 336-346.
51. Vanhollebeke, F., et al., *Large scale validation of a flexible multibody wind turbine gearbox model.* Journal of Computational and Nonlinear Dynamics, 2015. **10**(4): pp. 041006-041006.
52. LaCava, W., J. Keller, and B. McNiff. *Gearbox reliability collaborative: test and model investigation of sun orbit and planet load share in a wind turbine gearbox*. In *proc. 53rd Structures, Structural Dynamics, and Materials and Colocated Conferences (SDM)*. 2012. Honolulu, Hawaii.
53. LaCava, W., et al., *Determining wind turbine gearbox model complexity using measurement validation and cost comparison*, in *European Wind Energy Association annual event*2012: Copenhagen, Denmark.
54. Austin, J.L., *A multi-component analysis of a wind turbine gearbox using a high fidelity finite element model*, 2013, The Ohio State University.

55. Dong, W., et al., *Time domain-based gear contact fatigue analysis of a wind turbine drivetrain under dynamic conditions.* International Journal of Fatigue, 2013. **48**: pp. 133-146.

56. Greco, A., et al., *Material wear and fatigue in wind turbine systems.* Wear, 2013. **302**(1–2): pp. 1583-1591.

57. Guo, Y., et al., *Gearbox reliability collaborative analytic formulation for the evaluation of spline couplings.* National Renewable Energy Laboratory, Golden, Colorado, Technical Report NREL/TP-5000-60637, 2013.

58. Guo, Y., et al. *Model fidelity study of dynamic transient loads in a wind turbine gearbox*. In *proc. WINDPOWER Conference of the American Wind Energy Association, Chicago, IL, May*. 2013. pp. 5-8.

59. Link, H., et al., *Gearbox reliability collaborative phase 3 gearbox 2 test plan*, 2013, National Renewable Energy Laboratory (NREL), Golden, CO.

60. Lutschinger, D. and I. Howard, *Experimental tests of wind turbine main shaft motion on a laboratory test rig.* 2013.

61. Nejad, A.R., Z. Gao, and T. Moan, *Long-term analysis of gear loads in fixed offshore wind turbines considering ultimate operational loadings.* Energy Procedia, 2013. **35**: pp. 187-197.

62. Park, Y.-J., et al., *Characteristic analysis of wind turbine gearbox considering non-torque loading.* Journal of Mechanical Design, 2013. **135**(4): pp. 044501-044501.

63. Xing, Y. and T. Moan, *Multi‐body modelling and analysis of a planet carrier in a wind turbine gearbox.* Wind Energy, 2013. **16**(7): pp. 1067-1089.

64. Abouel-Seoud, S. and E. Mohamed, *Wind turbine planetary gearbox health diagnostic using time-varying meshing stiffness.* International Journal of Modern Engineering Research (IJMER), 2014. **2**(3): pp. 1440-1448.

65. Girsang, I.P., et al., *Gearbox and drivetrain models to study dynamic effects of modern wind turbines.* Industry Applications, IEEE Transactions on, 2014. **50**(6): pp. 3777-3786.

66. Jorgensen, M.F., et al., *Rigid MATLAB drivetrain model of a 500 kW wind turbine for predicting maximum gear tooth stresses in a planetary gearbox using multibody gear constraints.* Wind Energy, 2014. **17**(11): pp. 1659-1676.

67. Luo, H., et al., *Amplitude modulations in planetary gears.* Wind Energy, 2014. **17**(4): pp. 505-517.

68. Nejad, A.R., Z. Gao, and T. Moan, *On long-term fatigue damage and reliability analysis of gears under wind loads in offshore wind turbine drivetrains.* International Journal of Fatigue, 2014. **61**: pp. 116-128.

69. Nejad, A.R., et al., *Effects of floating sun gear in a wind turbine's planetary gearbox with geometrical imperfections.* Wind Energy, 2014.

70. Sawalhi, N., R.B. Randall, and D. Forrester, *Separation and enhancement of gear and bearing signals for the diagnosis of wind turbine transmission systems.* Wind Energy, 2014. **17**(5): pp. 729-743.

71. Xing, Y., M. Karimirad, and T. Moan, *Modelling and analysis of floating spar-type wind turbine drivetrain.* Wind Energy, 2014. **17**(4): pp. 565-587.

72. Zappala, et al., *Side-band algorithm for automatic wind turbine gearbox fault detection and diagnosis.* Renewable Power Generation IET, 2014. **8**(4): pp. 380-389.

73. Zhu, C., et al., *Dynamic analysis of the drive train of a wind turbine based upon the measured load spectrum.* Journal of Mechanical Science and Technology, 2014. **28**(6): pp. 2033-2040.

74. Zhu, C., et al., *Research on dynamical characteristics of wind turbine gearboxes with flexible pins.* Renewable Energy, 2014. **68**: pp. 724-732.

75. Bielecki, A., T. Barszcz, and M. Wójcik, *Modelling of a chaotic load of wind turbines drivetrain.* Mechanical Systems and Signal Processing, 2015. **54–55**: pp. 491-505.

76. Guo, Y., et al., *Improving wind turbine drivetrain designs to minimize the impacts of non-torque loads.* Wind Energy, 2015. **18**(12): pp. 2199-2222.

77. Guo, Y., J. Keller, and W. LaCava, *Planetary gear load sharing of wind turbine drivetrains subjected to non-torque loads.* Wind Energy, 2015. **18**(4): pp. 757-768.

78. Guo, Y., et al., *Design evaluation of wind turbine spline couplings using an analytical model*, in *Conference for Wind Power Drives*2015: Germany.

79. Jiang, Z., et al., *Long-term contact fatigue analysis of a planetary bearing in a land-based wind turbine drivetrain.* Wind Energy, 2015. **18**(4): pp. 591-611.

80. Park, Y.-J., et al., *Load sharing and distributed on the gear flank of wind turbine planetary gearbox.* Journal of Mechanical Science and Technology, 2015. **29**(1): pp. 309-316.

81. Perisic, N., P.H. Kirkegaard, and B.J. Pedersen, *Cost-effective shaft torque observer for condition monitoring of wind turbines.* Wind Energy, 2015. **18**(1): pp. 1-19.

82. Struggl, S., V. Berbyuk, and H. Johansson, *Review on wind turbines with focus on drive train system dynamics.* Wind Energy, 2015. **18**(4): pp. 567-590.

83. Wei, S., et al., *Dynamic response analysis on torsional vibrations of wind turbine geared transmission system with uncertainty.* Renewable Energy, 2015. **78**: pp. 60-67.

84. Xu, X., et al., *The nonlinear effects of flexible pins on wind turbine gearboxes.* Journal of Mechanical Science and Technology, 2015. **29**(8): pp. 3077-3082.

85. Zhu, C., et al., *Dynamic analysis of a megawatt wind turbine drive train.* Journal of Mechanical Science and Technology, 2015. **29**(5): pp. 1913-1919.

86. Wei, S., et al., *Dynamic analysis of parametrically excited system under uncertainties and multi-frequency excitations.* Mechanical Systems and Signal Processing, 2016. **72–73**: pp. 762-784.

87. Dong, W., Y. Xing, and T. Moan, *Time Domain Modeling and Analysis of Dynamic Gear Contact Force in a Wind Turbine Gearbox with Respect to Fatigue Assessment.* Energies, 2012. **5**(11): pp. 4350.

88. Guo, Y., et al., *Theoretical and experimental study on gear-coupling contact and loads considering misalignment, torque, and friction influences.* Mechanism and Machine Theory, 2016. **98**: pp. 242-262.

89. Park, Y., et al. *Characteristics analysis of wind turbine gearbox considering fatigue loads caused by wind fluctuation*. In *proc. ASME 2011 International Design Engineering Technical Conferences and Computers and Information in Engineering Conference*. 2011. American Society of Mechanical Engineers. pp. 611-620.

90. Wang, X. and S. Wu. *Nonlinear dynamic modeling and numerical simulation of the wind turbine's gear train*. In *proc. Electrical and Control Engineering (ICECE)*. 2011. IEEE. pp. 2385-2389.

91. Sun, W., T. Chen, and J. Wei, *Dynamic reliability of gears in a wind turbine gearbox under the conditions of variable wind speed and small samples.* Proceedings of the Institution of Mechanical Engineers, Part C: Journal of Mechanical Engineering Science, 2012. **226**(12): pp. 3032-3042.

92. Shi, W., et al., *Dynamic modeling and analysis of a wind turbine drivetrain using the torsional dynamic model.* International Journal of Precision Engineering and Manufacturing, 2013. **14**(1): pp. 153-159.

93. Shi, W., et al., *Dynamic analysis of three-dimensional drivetrain system of wind turbine.* International Journal of Precision Engineering and Manufacturing, 2014. **15**(7): pp. 1351-1357.

94. Zhao, M. and J.C. Ji, *Nonlinear torsional vibrations of a wind turbine gearbox.* Applied Mathematical Modelling, 2015. **39**(16): pp. 4928-4950.

95. Zhao, M. and J. Ji, *Dynamic analysis of wind turbine gearbox components.* Energies, 2016. **9**(2): pp. 110.

96. Ozguven, H.N. and D.R. Houser, *Mathematical models used in gear dynamics—a review.* Journal of Sound and Vibration, 1988. **121**(3): pp. 383-411.

97. Ozguven, H.N. and D.R. Houser, *Dynamic analysis of high speed gears by using loaded static transmission error.* Journal of Sound and Vibration, 1988. **125**(1): pp. 71-83.

98. Ozguven, H., *A non-linear mathematical model for dynamic analysis of spur gears including shaft and bearing dynamics.* Journal of Sound and Vibration, 1991. **145**(2): pp. 239-260.

99. Kahraman, A. and G.W. Blankenship, *Effect of involute contact ratio on spur gear dynamics.* Journal of Mechanical Design, 1999. **121**(1): pp. 112-118.

100. Al-shyyab, A. and A. Kahraman, *Non-linear dynamic analysis of a multi-mesh gear train using multi-term harmonic balance method: period-one motions.* Journal of Sound and Vibration, 2005. **284**(1–2): pp. 151-172.

101. Al-shyyab, A. and A. Kahraman, *Non-linear dynamic analysis of a multi-mesh gear train using multi-term harmonic balance method: sub-harmonic motions.* Journal of Sound and Vibration, 2005. **279**(1–2): pp. 417-451.

102. Al-Shhyab, A. and A. Kahraman, *A nonlinear torsional dynamic model of multi-mesh gear trains having flexible shafts.* JJMIE, 2007. **1**(1): pp. 31-41.

103. Blankenship, G.W. and A. Kahraman, *Steady state forced response of a mechanical oscillator with combined parametric excitation and clearance type non-linearity.* Journal of Sound and Vibration, 1995. **185**(5): pp. 743-765.

104. Kahraman, A. and G.W. Blankenship, *Experiments on nonlinear dynamic behavior of an oscillator with clearance and periodically time-varying parameters.* Journal of Applied Mechanics, 1997. **64**(1): pp. 217-226.

105. Amabili, M. and A. Rivola, *Dynamic analysis of spur gear pairs steady-state response and stability of the SDOF model with time-varying meshing damping.* Mechanical Systems and Signal Processing, 1997. **11**(3): pp. 375-390.

106. Liu, G. and R.G. Parker, *Impact of tooth friction and its bending effect on gear dynamics.* Journal of Sound and Vibration, 2009. **320**(4–5): pp. 1039-1063.

107. Parker, R.G., S.M. Vijayakar, and T. Imajo, *Non-linear dynamic response of a spur gear pair modelling and experimental comparisons.* Journal of Sound and Vibration, 2000. **237**(3): pp. 435-455.

108. Shen, Y., S. Yang, and X. Liu, *Nonlinear dynamics of a spur gear pair with time-varying stiffness and backlash based on incremental harmonic balance method.* International Journal of Mechanical Sciences, 2006. **48**(11): pp. 1256-1263.

109. Kim, W., H.H. Yoo, and J. Chung, *Dynamic analysis for a pair of spur gears with translational motion due to bearing deformation.* Journal of Sound and Vibration, 2010. **329**(21): pp. 4409-4421.

110. Siyu, C., et al., *Nonlinear dynamic characteristics of geared rotor bearing systems with dynamic backlash and friction.* Mechanism and Machine Theory, 2011. **46**(4): pp. 466-478.

111. Fernandez del Rincon, A., et al., *A model for the study of meshing stiffness in spur gear transmissions.* Mechanism and Machine Theory, 2013. **61**: pp. 30-58.

112. Kahraman, A., *Effect of axial vibrations on the dynamics of a helical gear pair.* Journal of Vibration and Acoustics, 1993. **115**(1): pp. 33-39.

113. Kahraman, A., *Dynamic analysis of a multi-mesh helical gear train.* Journal of Mechanical Design, 1994. **116**(3): pp. 706-712.

114. Kang, M.R. and A. Kahraman, *An experimental and theoretical study of the dynamic behaviour of double-helical gear sets.* Journal of Sound and Vibration, 2015. **350**: pp. 11-29.

115. Cai, Y., *Simulation on the rotational vibration of helical gears in consideration of the tooth separation phenomenon (A new stiffness function of helical involute tooth pair).* Journal of Mechanical Design, 1995. **117**(3): pp. 460-469.

116. Cooley, C.G., R.G. Parker, and S.M. Vijayakar, *A frequency domain finite element approach for three-dimensional gear dynamics.* Journal of Vibration and Acoustics, 2011. **133**(4): pp. 041004-041004.

117. Howard, I., S. Jia, and J. Wang, *The dynamic modelling of a spur gear in mesh including friction and a crack.* Mechanical Systems and Signal Processing, 2001. **15**(5): pp. 831-853.

118. Kubur, M., et al., *Dynamic analysis of a multi-shaft helical gear transmission by finite elements: model and experiment.* Journal of Vibration and Acoustics, 2004. **126**(3): pp. 398-406.

119. Ebrahimi, S. and P. Eberhard, *Rigid-elastic modeling of meshing gear wheels in multibody systems.* Multibody System Dynamics, 2006. **16**(1): pp. 55-71.

120. Spitas, C. and V. Spitas, *Calculation of overloads induced by indexing errors in spur gearboxes using multi-degree-of-freedom dynamical simulation.* Proceedings of the Institution of Mechanical Engineers, Part K: Journal of Multi-body Dynamics, 2006. **220**(4): pp. 273-282.

121. Spitas, C. and V. Spitas, *Direct analytical solution of a modified form of the meshing equations in two dimensions for non-conjugate gear contact.* Applied Mathematical Modelling, 2008. **32**(10): pp. 2162-2171.

122. Spitas, C. and V. Spitas, *Fast unconditionally stable 2-D analysis of non-conjugate gear contacts using an explicit formulation of the meshing equations.* Mechanism and Machine Theory, 2011. **46**(7): pp. 869-879.

123. Spitas, C., V. Spitas, and A. Amani, *Multi-parametric investigation of interference in non-standard spur gear teeth.* Mechanism and Machine Theory, 2015. **88**: pp. 105-124.

124. Spitas, C., et al., *Parametric investigation of the combined effect of whole depth and cutter tip radius on the bending strength of 20° involute gear teeth.* Acta Mechanica, 2014. **225**(2): pp. 361-371.

125. Iglesias, M., et al., *Planet position errors in planetary transmission: effect on load sharing and transmission error.* Frontiers of Mechanical Engineering, 2013. **8**(1): pp. 80-87.

126. Han, Q. and F. Chu, *Dynamic behaviours of a geared rotor system under time-periodic base angular motions.* Mechanism and Machine Theory, 2014. **78**: pp. 1-14.

127. Kahraman, A., *Load sharing characteristics of planetary transmissions.* Mechanism and Machine Theory, 1994. **29**(8): pp. 1151-1165.

128. Yuksel, C. and A. Kahraman, *Dynamic tooth loads of planetary gear sets having tooth profile wear.* Mechanism and Machine Theory, 2004. **39**(7): pp. 695-715.

129. Boguski, B., A. Kahraman, and T. Nishino, *A new method to measure planet load sharing and sun gear radial orbit of planetary gear sets.* Journal of Mechanical Design, 2012. **134**(7): pp. 071002-071002.

130. Sondkar, P. and A. Kahraman, *A dynamic model of a double-helical planetary gear set.* Mechanism and Machine Theory, 2013. **70**: pp. 157-174.

131. Velex, P. and L. Flamand, *Dynamic response of planetary trains to mesh parametric excitations.* Journal of Mechanical Design, 1996. **118**(1): pp. 7-14.

132. Lin, J. and R.G. Parker, *Analytical characterization of the unique properties of planetary gear free vibration.* Journal of Vibration and Acoustics, 1999. **121**(3): pp. 316-321.

133. Lin, J. and R.G. Parker, *Sensitivity of planetary gear natural frequencies and vibration modes to model parameters.* Journal of Sound and Vibration, 1999. **228**(1): pp. 109-128.

134. Lin, J. and R.G. Parker, *Structured vibration characteristics of planetary gears with unequally spaced planets.* Journal of Sound and Vibration, 2000. **233**(5): pp. 921-928.

135. Lin, J. and R.G. Parker, *Mesh stiffness variation instabilities in two-stage gear systems.* Journal of Vibration and Acoustics, 2001. **124**(1): pp. 68-76.

136. Lin, J. and R.G. Parker, *Planetary gear parametric instability caused by mesh stiffness variation.* Journal of Sound and Vibration, 2002. **249**(1): pp. 129-145.

137. Parker, R.G. and J. Lin, *Mesh phasing relationships in planetary and epicyclic gears.* Journal of Mechanical Design, 2004. **126**(2): pp. 365-370.

138. Parker, R.G., V. Agashe, and S.M. Vijayakar, *Dynamic response of a planetary gear system using a finite element/contact mechanics model.* Journal of Mechanical Design, 1999. **122**(3): pp. 304-310.

139. Parker, R.G. and V.K. Ambarisha, *Nonlinear dynamics of planetary gears using analytical and finite element models.* Journal of Sound and Vibration, 2007. **302**: pp. 577-595.

140. Eritenel, T. and R.G. Parker, *Modal properties of three-dimensional helical planetary gears.* Journal of Sound and Vibration, 2009. **325**(1–2): pp. 397-420.

141. Bahk, C.-J. and R.G. Parker, *Analytical solution for the nonlinear dynamics of planetary gears.* Journal of Computational and Nonlinear Dynamics, 2010. **6**(2): pp. 021007-021007.

142. Guo, Y. and R.G. Parker, *Dynamic modeling and analysis of a spur planetary gear involving tooth wedging and bearing clearance nonlinearity.* European Journal of Mechanics - A/Solids, 2010. **29**(6): pp. 1022-1033.

143. Parker, R.G. and X. Wu, *Vibration modes of planetary gears with unequally spaced planets and an elastic ring gear.* Journal of Sound and Vibration, 2010. **329**(11): pp. 2265-2275.

144. Guo, Y. and R.G. Parker, *Dynamic analysis of planetary gears with bearing clearance.* Journal of Computational and Nonlinear Dynamics, 2012. **7**(4): pp. 041002-041002.

145. Sun, T. and H. Hu, *Nonlinear dynamics of a planetary gear system with multiple clearances.* Mechanism and Machine Theory, 2003. **38**(12): pp. 1371-1390.

146. Chaari, F., et al., *Influence of manufacturing errors on the dynamic behavior of planetary gears.* The International Journal of Advanced Manufacturing Technology, 2006. **27**(7-8): pp. 738-746.

147. Hbaieb, R., et al., *Dynamic stability of a planetary gear train under the influence of variable meshing stiffness.* Proceedings of the Institution of Mechanical Engineers, Part D: Journal of Automobile Engineering, 2006. **220**(7): pp. 1711-1725.

148. Dhouib, S., et al., *Free vibration characteristics of compound planetary gear train sets.* Proceedings of the Institution of Mechanical Engineers, Part C: Journal of Mechanical Engineering Science, 2008. **222**(8): pp. 1389-1401.

149. Kim, W., J.Y. Lee, and J. Chung, *Dynamic analysis for a planetary gear with time-varying pressure angles and contact ratios.* Journal of Sound and Vibration, 2012. **331**(4): pp. 883-901.

150. Xue, S., et al., *The spur planetary gear torsional stiffness and its crack sensitivity under quasi-static conditions.* Engineering Failure Analysis, 2016. **63**: pp. 106-120.

151. Karray, M., et al., *Modal Analysis of Helical Planetary Gear Train Coupled to Bevel Gear.* Mechatronic Systems: Theory and Applications, 2014: pp. 149-158.

152. Kwon, H.S., et al., *An automated design search for single and double-planet planetary gear sets.* Journal of Mechanical Design, 2014. **136**(6): pp. 061004-061004.

153. Siemens. *Horizontal-axis wind turbine*. Available from: http://www.archiexpo.com/prod/siemens/product-88089-

938754.html?utm_source=ProductDetail&utm_medium=Web&utm_content=SimilarProduct&utm_campaign=CA.

154. WWEA. *Drive Train: An Overview*. 2006 [cited 2012 6th September]; Available from: http://www.wwindea.org/technology/ch01/estructura-en.htm.

155. Akinnuli, B., T. Ogedengbe, and K. Oladosu, *Computer aided design and drafting of helical gears.* Journal of Emerging trends in Engineering and Applied Sciences (JETEAS), 2012. **3**(6): pp. 959-968.

156. Ragheb, A. and M. Ragheb. *Wind Turbine Gearbox Technologies*. In *proc. Nuclear & Renewable Energy Conference (INREC), 2010 1st International*. 2010. IEEE. pp. 1-8.

157. Chang, C.J. *Spur gear modeling*. 2006 [cited 2012 16 September]; Available from: http://coewww.rutgers.edu/classes/mae/mae488/hw/lectures/gear/gear.htm.

158. Rasmussen, F., K. Thomsen, and T.J. Larsen, *The gearbox problem revisited*, 2005.

159. Todorov, M. and G. Vukov. *Parametric Torsional Vibrations Of A Drive Train In Horizontal Axis Wind Turbine*. In *proc. Proc. of the 1ère Conférence Franco-Syrienne sur les Energies Renouvelables, Damas, Syrie*. 2010. pp. 1-17.

160. Qin, D. and F. Tang, *Study on Dynamic Characteristics of Gear Transmission System of Wind Turbine*, in *13th World Congress in Mechanism and Machine Science*2011: Guanajuato, Mexico.

161. Wang, X. and S. Wu, *Nonlinear Dynamic Modeling and Numerical Simulation of the Wind Turbine's Gear Train*, in *International Conference on Electrical and Control Engineering*2011, IEEE Xplore: Yi Chang. pp. 2385-2389.

162. Yu, Y., H. Yuan, and Z. Huang, *Dynamic Characteristics of Gear Transmission System for Wind Turbine Gearbox.* Advanced Materials Research, 2012. **482-484 (2012)**: pp. 2327-2330.

163. Guo, Y., J. Keller, and R. Parker, *Dynamic Analysis of Wind Turbine Planetary Gears Using an Extended Harmonic Balance Approach: Preprint*, 2012, National Renewable Energy Laboratory (NREL), Golden, CO.

164. Holm-Jørgensen, K., *Nonlinear Multibody Dynamics of Wind Turbines*, in *Division of Structural Mechanics, Department of Civil Engineering*2009, Aalborg University: Denmark.

165. Link, H., et al., *Gearbox Reliability Collaborative Project Report: Findings from Phase 1 and Phase 2 Testing*, 2011, National Renewable Energy Laboratory. pp. 88.

166. Keller, J., et al. *Gearbox Reliability Collaborative Phase 1 and 2: Testing and Modeling Results*. In *proc. Proceedings of International Conference on Noise and Vibration Engineering*. 2012. pp. 4381-4389.

167. Peeters, J., D. Vandepitte, and P. Sas, *Structural Analysis of A Wind Turbine And Its Drive Train Using the Flexible Multibody Simulation Technique.* Proceedings of ISMA, 3665e3679, 2006.

168. Sun, T. and H.Y. Hu, *Nonlinear Dynamics of a Planetary Gear System with Multiple Clearances.* Mechanism and Machine Theory, 2003. **38**(12): pp. 1371-1390.

169. Kahraman, A. and R. Singh, *Nonlinear Dynamics of a Spur Gear Pair.* Journal of Sound and Vibration, 1990. **142**(1): pp. 49-75.

170. Masters, G.M., *Renewable and efficient electric power systems*2005: John Wiley & Sons.

171. Norton, R.L., *Machine design: an integrated approach*. Vol. 3. 2006: New Jersey: Pearson Prentice Hall.

172. ISO, *6336-1: 1996, Calculation of Load Capacity of Spur and Helical Gears–Part 1: Basic Principles, Introduction and General Influence Factors*, in *International Organization for Standardization, Geneva, Switzerland*1996.

173. Oyague, F., *Gearbox Modeling and Load Simulation of a Baseline 750-kW Wind Turbine Using State-of-the-Art Simulation Codes*, 2009, National Renewable Energy Laboratory (NREL), Golden, CO.

174. Association, A.G.M., *Standard for Design and Specification of Gearboxes for Wind Turbines*, in *ANSI/AGMA/AWEA 6006-A03*2004: Alexandria, VA, American Gear Manufacturer Association.

175. Singh, R., D.R. Houser, and A. Kahraman, *Non-Linear Dynamic Analysis of Geared Systems*, 1990, DTIC Document.

176. Holm-Jorgensen, K., *Nonlinear Multibody Dynamics of Wind Turbines*, in *Division of Structural Mechanics, Department of Civil Engineering*2009, Aalborg University: Denmark.

177. Sheng, S., M. McDade, and R. Errichello, *Wind Turbine Gearbox Failure Modes: A Brief*, 2011.

178. Link, H., et al., *Gearbox reliability collaborative project report: findings from phase 1 and phase 2 testing*, 2011.

179. Sheng, S., *Wind turbine gearbox condition monitoring round robin study - Vibration analysis*, 2012. pp. 275-3000.

180. Standardization, I.O.f., *Wind turbines - Part 4: Design and specification of gearboxes*, in *ISO 81400-4:2005(E)*2005: Switzerland. pp. 94.

181. NSK, *Technical report*, 2013: Japan.

182. Radzevich, S.P., *Gear Tooth Design*, in *Dudley's Handbook of Practical Gear Design and Manufacture, Second Edition*2012, CRC Press. pp. 85-175.

Publications

International journal publications:

(1). Zhao, M. and J.C. Ji, *Nonlinear torsional vibrations of a wind turbine gearbox.* Applied Mathematical Modelling, 2015. **39**(16): p. 4928-4950.

(2). Zhao, M. and J. Ji, *Dynamic analysis of wind turbine gearbox components.* Energies, 2016. **9**(2): p. 110.

International journal publications under review:

Zhao, M. and J. Ji, *The effects of bending moments on the dynamic responses of wind turbine planetary gearbox components*. Applied Mathematical Modelling, 2015. Ref. No. APM-D-16-01595

The candidate has been the reviewer of the following international journal:

(1). Wind energy

(2). Part C: Journal of Mechanical Engineering Science

(3). IET Renewable Power Generation